Electron bunch diagnostics for laser-plasma accelerators, from THz to X-rays

Guillaume Plateau

Dissertation submitted in partial satisfaction of the requirements
for the degree of

Doctor of Philosophy in Physics

in the graduate division of the

École Polytechnique

Electron bunch diagnostics for laser-plasma accelerators, from THz to X-rays

by

Guillaume Plateau

Committee in charge:

M. Patrick Mora	Chair
M. Wim Leemans	Thesis co-supervisor
M. François Amiranoff	Thesis co-supervisor
Mme Brigitte Cros	Reader
M. Guy Bonnaud	Reader
M. Jean-Raphaël Marquès	
M. Gwénaël Fubiani	
M. Jérôme Faure	

For my mother.

Table of contents

Chapter 1

General Introduction

1.1 About this Thesis

The work presented in this dissertation was performed in the LOASIS facilities at the Lawrence Berkeley National Laboratory (LBNL) in Berkeley, California. As a graduate student at École Polytechnique, I was supervised by Dr. François Amiranoff, director of the Laboratoire pour l'Utilisation des Lasers Intenses (LULI) and Dr. Wim Leemans, director of the LOASIS group at LBNL.

This dissertation describes a full set of single-shot non-intrusive diagnostics for the laser-plasma accelerator (LPA). Both a gas jet and a capillary-based LPA were used during this PhD. Using the gas jet-based accelerator, three injection mechanisms were characterized: channeled and self-guided self-injection, plasma down-ramp injection, and two-beam colliding pulse injection.

A new technique for plasma density measurements based on wavefront sensing was demonstrated at LBNL[1] [1]. The technique, which offers greater sensitivity and ease of use, was used to characterize and optimize the plasma density profiles during gas

[1] *Wavefront-sensor-based electron density measurements for laser-plasma accelerators*, G. R. Plateau, N. H. Matlis, C. G. R. Geddes, A. J. Gonsalves *et al.*, Review of Scientific Instruments, **81**(3), 033108 (2010)

jet experiments. In addition, two analysis softwares were developed for both transverse interferometry and electron spectrometry which provided the plasma density and the electron bunch energy and divergence distribution, respectively.

Stable low absolute momentum-spread electron bunches were produced using plasma density gradients to control the wake phase velocity and trapping threshold in the accelerator [2] [2]. In combination with simulations, coherent transition radiation (CTR) in the terahertz (THz) regime showed the bunches ($\leq$ 30 fs) could be used as LPA injectors.

Extensive work was performed on characterizing and optimizing the THz radiation emitted by the electrons as they exit the plasma [3] [4] [3, 4]. In this dissertation, one of the new techniques for single-shot THz measurements which resolves both time and one dimension of space is presented. The two-component structure of the bunches observed by the electron spectrometer during self-guided self-injection regime experiments was confirmed and correlation between bunch duration and accelerator performance was observed.

The sub-micron transverse size and emittance of the electron bunch was demonstrated by single-shot direct measurements of the betatron X-ray radiation emitted by the electrons inside the plasma [5] [6] [5, 6]. Single-shot betatron spectra were measured with 250 eV resolution using the Single Photon Absorption Event (SPAE) technique,

[2] *Plasma-Density-Gradient Injection of Low Absolute-Momemtum-Spread Electron Bunches*, C. G. R. Geddes, K. Nakamura, G. R. Plateau, Cs. Tóth *et al.*, Physical Review Letters, **100**(21), 215004 (2008)

[3] *Single-shot spatiotemporal measurements of ultrashort THz waveforms using temporal electric-field cross correlation*, N. H. Matlis, G. R. Plateau, J. van Tilborg and W. P. Leemans, Journal of the Optical Society of America B, **28**(1), 23 (2011)

[4] *Single-shot measurement of the spectral envelope of broad-bandwidth terahertz pulses from femtosecond electron bunches*, J. van Tilborg, Cs. Tóth, N. H. Matlis, G. R. Plateau and W. P. Leemans, Optics Letters, **33**(11), 1186 (2008)

[5] *Ultra-low-emittance electron bunches from a laser-plasma accelerator measured using single-shot x-ray spectroscopy*, G. R. Plateau, C. G. R. Geddes, M. Chen, D. B. Thorn *et al.*, Physical Review Letters, submitted (2011)

[6] *Single-shot direct X-ray spectra of betatron emission from a laser-plasma accelerator*, G. R. Plateau, C. G. R. Geddes, D. B. Thorn, M. Chen *et al.*, Physics of Plasmas, in preparation (2011)

and confirmed the synchrotron nature of the emission [7] [8] [7, 8]. In addition, the LPA is shown to provide a scalable, bright, broadband, femtosecond source of keV X-rays intrinsically temporally synchronized to the driver laser pulse, enabling pump-probe studies in ultra-fast science.

This dissertation is separated into six Chapters. The first Chapter presents an overview of the research field of laser-plasma acceleration. Chapter 2 introduces the basic physics of the LPA and an overview of the concepts of plasma wave, laser propagation, electron trapping, and acceleration is presented and provides the foundations for the analyses and discussions following in this dissertation.

Chapter 3 presents two aspects of the optimization of a laser-plasma accelerator. First, because the performance of an LPA depends on the plasma wavelength, *i.e.*, on the electron density, part of this Chapter focuses on the characterization of the electron density. A novel technique using direct wavefront analysis of a probe laser beam is presented. Density measurements using a conventional folded-wave interferometer and using a commercial wavefront sensor are compared for different regimes of the laser-plasma accelerator. It is shown that direct wavefront measurements agree with interferometric measurements and, because of the robustness of the compact commercial device, have greater phase sensitivity, simplifies analysis, thus improving shot-to-shot plasma-density diagnostics.

The second part of Chapter 3 focuses on one of the key challenges to achieve compact, reliable, tunable LPAs: decoupling injection from acceleration. In colliding pulse injection the beat between multiple laser pulses can be used to control energy, energy spread, and emittance of the electron beam by injecting electrons in momentum and

[7] *Spectroscopy of betatron radiation emitted from laser-produced wakefield accelerated electrons*, D. B. Thorn, C. G. R. Geddes, N. H. Matlis, G. R. Plateau *et al.*, Review of Scientific Instruments, **81**(10), 10E325 (2010)

[8] *On the betatron radiation calculation of laser-plasma accelerators*, M. Chen, C. G. R. Geddes, G. R. Plateau, C. B. Schroeder, E. Esarey and W. P. Leemans, Physical Review Special Topics – Accelerators and Beams, in preparation (2011)

phase into the accelerating phase of the wake trailing the driver laser pulse. Using automated control of spatiotemporal overlap of laser pulses, two-pulse experiments show stable operation and reproducibility over hours of operation. Arrival time of the colliding beam is scanned, and the measured timing window and density of optimal operation agree with simulations. The accelerator length is mapped by scanning the collision point.

As discussed in Chapter 1, the ability of laser-plasma accelerators to generate ultrashort electron bunches in a compact setup offers the unique possibility of providing a compact source of radiation ranging from terahertz to γ-rays. In the course of this thesis, two particular forms of radiation have been measured using both single-shot and scanning techniques: THz and X-ray radiation.

Chapter 4 presents the detection of coherent transition radiation (CTR) in the terahertz (THz) regime. After a brief overview of the theory of transition radiation, bolometric measurements of CTR emitted by downramp injected electron bunches are reported. A plasma downramp in a gas jet is used to control the wake phase velocity and trapping threshold, producing low energy (0.76 ± 0.02 MeV/c) stable electron bunches with longitudinal and transverse momentum spreads more than 10 times lower than in previous experiments (0.17 and 0.02 MeV/c FWHM, respectively). The temporal characterization of the electron bunch, combined with simulations, indicate that the technique could be used as an LPA injection mechanism and could lead to $< 0.1\%$ energy spread GeV-class electron beams.

Also in Chapter 4, transition radiation of self-injected electron bunches is measured using two-dimensional electro-optic measurements which reveal a strong spatiotemporal coupling of the THz pulse at focus, motivating the development of a single-shot technique capable of solving both space and time. The last section of Chapter 4 presents a new high-resolution ($\lesssim 50$ fs) single-shot technique for measuring the spatiotemporal phase and amplitude of an optical probe, based on linear spectral interferometry between a

temporally short reader pulse and a temporally long probe pulse. The technique is used to characterize self-injected electron bunches. The presence of strong spatiotemporal coupling in the THz waveforms is also observed and a complex temporal electron bunch structure is determined.

In the last Chapter (Chapter 5), single-shot direct spectral measurements of betatron X-ray radiation from electrons produced by both gas jet- and capillary-based LPAs are demonstrated and used to study the X-ray source and the accelerated electrons. The X-ray radiation from betatron emission is collected by a photon-counting pixelated Silicon-based detector with a 1–20 keV sensitivity range. Single-shot betatron spectra are measured with 250 eV resolution using the SPAE technique. Analysis of the X-ray spectra, together with simultaneous electron energy spectra and divergence measurements, indicate the electron bunch source size is of the order of 0.1–0.2 μm, in agreement with particle-in-cell code simulations, and the normalized transverse geometric emittance is $\epsilon_x < 0.4$ mm.mrad. Single-shot measurements of the energy (~ 0.5 GeV, $< 10\%$ energy-spread), the divergence ($\sim$ 1 mrad), and the transverse size ($\sim$ 0.1 μm) of electron bunches suitable for injection into a free-electron laser (FEL) are reported. Comparison of X-ray spectra calculated using synchrotron radiation theory with measured spectra further allows estimation of the wakefield amplitude. In addition to providing single-shot diagnostics of bunch size and plasma wake structure, this table-top setup is shown to provide a bright source of keV X-rays suitable for pump-probe experiments.

Lastly, Chapter 6 presents conclusions and possible directions of future work.

1.2 Motivation for plasma-based acceleration

The main reason to study particle accelerator physics is to provide accelerators to be used as tools to study and manipulate fundamental processes in matter (radiotherapy, medical imaging, X-ray lithography, electron beam welding, ion implantation), or to study fundamental particles, their interactions, and test theoretical models. Over the last century conventional accelerators (*e.g.*, linear accelerators, cyclotrons, synchrocyclotrons, and synchrotrons) were designed, built, and improved to produce high quality particle bunches for both low and high energy physics. In this thesis the focus is on electron acceleration only. Charged particles radiate when accelerated, this is called synchrotron radiation for circular motion, it strongly limits the accelerator efficiency for light particles like electrons. One way to limit the loss by synchrotron radiation is to increase the radius of curvature for circular machines, like for the former Large Electron-Positron (LEP) collider at the Centre Européen de Recherche Nucléaire (CERN) which had a circumference of 27 km and produced electrons with energies up to 104.5 GeV. Another way to accelerate electrons efficiently is to use linear structures, like the International Linear Collider (ILC) project which will be 31 km in length and accelerate electrons to energies of 500 GeV (500 billion-electron-volts). Particle accelerators are key tools for both fundamental and applied sciences but for obvious budgetary reasons there is a need to find more compact, more efficient ways to accelerate particles.

To increase the energy of a bunch of electrons an electric field is required. The simplest way to produce an electron bunch is to heat a piece of metal, place a positively charged plate in front with a hole in it: heat boils electrons off the metal, the potential difference provides an accelerating force and the electrons making it through the hole form the bunch. To reach high energies, the direct current (dc) voltage applied to the plate has to increase as well. Since it is difficult to generate very high dc voltages, methods were developed to accelerate electrons using alternating current voltage,

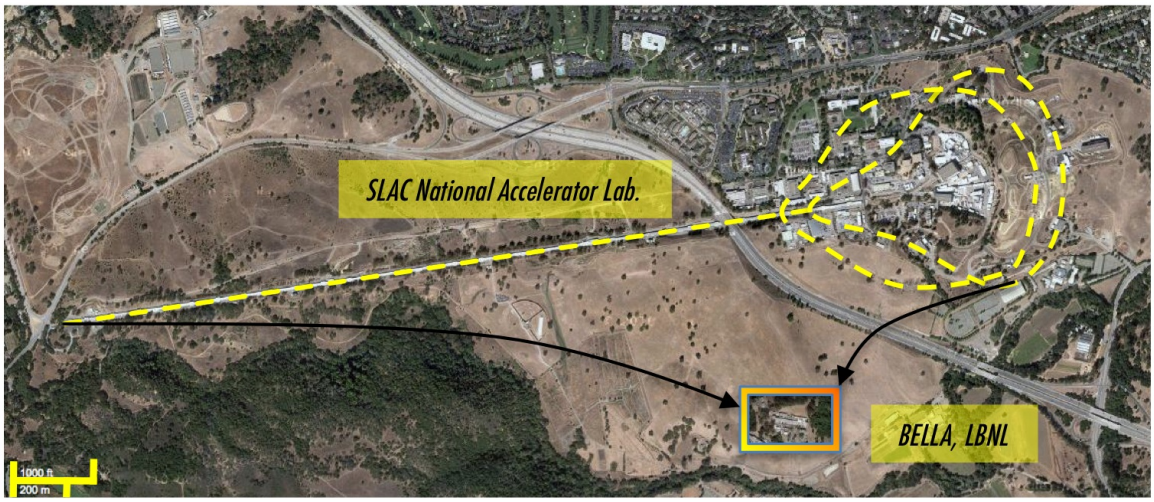

Figure 1.1: An example of conventional linear accelerator facility, the SLAC national accelerator laboratory; and an example, at the same scale, of laser-plasma accelerator, BELLA at the LBNL. *©2010 Google – Imagery ©2010 DigitalGlobe, USDA Farm Service Agency, GeoEye, U.S. Geological Survey*

generated by radio-frequency (RF) electronic oscillators. For this reason, conventional accelerators are also called RF accelerators. In a RF accelerator, the polarity of a series of accelerating structures is alternated as the electrons travel through one of them, so that they always see an accelerating electric field. From the 1928 Wideröe drift tube structure to the RF cavities of the ILC, conventional accelerators have had two major limitations: the maximum voltage, thus accelerating gradient, which can be applied to an element of the structure without damaging it, and its elements size. For example, the ILC will have accelerating gradients on the order of 30 MV/m. At these gradients, more than 30 meters are needed to accelerate an electron up to 1 GeV. In 2006, 27 years after the enunciation of its principles by T. Tajima and J. M. Dawson [9], a laser-plasma accelerator produced 1 GeV electron beams using a single 3.3 cm long stage [10].

A plasma is a distinctive state of matter where atoms are ionized. Unlike any gas, plasma particles behave collectively because local charge concentrations may occur, creating local electric fields which put particles into motion and induce magnetic fields which

affect surroundings particles motion, and so forth. External electromagnetic fields can be used to manipulate plasmas, and create local charge separations between electrons and ions of the medium, thus generate local electric fields suitable for electron and positron acceleration. Like a gas, a plasma is characterized by its constituents and its density. For electron densities (n_e) of 10^{18} – 10^{19} electrons per cubic-centimeter [e^-/cm^3], plasmas can sustain local accelerating electric fields in excess of 100 – 300 GV/m, which is a thousand to 10 thousand times greater than what conventional accelerators have achieved, making it possible to reach high energies over thousand times smaller distances (30 meters becomes 3 cm, Fig. 1.1).

However, plasma-based accelerators [11] face several challenges before they can produce the high energy, high quality electron bunches that are typically generated by state-of-the-art RF accelerators. For an accelerator user, some of the important parameters are the type of particles accelerated (electrons in this thesis), the repetition rate of the accelerator, the average energy, the energy spread, the total amount of charge, the transverse size, the duration, the divergence of the bunch, and the cost of the accelerator. Laser-plasma accelerators, on which this thesis focuses, have demonstrated electron bunches of 1 GeV and few percent energy spread but need to reach even higher energies to compete with state-of-the-art RF accelerators. Also, in order to use laser-plasma accelerators (LPA) as colliders for high energy physics, higher repetition rates (*i.e.*, number of bunches per second) have to be achieved. Nevertheless, laser-plasma accelerators already represent a competitive alternative to RF accelerators as a radiation source (*e.g.*, laser, electrons, ions, X-rays, THz radiation, γ-rays, EUV/UV emission). Laser-plasma accelerators benefit from research and development in laser technologies which are of interest for numerous industries (*e.g.*, military, medical, commercial). Finally, cavity wall breakdown is irrelevant when using plasmas, which can easily be replaced after a bunch was accelerated by simply replenishing some fresh gas.

1.3 The laser-driven plasma wakefield accelerator

The laser-plasma accelerator was first proposed by T. Tajima and J. M. Dawson [9]. A comprehensive review of the laser-plasma accelerator is presented in E. Esarey *et al.* [12]. In an LPA, a focused intense laser pulse, typically $I > 10^{18}$ W/cm^2, propagates through a plasma, typically of Hydrogen (H^+) or Helium (He^{2+}). The laser ponderomotive force pushes background plasma electrons away from the surroundings ions. The charge displacements induce a train of electrons oscillations behind the laser pulse, called a wakefield or plasma wave, an electron density oscillation with a phase velocity close to the laser group velocity. The large electric fields ($\gtrsim$ 100 GV/m) generated by the plasma wave are used to accelerate electrons to high energies over short distances (Fig. 1.2). Various schemes for injecting electrons into the accelerating phase of the plasma wave have been discussed in the literature and demonstrated in the laboratory (*e.g.*, self-trapping [13, 14, 15], external injection [16, 17, 18], plasma density ramp [19, 2], colliding laser pulses [20, 21, 22]).

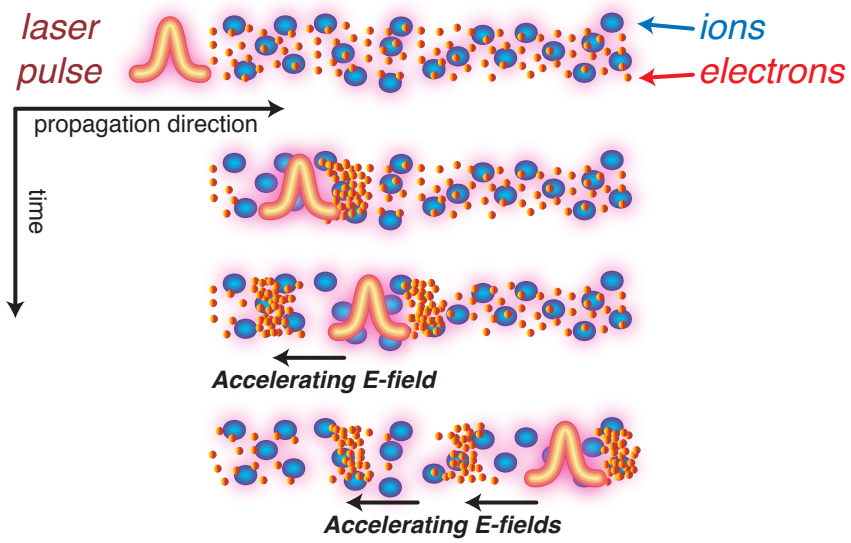

Figure 1.2: In a laser-plasma accelerator, the ponderomotive force of an intense laser pulse expels the electrons of the plasma, creating high and low electron density regions. Hence, high longitudinal electric fields are generated that are suitable for electron acceleration.

From the early 1980's to the mid-2000's, the field of plasma-based accelerators has become a competitive alternative to conventional accelerators (*c.f.* 1.2). Thanks to the significant progress already made and the promise for future successes, research programs are present, in alphabetical order, including in China, Denmark, France, Germany, Greece, Italy, Japan, the Netherlands, Portugal, South Korea, Sweden, Taiwan, the United Kingdom, and the United States. It was with the late 80's and early 90's development of intense ($> 10^{18}$ W/cm^2), high power ($\gtrsim$ TW), ultrashort lasers (< 1 ps) that suitable plasma waves [23, 24] for electron acceleration could be generated.

Applying a technique used in radar communication of short and energetic pulses [25], D. Strickland and G. Mourou [26] introduced in 1985 the chirped-pulse amplification (CPA) technique, on which state-of-the-art tera- and petawatt (10^{12} and 10^{15} Watts) laser systems are based [27, 28]. The CPA technique allows the amplification of an ultrashort high-peak-power optical pulse, which otherwise is often limited by nonlinear effects such as self-focusing and saturation in the optical amplifier [29]. Following the example of the LOASIS laser system, an initial low energy ($\sim$ 40 nJ), short laser pulse (800 nm, $\simeq$ 20–30 fs) is stretched ($\sim$ 200 ps) by use of a chirp filter ("stretcher"), which means that the instantaneous frequency of the stretched pulse is time varying. While the energy of the pulse can be conserved, its peak-power is lowered. By distributing the energy over a longer time, saturation of the optical amplification of the laser pulse energy in a Titanium-sapphire crystal (Ti:Al_2O_3) is reached at the Joule per square-centimeter level ($\simeq$ 0.5–1.5 J/cm^2). In order to avoid damaging beam transport optics, the laser beam is typically simultaneously enlarged to limit its fluence. Finally, the laser pulse is compressed back to its original duration by use of a chirp filter ("compressor") of roughly equal magnitude and opposite sign as the stretcher and compensating for all the dispersion encountered while the pulse propagated through the amplifier chain. Such laser pulses ($\simeq$ 35–50 fs), focused down to 5–20 μm spot sizes yield peak-intensities in

excess of 10^{19} W/cm^2, suitable to drive nonlinear plasma waves.

Eight years after the first direct observation in 1985 of a laser-driven plasma wakefield [30], the first electron bunches accelerated by a laser-plasma accelerator were reported using external injection by C. E. Clayton *et al.* [18]. Laser-plasma acceleration was demonstrated by several groups throughout the late 1990's [31, 13, 32, 33, 34, 35, 36, 37, 38] but these initial electron beams were low energy ($\lesssim$ 30 MeV) beams with large energy spreads, typically an exponential energy distribution extending to high energy ($\sim$ 100 MeV), limiting their use for potential applications.

In 2004, three groups, in the U.K. at Imperial College (S. P. D. Mangles *et al.* [39]), in the U.S.A. at LBNL (C. G. R. Geddes *et al.* [40]) and in France at the École Polytechnique's LOA (J. Faure *et al.* [41]), simultaneously reported the production of high-quality electron bunches with less than 10% energy spread, energies on the order of 100 MeV, and 20 to 500 pC of charge. These results were the fruit of a better understanding of the underlying physics of the laser-plasma accelerator, especially the self-focusing effects of intense laser pulses in plasmas, the resonant excitation of plasma waves by self-modulation of the laser pulse when its length exceeds a plasma wavelength and in the case of the LBNL group the guiding of laser pulses, and the importance of matching the accelerator length to the dephasing length, which is the distance it takes the accelerated electrons to outrun the wave. Each of these publications was supported by the development in the early 2000's of simulation tools using particle-in-cell (PIC) numerical codes [42] such as OSIRIS [43], VORPAL [44], VLPL [45], which, to date, are routinely used to understand and optimize plasma-based accelerators.

The formulation of an analytical description of nonlinear laser-driven plasma waves was presented in 1990 by P. Sprangle *et al.* [46, 47] (Chapter 2) based on previous work on plasma wave excitation [48, 49]. In this model the plasma is described as a one-dimensional fluid and the laser pulse is assumed to not evolve. This work was based,

among others, on the work of A. I. Akhiezer and R. V. Polovin [50], J. .M. Dawson [51], T. P. Coffey [52], T. Katsouleas [53] who had found the maximum amplitude of, respectively, relativistic cold (1956), non-relativistic cold (1959), non-relativistic warm (1971), and relativistic warm plasma waves (1988). Soon after, in 1992, P. Sprangle *et al.* [54] presented a two-dimensional relativistic fluid model of laser propagation in a plasma for both short and long pulses, for which self-modulation at the plasma period occurs [55]. The trapping and the energy gain of an electron in a cold fluid plasma wave was provided by E. Esarey and M. Pilloff in 1995 [56]. C. B. Schroeder *et al.* presented a warm relativistic fluid theory of the breaking of plasma waves in a non-relativistic plasma (2005) [57], and of the minimum initial electron momentum for trapping (2006) [58].

In order to generate high-quality electron beams at higher energies while keeping the power, the size and cost of the laser relatively low ($<$ 100 TW), the acceleration length needs to be increased, which can be achieved by optical guiding, and the plasma density decreased as to extend the dephasing length. An extensive description of optical guiding of intense laser pulses in plasmas is provided by E. Esarey *et al.* [59]. Much like an optical fiber, a preformed plasma density channel can provide refractive guiding to an intense laser pulse. In 2004, C. G. R. Geddes *et al.* [40] reported the production of 320 pC, 86 MeV, 4% full width at half-maximum (FWHM) energy spread electron beams by guiding a 0.5 J, 55 fs FWHM laser pulse in a 2.4 mm long supersonic Hydrogen gas jet using the "ignitor-heater" technique [60]. In this technique, an initial ultrashort laser pulse (60 fs) is used to ionize a cylindrical filament of plasma, and a longer (250 ps) laser pulse is used to heat it as to obtain an expanding hot plasma (tens of electronvolts) which forms a nearly parabolic transverse density profile, hence, index of refraction. Unfortunately, laser plasma heating is inefficient at the low densities ($< 10^{19}$ e^-/cm^3) necessary to reach centimeter-scale dephasing lengths. In 2006, W. P. Leemans *et al.* [10]

reported the production of a 1 GeV (1000 MeV), 30 pC, 2.5% root-mean-square (*rms*) energy spread, 1.6 mrad divergence electron beam by guiding a 40 TW peak power, 40 fs FWHM laser pulse through a 3.3 cm-long Hydrogen gas-filled capillary discharge waveguide [61, 62], where the hot plasma is obtained by an electric discharge between two electrodes located on each side of a gas-filled waveguide.

However, reaching high energies is not the only challenge that plasma-based accelerators face. Plasma-based accelerators have to provide reliable and tunable sources of electrons and photons, which require decoupling injection from acceleration. Hence, advanced diagnostics are needed for a good understanding of laser-plasma acceleration physics. An independent controlled injection mechanism leads to an engineered beam quality, and the freedom to design the plasma structure for high efficiency. In this thesis, three different injection regimes have been explored: self-injection, downramp injection, and colliding pulses injection. Self-injection relies on temperature spread of the plasma to capture background electrons in the accelerating phase of the wave. In this scheme, which typically requires generation of large amplitude plasma wakefields, injection and acceleration are strongly coupled. In the downramp injection scheme, a downward transition is introduced to slow-down the phase velocity of the wake. Trapping occurs behind the laser pulse where the phase velocity of the wake matches the fluid velocity [63, 64, 65, 2]. This technique could provide small energy spread electron bunches to secondary acceleration structures. Additional laser pulses can be used to optically trigger the injection of electrons into the wake. The beat wave between multiple laser pulses can be used to control energy, energy spread, and emittance of the electron beam [20, 21, 66, 22, 67].

1.4 Radiation from an LPA and diagnostics

To increase understanding of the laser-plasma accelerator, insightful diagnostics of both the laser-plasma interaction and the accelerated electron beams need to be developed in order to provide comparison between experiments, numerical PIC simulations, and analytical models. Laser-plasma accelerators have several features which require re-evaluation of electron bunch diagnosis used for conventional accelerators, and the development of new ones. For example, the energy distribution of the produced electron bunches can be broad and require the acquisition of a large energy range [68] (1–2 orders of magnitude, *e.g.*, 10–100 MeV). Another remarkable feature of LPAs is their ability to produce ultrashort [69, 70] ($\leq$ 50 fs *rms*), small transverse size electron bunches [6] ($\sim$ μm *rms*). Such small bunches require the development of detection method with ultrahigh resolution. Moreover, laser-plasma accelerators still suffer from shot-to-shot fluctuations in the plasma, laser, and consequently electron bunch and secondary radiation (THz, X-ray) parameters. For this reason, LPA diagnostics need to provide single-shot, non-invasive measurements of these actors simultaneously.

In this thesis, laser, plasma, and electron diagnostics are investigated. Laser measurements include high-resolution temporal intensity profile via third-order cross-correlation, and a new technique is proposed for plasma density diagnostics [1]. An electron beam is characterized by its charge, energy distribution, divergence, emittance, duration and size. The charge is provided by mean of an integrating charge transformer (ICT) and of an electron magnetic spectrometer. Part of the technical work of this thesis was to implement the analysis of this electron spectrometer which provides single-shot charge, energy distribution and divergence of the accelerated electron beams.

1.4.1 Coherent Transition Radiation

The bunch duration is measured indirectly by a widely-used technique, in both conventional and plasma-based accelerators, called electro-optic sampling. This technique measures the change of birefringence in an electro-optic (EO) active crystal (*e.g.*, ZnTe, GaP) by the effect of an external electric-field. Two electromagnetic signatures of the electron bunch can be used to induce birefringence in the crystal: either the Coulomb field of the bunch, or the coherent transition radiation emitted when the electron bunch passes through the interface between two media with different dielectric constant (relative permittivity ϵ_r) [71]. In the harsh environment of the laser-plasma accelerator where the intense defocusing laser pulse, after interaction with the plasma, can damage the EO crystal, direct probing of the bunch self-field can be difficult. On the other hand, coherent transition radiation (CTR) which is in the terahertz (10^{12} Hz or THz) frequency band can be collimated and transported to a secondary setup and be used either as a bunch diagnostics or as a source of energetic (> 1 μJ), short (~ 1 ps) THz pulses. Figure 1.3 provides a heuristic picture of transition radiation at a sharp metal–vacuum interface. The relative permittivity, which is basically a measure of the ratio of polarization of a medium to the applied electric field [72] ($\epsilon_r = 1 + \mathbf{P} \cdot \mathbf{E}/\epsilon_0 \mathrm{E}^2$), is large for a metal since it can sustain large polarization ($\epsilon_r \gg 1$). Such polarization causes the electric field inside the conductor to be small (electrostatic equilibrium). Thus, the Coulomb field of a relativistic electron bunch, which can be shown to be transverse to the direction of propagation in the laboratory frame, traveling through a metal is partially screened by the surrounding electrons. On the other hand, in vacuum the field expands due to the lack of screening. At the transition, as the field expands it repels its surroundings electrons, resulting in a near single-cycle radial oscillation of the surface electrons around their neighboring ions which is responsible for the emission of a forward near single-cycle electromagnetic wave (transition radiation), as illustrated in Fig. 1.4.

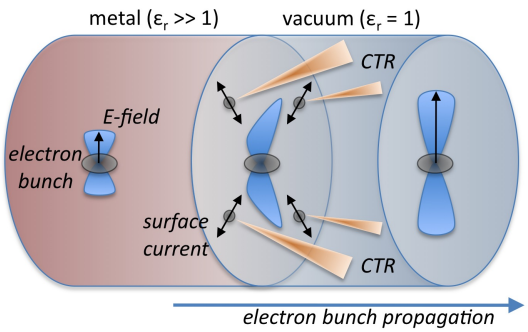

Figure 1.3: Heuristic picture of transition radiation emitted at a sharp metal–vacuum boundary. As the bunch propagates through the plasma, its Coulomb field expels the surrounding electrons. At the plasma-vacuum interface (critical density for THz waves), the CTR emission induced by this transverse current can propagate forward.

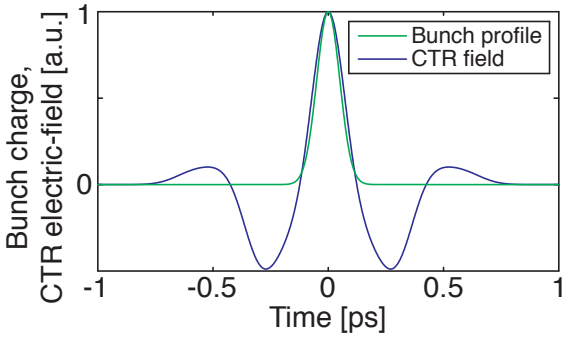

Figure 1.4: Example of temporal electric field profile (CTR pulse) emitted at a plasma–vacuum boundary (*blue* curve) and the electron charge distribution (*green* curve) which induced its generation upon exiting the plasma. The delay between the THz pulse and the electron bunch is not represented for clarity sake.

In a conventional accelerator CTR is produced by placing a thin metallic foil [73, 74, 75] in the path of the electron bunch, thus providing a discontinuity vacuum ($\epsilon_r = 1$) – metal ($\epsilon_r \gg 1$) – vacuum ($\epsilon_r = 1$). In a laser-plasma accelerator, this technique can be difficult to implement for two reasons: risks of damaging the foil with the remaining energy of the laser pulse after the interaction with the plasma, and because of important space-charge effects [76] due to a high charge density ($> 10^{19}$ e^-/cm^3), a relatively low energy (< 100 MeV), and a large energy spread of the electron bunch in some regimes of the accelerator (*e.g.*, self-trapping), the bunch is subject to spread both longitudinally and transversely, limiting the coherency of the transition radiation.

Fortunately, in a plasma-based accelerator coherent transition radiation is emitted at the plasma–vacuum boundary [77]. In the absence of magnetic fields, the relative permittivity of a cold plasma [78] is $\epsilon_r(\lambda) \simeq 1 - \lambda^2/\lambda_p^2$, where $\lambda_p\,[\mu\mathrm{m}] \simeq 3.34 \cdot 10^{10}/\sqrt{n_e\,[e^-/\mathrm{cm}^3]}$ is the plasma wavelength [79], n_e is the plasma density (electrons per unit of volume) which, in the experiments, typically ranges from 10^{18} to $5 \cdot 10^{19}$ e^-/cm^3 ($\lambda_p \simeq 5$ to 33 μm), and λ is the radiated light wavelength. Because of the severe drop in relative

permittivity for wavelengths greater than the plasma wavelength, the plasma-vacuum interface acts as a sharp boundary between two media with different dielectric constants. An additional argument in favor of approximating the interface as a sharp boundary is the consideration of the distance over which the transition radiation develops, also called the formation length, which will be shown in Chapter 4 to be larger than the thickness of the interface for relativistic electrons.

Ultrashort terahertz pulses with energies in the μJ range, with high peak-electric-field (MV/cm) suitable for pump-probe experiments, have been measured and used for high-resolution (femtosecond-scale, one millionth of a billionth of a second: 10^{-15} s) temporal characterization of the electron bunches produced by the accelerator [77, 70, 3]. Theoretical analysis [80, 81] reveals a strong dependence of the THz (CTR) peak-power on the bunch charge, plasma size (diffraction effects), bunch length (coherence effects), and electron energy. Since each electron in the bunch emits independently, the radiation only constructively interferes if the bunch is shorter than the emitted wavelength. The bunch length thus sets the cut-off frequency of the THz spectrum (typically 5–10 THz). An example of CTR electric-field, based on the equations in Ref. [80], is given in Figure 1.4, for a Gaussian distribution of the electron bunch (50 fs *rms* long), a plasma density and radius of $3 \cdot 10^{19}$ e^-/cm^3 and 300 μm, respectively.

1.4.2 Betatron X-ray radiation

In addition to generating intense THz pulses, laser-plasma accelerators offer the possibility of generating femtosecond [82, 83] kiloelectronvolt (keV) X-ray pulses. At present, an immediate application of relativistic electron beams is the generation of X-rays for biological, medical, and material science applications. Conventionally, kiloelectronvolt X-rays are produced by injecting multi-GeV electron bunches into permanent magnetic undulators, typically of centimeter- or millimeter-scale periods. Replacing these large fa-

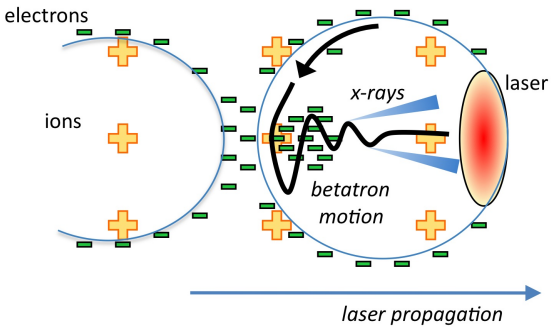

Figure 1.5: Heuristic picture of X-ray radiation emitted by betatron motion of self-trapped electrons in the *bubble* regime. The volume of positive charge behind the intense laser pulse acts as a wiggler.

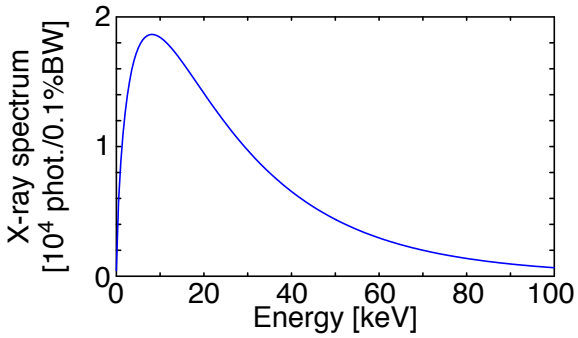

Figure 1.6: Example of X-ray spectrum emitted by a 100 MeV, 3 μm *rms* radius electron bunch undergoing betatron oscillations in a laser-driven plasma wakefield. The spectrum was calculated for a 3 mrad collection angle.

cilities (*e.g.*, synchrotron facilities) by smaller scale university, or hospital facilities would enable a large range of applications to become possible. In a laser-plasma accelerator, the wakefield generated behind the driver laser pulse acts as a strong focusing channel in which off-axis injected electrons undergo oscillations, typically of sub-millimeter period, suitable for generating collimated keV X-ray radiation from sub-GeV electron bunches [84, 85, 86, 87, 6].

For high laser intensities, the ponderomotive force of the laser pulse expels all plasma electrons. In this regime, referred to as the "bubble" or "blow-out" regime [88, 89, 90, 91, 92] because a somewhat spherical cavity free from plasma electrons is formed behind the laser pulse, the wake undergoes a transverse wavebreaking [19, 12] which results in off-axis injection of background electrons. The transverse wavebreaking is due to a curvature of the wavefront of the plasma wave for nonlinear regimes [93]. Because the laser intensity peaks on-axis, the plasma wave amplitude is maximum on axis, and because the nonlinear plasma wavelength increases with the wave amplitude, the plasma wavelength varies as a function of the distance from the axis of propagation, so that the wavefront takes the shape of a "C". The very large radial focusing field inside the bubble causes the electrons to undergo betatron oscillations [94], as illustrated in Figure 1.5.

Since the bubble travels near the speed of light behind the laser pulse, it can be described as a static ion column [82], for which the betatron wavelength of a single electron, in the absence of acceleration, can be calculated to be $\lambda_\beta = \lambda_p\sqrt{2\gamma} \propto \sqrt{\gamma/n_e}$, where γ is the relativistic factor of the electron. At a plasma density of $3 \cdot 10^{19}$ e^-/cm^3 and for typical electron distributions ranging from 10 to 100 MeV, $\lambda_p \simeq 6$ μm, $\gamma \simeq 20 - 200$, and $\lambda_\beta \simeq 38 - 120$ μm. This betatron motion induces directional synchrotron radiation within a cone of angle $\theta \simeq a_\beta/\gamma$, where $a_\beta \propto \sigma_r$ is the betatron strength parameter, the equivalent to the undulator strength for conventional accelerators, and σ_r is the amplitude of the radial oscillation of the electron. In this geometry, the cut-off energy ($\hbar\omega_c$) of the X-ray spectrum is given, in practical units, by $\hbar\omega_c[\mathrm{keV}] \simeq 1.1 \cdot 10^{-4}\gamma^2\, n_e[10^{19}\ e^-/\mathrm{cm}^3]\, \sigma_r[\mu\mathrm{m}]$. For a 100 MeV electron beam, an electron density of $2 \cdot 10^{19}$ e^-/cm^3, and a bunch radius of 3 μm *rms*, $\hbar\omega_c \simeq 25$ keV. The expected spectrum within a 3 mrad collection angle, assuming a bunch charge of 300 pC, an energy spread of 3%, and a plasma channel of 1 mm length, is given in Fig. 1.6. Hence, in addition to providing a source of collimated keV X-ray beams, betatron radiation provides insightful information on the electron bunch transverse profile, both through its spatial distribution and its spectrum.

Chapter 2

Laser-Plasma Acceleration

2.1 Ionization and plasma waves

As introduced in Chapter 1, plasmas are attractive media for particle acceleration because they can sustain high electric fields. Electric fields can be generated inside a plasma by creating local variations of the electron densities. In a laser-plasma accelerator, this charge displacement is the result of the ponderomotive force applied by an intense laser pulse onto the background plasma electrons (Fig. 2.1). In the experiments described in this thesis, laser intensities vary from 1.5×10^{18} to 3.5×10^{19} W/cm^2 and the gas used to form a plasma is either Hydrogen (H^+) or Helium (He^{2+}) at densities ranging from 10^{18} to 8×10^{19} e^-/cm^3. At these high laser intensities and at these gas densities, the gas turns into a fully ionized plasma since the minimum ionization intensity, $I_{\rm min}$, is much smaller than the laser intensities $I_{\rm min}^{\rm H_2} < I_{\rm min}^{\rm He} \simeq 8.8 \times 10^{15}$ W/cm^2 $\ll 10^{18}$ W/cm^2). Also, the laser energy loss by ionization, $\mathcal{E}_i$, is typically neglected. For instance, for a 2 mm long, 0.2 mm radius fully ionized column of Helium gas at a density of $3 \cdot 10^{19}$ e^-/cm^3 the energy loss by ionization can be estimated by $\mathcal{E}_i \sim n_e \pi r_p^2 L E_i / Z \simeq 33$ mJ $\ll$ 0.5–2 J where $Z = 2$, $E_i = 54.416$ eV.

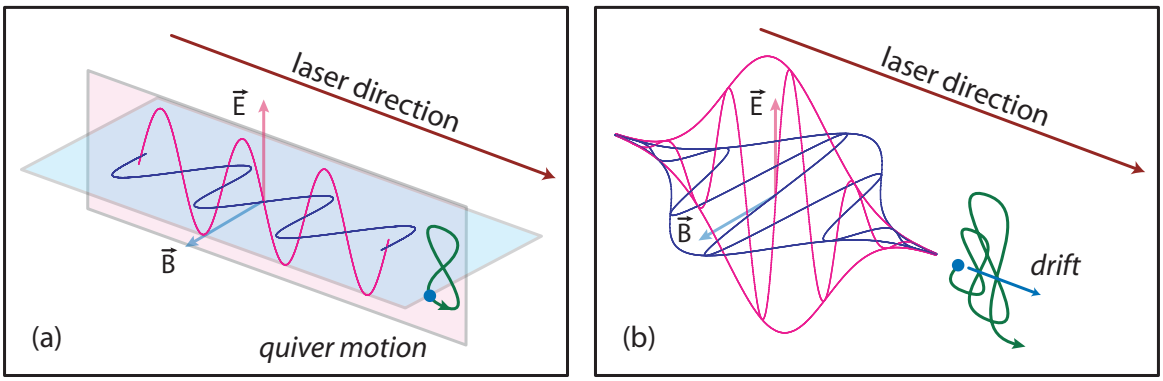

Figure 2.1: An electron in a oscillating electromagnetic field with constant amplitude experiences a quiver motion (a). In presence of an intensity gradient, the electron experiences a net drift in addition of an increasing quiver motion (b).

As the ultrashort laser pulse propagates through the plasma, electrons are displaced from the uniform background of ions. This displacement is due to the intensity gradient of the laser pulse which adds a net drift (Fig. 2.1b) to the regular quiver motion electrons would experience in presence of a constant amplitude oscillating field (Fig. 2.1a). The electrostatic force of the ions onto the electrons causes the electrons to oscillate around their equilibrium positions at the *angular* plasma frequency [79]:

$$\omega_p = \sqrt{\frac{n_e e^2}{\epsilon_0 m_e}} \tag{2.1}$$

$$\omega_p\,[\mathrm{rad/s}] \simeq 5.64 \cdot 10^{13} \sqrt{n_e\,[10^{18}\ \mathrm{cm}^{-3}]} \tag{2.2}$$

where n_e is the plasma density, e is the elementary charge, ϵ_0 is the vacuum permittivity, and m_e is the electron mass. In Hydrogen gas, for typical densities ($n_e = 1$ to 80×10^{18} e^-/cm^3), the electron time response ($t_p = 2\pi/\omega_p$) is on the order of 10–100 fs ($\sim \tau_L$), and the ion (proton for H_2) time response is on the order of 0.5–5 ps ($\gg \tau_L$), with τ_L the laser pulse duration (30–50 fs FWHM). Hence, models presented in this thesis neglect the ion motion.

As it propagates in the plasma the laser excites a plasma wave which moves along the

laser with a phase velocity equal to the laser group velocity, as discussed in Sec. 2.4, which is given by [9]: $v_p \simeq v_g^L = d\omega/dk = c(1-\omega_p^2/\omega^2)^{1/2} \lesssim c$, with ω the laser frequency, and c the speed of light in vacuum. In order to provide an analytical description, the plasma is described as an Eulerian fluid and the plasma fluid is considered "cold" since the kinetic energy of the electrons oscillating in the laser field, $\mathcal{E}_k = (\sqrt{1+(e\mathrm{E}_0/m_e\omega c)^2}-1)m_ec^2 \simeq$ 0.15–15 keV where $\mathrm{E}_0 \simeq 10^{11}$–$10^{12}$ V/m is the laser peak electric field, is much higher than the thermal energy of background electrons $k_BT_e \simeq P/n_e \sim$ 5–50 eV [95].

Introducing $u = \gamma\beta$, $k_p = \omega_p/c$, the normalized vector potential of the laser $\mathbf{a} = e\mathbf{A}/m_ec$, and the normalized scalar potential of the plasma $\phi = eV/m_ec^2$, it can be shown that the laser-plasma interaction for a cold fluid plasma is described by the following general set of equations:

$$\nabla^2\phi = k_p^2\,(n/n_0 - 1) \tag{2.3a}$$

$$\nabla\cdot(n\mathbf{u}/\gamma) = -\,\partial n/\partial t \tag{2.3b}$$

$$\left(\nabla^2 - \frac{1}{c^2}\frac{\partial^2}{\partial t^2}\right)\mathbf{a} = k_p^2\frac{n\mathbf{u}}{\gamma n_0} + \frac{1}{c}\frac{\partial}{\partial t}\nabla\phi \tag{2.3c}$$

$$\partial\mathbf{u}/\partial t = c\nabla(\phi-\gamma) + \partial\mathbf{a}/\partial t \tag{2.3d}$$

2.2 One-dimensional plasma wake

To date, there are no general solutions to the set of coupled equations (2.3) on $\{\mathbf{a}, \phi, \mathbf{u}, n\}$, and for a three dimension laser pulse, in the high-intensity limit, the plasma wakefield is typically modeled numerically [45, 43, 44]. However, as discussed in this Section, a solution can be found in the one-dimensional (1D) regime under the assumption that the laser pulse does not evolve over the transit time of the plasma through the laser pulse, *i.e.*, the plasma experiences a constant laser electric field. This assumption is referred to as the quasi-static approximation (QSA) [46].

It is possible to express the wake in terms of the plasma density where ϕ is solution of the differential equation:

$$\frac{\partial^2 \phi}{\partial \xi^2} = \frac{k_p^2}{2}\left[\frac{\gamma_\perp^2}{(1+\phi)^2} - 1\right] \tag{2.4}$$

where $\gamma_\perp^2 = 1 + u_\perp^2 = 1 + a^2$ and $\xi = z - ct$ is the coordinate in the frame co-propagating at $v_p = c$ with the laser pulse.

Equation (2.4) can be rewritten, after some tedious algebra, for $v_p \simeq v_g^L \neq c$ using the new change of variable $(z, t) \mapsto (\psi, \tau)$, with $\psi = k_p(z - v_p t)$ and $\tau = t$ as [96, 97]:

$$\frac{\partial^2 \phi}{\partial \psi^2} = \gamma_p^2 \left\{ \beta_p \left(1 - \frac{\gamma_\perp^2}{\gamma_p^2 (1+\phi)^2}\right)^{-1/2} - 1 \right\} \tag{2.5}$$

where $\beta_p = v_p/c$ and γ_p is the relativistic Lorentz factor associated with the phase velocity of the plasma wave, with λ_p and λ are respectively the plasma and laser wavelengths.

Figure 2.2 plots two numerical solutions of Eq. (2.4) corresponding to the wakefield generated by a low (Fig. 2.2a) and high (Fig. 2.2b) intensity linearly polarized laser in a plasma with initial density $n_0 = 10^{18}\ e^-/\mathrm{cm}^3$. The laser intensity is plotted as the square of the normalized laser potential function $a^2(\xi)$. The amplitude a_0 of $a(\xi)$ is

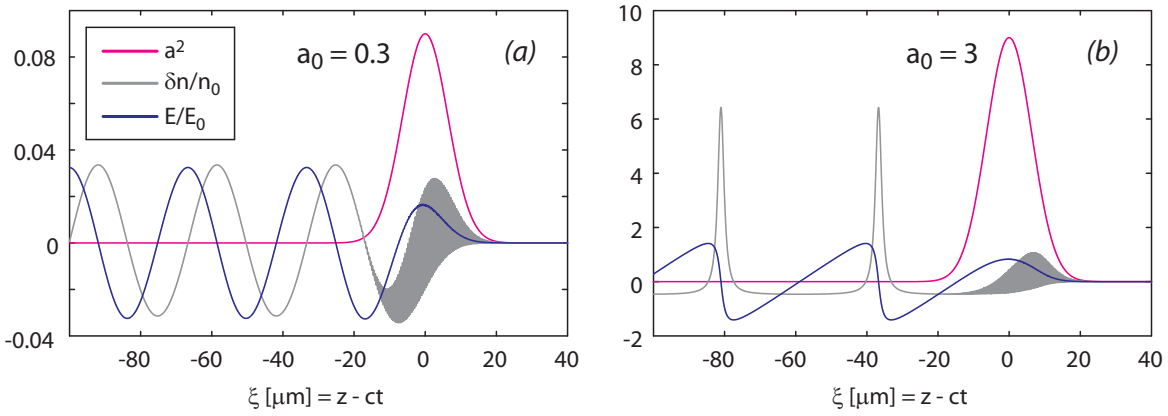

Figure 2.2: Density profiles $\delta n/n_0 = (n - n_0)/n$ *(gray)* and longitudinal electric field profiles E/E_0 *(blue)* driven by a laser pulse *(magenta)* with *(a)* $a_0 = 0.3$ and *(b)* $a_0 = 3$. The laser pulse has a Gaussian temporal profile with a duration of 50 fs FWHM ($c\,\tau_{\mathrm{FWHM}} \simeq 15$ μm). The horizontal axis represents the relative position to the laser pulse.

called the laser strength parameter and for $a_0 \geqslant 1$ [12] the wakefield becomes nonlinear:

$$a_0 = \left(\frac{e^2}{2\pi\epsilon_0 m_e^2 c^5}\lambda^2 I_0\right)^{1/2} \tag{2.6}$$

$$\simeq 8.54 \cdot 10^{-10}\,\lambda\,[\mu\mathrm{m}]\,\sqrt{I_0\,[\mathrm{W/cm^2}]} \tag{2.7}$$

For clarity the plasma density and the electric field are respectively normalized to the initial plasma density ($\delta n/n_0 = (n - n_0)/n_0$), and E_0 the non-relativistic cold wavebreaking electric field [51]:

$$E_0 = c\sqrt{m_e n_0/\epsilon_0} \tag{2.8}$$

$$E_0\,[\mathrm{V/m}] \simeq 96\sqrt{n_0\,[e^-/\mathrm{cm}^3]} \tag{2.9}$$

which for densities ranging from $n_e = 1$ to $80 \cdot 10^{18}$ e^-/cm^3 varies from 96 to 860 GV/m. In Figure 2.2, $E_0 \simeq 96$ GV/m and for $a_0 = 3$ (Fig. 2.2b) the peak electric field induced by the plasma density wave is $E_{\mathrm{max}} \simeq 135$ GV/m. This ability to sustain such high electric fields makes plasmas an attractive medium for particle acceleration.

2.3 Blow-out regime

The blow-out or "bubble" regime is a particular operational mode of the laser-plasma accelerator where the laser is intense enough to generate highly-nonlinear waves ($a_0 \gg 1$). In this regime, the plasma density wake no longer has the shape of a sinusoidal wave oscillating at the plasma period λ_p (Fig. 2.2a) and starts to spike at a larger period, shaping the electric field to a "sawtooth"-like function (Fig. 2.2b) with maximum amplitude $E_{\max} > E_0$. In the limit $\gamma_p \gg 1$, the nonlinear plasma wavelength is given by [49, 98, 11]:

$$\lambda_{\rm nl} = \frac{2\lambda_p}{\pi}\frac{E_{\max}}{E_0} \tag{2.10}$$

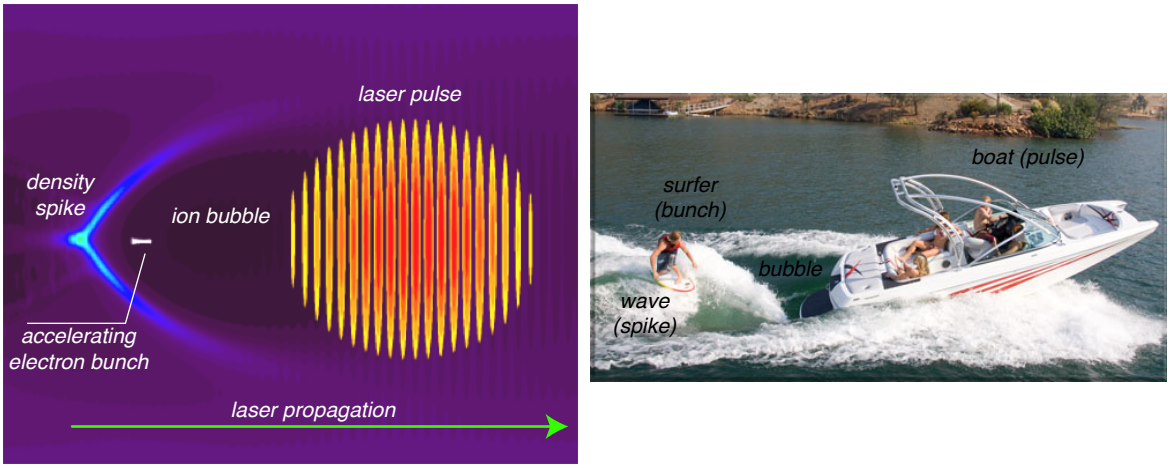

Figure 2.3: Analogy between particle-in-cell simulations of the laser-plasma accelerator in the bubble regime *(left)* and a wakeboarder surfing the wave generated at the back of a speedboat *(right). Photo: http://www.high-country-tours.com/mbsports.html*

The lengthening of the plasma period has an important effect on the transverse shape of nonlinear 3D plasma waves. Typically, the laser pulse has a Gaussian radial profile so that the wave is driven more strongly on-axis where the laser intensity is maximum. The plasma wavelength varies as function of the radial distance and it results a curved wavefront of the plasma wave. For sufficiently large plasma waves, a volume behind the laser pulse is cleared of all electrons, so called ion bubble [88, 89, 90, 91]. The

bubble regime has the advantage to provide a stable accelerating structure with strong transverse focusing fields and an accelerating longitudinal electric field over the full plasma wavelength (Fig. 2.2b). While analytical models exist to describe either the mildly relativistic regime ($a_0 < 1$) in 3D, or the nonlinear regime ($a_0 \gg 1$) in 1D, the shape of the plasma in 3D, required for the understanding of the bubble regime, must be computed numerically using particle-in-cell (PIC) simulations code.

The bubble regime has been successfully used to produce low emittance electron bunches [5, 6] suitable for radiation sources [99, 100] in quantitative agreement with three-dimensional simulations, confirming accurate understanding of trapping and emittance in LPAs. Recent 3D PIC simulations [101, 102] showed production of 0.1 μm *rms* transverse size, 1.3 mrad *rms* divergence, 300 MeV with 5% FWHM energy spread, and 2 fs FWHM length bunches in the bubble regime, in agreement with the data measured for similar laser-plasma parameters [5, 6]. This indicates that the physical picture of trapping observed in simulations [103, 101] is quantitatively correct; particles trap transversely in the wake, and the spike in plasma density at the back of the bubble has an important role in injection, as particles on injection trajectories pass close to it and its field repels them. Simulations [101] previously observed that 3D bunch divergence was lower and more closely agreed with experiments than 2D simulations, due to differing wake structure.

2.4 Laser propagation

The laser pulse propagation is described by the wave equation given in Eq. (2.3c) with $n_0 = n_i(r = 0)$ where n_i is the initial density profile and $r = 0$ corresponds in a cylindrical geometry to the propagation axis **z**. The wave equation can be simplified using four considerations: an under-dense plasma, the QSA, the paraxial approximation and the slowly varying envelope approximation (SVEA).

For an under-dense plasma ($\omega_p \ll \omega$), laser and plasma variables can be separated in high and low frequency components so we can write $\mathbf{a} \sim \mathbf{a}_f$, $\mathbf{u} = \mathbf{u}_f + \mathbf{u}_s$, $\phi \sim \phi_s$ and $n \sim n_s$ where the subscripts "$_f$" and "$_s$" denote the fast and slow response of each variable, respectively. In the QSA, Eq. (2.3c) can be approximated by the paraxial wave equation:

$$\left(\nabla_\perp^2 + \frac{2ik}{c}\frac{\partial}{\partial\tau}\right)\mathbf{a}_s = k_p^2\rho\,\mathbf{a}_s \tag{2.11}$$

A particular set of solutions to the paraxial wave equation are the Gaussian beams. Gaussian modes are of interest because in the experiments the laser pulse transverse profiles are close to Gaussian distributions. In vacuum, the Gaussian modes have the form:

$$a_s = A_0\frac{w_0}{w(z)}e^{-r^2/w(z)^2}e^{-ikr^2/2R(z)+i\zeta(z)} \tag{2.12}$$

where A_0 is a constant, $w_0 = \sqrt{\lambda z_0/\pi}$ is the beam waist at focus, $z_0 = kw_0^2/2$ is the Rayleigh length, $R(z) = z[1 + (z_0/z)^2]$ is the radius of curvature of the wavefront, $w(z) = w_0\sqrt{1 + (z/z_0)^2}$ is the waist of the beam and $\zeta(z) = \arctan(z/z_0)$ is the Gouy phase shift, *i.e.*, the phase difference between a Gaussian and a plane wave traveling along the propagation axis **z**.

The intensity of the Gaussian beam $I \propto |a_s|^2$ is given by:

$$I(r,z) = I_0 \frac{w_0^2}{w(z)^2} e^{-2r^2/w(z)^2} \tag{2.13}$$

$$= \frac{2P}{\pi w(z)^2} e^{-2r^2/w(z)^2} \tag{2.14}$$

where P is the total power carried by the beam at any transverse plane.

Other beam-like solutions to the Helmholtz paraxial equation exist and can be useful to describe non-uniformities of the beams in the experiments. Two sets of solutions are of particular interest [29]: the Hermite-Gaussian beams, which exhibit non-Gaussian intensity distributions while keeping paraboloidal wavefronts, are well suited to describe waves in an optical resonator; and the Bessel-Gaussian beams which have planar wavefronts but have non-uniform transverse intensity distributions.

For laser powers near or above the critical power [55, 104, 105], nonlinear effects such as self-focusing can occur:

$$P_c = \frac{c}{2\pi\epsilon_0} \left(\frac{e}{r_e}\right)^2 \tag{2.15}$$

$$P_c\,[\mathrm{GW}] \approx 17.4 \times (\omega/\omega_c)^2 \tag{2.16}$$

where $r_e = e^2/4\pi\epsilon_0 m_e c^2$ is the classical electron radius and $n_c = m_e\epsilon_0\omega^2/e^2$ is the critical density (Appendix A). At $P \geq P_c$ relativistic plasma dynamics produce nonlinear effects such as self-modulation and self-focusing by creating nonlinearities in the index of refraction (*e.g.*, $\eta = \eta_0 + \eta_2 I$) [55].

The index of refraction for a plane wave traveling in a plasma is given by:

$$\eta = \sqrt{1 - \omega_p^2/\omega^2} \tag{2.17}$$

and the phase velocity of the laser by:

$$v_p = c\,(1 - \omega_p^2/\omega^2)^{-1/2} \tag{2.18}$$

In the nonlinear regime, a corrective factor is applied to ω_p and the nonlinear index of refraction is given by:

$$\eta(r) = \sqrt{1 - \frac{n(r)\omega_{p,0}^2}{n_0\gamma(r)\omega^2}} \tag{2.19}$$

For a maximum on-axis, the radial dependency of the index of refraction can be used to provide refractive guiding of the laser pulse beyond the diffraction limited acceleration length, which is typically of the order of the Rayleigh length. In the presence of a preformed plasma channel of radius r_0, modeled by a quadratic function centered on-axis, and a laser-induced plasma density perturbation $\delta n(r)$, the density profile is given by $n = n_0 + [n(r_0) - n_0]r^2/r_0^2 + \delta n(r) \equiv n_0 + \Delta n(r) + \delta n(r)$. Hence, the index of refraction can be written:

$$\eta(r)^2 \approx 1 - \frac{\omega_{p,0}^2}{\gamma_\perp(r)\omega^2}\left[1 + \frac{\Delta n(r)}{n_0} + \frac{\delta n(r)}{n_0}\right] \tag{2.20}$$

From Eq. (2.20), it appears the phase velocity ($v_p = c/\eta$) increases as a function of the radial distance r for $\partial n/\partial r > 0$ or $\partial a_f/\partial r < 0$. A preformed plasma density channel with a minimum on-axis (channel guiding) or a laser pulse peaked on-axis (self-guiding) can lead to a propagation length inside the plasma of several Rayleigh lengths, a greater acceleration length and consequently higher electron energies [12].

2.5 Electron acceleration

In the previous Sections, both plasma and laser responses have been presented. In this Section, we describe how electrons experience the accelerating and decelerating fields of the wake, *i.e.*, how the laser-plasma interaction can be used for electron acceleration. To describe the injection and acceleration of electrons in a plasma wave, it is possible to analyze the motion of a test electron in a 1D plasma wave using Hamiltonian dynamics [56], *i.e.*, calculating the energy of that particle. In the moving frame, the normalized Hamiltonian ($H = H_{\mathrm{T}}/(\gamma_p m_e c^2)$) [56] of a test electron is given by:

$$H = \gamma(1 - \beta_p \beta_z) - \phi \tag{2.21}$$

where $\gamma = (1 - \beta_z^2)^{-1/2}$ is the Lorentz factor associated with the electron.

Figure 2.4 shows in phase space the electrons trajectories calculated using cold fluid theory of laser-plasma acceleration. The parameters used for this map are close to experimental results presented in this thesis (*c.f.* Chapter 5), the laser is 50 fs FWHM long and has an intensity of $a_0 = 1$, and the plasma density is 4×10^{18} e^-/cm^3. A general solution of Eq. (2.21) can be found in terms of γ for an electron with initial position ξ_0, initial potential ϕ_0 and initial energy γ_0 by solving $H = H_0 = \gamma - \beta_p u_z - \phi = \gamma - \beta_p \sqrt{\gamma^2 - 1} - \phi$:

$$\gamma = \gamma_p^2 (H_0 + \phi) \pm \beta_p \gamma_p \sqrt{\gamma_p^2 (H_0 + \phi)^2 - 1} \tag{2.22}$$

For an electron initially at rest, $H_0 = 1$ since $\phi_0 = 0$ and $\gamma_0 = 1$, the momentum equation becomes:

$$\gamma = \gamma_p^2 (1 + \phi) \pm \beta_p \gamma_p \sqrt{\gamma_p^2 (1 + \phi)^2 - 1} \tag{2.23}$$

and describes an open orbit in phase-space (Fig. 2.4b, *blue curve*) or "fluid" orbit.

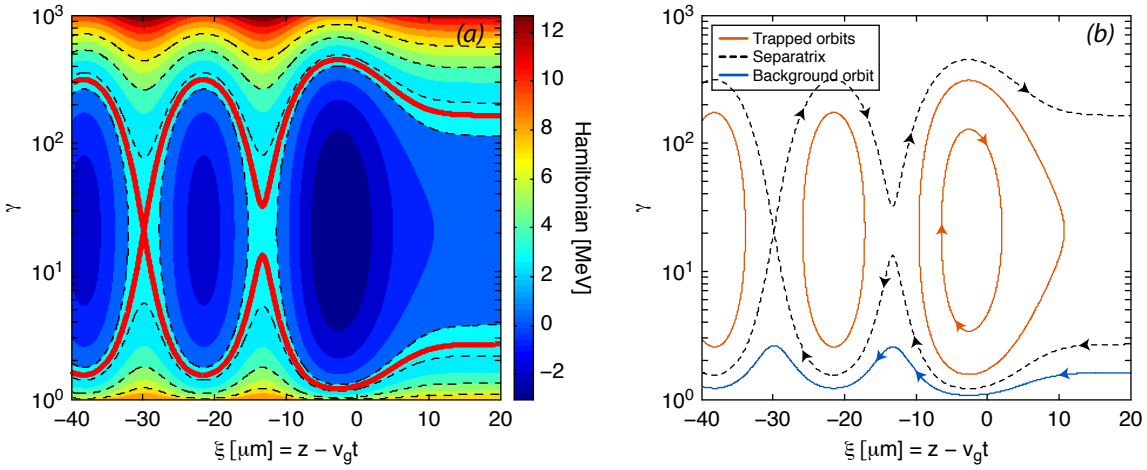

Figure 2.4: Orbits in momentum-phase space of constant Hamiltonian H_{T} for $a_0 = 1$, a pulse duration of 50 fs FWHM and a plasma density of 4×10^{18} e^-/cm^3. *(a)* The solid red lines are the *upper* and *lower* separatrix separating the closed orbits from the open orbits. The dashed lines are examples of fluid and trapped orbits. *(b)* Direction of propagation for different orbits.

As was introduced in Chapter 1, laser-plasma accelerators can sustain high accelerating gradients allowing electrons to be accelerated to relativistic energies over short distances. As shown in Fig. 2.4, one can establish the condition for an electron to be on a "trapped" orbit (closed orbits in Fig. 2.4b, *red curves*) and calculate the maximum energy gain for that electron. The Hamiltonian map of Fig. 2.4a shows local minima (stable points) and maxima (unstable points) where the potential ϕ is respectively maximum and minimum. The separatrix is a boundary in phase-space separating the fluid orbits from the trapped ones (Fig. 2.4b, *black dashed curves*). The maximum energy gain occurs when an electron is trapped on the closed orbit just inside the *lower* separatrix and exit the plasma after reaching the maximum of the *upper* separatrix (ideal case). It can be shown [12] (Appendix A) that the maximum energy gain is given by:

$$\Delta\gamma = 2\beta_p\gamma_p\sqrt{(1+\gamma_p\Delta\phi)^2 - 1} \tag{2.24}$$

where $\Delta\phi = \phi_{\max} - \phi_{\min}$ and $\Delta\gamma = \gamma_{\max} - \gamma_{\min}$. In the example of Fig. 2.4, $\phi_{\min,\,\max}$

are found by solving Eq. (2.4) to be $\phi_{\min} \simeq -0.147$ and $\phi_{\max} \simeq 0.331$. Since it is a mildly nonlinear case ($a_0 = 1$), the phase velocity is calculated using the linear formula: $v_p = c(1-\omega_p^2/\omega^2)^{1/2}$; and we get $\beta_p \simeq 1-1.15\times10^{-3}$ and $\gamma_p \simeq 20.9$. Thus, the maximum energy gain is calculated to be $\Delta\gamma \simeq 456$, for which the maximum electron energy at the exit of the plasma is $\mathcal{E}_{\max} = (\gamma_{\max} - 1)m_e c^2 \simeq 230$ MeV.

For larger a_0 [56], $\gamma_{\min}$ decreases and $\gamma_{\max}$ increases. Eventually, the lower separatrix overlaps with the orbit of background electrons initially at rest so that $\gamma_{\min} = 1$ and $\Delta\phi = 1 - 1/\gamma_p$. However, the background electrons ($\gamma_0 = 1$) flow backward in the frame of the laser at a speed $-v_p$ and undergo fluid oscillations without being trapped by the plasma wave. As a_0 increases [56], $\gamma_{\min}$ eventually increases back up allowing electrons with negative velocities to be trapped. For the example shown in Fig. 2.4 (50 fs Gaussian pulse, 4×10^{18} e^-/cm^3), it can be computed that $\gamma_{\min} = 1$ for $a_0 \simeq 1.47$. At this point, wavebreaking occurs and background plasma electrons are trapped in the plasma wave and accelerated.

In the cold fluid relativistic model, wavebreaking occurs as a limitation of the model; Eq. (2.5) presents a singularity for $\phi \to -1 + \gamma_\perp/\gamma_p$ ($x_{\text{m}} \to 1/\gamma_p \in [0, 1]$). The cold fluid relativistic wavebreaking electric field [50, 56] is found to be:

$$E_{\text{WB}} = \sqrt{2(\gamma_p - 1)}E_0 \tag{2.25}$$

For a plasma density of 4×10^{18} e^-/cm^3 (Fig. 2.4), $E_0 \simeq 1.9$ GV/cm and $E_{\text{WB}} \simeq 6.3 \times E_0 \simeq 12$ GV/cm. The maximum electron energy at the exit of the plasma is calculated to be $\mathcal{E}_{\max} \simeq 18.5$ GeV.

However, in the experiments the background plasma electrons have an initial thermal energy spread which induces injection before wavebreaking is reached, reducing the maximum accelerating field amplitude achievable ($E \leq E_{\text{WB}}$) and limiting the maximum energy gain. Although the self-trapping injection scheme is often used in laser-plasma

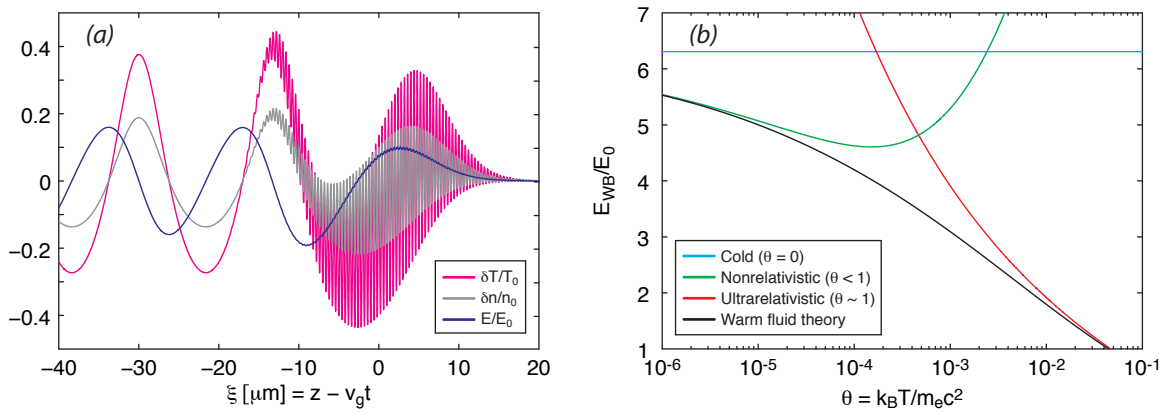

Figure 2.5: Effects of the background thermal energy spread on the laser-plasma accelerator. *(a)* Modulation of the temperature profile ($\delta T/T_0 = T/T_0 - 1$, *magenta*) by the plasma density wave (*gray*: $\delta n/n_0$; *blue*: E/E_0) excited by a 50 fs FWHM Gaussian laser pulse with peak intensity $a_0 = 1$ propagating in a plasma of initial density 4×10^{18} e^-/cm^3. *(b)* Maximum plasma electric fields for different initial background plasma temperatures ($\theta = k_B T/m_e c^2$) behind the laser pulse ($\gamma_\perp = 1$) using Eq. (2.25) (*cyan*), Eq. (2.28) (*green*), Eq. (2.27) (*red*) and Eq. (2.26) (*black*). After [57, 58].

accelerator experiments [12], it can become a source of undesired dark current in other injection schemes (*e.g.*, colliding pulses, see Sec. 3.2). Typically, for laser-driven plasma wakefield accelerators the initial temperature of the plasma (mean local kinetic energy) is of the order of $k_B T_0 \sim 5$–50 eV [95], *i.e.*, nonrelativistic plasma temperatures, with k_B the Boltzmann constant and T_0 the initial center electron plasma temperature. C. B. Schroeder *et al.* [57, 58] developed a fluid theory for warm plasmas. As expected, the local temperature of the plasma is modulated by the plasma density wave (Fig. 2.5a) such that [58] $T/T_0 = (n/n_0\gamma_f)^2$, with γ_f the fluid orbit, for a nonrelativistic plasma ($k_B T/m_e c^2 \leq 1$). This modulation enhances the effect of temperature-induced self-injection, further limiting the wavebreaking electric field. The general expression for the maximum electric field is found to be [57]:

$$(E_{\mathrm{WB}}/E_0)^2 = \gamma_\perp(\chi_0 + 1/\chi_0 - 2) + (\theta/\gamma_\perp)\,[F(\chi_0) - 1] \tag{2.26}$$

where $\theta = k_B T/m_e c^2$ is the temperature of the plasma and, χ_0 and $F(\chi_0)$ are functions

of β_p, γ_p, θ and $\gamma_\perp$ (Fig. 2.5b). In the case of an ultrarelativistic plasma ($1/\gamma_p^2 \ll \theta \ll 1$), Eq. (2.26) simplifies as [57]:

$$(E_{\mathrm{WB}}/E_0)^2 \simeq \sqrt{8\gamma_\perp^4/27\theta}\left(1-\gamma_\perp^{-1}\sqrt{3\theta/2}\right)^3 \tag{2.27}$$

In the asymptotic limit $\theta \ll \gamma_\perp^2/\gamma_p^2 \ll 1$, *i.e.*, a nonrelativistic plasma, the corrected fluid wavebreaking electric field is given by [57]:

$$(E_{\mathrm{WB}}/E_0)^2 \simeq 2\gamma_\perp(\gamma_p-1) - 2\gamma_p\left[\frac{4}{3}(3\gamma_p^2\gamma_\perp^2\theta)^{1/4} - (3\gamma_p^2\theta)^{1/2}\right] \tag{2.28}$$

In the example shown in Fig. 2.4 and Fig. 2.5a, behind the laser pulse ($\gamma_\perp = 1$) Eq. (2.28) applies since $\theta \sim 10^{-5}$–10^{-4} and $\gamma_\perp^2/\gamma_p^2 \simeq (1/20.9)^2 \simeq 2.3\times10^{-3}$. Assuming $\theta m_e c^2 =$ 10 eV, the wavebreaking electric field in this example is reduced to $E_{\mathrm{WB}} \simeq 4.9 \times E_0$, *i.e.*, $\sim 22\%$ lower than for a cold plasma.

2.6 Limits to the acceleration and beam quality

The injection and acceleration of electrons in an LPA is limited by several phenomena. Of particular importance are beam loading, laser-plasma instabilities and diffraction, dephasing and depletion of the laser.

Beam loading is the process by which the accelerating electron bunch has enough charge to drive a wake which significantly interferes with the accelerating plasma wave. Besides intense laser pulses, wakefields in plasmas can also be driven by relativistic charged particle bunches [106]. Instead of the ponderomotive force, for an electron bunch the wake is driven by the electrostatic forces of the bunch. As with a laser pulse, the electrons of the plasma will be expelled from the relativistic bunch and will start to oscillate around the quasi-static ions. To include the effects of a trapped electron bunch on the laser-driven wakefield, two terms need to be added to the set of equations Eqs. (2.3): $q_b = -en_b$ and $\mathbf{j}_b = -en_b\mathbf{v}_b$ corresponding to the volume charge density and current of the bunch respectively [107, 108]. In the linear perturbation theory, the laser propagation is then described by adding the electron bunch current to the wave equation Eq. (2.3c):

$$\left(\nabla^2 - \frac{1}{c^2}\frac{\partial^2}{\partial t^2}\right)\mathbf{a} = k_p^2\frac{n\mathbf{u}}{\gamma n_0} + k_p^2\frac{n_b\mathbf{u}_b}{\gamma_b n_0} + \frac{1}{c}\frac{\partial}{\partial t}\nabla\phi \tag{2.29}$$

where $u_b = \gamma_b\beta_b$ with γ_b the relativistic Lorentz factor associated with the electron beam. In the same manner, the plasma density wave is described by adding the charge density of the electron bunch to Poisson's equation Eq. (2.3a):

$$\nabla^2\phi = k_p^2\left(\frac{n + n_b}{n_0} - 1\right) \tag{2.30}$$

In the frame of the driver Poisson's equation can be written as (Appendix A):

$$\frac{\partial^2\phi}{\partial\xi^2} = \frac{k_p^2}{2}\left[\frac{\gamma_\perp^2}{(1+\phi)^2} - 1\right] + k_p^2\frac{n_b}{n_0} = k_p^2\frac{\delta n}{n_0} + k_p^2\frac{n_b}{n_0} \tag{2.31}$$

This expression shows that as the charge density of the bunch increases, it compensates for the potential of the wake generated by the laser and eventually cancels out the wake ($\delta n = -n_b$). Hence, beam loading can severely limit the achievable current of the accelerated bunch, as well as the bunch quality. In the region behind the laser pulse, each plasma bucket, *i.e.*, the region confined in a given plasma period, can trap an electron bunch. Each trapped electron bunch will drive its own wake which will be out of phase with the accelerating wave, thus reducing its strength. Since this effect is cumulative the strength of the wake in the nth bucket is affected by the $(n-1)$ bunch-driven wakes preceeding it. Hence, the total wake is sufficiently strong to support injection only in the first few buckets $\sim$ 1–10. At typical density for gas-jet experiments at the LOASIS, *e.g.*, 3×10^{19} e^-/cm^3, the plasma wavelength is of the order of $\lambda_p \simeq 6$ μm and the total bunch duration can be estimated to be $\simeq$ 6–60 μm (20–200 fs).

Several other mechanisms can limit the performance of the LPA. The main limitations are summarized in the expression of 3 distances: diffraction, dephasing and depletion. The diffraction length is the length over which the laser stays focused enough as to create the intensity required to generate a plasma wave. In Sec. 2.4, the Gaussian beam was introduced as a solution of the paraxial wave equation Eq. (2.11). It was shown that in vacuum its waist evolves according to $w(z) = w_0\sqrt{1+(z/z_0)^2}$ where $z_0 = kw_0^2/2$ is the Rayleigh length of the beam. From Eq. (2.13), the peak intensity of the Gaussian beam is given by $I(r=0,z) \propto w_0^2/w(z)^2 = 1/(1+(z/z_0)^2)$ and the laser-plasma interaction length is limited to a few z_0. For $w_0 = 20$ μm and an 800 nm laser pulse, the Rayleigh length is of the order of $z_0 \simeq 2$ mm and the intensity on-axis is reduced by 99% after 20 mm of propagation. However, it was discussed in Sec. 2.4 that the laser pulse can be guided over several Rayleigh lengths by either self-focusing effects when the laser power exceeds the critical power, Eq. (2.15), or by using a preformed plasma channel.

For a given plasma bucket, the dephasing length is the distance the accelerated

electron bunch travels before outrunning the wave. As it accelerates the electron bunch velocity approaches the speed of light $v_z \to c$ and eventually exceeds the phase velocity of the plasma wave $v_p < c$, allowing the electrons to outrun the accelerating phase of the wave. In a 1D linear plasma wave of the form $E_z = E_{\max}\cos[k_p(z - v_p t)]$, the electron can be accelerated at most over half a plasma wavelength. Three-dimensional plasma wave effects include the transverse focusing field which is offset from the longitudinal accelerating field by a quarter of λ_p. Thus, the wave is both accelerating and focusing over $\lambda_p/4$ and the dephasing length can be determined by solving: $k_p(z - v_p t) \equiv k_p(L_\phi - v_p t_\phi) = \pi/2$. Assuming $v_z \simeq c$, we have $t_\phi = L_\phi/c$ and $L_\phi = \lambda_p/[4(1-\beta_p)] = \lambda_p/[4(1 - \sqrt{1-1/\gamma_p^2})]$ which, for $\gamma_p \gg 1$, yields:

$$L_\phi \simeq \gamma_p^2 \lambda_p/2 \tag{2.32}$$

$$\simeq \lambda_p^3/2\lambda^2 \tag{2.33}$$

since the phase velocity of the plasma wave is approximately equal to the group velocity of the electromagnetic wave propagating through the plasma [9, 24], $v_p \simeq v_g^{\text{laser}} = c(1 - \omega_p^2/\omega^2)^{1/2}$, *i.e.*, $\gamma_p \simeq \omega/\omega_p = \lambda_p/\lambda$. In the example of a uniform plasma density of $n_0 = 10^{18}\ e^-/\text{cm}^3$ and a 800 nm laser pulse, $\gamma_p \simeq 42$ and the dephasing length is of the order of $L_\phi \simeq 29$ mm.

In exciting the plasma wave, the laser pulse transfers energy to the medium. This mechanism is referred as pump depletion [109] and the depletion length L_d is the distance after which the laser lost its energy. The energy contained in a laser pulse of length L_L, waist w_0 and peak electric field E_L is given by $\mathcal{E}_L \sim \pi w_o^2 L_L \epsilon_0 E_L^2/2$ [72]. The electric energy contained in the plasma wave is given by $\mathcal{E}_p \sim \pi w_o^2 L_p \epsilon_0 E_z^2/2$ where L_p is the length of the plasma and E_z the longitudinal electric field of the plasma wave. Assuming the laser is guided until it reaches full depletion, the depletion length can be determined

by equating the energy of the laser and of the plasma wave, $\mathcal{E}_L = \mathcal{E}_p(L_p = L_d)$, which gives:

$$L_d = L_L(E_L/E_z)^2 \tag{2.34}$$

In addition [110],

$$E_L \simeq \sqrt{\Omega_0 I_0/2} = \frac{\omega a_0}{4\pi}\sqrt{\frac{\Omega_0 m_e c}{r_e}} \tag{2.35}$$

where $\Omega_0 \simeq 377\ \Omega$ is the impedance of free space; and in the linear regime ($a_0^2 \ll 1$) a general solution to Poisson's equation, Eq. (2.4), can be found for the potential [12] providing a solution for the electric field of the form $E_z/E_0 = (\sqrt{\pi}/2)a_0^2 k_p L_L \exp(-k_p^2 L_L^2/4) \times \cos(k_p\xi)$. Note that with this expression the maximum electric field is achieved for $L_L = \sqrt{2}/k_p = \lambda_p/\sqrt{2}\pi$; this condition is known as the *resonance* condition. At the resonance and for $a_0 \ll 1$, the peak electric field is then given by:

$$E_z = \sqrt{\frac{\pi}{2}}\frac{a_0^2}{\exp(2)}E_0 \tag{2.36}$$

Using Eq. (2.1) and Eq. (2.8), the depletion length can be written in this regime as:

$$L_d = \frac{\exp(4)\sqrt{2}}{8\pi^3}\cdot\frac{\Omega_0\epsilon_0}{r_e}\cdot\frac{\gamma_p^2\omega_p}{a_0^2 n_e} \tag{2.37}$$

$$= \frac{\exp(4)\sqrt{2}}{4\pi^2}\cdot\frac{\Omega_0\epsilon_0 c}{r_e}\cdot\frac{\lambda_p}{a_0^2\lambda^2 n_e} \tag{2.38}$$

$$L_d\,[\mu\mathrm{m}] \simeq 695 \times \frac{\lambda_p\,[\mu\mathrm{m}]}{a_0^2\,(\lambda\,[\mu\mathrm{m}])^2\,n_e\,[10^{18}\ \mathrm{cm}^{-3}]} \tag{2.39}$$

Following the previous example of a plasma density of $10^{18}\ e^-/\mathrm{cm}^3$ and a 800 nm laser pulse with $w_0 = 20\ \mu$m, the resonance condition implies a pulse duration of $\tau_L \simeq 25$ fs ($L_L \simeq 7.5\ \mu$m). Assuming an energy on target of $\mathcal{E}_L \simeq 50$ mJ, the peak intensity is given by $I_0 = 2\sqrt{\ln 2/\pi}\mathcal{E}_L/\tau_L\pi w_0^2 \simeq 1.5\times10^{17}\ \mathrm{W/cm}^2$, $a_0 \simeq 0.26 < 1$ and, neglecting all other sources of energy loss, $L_d \sim 0.5\ \mathrm{m} \gg L_\phi > z_0$. Note that for more realistic experimental

parameters (*e.g.*, higher density, longer pulse duration, higher laser energy), E_z has to be computed numerically and an estimate of L_d is given by Eq. (2.34).

Chapter 3

LPA Experimental Optimization

3.1 Plasma density measurements

As introduced in the previous Chapter (Sec. 2.6), the electron density, n_e, determines key parameters of the accelerator such as the dephasing length, the pump depletion length, and the maximum amplitude of a nonlinear plasma wave [12]. The present generation of LPAs is being developed to serve as a unique source for generating THz and X-ray light [77, 111, 84]. The performance of such light sources is determined in particular by the plasma shape and density. For instance, the radiated energy and duration of ultrashort THz pulses produced by accelerated electron bunches crossing the plasma-vacuum boundary (coherent transition radiation), depends on the sharpness of the transition and on the transverse size of the plasma [112, 113, 80]. Mapping the electron density of the plasma is therefore necessary to understand the THz generation mechanism. In betatron based X-ray sources, the X-ray energy is in part determined by the plasma density [82, 85, 114].

Plasma density measurements are conventionally performed using non-perturbative laser interferometric techniques (Michelson, Mach-Zender configurations). In these tech-

niques a laser beam, usually a short (< 1 ps) pulse, is split and propagates along two beam paths. In one arm the laser pulse goes through the plasma and experiences a phase shift due to a local variation of the refractive index. By interfering the laser pulse from this arm with the laser pulse in the other arm, called the reference arm, the relative phase is retrieved by Fourier analysis. The electron density is finally deduced from the phase map via its relation to the refractive index [78]. For most interferometers, the reference and probe laser pulses travel along significantly different paths, and effects such as vibration of the optics can cause shot-to-shot change in the relative phase. This increases the noise in the measurement. In this thesis, an alternative technique [115, 116, 117, 118] using a wavefront sensor is demonstrated in which only one laser pulse is required. Several types of wavefront sensors are commercially available (Hartmann, Shack-Hartmann, shearing interferometer). The setup used for both folded-wave interferometry and wavefront sensing as well as both analysis and density map reconstruction are discussed in Sec. 3.1.1. Electron density measurements using this new technique were benchmarked with interferometric measurements for a range of plasma densities as shown in Sec. 3.1.2 and the ability to resolve strong density gradients was successfully demonstrated. Furthermore, it is shown that for the setup presented, phase sensitivity and hence accuracy in determining the electron density can be significantly improved by using a wavefront sensor.

3.1.1 Electron density map reconstruction

The experiments were performed using a laser-driven plasma-wakefield accelerator in the self-modulated regime [119, 120] relying on self-trapping of background electrons. A laser pulse of central wavelength 800 nm ($\geqslant 40$ fs, up to 0.5 J) was focused ($w_0 \simeq 6$ μm, $> 10^{19}$ W/cm^2) into Helium or Hydrogen supersonic gas from a supersonic nozzle [2]. The focus was 1 mm above the nozzle. The laser pulse excited a plasma density

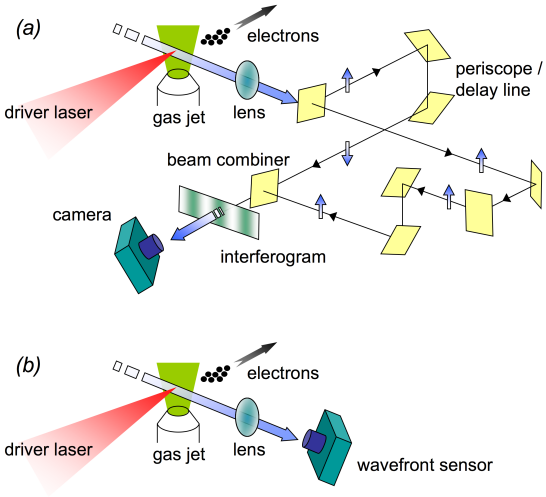

Figure 3.1: Schematic of the plasma density diagnostics. When using the folded-wave interferometer the wavefront sensor is operated as a camera, both arms of the interferometer are used and interferograms are recorded (a). When using the wavefront sensor for phase front measurements of the probe beam only one arm is used (b).

wave which trapped and accelerated up to 10's of MeV electron bunches with $\sim$ 1 nC of charge. Typical electron densities were on the order of $3 \cdot 10^{19}$ electrons per cubic centimeter (e^-/cm^3), which corresponds to a plasma wavelength of $\lambda_p \simeq 6$ μm. Optical measurements are possible at these densities using wavelengths shorter than ~ 6 μm. In these experiments measurements were carried out using a laser pulse of central wavelength 400 nm and 70 fs FWHM duration.

Both a wavefront sensor and a folded-wave interferometer [121] were used to characterize the electron density of the plasma. In the folded-wave interferometer, the lower part of a probe beam, which has a large transverse size compared to the plasma diameter, passed through the plasma. After passing through the plasma, the probe beam was split into two laser beams of equal intensity. By spatially inverting the beam in one arm before recombining the two beams, the area of each laser beam unaffected by the plasma interfered with the affected area to the other (Fig. 3.1a). Each arm therefore served as the reference of the other.

The setup with wavefront sensor is shown in figure 3.1b. The sensor measures directly the phase front curvature of an incoming laser beam and therefore does not require the folded-wave interferometer. The amount of phase introduced in the laser beam passing through the plasma is retrieved by subtracting a reference phase map obtained when the plasma is absent.

Wavefront sensor and interferometric measurements use different algorithms to recover the phase information. The wavefront sensor used in these experiments was a commercial 4-wave shearing interferometer (SID4 from Phasics S.A.). Measurements are based on a modified Hartmann test [122], in which diffraction-based limitations are greatly reduced by adding a phase chessboard to the classical Hartmann mask. A classical Hartmann test uses a mask of holes splitting the incoming light into beams whose deflections are proportional to the local distortions of the analyzed wavefront. By adding a second mask, a 2D diffraction grating is created, which replicates the incoming beam into 4 identical waves propagating along different directions. A Fourier analysis of the interference grid allows reconstruction of the phase gradient in 2 orthogonal directions. The phase map is obtained by integration of these gradients. The phase recovery routine is provided by the manufacturer.

Using the folded-wave interferometer, the plasma density was recovered from the interferograms by fringe pattern analysis [123, 124, 125]. A fast-Fourier-transform (FFT) was applied line-by-line on the interferograms (Fig. 3.2, *left*). Filtering out the carrier frequency and computing the inverse Fourier transform, the phase information was retrieved as the phase of the complex space-domain signal (Fig. 3.2, *center*).

The fringe pattern of a folded-wave interferogram has the form $f(x,y) = a(x,y) + b(x,y)\cos[2\pi f_0 x + \phi(x,y)]$ where $a(x,y)$ and $b(x,y)$ are due to non-uniformities of the intensity profile in the probe beam, $\phi(x,y)$ is the phase difference due to the presence of the plasma and/or optics, and f_0 is the spatial-carrier frequency. In complex notations

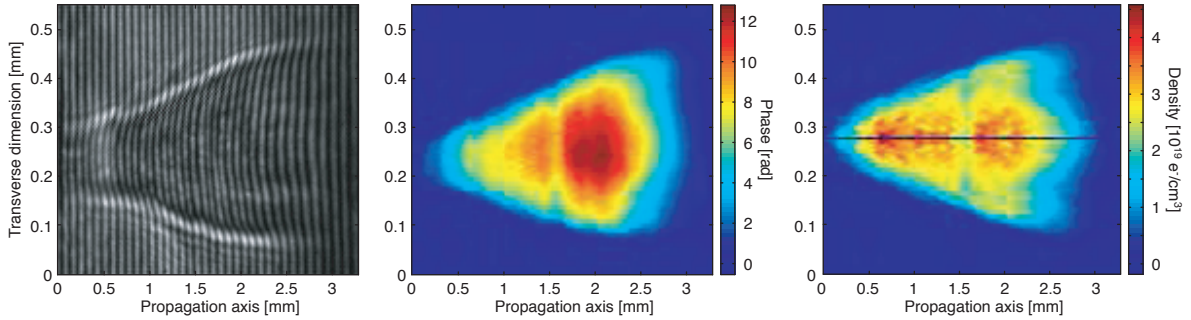

Figure 3.2: *Left*, interferogram obtained for a back pressure of the gas jet of 600 psi Hydrogen (1 psi $\simeq$ 6895 Pa). *Center*, phase map [radians] retrieved from Fourier analysis of the interferogram. *Right*, electron density map [10^{19} electrons/cm^3] retrieved after symmetrization of the phase map and Abel inversion.

the fringe pattern can be written:

$$\begin{cases} f(x,y) = a(x,y) + c(x,y)\exp(2\pi j f_0 x) + c^*(x,y)\exp(-2\pi j f_0 x) \\ \\ c(x,y) = 1/2 \cdot b(x,y)\exp[j\phi(x,y)] \end{cases} \tag{3.1}$$

where * denotes the complex conjugate. An FFT of this equation yields:

$$F(f,y) = A(f,y) + C(f-f_0,y) + C^*(f+f_0,y) \tag{3.2}$$

The phase information is simply retrieved as the argument of the inverse-FFT of the term $C(f-f_0,y)$, $\mathfrak{F}^{-1}[C(f-f_0,y)] = 1/2 \cdot b(x,y)\exp\{j[\phi(x,y)+2\pi j f_0 x]\}$. A linear fit on an unperturbed part of the interferogram provides f_0 whose contribution can then be subtracted.

The phase information is retrieved within $[-\pi;\pi]$ and to avoid any non-physical discontinuities the phase map needs to be "unwrapped". When the difference between two adjacent values along the horizontal axis exceeds π it is compensated. The formula

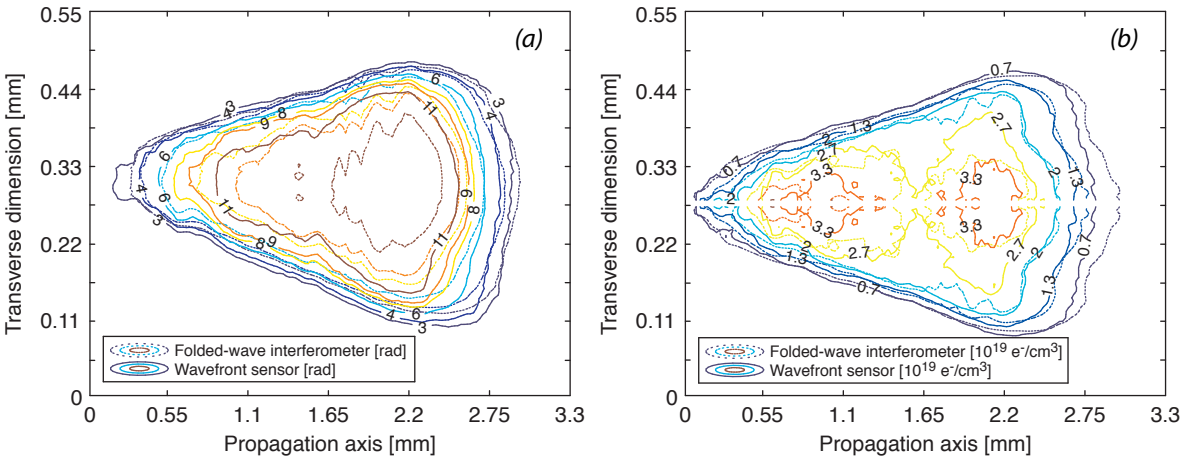

Figure 3.3: Contour plots from wavefront sensor and interferometer of average phase maps (a) and average electron density maps (b) obtained at 600 psi Hydrogen. The average was performed on over 50 phase maps in both cases, wavefront sensor (*solid lines*) and folded-wave interferometer (*dashed lines*).

used for these experiments is: $\phi_{unwrapped}(0) = \phi(0)$ and $\forall i \in \{1; \ldots; n-1\}$,

$$\phi_{unwrapped}(i) = \phi(i) - 2\pi \times \lfloor 1/2 + (\phi(i) - \phi(i-1))/2\pi \rfloor \tag{3.3}$$

where n is the number of pixels on the axis and $\lfloor\ \rfloor$ denotes rounding to the lowest value. The unwrapping is applied on each line and each column of the phase map.

For both diagnostics the electron density map (Fig. 3.2, *right*) was computed, using its relation to the plasma refractive index of refraction, by an Abel inversion [78, 126]. As discussed in Sec. 2.4, for a non-magnetic plasma and in the absence of a relativistically intense laser pulse, the refractive index is given by, *c.f.* Eq. (2.17), $\eta_p^2 = 1 - \omega_p^2/\omega^2 = 1 - n_e/n_c(\omega)$ where ω is the angular frequency of the probe beam and $n_c(\omega) = \epsilon_0 m_e \omega^2/e^2$ is the critical density. For $n_e < n_c$ and $\eta_{gas} \simeq 1$, the phase lag between reference and probe is then

$$\phi = \frac{\omega}{c} \int (1 - \eta_p(\omega))\, dl \tag{3.4}$$

where the integral is performed along the beam path in the plasma and c is the vacuum

speed of light. Substituting the definition of η_p in this equation yields:

$$\phi(x,y) = \frac{\omega}{c}\int (1 - \sqrt{1 - \frac{n_e(x,y)}{n_c(\omega)}})\, dl \tag{3.5}$$

Here, the phase is a measure of the average refractive index along the path in the plasma. Assuming the plasma is cylindrically symmetric, the measured phase is therefore an Abel transform of the actual physical quantity. After symmetrization of the unwrapped phase map, using the vertical location of its center of mass as axis of symmetry (Fig. 3.2, *right*), an Abel inversion is computed:

$$\Phi(x,r) = -\frac{1}{\pi}\int_r^R \frac{\partial\phi(x,y)}{\partial y}\cdot\frac{1}{\sqrt{y^2 - r^2}}\, dy \tag{3.6}$$

where $\phi(x,R) = 0$, r is the radial position and $R = r_{\max}$. From the unwrapped and Abel inverted phase map, the electron density of the plasma can be calculated by inverting the previously established relation between phase and density:

$$n_e(x,r) = n_c(\omega)\left[1 - \left(1 - \frac{c}{\omega}\cdot\Phi(x,r)\right)^2\right] \tag{3.7}$$

For both phase maps retrieved from folded-wave interferometry and wavefront sensing, symmetrization, Abel inversion, and conversion to electron density were computed. In the next section, the difference between the two types of measurements is studied.

3.1.2 Plasma density measurements using a wavefront sensor

Measurements were performed for different back pressures of the gas jet, namely 500 psi, 600 psi, and 700 psi Hydrogen. For each of these pressures, wavefront-sensor-based measurements and folded-wave interferograms were alternatively taken. A mean phase map of over 50 pictures was computed for both types of measurements. Both mean phase

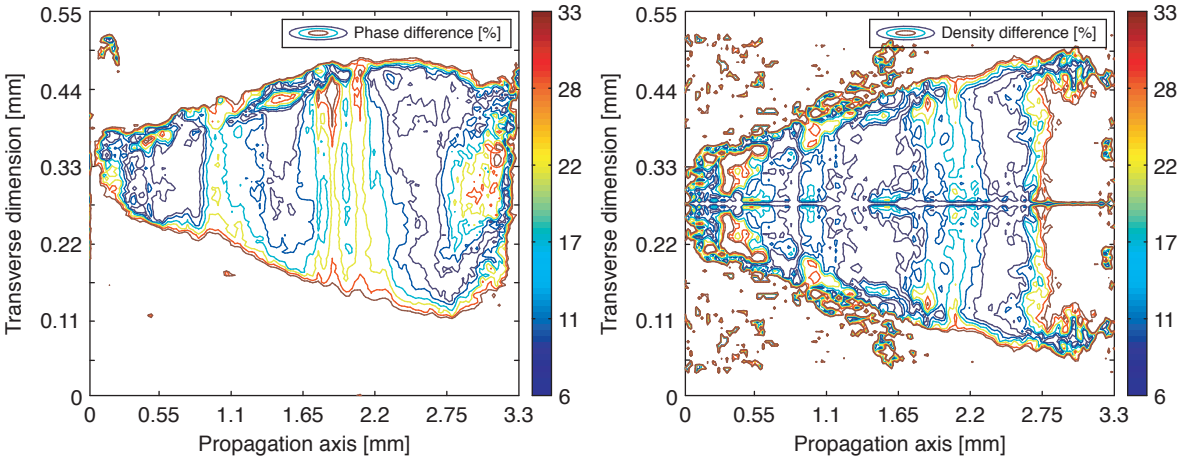

Figure 3.4: Contour plots of the difference in percent between average phase maps (*left plot*) and average electron density maps (*right plot*) from wavefront sensing and folded-wave interferometry obtained at 600 psi Hydrogen. The average was performed on over 50 phase maps in both cases. In the region of interest, the difference between density measurements does not exceed 20%.

maps were then symmetrized, Abel inverted, and converted to electron density according to the equations presented in Sec. 3.1.1. Analysis shows good agreement between the two types of measurements. An example would be the contour plots of the mean phase maps and mean density maps at 600 psi Hydrogen are compared in Fig. 3.3. The two contours of density in Fig. 3.3b differ from each other near the symmetry axis. This difference is attributed to the Abel inversion, which is sensitive to noise close to the symmetry axis since the integration $\int_r^R 1/\sqrt{(y^2 - r^2)}\, dy$ diverges for $r \simeq 0$. A discrepancy between the phase maps is also observed for higher phase shifts (Fig. 3.3a) ranging from 6% at the center of the plasma to 22% near the plasma edge where noise is more problematic around $z \simeq 1$, 1.8 and 3 mm (Fig. 3.4). The difference in density measurements ranges from 6% to 17% in the center of the plasma and increases at low densities where the signal-to-noise is small (~ 1).

In addition, the ability to resolve strong density gradients was tested using a damaged gas jet nozzle which produced a strongly perturbed gas flow for Helium gas. Both measurements provide similar resolution of the perturbed density profile (Fig. 3.5).

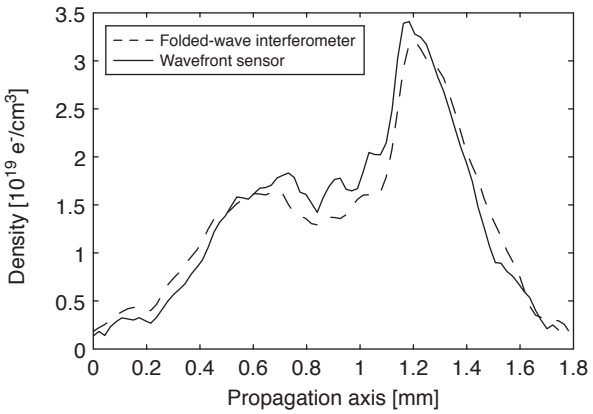

Figure 3.5: Comparison between direct wavefront sensor measurements and folded-wave interferometry on a line out of the density maps obtained using a damaged gas jet nozzle (600 psi, Helium). Both measurements are capable of resolving the "shock" in the gas flow.

	Folded-wave interferometer	Wavefront sensor
500 psi	2.06 ± 0.25	2.26 ± 0.25
600 psi	2.43 ± 0.30	2.56 ± 0.26
700 psi	2.69 ± 0.32	2.56 ± 0.27

Table 3.1: Comparison between direct wavefront sensor measurements and folded-wave interferometry for three different pressures. Values correspond to average and *rms* shot-to-shot deviation of the phase maps, and are indicated in $10^{19} e^{-}/\mathrm{cm}^3$.

In order to compare the scaling laws of the two techniques, the plasma density was analyzed as a function of gas pressure. Averages of the density maps were calculated over the plateau region where the density is nearly flat, excluding the zone near the axis where the Abel inversion fails. The shot-to-shot errors are dominated by fluctuations in gas flow (Table 3.1). The in-quadrature contribution of the instrument resolution to the *rms* deviations is less than 4.4% for the wavefront sensor and 33% for the folded-wave interferometer (Fig. 3.6).

The phase sensitivity of both techniques was evaluated by measuring 188 consecutive phase maps in the absence of plasma and under the same experimental conditions. An *rms* deviation phase map was calculated for both types of measurement (Fig. 3.6). The averages of the maps are 95.7 mrad and 11.4 mrad for respectively the folded-wave

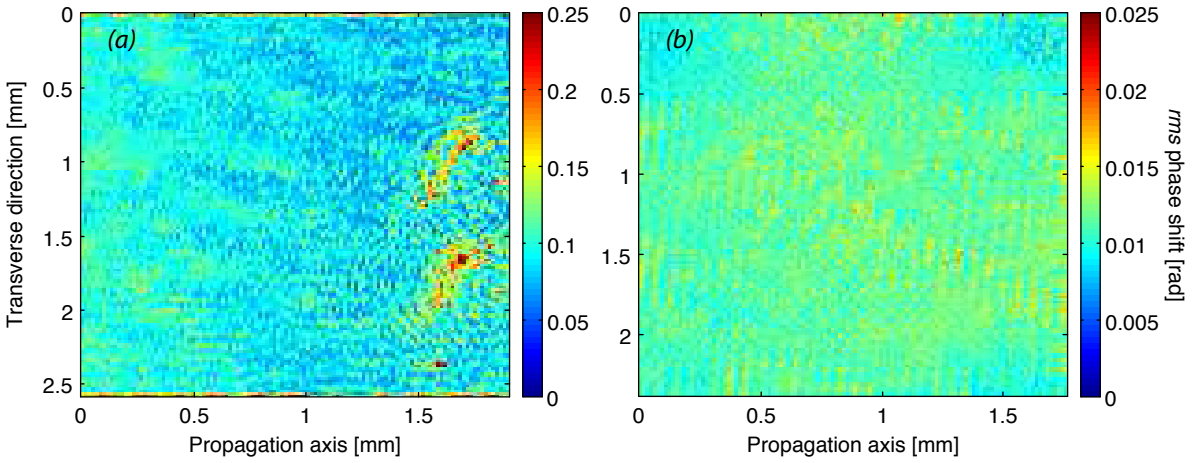

Figure 3.6: Sensitivity measurements for folded-wave interferometry (a) and wavefront sensing (b). Each figure is the *rms* deviation of 188 phase maps obtained without plasma. Wavefront-sensor-based measurements are $\simeq$ 8.4 times more sensitive and the noise is more homogeneously distributed.

interferometer and the wavefront sensor, making the wavefront sensor-based technique $\simeq$ 8.4 times more sensitive. In addition, fluctuations over the phase maps are more homogeneous for the wavefront sensor measurements.

The spatial resolution of the diagnostic is determined by the intrinsic camera resolution and the magnification of the imaging system. The wavefront sensor camera was used for both types of measurements to avoid ambiguity in the interpretation of the images. It has 480 $\times$ 640 pixels of 7.5 μm for both dimensions. Because the wavefront sensor is a 4-wave shearing interferometer the size of a measurement point does not correspond to a pixel. The wavefront sensor produces intensity and phase maps of 120 $\times$ 160 measurements points with a spatial resolution of 29.6 μm for both dimensions. Whereas the wavefront sensor has a fixed CCD chip and pixel size chosen by the manufacturer, it is in principle possible to choose a different camera to increase resolution of the folded-wave interferometer.

Plasmas produced by the laser-gas interaction were typically 2 mm long and had a diameter of 0.2 mm. After imaging the plasma to a primary focus shortly after the beam

combiner (Fig. 3.1) with a $f/7$ achromat lens, an imaging system using aspherical and cylindrical optics was used to provide higher resolution in the vertical direction to the wavefront sensor, 21.3 μm per measurement point in the horizontal plane and 4.8 μm per point in the vertical plane.

In conclusion, a simple single-shot wavefront-sensor-based electron density diagnostic is presented that relies on the use of a wavefront sensor. The design requires only one arm of a non-perturbative probe laser beam. Post-analysis requires only the computation of an Abel inversion. Successful resolution tests were performed by comparing wavefront sensing and folded-wave interferometry-based measurements for different pressures, thus electron densities and, for steep density gradients. The technique, which can be used for any phase sensitive measurement, was found to provide the same information as a regular interferometer with improved phase noise and with greater ease of operation.

3.2 Off-axis colliding pulse injection

Decoupling injection from acceleration is a key challenge to achieving compact, reliable, tunable laser-plasma accelerators (LPAs) [9, 12]. Although capillary-guided LPAs have demonstrated high-quality electron beams at 1 GeV [10] with 2.5% *r.m.s.* energy spread, most of present LPAs [39, 41, 40] still rely on transverse wavebreaking effects [19] of highly nonlinear waves [57] to inject electrons into the accelerating phase of the electron density wave. In this scheme, injection and acceleration are coupled, limiting control of the acceleration structure which is essential for LPAs' applications such as free-electron lasers [127], THz [77, 70] and X-ray radiation sources [84, 85, 128]. Electrons injected at different longitudinal positions behind the laser pulse, *i.e.*, different phases of the periodic structure of the accelerating wakefield, experience different electric fields, due for example to beam loading effects (Sec. 2.6), which can lead to a large energy spread. Several methods to control trapping of the electrons have been proposed and demonstrated: external injection of an electron beam from a conventional accelerator [16, 17, 18], triggering injection in plasma density gradients with density decreasing in the laser propagation direction [63, 2], and using additional laser pulses [20, 66, 129, 22, 67].

In this Chapter, a two-pulse configuration of the colliding pulse injection (CPI) [21] is presented. In colliding pulse injection the beat between multiple laser pulses can be used to control energy, energy spread, and emittance of the electron beam by injecting electrons in momentum and phase into the accelerating phase of the wake trailing the driver laser pulse [20, 21, 76, 129, 22]. Using automated control of spatiotemporal overlap of laser pulses, two-pulse experiments showed stable operation and reproducibility over hours of operation. The length of the accelerating structure was scanned by varying the intersection point of the collider beam. Two-dimensional particle-in-cell (PIC) simulations reproduce the observed timing window for the experimental parameters [130].

Both plasma density and intensity of the collider beam were scanned. Injection reaches a plateau for a normalized vector potential, a_1, of the collider laser pulse greater than 0.9 as predicted by simulations. To provide higher energy electron beams in coming CPI experiments, guiding of the driver laser pulse alone through several Rayleigh lengths by a third laser pulse was successfully demonstrated. Combined with CPI, 2–400 MeV beam of several pC and with narrow energy spread could be produced [66].

3.2.1 Two-pulse colliding pulse injection

The idea of using an additional laser pulse to control the injection of background plasma electrons was first reported in Umstadter *et al.* [20]. The proposed scheme involved two laser pulses propagating in perpendicular directions. Injection occurs due to the direct ponderomotive force of the envelope of the injection pulse (colliding pulse). Although simulations [20] indicated production of ultrashort electron bunches with low energy spreads ($\sim$ 10 fs, $\sim$ 21 MeV, $\Delta E/E \sim 6\%$), this required relatively high intensities for both pulses (normalized vector potentials $a \simeq 2$). Esarey *et al.* [21, 131, 132] provided theoretical description and simulations of a colliding pulse injection scheme with 3 pulses, a driver and both a forward and a backward going injection pulses, and showed production of 27 MeV, $\sim$ 3 fs and $\sim$ 0.3% energy spread. When the injection beams intersect some distance behind the driver beam, their interference creates a laser beat wave. Because of its small characteristic spatial scale, this standing wave has a large ponderomotive force which can accelerate a fraction of the plasma electrons such that they become trapped in the wakefield.

In the colliding pulse scheme presented here, a single off-axis counter-propagating laser pulse is used to simplify the implementation of a laser triggered injection technique [66, 129, 22, 67, 133], minimize the risk to the laser system when doing a co-linear counterpropagating geometry, and to facilitate secondary radiation extraction [134, 135].

In this simplified configuration of the CPI, background plasma electrons are injected into the wake by the ponderomotive force associated with the beat wave between the off-axis backward going injection pulse with the trailing portion of the driver laser [66, 67]. As discussed above, in the self-injection regime, injection and acceleration are coupled, limiting control of the accelerated electron bunch. In CPI experiments the self-trapping threshold is not reached and the interference between the two injection pulses are used to move background electrons from fluid orbits to trapped orbits.

A simple description of colliding pulse injection can be provided for two counter-propagating circularly polarized lasers [66, 67]. In Chapter 2, the one-dimensional plasma wakefield generated by the driver pulse was described and the Hamiltonian of the system was found to be, *c.f.* Eq. (2.21), $H = \gamma(1 - \beta_p\beta_z) - \phi$. Assuming the plasma background electrons are initially at rest ($H_0 = 1$), Eq. (2.23) gives the lower background fluid orbit: $\gamma_{\rm fluid}^{\rm min} = \gamma_p^2(1 + \phi_{\rm max}) - \beta_p\gamma_p\sqrt{(1 + \phi_{\rm max})^2\gamma_p^2 - 1}$. It can be also found that the lower separatrix is given by: $\gamma_{\rm sep}^{\rm min} = \gamma_p(1 + \gamma_p\Delta\phi) \pm \beta_p\gamma_p\sqrt{(1 + \gamma_p\Delta\phi)^2 - 1}$ with $\Delta\phi = \phi_{\rm max} - \phi_{\rm min}$. In addition, the Hamiltonian of the beat wave alone ($\phi = 0$) is given by [66] $H_b = \sqrt{1 + \mathbf{a}_b^2 + u_z^2} - \beta_b u_z - \phi_b$ where $\mathbf{a}_b^2 = (\mathbf{a}_0 + \mathbf{a}_1)^2$ is the laser intensity resulting from the interference of the two pulses and ϕ_b is the space charge potential driven by the beat wave. For circularly polarized laser pulses the normalized vector potentials can be written as $\mathbf{a}_{(0,1)} = a_{(0,1),s}(\xi)[\cos(k_{(0,1)}\xi_{(0,1)})\mathbf{x} + \sin(k_{(0,1)}\xi_{(0,1)})\mathbf{y}]$ with $k_1 = -k_0$ ($\beta_b = 0$) and $\xi_{(0,1)} = z \mp v_p t$ [67]. It yields $\mathbf{a}_b^2 = a_{0,s}^2 + a_{1,s}^2 + 2a_{0,s}a_{1,s}\cos(2k_0 z)$. Assuming $\phi_b \ll a_{0,s}a_{1,s}$ the Hamiltonian for electron trajectories in the beat wave reduces to $H_b = \sqrt{1 + \mathbf{a}_b^2 + u_z^2}$ so that on the separatrix electrons oscillate between $\gamma_{b,\rm sep} = \pm\sqrt{1 + 4a_{0,s}a_{1,s}}$. Thus, an estimate of the threshold value of $a_{1,s}$ for injecting background electrons into the accelerating phase of the wakefield is obtained by satisfying two conditions: the lower beat wave separatrix has to be less than the fluid orbit, *i.e.*, $\gamma_{b,\rm sep}^{\rm min} \leq \gamma_{\rm fluid}^{\rm min}$, and the higher beat wave separatrix has to exceed the lowest trapped

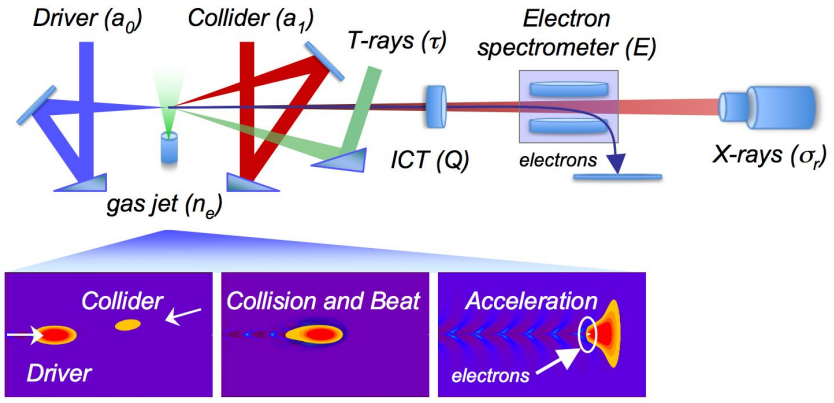

Figure 3.7: Schematic of the experimental setup. The laser beams, with strengths a_0 and a_1, are focused using off-axis parabolic mirrors onto a supersonic gas jet of neutral electronic density n_e. Temporal duration (τ), charge (Q), energy (E) distribution, and source size (σ_r) can be monitored. The inset describes the principles of colliding pulse injection: at overlap a ponderomotive beat wave provides momentum and phase kick to some background electrons which are then accelerated.

orbit, *i.e.*, $\gamma_{b,\mathrm{sep}}^{\mathrm{max}} \geq \gamma_{\mathrm{sep}}^{\mathrm{min}}$.

3.2.2 Experimental setup and diagnostics

Two ultrashort 800-nm laser pulses were focused into Helium or Hydrogen gas (3–9 $\times$ 10^{18} e^-/cm^3) from a 2.2 mm inner diameter supersonic nozzle. Both laser pulses were produced using the 10 Hz Ti:Al_2O_3 chirped-pulse-amplification LOASIS laser system. The first laser pulse (driver beam), an s-polarized pulse of $\simeq$ 0.4 J/pulse in $\simeq$ 45 fs FWHM, was used to drive the plasma wave. The driver was focused to a 4.4 μm focal spot ($1/e^2$ intensity radius) which gave a peak intensity of 3×10^{19} W/cm^2 and $a_0 = 3.75$. The second laser pulse (collider beam), an s-polarized pulse of $\simeq$ 0.25 J/pulse in $\simeq$ 45 fs FWHM, intersected the driver at both foci from the downstream direction at a 19 degree angle. The experimental setup is shown in Fig. 3.7. The collider beam energy had a focal spot of 5.7 μm ($1/e^2$ intensity radius), and its energy was $\sim$ 0.1 J, which gave $a_1 \simeq 1$.

The alignment of the both driver and collider beam foci was performed in two steps:

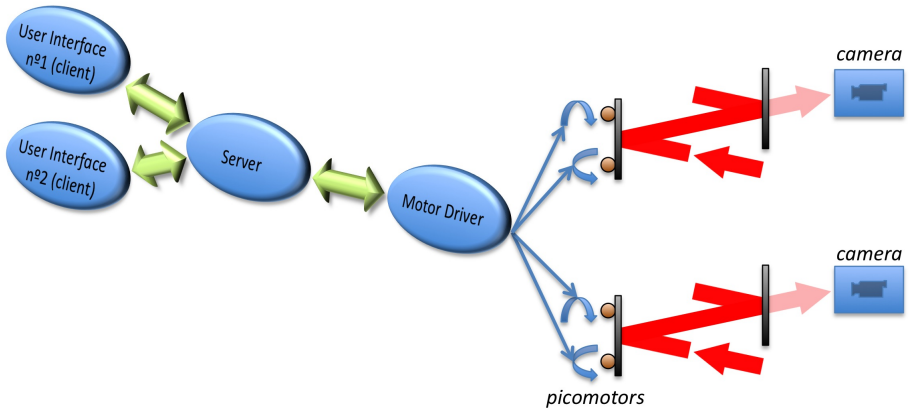

Figure 3.8: Schematic of the automated laser alignment system. The beam is steered using Picomotor-driven mirrors (high precision motors) and the beam position is monitored by a webcam placed behind a mirror downstream. Picomotors are controlled by motor driver called "Picopad". A server-client structure is used to handle simultaneous user commands.

first, by propagating both pulses in backfill gas, the waists of the ionization contours could be overlapped using a top view camera (horizontal plane); second, the arrival times were synchronized by referencing each beam relative to a third $\sim$ 70 fs 400-nm beam which provides side view shadowgrams. These shadowgrams allow also vertical overlap of the two beams (vertical plane). To maintain this alignment within a few microns and 10's of femtoseconds, an active pointing system was implemented which controls the laser beam path at many locations throughout the lab.

The laser beam is steered using precision-motor-driven mirrors (Fig. 3.8). By monitoring the beam position downstream, automated control of the beam alignment can be achieved. The high precision ($<$ 30 nm) motors used to control a mirror's position are called Picomotors. They are made of a piezoelectric transducer which is used to turn a screw and adjust the steering angle of the mirror. The Picomotors are connected to a driver (*e.g.*, New Focus 8732 Picopad) which can be remotely controlled using a General Purpose Interface Bus (GPIB) connection. Feedback on the laser position is provided by a common webcam observing the leakage through a downstream mirror. To control the many pairs of Picomotors/webcam placed throughout the lab, a client-server

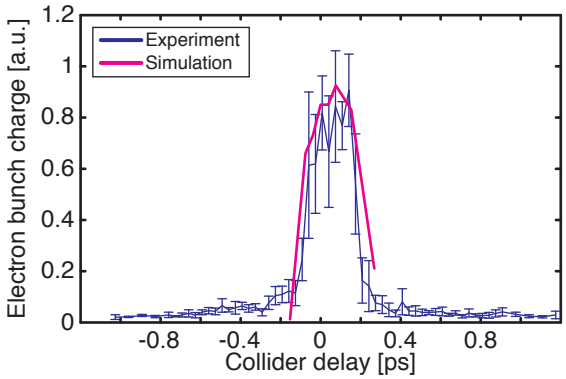

Figure 3.9: Timing scan in 5×10^{18} e^-/cm^3 H^{2+} of the collider beam ($a_1 \simeq 1$) arrival time relative to the driver beam ($a_0 \simeq 3.5$). The timing window is consistent with simulations (*magenta curve*, $a_1 \simeq 0.5$). At overlap, charge stability is $\simeq 20\%$.

architecture has been implemented with a server per driver.

A series of single-shot diagnostics was used to characterize the generated electron beams: the total, *i.e.*, including low-energy (< 10 MeV) tail, electron beam charge was monitored using an integrating current transformer (ICT) [136, 137]. The ICTs used at LOASIS were recently crossed-calibrated using an activation based measurement [36] which is immune to electromagnetic pulse (EMP) noise [137]; it was found that both charge diagnostics agree within $\pm 8\%$, making the ICT an accurate non-invasive charge measurement for LPAs. A magnetic dipole spectrometer was used to provide single-shot energy and divergence of the accelerated electron bunches [138, 68, 139]. Electron beam spectrum over a broad spectral range (10–100 MeV) is provided by combining a dipole magnet with scintillating screens (Kodak Lanex Fast scintillating screens) which, with a fluorescence decay time of less than 10 ms, are particularly suited for 10 Hz repetition rate, and can be cross-calibrated [68, 137] to provide absolute charge measurements [charge/MeV] and allow large areas to be imaged with reasonable sensitivity and cost.

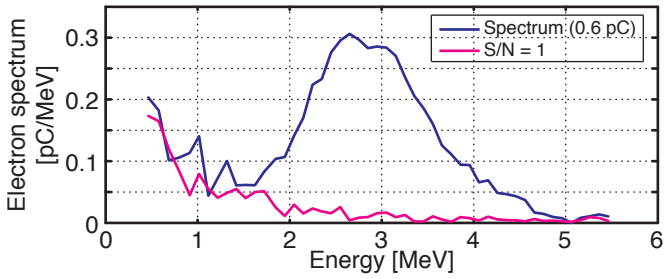

Figure 3.10: Example of colliding pulse injection produced electron beam distribution. The total charge in the beam, at the dipole magnetic spectrometer, is 0.6 pC.

3.2.3 Experimental results

Experimental parameters were chosen so that, when the driver was fired alone, no electron beam was produced. To operate below self-injection threshold, the plasma density was set below 5×10^{18} e^-/cm^3. Prior to lowering the plasma density, by varying the backing pressure of the gas jet, the longitudinal position of the gas jet was adjusted so that the focus of the driver beam lay on the upstream edge of the density plateau where, at higher pressures, self-injection was maximum.

By scanning the arrival time of the collider beam, one could scan the location of the beat wave in phase space. As the collider timing was scanned, the injection was successively turned on and off as illustrated in Fig. 3.9. The experiments show the expected timing signature as the collider timing was scanned with respect to the drive beam. The experiments also showed dependence of injection on density reasonably consistent with simulations. Colliding pulse experiments were conducted and have demonstrated reproducible injection of electron beams using the colliding pulses, so far at low energies (Fig. 3.10).

A possible explanation for this low energy electron spectra is the combination of a short ($\simeq$ 75 μm) defocusing length of the driver beam, and the non-uniformity of the plasma density profile, with a $\sim$ 25% rise from the upstream to the downstream edge of the profile, which would prematurely stop the injection. Future experiments will

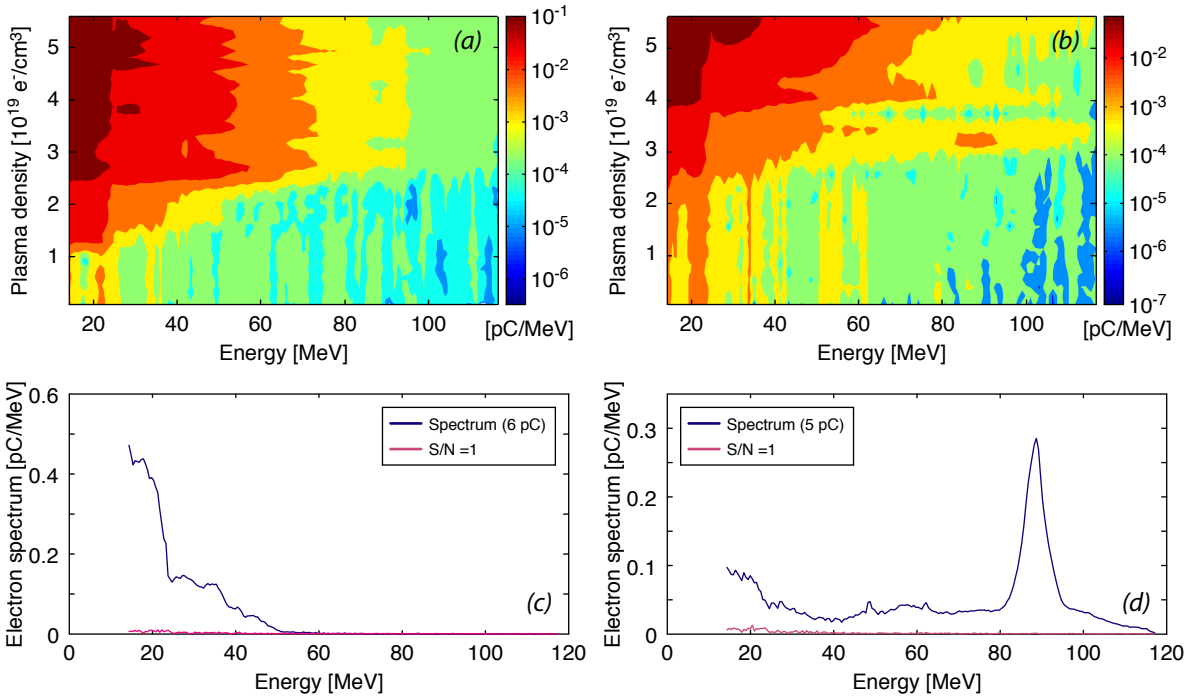

Figure 3.11: Density scan without *(a)* and with *(b)* pre-ionizing laser pulse in the self-injection regime. The charge produced (*colormap*) is displayed as function of the electron energy (*x-axis*) and plasma density (*y-axis*). *(c)* and *(d)* are examples of un/channeled single-shot electron beam spectra (*charge vs. electron energy*) for a plasma density of 3.2×10^{19} e^-/cm^3.

include guiding [40] of the driver beam to increase the acceleration length of colliding pulse injected beams. In preparation for guided experiments, where a third pre-ionizing laser pulse creates a plasma channel allowing extended acceleration lengths, guiding of the driver alone was performed. Increasing the density (0.5–5×10^{19} e^-/cm^3) to reach self-trapping, 90-MeV electron beams were generated near 3×10^{19} e^-/cm^3 (Fig. 3.11d), using a pre-ionizing igniter laser pulse to produce a plasma channel and guide the driver over many Rayleigh length ($\simeq$ 1.6 mm), similar to [40]. Combined with CPI, 200–400 MeV beams of several pico-coulombs of charge and narrow energy spread should be anticipated based on simulations.

Because CPI experiments rely on the spatiotemporal overlap of the colliding beams, an active beam pointing system was developed in order to provide amplifier and tar-

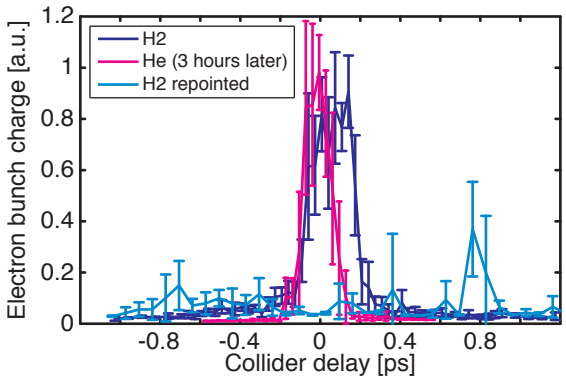

Figure 3.12: Three timing scans of the collider beam arrival time relative to the driver beam. The first and third curves show the importance of having an active beam pointing system. Using active beam pointing, the first and second curves, conducted using respectively Hydrogen and Helium gas, show a good stability of the timing window over several hours.

get pointing stability, and consequently stability of electron beam properties. Relative arrival time and focus positions of the two beams were measured using a conventional folded-wave interferometer [1], also used to measure the density profile of the plasma. Few micron on-target stability was achieved, with less than 50 fs timing drift over an hour, and $\sim$ 100 fs over 8 hours. To illustrate this stability, Fig. 3.12 shows two timing scans, one using Hydrogen gas and the other using Helium gas, which were conducted 3 hours from each other. Because of differences between the two gases, timing windows differed from each other but the overlap stayed identical, and both cases showed an *r.m.s.* charge stability of $\simeq 20\%$. Finally, Fig. 3.12 displays a case, using Hydrogen gas, where the collider beam had been purposely detuned, focusing the collider downstream of the driver focus, to show correlation between charge, timing overlap and laser pointing.

In addition to the timing scans, both pressure and collider strength (a_1) were scanned, and in both cases results were consistent with simulations. In Hydrogen, colliding pulse injection turned on at about 2×10^{18} e^-/cm^3 and turned off at about 5×10^{18} e^-/cm^3, before self-trapping mechanisms started to produce low energy, broad-band, high charge electron beams. In scanning the collider beam intensity, injection reached a plateau for $a_1 > 0.9$ as predicted by simulations [130], producing high charge, low energy electron

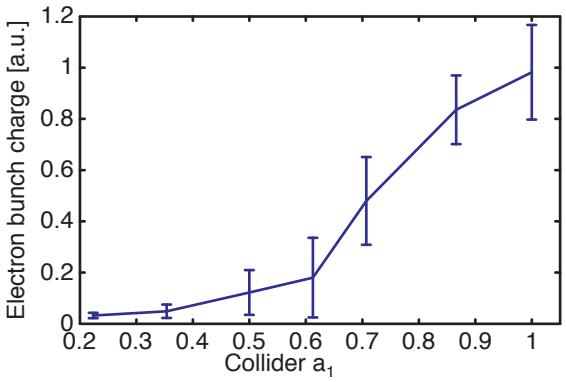

Figure 3.13: Experimental scan of collider beam normalized vector potential agree with simulations [130]. Injection occurs for $a_1 \gtrsim 0.2$ and saturates for $a_1 \simeq 1$. Due to beam loading, as the charge in the bunch increases the final energy decreases and the energy spread increases.

beams (Fig. 3.13). Because of laser output power limitations, the scan could not be performed beyond $a_1 \simeq 1$.

In conclusion, the successful implementation of an active beam pointing system led to the production of stable ($\simeq 20\%$ *r.m.s.* charge stability) electron beams in the colliding pulse injection scheme. Timing scans in both Hydrogen and Helium were performed, showing consistent timing window with two-dimensional PIC simulations. Pressure and collider beam intensity were scanned as well, showing CPI occurring for plasma densities below 5×10^{18} e^-/cm^3, with a driver strength of $a_0 = 3.75$. Injection reached a plateau as simulations predicted for $a_1 > 0.9$. Future experiments will focus on guiding the driver laser pulse over several Rayleigh lengths at the low densities CPI needs to operate at, and the production of stable, high-energy electron beams.

Chapter 4

Coherent Transition Radiation

4.1 THz source optimization

One of the primary focuses of this thesis was the development of an intense THz radiation source, as introduced in Chapter 1. The key objectives were to understand and optimize the THz source performance including spatial beam profile, temporal waveform and spectrum, energy and stability. Measurements of aberration-corrected spatial THz beams are presented, and novel techniques for measuring the pulse waveform have been developed. Work on increasing THz pulse energies, including increasing the radiator plasma size through the use of a pre-ionizing laser beam, and work on main drive laser beam pre-pulse control and pointing stability has been carried out. Two important technical improvements to the laser-plasma accelerator have been implemented that are found to be essential for obtaining stable performance of both the electron beam and THz beam: laser pre-pulse control and active beam stabilization.

Three different methods of pre-pulse control were evaluated: introducing a second colinearly propagating laser pulse to act as a controllable pre-pulse with adjustable timing; adjusting the timing of a Pockels cell to selectively attenuate laser energy arriving

prior to the main pulse; and a contrast improvement system based on the cross-polarized wave technique. Significant enhancement factors, > 5, were obtained using the cross-polarized wave (XPW) technique [140] allowing generation of μJ-class THz pulses.

4.1.1 THz collection efficiency: spatial beam profiles

In a laser-plasma accelerator, electron bunches are produced through the interaction of an intense focused near-infrared (NIR) laser with a plasma. The radiation pressure of an intense laser drive beam excites a plasma wake, accelerating electrons which emit THz radiation as they exit the plasma. Coherent THz radiation is emitted as the bunches exit the plasma-vacuum boundary [77, 80]. The details on the specific geometry of the LPA used for the experiments described in this thesis, as well as their THz emission, have been presented in previous work [77, 141, 69, 70, 142, 143].

THz experiments have been carried out with the goal of producing 10 μJ stable THz output suitable for pump-probe experiments and THz nonlinear optics [144]. The experiments were conducted using the Ti:sapphire based lasers at the LOASIS facility. The facility has three main amplifier chains (Godzilla, Chihuahua and TREX) and two target areas. All the THz experiments reported in this Chapter were done with the 10 TW Godzilla and multi-pulse Chihuahua amplifiers.

A 800-nm laser pulse (up to 0.5 J in 40–50 fs) is focused ($w_0 \simeq 6$ μm) onto Hydrogen or Helium gas from a supersonic gas jet. The plasma density is dependent on gas jet backing pressure and ranges from $n_e \sim 1$ to 8×10^{19} [e^-/cm^3]. Through the laser-plasma interaction, an electron bunch containing up to 10^{10} electrons propagates through the plasma-vacuum interface, producing coherent transition radiation (CTR) pulses. Part of the THz radiation ($\simeq 0.178$ sr) is collected and collimated by an off-axis parabola (OAP), with an incident angle $\theta = 19^o$, and focused by a second OAP outside the target chamber on an electro-optic crystal (Fig. 4.1). A model of the THz transport line is presented in

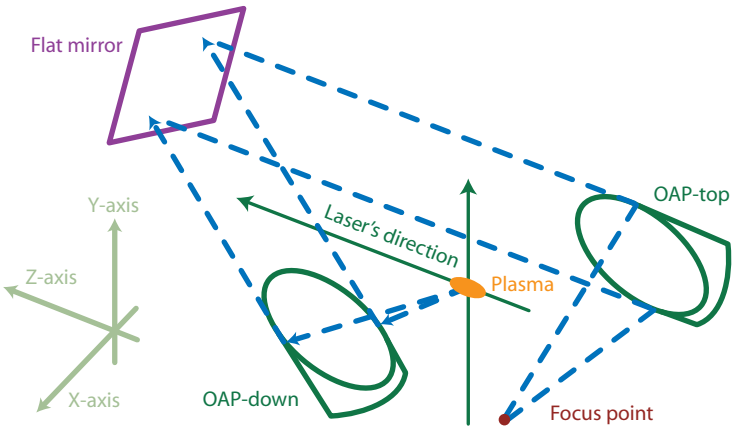

Figure 4.1: Sketch of the optical line. OAP-down collects transition radiation emitted by electrons while they cross the plasma-vacuum boundary and the couple flat mirror – OAP-top refocus the collimated beam onto an electro-optic crystal (for the EOS experiment).

Appendix B. A pair of polarizers (input polarizer/analyzing polarizer, called analyzer) and a quarter-wave plate ($\lambda/4$-plate) regulate the energy transmission of a probe beam onto a 12-bit camera. Through electro-optic (EO) effect, the THz pulse induces a change in crystal birefringence, which affects the analyzer transmission of the probe beam. By scanning the temporal delay between THz and probe pulse, a sign-resolved field profile of the THz pulse can be recorded. The recorded EO waveform $S_{\mathrm{EO}}(\tau)$ is a convolution of the original THz pulse $E_{\mathrm{THz}}(t)$ and known crystal parameters [145]. Alternatively, a Golay cell or bolometer is placed instead of the crystal to measure energy directly.

The amount of CTR produced by an LPA is characterized by its spatial beam profile, temporal waveform and spectrum, and its total energy. A two-dimensional (2D) electro-optic diagnostic [146, 147, 148] was used to measure the THz spatial profile (Fig. 4.2). A collimated, linearly polarized probe beam was overlapped with the focused THz pulse in an EO active crystal (*e.g.*, GaP or ZnTe $\langle 110 \rangle$). The high amplitude, low frequency field of the THz acted as an electrical bias on the crystal, inducing a localized, spatially varying birefringence. The probe beam, which is significantly larger than the THz focus, experiences a localized polarization rotation where it overlaps the THz, which is

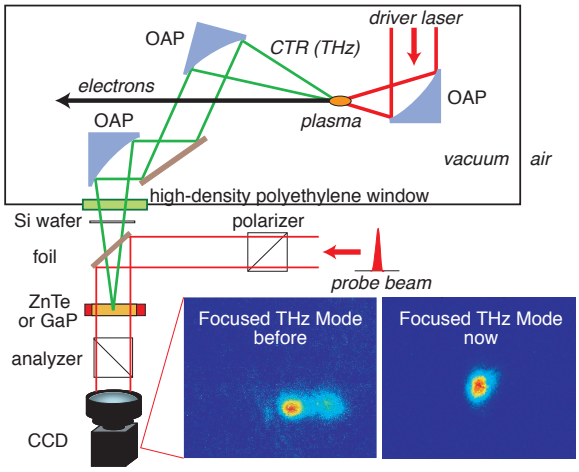

Figure 4.2: Setup for THz spatial profile measurement through EO sampling in a GaP or ZnTe crystal, using a 50 fs optical probe beam. Both EO images are integrated through the duration of the pulse and normalized in intensity; the new (*right*) pulse has a 0.52 mm $1/e^2$ intensity radius.

proportional to the field strength of the THz. The polarization rotation is analyzed and recorded with a crossed polarizer and CCD camera.

The conceptual lay-out for measuring the 2D profile is depicted in Fig. 4.2. The THz radiation, collected and collimated by an off-axis parabola, was focused by a second OAP outside the target chamber on a 100 μm thick GaP crystal. Also incident on the crystal was a collimated laser probe beam ($\lambda = 800$ nm) that overfilled the THz spot at the crystal plane. The probe polarization was rotated by the THz-induced birefringence and a camera read out the THz spatial mode by looking at the light passing through a crossed polarizer.

The probe beam was split off from the pre-amplified beam that seeds the TREX amplifier and was subsequently split in two beams, each of which was sent to a separate compressor. The first probe beam was partially compressed and was brought onto the same path as the THz beam and the second probe beam was used for the non-collinear optical mixing. In previous experiments [142], optical aberrations in the THz optical path (*e.g.*, astigmatism, coma) were observed. Elimination of aberrations caused by

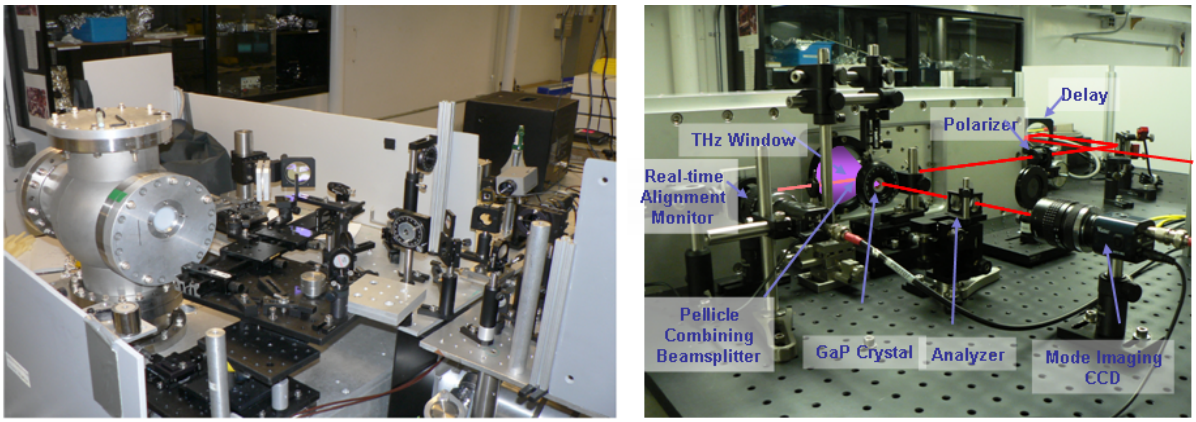

Figure 4.3: Old proof-of-principle setup (*left*) and new application-oriented setup (*right*).

misalignments in the THz imaging optics motivated the construction of an entirely new setup employing motorization of the vacuum THz imaging optics to allow *in-situ* optimization of the THz focused mode. In addition, the spatiotemporal diagnostics were completely re-engineered to create a dedicated, applications-oriented test and measurement platform (Fig. 4.3). The new experimental setup allows rapid switching between spatial and temporal diagnostics, and was engineered for increased repeatability.

Measurements of the THz focus using the new imaging system showed a dramatically improved mode shape (Fig. 4.2). While the modes in the initial experiments were irregular and astigmatic, the setup produced an alignment-corrected mode profile that is round and Gaussian with $1/e^2$ intensity radius $\simeq 0.52$ mm, and little or no observable aberration. The measured spot size is close to the diffraction limit for the $f/3$ focusing off-axis parabola.

Although the image in Figure 4.2 have been temporally integrated, this technique is capable of resolving temporal variations in the spatial field profile with a resolution of the probe pulse duration ($\simeq 45$ fs) by scanning delay. Unfortunately, this requires scanning of the relative timing between the probe and the THz pulse, and accumulation of the temporal field over multiple shots.

4.1.2 THz pulse energy

One of the key deliverables was to demonstrate the possibility of generating > 1 μJ energy per THz pulse. Initial experiments had been carried out using a liquid Helium cooled bolometer [149] which was calibrated at the infrared beam line at the Advanced Light Source (ALS) [142]. The possibility to use a Golay cell instead was explored. The Golay cell has many advantages over the bolometer detector. Among these are that the Golay cell is much smaller, and so is portable and maneuverable; it does not require cooling by liquid Helium, and so may be used continuously for many hours without lengthy preparations; and data is available giving an absolute energy calibration. The downside of the Golay cell is that it is 3–4 orders of magnitude less sensitive and that it is only available from a single manufacturer worldwide, in Russia. This resulted in nearly 18 months waiting time instead of the promised 6 month delivery time. The calibration of the Golay cell response in the THz band was done by E. Chiadroni *et al.* [150] at the FELIX facility in the Netherlands, and was found to be 0.59 μJ/V. Because the saturation voltage of the Golay cell is 1.44 V, its full-scale detection limit is only 0.85 μJ. A series of measurements of THz energies was done as a function of various interaction parameters using this detector, and will be discussed in Section 4.1.4.

During initial experiments, preceding THz energy optimization, energies on the order of 0.1 μJ had been detected using the bolometer. In order to increase the collected energy, several approaches have been pursued. The first one relied on simply increasing the collection efficiency. The new setup implemented (Sec. 4.1.1) improved collection efficiency and THz beam transport.

The second approach relied on maximizing two quantities which influence THz energy: the amount of charge in the bunch and the plasma size at the exit of the plasma through the introduction of a second beam to pre-ionize the plasma. This approach was motivated by theoretical analysis of the generation of coherent transition radia-

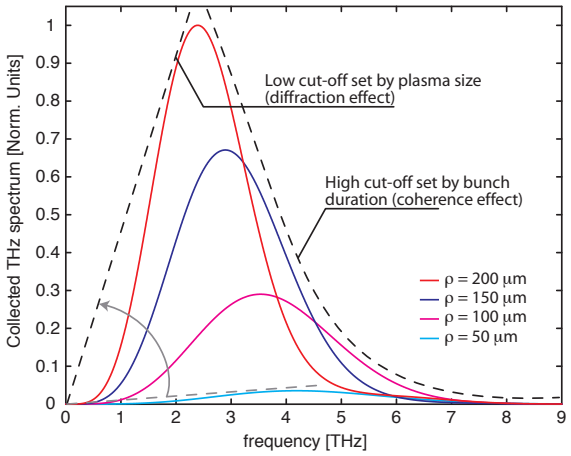

Figure 4.4: Predicted spectra (0.5 nC, $\sigma_z = 15$ μm, $E_c = 45$ MeV) of CTR collected by a 6-inch OAP (19^o off-axis) for different plasma transverse boundary sizes (ρ). The amount of emitted energy is strongly affected by the transverse boundary size of the emitting region.

tion (CTR) by the electron bunch. Analytic expressions for coherent THz radiation show that the energy is quadratically dependent on the charge of the electron bunch. Furthermore the spectrum is strongly dependent on the size, ρ, of the plasma at the transition surface and on the electron bunch longitudinal size, σ_z. The reason for the sensitivity to bunch length is the requirement for coherent THz emission. Since each electron in the bunch acts as an independent emitter of terahertz radiation, the radiation can only constructively interfere (*i.e.*, remain coherent) if the bunch is shorter than the emitted wavelength. Higher frequencies thus suffer more destructive interference and are consequently weaker, resulting in an upper limit on the THz spectrum (typically 3–6 THz, *c.f.* Fig. 4.4). The sensitivity to the plasma size is caused by diffraction effects when $\rho \sim \gamma\lambda_r/2\pi$ where γ is the Lorentz factor of the electron and λ_r the wavelength of the emitted radiation. As with Gaussian-beam propagation in general, the diffraction limit to the spot size is proportional to the wavelength. If the source is smaller than the diffraction limit, the THz energy will not couple efficiently to the propagating mode, and will be lost instead to evanescent waves. This effect thus provides a lower limit to

the THz spectrum (0.1–0.2 THz, *c.f.* Fig. 4.4).

An igniter beam, typically with energy significantly less than that in the main drive beam, has the potential to improve each of these properties. Unconstrained by the need to achieve the highest intensity possible to drive the LPA, the igniter can be focused with a large $f/\#$ to achieve a large focused spot size and hence create a large plasma. In addition, by pre-ionizing the plasma, the igniter can mitigate the effects of any existing pre-pulses on the main drive beam, and can create a guiding structure [151, 152, 40]; both of these effects enhance the operation of the accelerator, producing greater charge and more energetic, shorter electron bunches.

Analytical expressions predict that for beams of charge ~ 1 nC produced in large-radius ($\rho \gtrsim 200$ μm) pre-ionized channels, collected THz pulses of ~ 7 μJ are achievable. If in addition the size of the collection parabola could be increased to 6-inches, the collected THz pulse energy could increase to as much as 30 μJ per pulse.

4.1.3 Effects of laser pre-pulse

We now describe a description of experimental results that pre-date the installation of a contrast improvement system. The experiments aimed at understanding the basic parameters that control the performance of the accelerator in terms of emitted THz energy. To evaluate the performance the THz energy was monitored using a bolometer. As the accelerator can be optimized for different modes of operation (*e.g.*, high charge, high electron energy, etc.), it is important that optimization be done with the terahertz signals directly, and not with other related parameters such as the bunch charge or the strength of the γ or neutron radiation produced. Comparison of the optimal parameters for these different outputs can, however, elucidate the physical mechanisms at work. The following parameters were scanned:

1. Plasma density:

   This was done by changing the backing pressure of the solenoidal gas jet.

2. Plasma pre-ionization state and plasma size:

   This was done by using the "igniter" beam which is another laser pulse introduced on the same path as the main drive laser pulse through a polarizing beam splitter, with variable time delay and pulse duration.

3. Main drive beam pre-pulse level:

   In the first round of experiments, this was done by using the switch-out Pockels cell of the regenerative amplifier and a clean-up Pockels cell at the entrance to the next amplifier in the laser chain. The results of these experiments motivated a major effort and investment into cleaning up the contrast of the main drive laser pulse which will be discussed in Section 4.1.4.

The scan of gas jet backing pressure, and hence plasma density, showed a general increase in THz and γ radiation with density, peaking near 900 pounds-per-square-inch (psi, 1 psi $\simeq$ 6894.7573 Pa) H_2, consistent with operation in the self-modulated laser wakefield regime (Fig. 4.5). At low densities, the laser power was sub-critical, so self-focusing and electron trapping did not occur. At high pressure, the laser pulse should no longer be resonant, and should not drive the plasma wave efficiently, again shutting off the THz generation mechanism.

As illustrated in Figure 4.5, the igniter did enhance the generation of THz overall at all densities, while the trend with density was similar with and without the igniter beam. The primary effect of the igniter was found to be the optimization of the accelerator through a decrease in uncontrolled pre-pulse effect and guiding of the main drive beam. Figure 4.6 shows the dependence of the enhancement factor of the THz and γ radiation on the relative timing between the igniter and the drive beam. At small negative delays

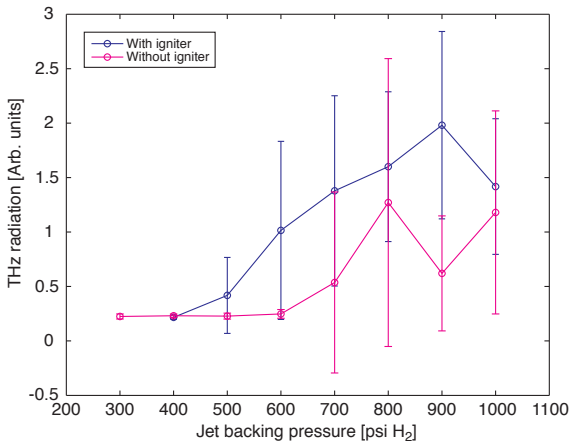

Figure 4.5: THz radiation signal amplitude, measured with the bolometer in the focus of the THz radiation collection beam path, as the function of the Hydrogen backing pressure of the gas jet. This backing pressure is directly proportional to the initial gas density at the interaction region.

(igniter arriving just before driver), the igniter appeared to act as a pre-pulse, creating a partially ionized volume which disrupted the propagation of the driver beam by creating a radially varying index profile that defocused it. The THz radiation in this regime is diminished by $\sim 50\%$ (*c.f.* close-up in Fig. 4.6). For larger negative delays, when the igniter was coming more than 200 ps before the drive beam, an enhancement appeared. This timescale, and the coincident behavior of the γ radiation implies that there was an evolution of the plasma that created conditions that enhanced the operation of the laser-plasma accelerator. This timescale is also correct for gas dynamic and thermodynamic effects to play a role, making it not unreasonable to attribute the enhancement effect to guiding of the main drive pulse as observed in previous work [40, 153, 154], resulting in higher electron beam energy and possibly shorter electron bunches (lower space charge effects).

Initial efforts with the igniter beam have not however resulted in plasmas of increased size as hoped for. In spite of this, the presence of the igniter did yield significant enhancements in the THz generation for the other reasons mentioned above. However,

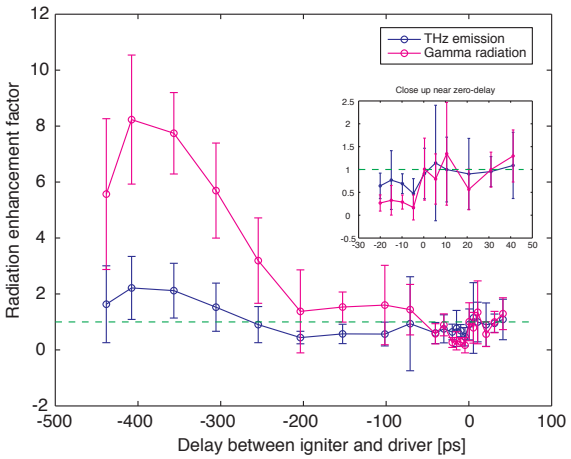

Figure 4.6: THz and γ radiation enhancement (defined as the ratio of signals with and without the presence of igniter pulse) as a function of the relative time delay between the igniter and driver pulses. Negative delay corresponds to earlier arrival of the igniter pulse.

the dynamics of the interaction between the igniter, the plasma and the drive beam are complex.

The presence of a pre-pulse on the drive beam can have a significant effect on the dynamics of the interaction of the drive pulse with the plasma [155], and hence can impact the amount of terahertz radiation produced. The timing of the Pockels cell controlling the ejection of the laser pulse from the regenerative amplifier cavity was next optimized to maximize the THz radiation produced by the accelerator. In order to effectively filter pre-pulse energy, the timing had to be adjusted to closely overlap with the front edge of the main pulse. However, since the time-scale for the Pockels cell state-change was on the order of a nanosecond, pre-pulses in the sub-nanosecond could still leak out of the cavity. To minimize the pre-pulse level required cutting into the main pulse and the procedure thus represented a compromise between eliminating pre-pulse energy and efficiently ejecting the main laser pulse.

As the deleterious effects of the pre-pulse were mainly due to partial ionization of the interaction volume (disrupting the interaction of the main pulse with the plasma), they

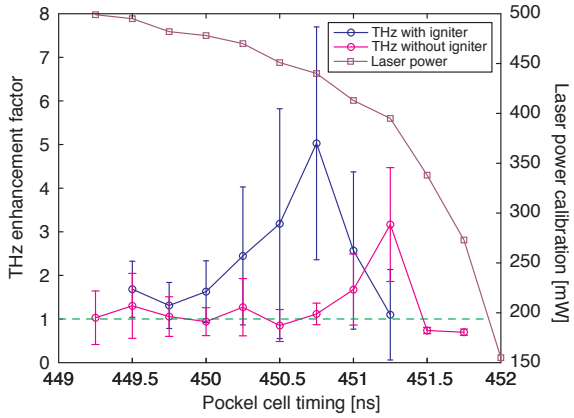

Figure 4.7: Control of the THz signal amplitude (*left* vertical axis) by controlling the ns-range, pre-pulse level of the laser via Pockels-cell timing adjustment in the regenerative amplifier (*horizontal axis*). *Blue* curve: measurements taken with the presence of additional igniter; *Magenta* curve: without igniter pulse. The *purple* decreasing curve (*right* vertical axis) represents the decrease of the output laser energy, as a consequence of cutting into the main pulse more and more, as the Pockels-cell timing value increases.

could be somewhat mitigated by employing the igniter to pre-ionize the plasma. This modification affected the optimum timing of the Pockels cell, an effect which is clearly seen in Fig. 4.7. Without the igniter, filtering the pre-pulse resulted in an enhancement of the terahertz emission by a factor 3.2 at a Pockels cell timing corresponding to a loss of about 20% of the amplified laser energy. With the igniter, the enhancement factor was greater, $\simeq 5$, at an optimum timing that was 0.5 ns earlier, corresponding to a loss of only 10% of the laser energy. It is clear that optimization of the timing had to be done with the igniter on, and that more energy would be available on target as a result. These results strongly motivated the implementation of techniques to eliminate the pre-pulse without compromising the energy of the drive beam. To this end, a module was built, in collaboration with Dr. O. Albert of the Physique du Cycle Optique (PCO) group at Laboratoire d'Optique Appliquée (LOA) in France, which uses a Cross-Polarized-Wave intensity filtering (XPW) method to increase the contrast of the laser pulse by 4 orders of magnitude.

4.1.4 Laser contrast enhancement

Based on the results described above, three critical techniques to improve the performance of the laser-plasma accelerator and electron source were identified: control of the laser pre-pulse, stabilization of laser performance and controlled electron injection. This section focuses on the development of the first two techniques. Results on controlled injection were discussed in Section 3.2.

A laser pulse contrast improvement technique based on crossed wave polarization filtering has been implemented to control pre-ionization and improve the laser-plasma accelerator performance. As the evaluation of preliminary experiments indicated, optical pre-pulses, inherent in most Chirped Pulse Amplification (CPA) laser systems, have a strong effect on the stability of the laser accelerator and the yield of THz radiation.

XPW, or "crossed-polarized-wave" filtering is a nonlinear optical method to minimize the relative amplitude of any optical pulse ("pre-pulse") or slowly emerging optical energy ("pedestal" or ASE for amplified spontaneous emission) preceding the arrival of the main, ultrashort laser pulse in optical systems [140]. The method is based on cubic anisotropy induced by intense laser pulses in special nonlinear crystals, such as BaF_2 with high third order non-diagonal coefficients. The nonlinear crystal is preceded by a polarizer and followed by an analyzing polarizer (analyzer). The main pulse, which induces strong enough polarization rotation for itself, is transmitted with good efficiency through the analyzer. On the other hand, relatively small pre-pulses and pedestal do not create enough induced anisotropy and are then suppressed. The difference in these transmission values through the crossed polarizers results in significant contrast enhancement and pulse contrast up to 10^{-11} have been achieved using this method [156].

A detailed characterization of the laser pulses before and after the XPW setup was performed during the implementation process, and continuous monitoring equipment (*e.g.*, photodiodes for relative energy measurements, cameras for alignment monitoring

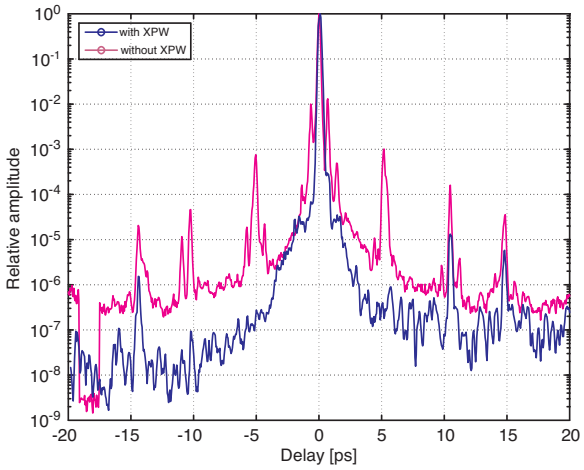

Figure 4.8: Optical contrast of the fully amplified driver laser at the interaction point before (*magenta* curve) and after (*blue* curve) installation of the XPW contrast filter.

and an optical spectrometer for measurement of spectral changes to ensure correct operation of the XPW filter) was installed. The most important parameter, *i.e.*, the contrast enhancement factor at different time regions before the arrival of the main pulse was measured with a commercial third-order cross-correlator device ("Sequoia" from Amplitude Technologies). A contrast enhancement of 3 orders of magnitude was achieved on the -0.75 ps pre-pulse and up to 4 orders on the other pre-pulses (Fig. 4.8).

New sets of experiments were performed with the contrast-enhanced laser to gauge the effectiveness of increasing the pulse contrast in improving the performance of the accelerator and the production of THz and other radiations. The results showed not only dramatic increase in the production of charge, THz, γ-s, and neutrons, but also a dramatic decrease in shot-to-shot variability, which were at the 100% level prior to XPW implementation, and are now roughly at the 10% level. The results of the new scans are summarized below. These scans all contribute to show that optimization of the THz radiation occurs in a multi-parameters space, and that varying different experimental knobs causes variations in different numbers of these parameters, which may or may not be interdependent.

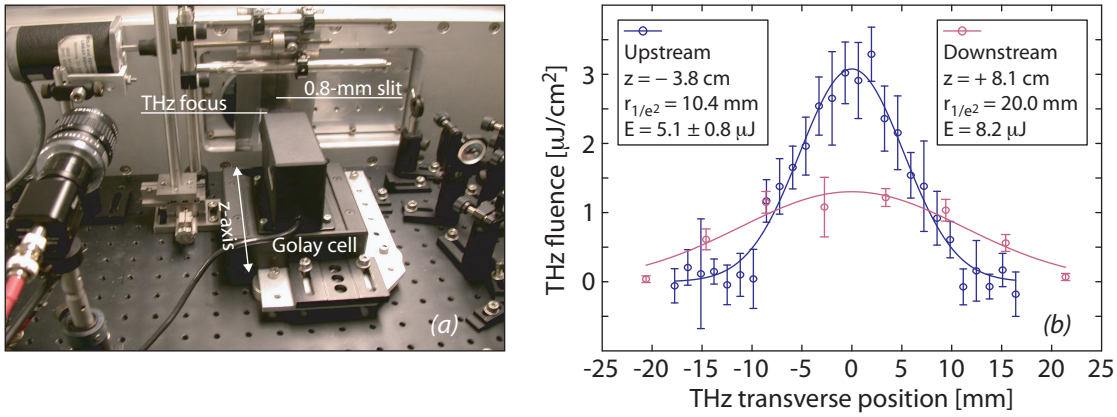

Figure 4.9: Golay cell measurements of the THz energy prior XPW-filtering implementation. *(a)* Photograph of the Golay cell mounted at the THz focus behind a motorized slit and observing the collected THz energy. The CCD camera on the left is monitoring the set-up. A slit of width 0.8 mm was scanned across the THz beam upstream of focus. *(b)* Measurements of the THz spatial energy distribution at an upstream position from the THz focus (detector at focus and a slit at $z = -3.8$ cm), and a downstream position of $z = +8.1$ cm from the focus (no slits and scanning the Golay cell position). The upstream profile has a radius ($1/e^2$) of 10.4 mm and an energy of 5.1 μJ, and the downstream profile has a radius of 20.0 mm and an energy of 8.2 μJ.

Golay cell measurements were performed to characterize the energy of the THz pulses generated both before and after laser contrast enhancement. During the course of initial measurements of THz pulse energy, it was found that the Golay cell was strongly saturated, requiring development of secondary techniques to recover the energy. In the first technique, the detector was moved 8.1 cm downstream of the THz focus until the signal was reduced below saturation by only collecting a small portion of the expanding THz beam. The detector was then scanned transversely to the beam to recover the radial distribution of the THz energy (Fig. 4.9a), allowing a calibration of the fractional portion of the beam energy collected by the Golay cell (assuming cylindrical symmetry of the THz beam). After accounting for the calibration, the THz beam energy was then measured to be 8.2 μJ (Fig. 4.9b). In the second technique, the Golay cell was placed at the THz focus, and a narrow slit-aperture was placed across the THz beam at a plane

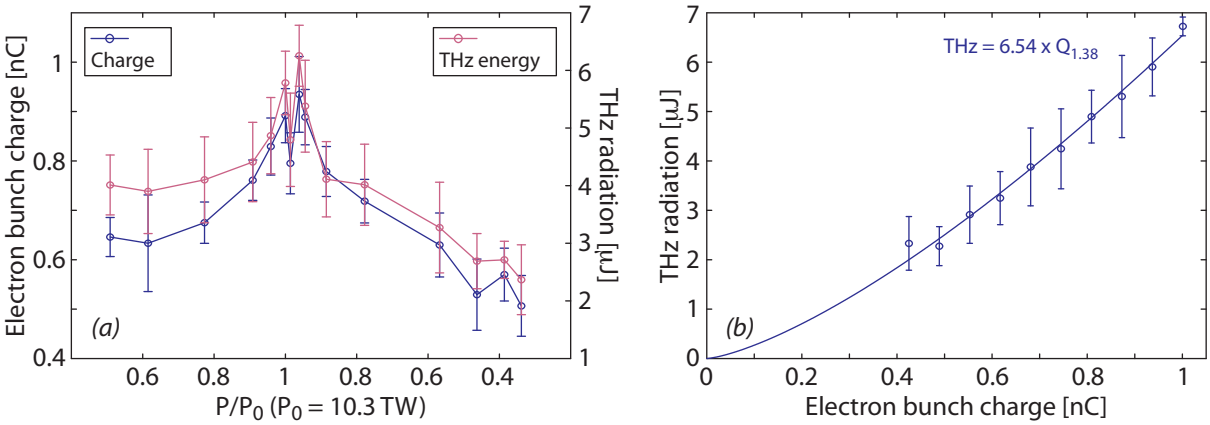

Figure 4.10: *(a)* Scan of THz and charge yield versus laser pulse compression. The pulse compression was scanned by varying the grating separation in the compressor while keeping the pulse energy constant. The pulse compression is expressed in terms of the laser power relative to the power at best compression (P/P_0). Values on the left of the peak correspond to negative chirp, and those on the right to positive chirp. *(b)* Dependence of THz radiation on electron bunch charge for the laser pulse compression scan. The fit is a power law of the form $E = A \times Q^B$, with $A = 6.54$ and $B = 1.38$.

3.8 cm upstream of the focus (Fig. 4.9a). The resulting distribution of energy density was then integrated to yield a full energy of the beam of 5.1 μJ, in reasonable agreement with the first technique. It should be noted that the second technique employed no assumptions about the shape of the beam profile, making it theoretically more accurate. In fact, as theory predicts that there will be strong chirping (*i.e.*, time-dependent frequency variation) of the beam in the direction perpendicular to the one scanned, it is then possible that the mode profile was not perfectly axis-symmetric, accounting for some discrepancy in the two measurements. To be conservative, the energy measurement from the second technique was used to provide an absolute energy scaling for the other THz measurements.

The most dramatic effect of the XPW was the increase in performance of the accelerator as measured by the yield of radiation. Before implementation of the XPW, a peak charge of 0.25 nC, measured with an 5.5 cm inner diameter ICT located 40 cm

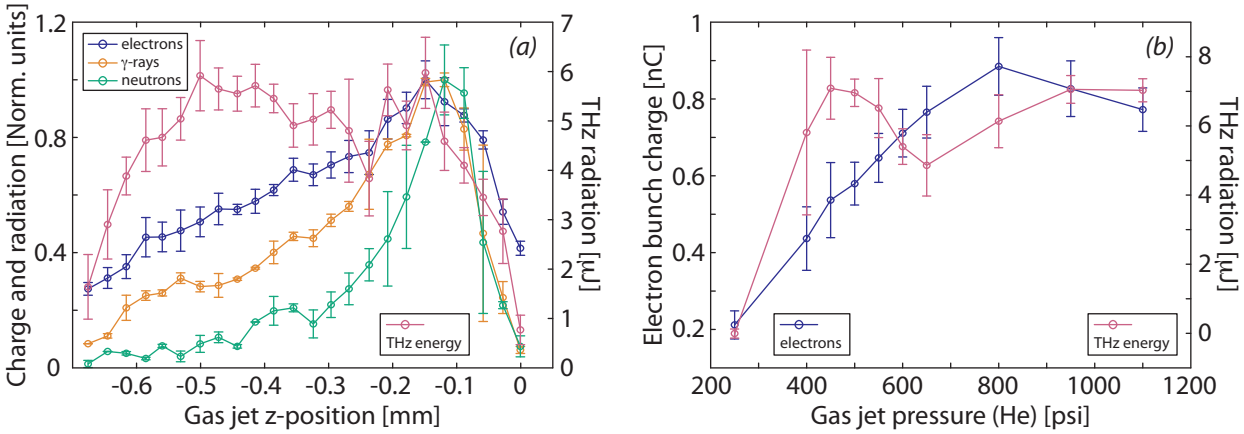

Figure 4.11: *(a)* Scan of THz, charge, neutron and γ yield versus longitudinal position (z) of the gas jet with respect to the laser focus. *(b)* Scan of THz and charge yield versus backing pressure of the gas jet.

downstream from the gas jet, was achieved after tuning the laser system for several days. After XPW implementation, a peak charge of 0.95 nC (*i.e.*, a factor 4 enhancement) was achievable with relatively little laser tuning. Figure 4.10a shows the dependence of the bunch charge and THz energy with laser peak power by carrying out a compressor scan. The observed asymmetry of the yield in charge and THz radiation is consistent with previous experiments on investigating the effect of pulse shaping on the performance of the LPA [37]. Pulse shapes can become skewed away from optimum compression [157]. The dependence of THz on charge is plotted in Fig. 4.10b. The fit through the data indicates that the collected THz energy scaled as the amount of charge to the power 1.4, *i.e.*, different than the simple quadratic dependence. This can be attributed to the fact that the expectation of quadratic dependence does not account for the variation in other parameters (*e.g.*, electron bunch energy, electron bunch duration and plasma emitter size) that may occur when scanning the compression.

Figure 4.11a shows the dependence of THz, neutron, γ-ray yields and charge on position of the gas jet with respect to the focal position of the laser. As evidenced by the charge, γ and neutron radiation yield, the accelerator performance was optimized

when focusing the laser at the upstream edge of the gas jet, which is well known [153]. At positions where the accelerator was not optimized, strong THz continued to be emitted. In fact, the data indicate that the THz emission was constant over a significant range of gas jet positions. At first glance, there is a discrepancy in the data: the same levels of THz were produced at significantly different ICT charge levels. However, the total charge that passes through the ICT is dependent on the divergence of the electron beam: high energy beams have significantly lower divergence than lower energy beams. Magnetic spectrometer data indicate that the energy was lower and divergence may have been broader when the laser was focused at the downstream edge. At the location of the ICT at the time of the experiments, about 40 cm away from the gas jet, only a fraction of the charge was captured for high divergence beams. Earlier data showed that beam divergence angle can exceed the ICT acceptance for such beams ($\simeq$ 140 mrad). This indicates that the ICT may have underestimated the bunch charge when the laser was focused at the downstream edge of the jet, which would explain the observation of increased ICT-to-THz ratio at that location in Fig. 4.11a.

The effect of plasma size on this data set was also investigated. Theory predicts that the size of the THz emission region can have a strong effect on the amount of THz emission for a given amount of charge (*c.f.* Fig. 4.4). By analyzing the plasma shape for shots taken on the left side of the jet where the charge was less optimized, and other cases on the right side of the gas jet where the collected charge was high, it is found that the plasma size at the output of the interaction was similar.

Of the scans, the dependence of THz on gas-jet backing pressure showed the most unexpected behavior: the charge in the electron bunches showed a predictable increase with backing pressure up to an optimal value of 800 psi. However, the THz radiation, after rising initially with pressure, counter-intuitively dipped markedly between 600 psi and 700 psi (Fig. 4.11b). This dipping behavior was also present in the pre-XPW data,

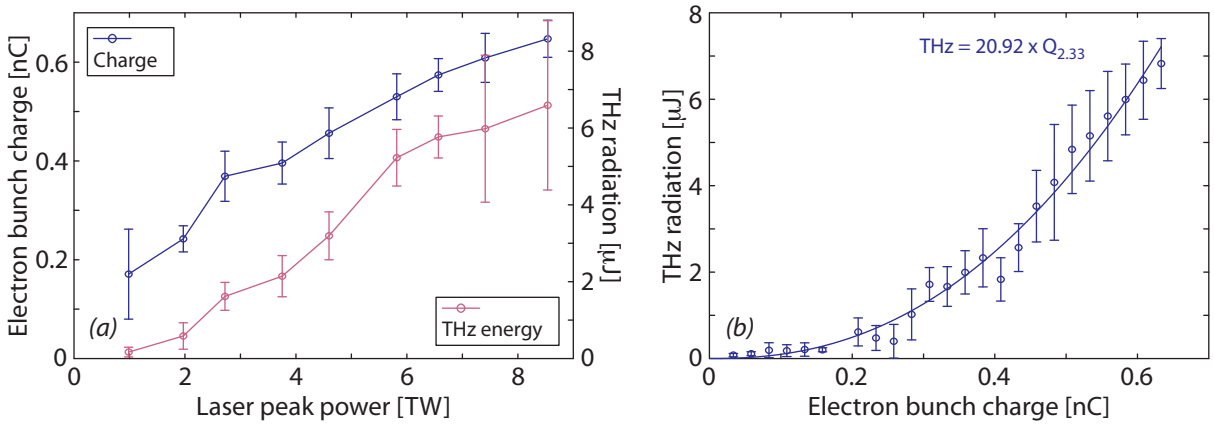

Figure 4.12: *(a)* Scan of THz and charge yield versus laser pulse peak power. The peak power was scanned by varying the degree of amplification in the final amplifier to adjust the final pulse energy while keeping the pulse duration constant. *(b)* Dependence of THz radiation on electron bunch charge for the pulse energy scan. The fit is a power law of the form $E = A \times Q^B$, with $A = 20.92$ and $B = 2.33$.

Fig. 4.5. The non-quadratic relationship is not yet understood.

Figures 4.12a and 4.12b show the charge and THz yield as function of laser peak power by scanning the laser pulse energy and the THz yield vs. charge, respectively. In this scan, peak powers in the compressed pulse was varied from 1 to 9 TW by changing the degree of amplification in the final amplifier. The dependence of THz on charge during a laser-power scan is found to be near quadratic, as expected since both plasma density and pulse duration are constant thus reducing variations in plasma size and electron bunch duration. It should be noted that the THz yield was also significantly improved in shot-to-shot stability with the XPW. The yield fluctuated by 10% as opposed to 100% without XPW under the same conditions. In addition, results in Figure 4.12a demonstrate that 1–2 μJ ultrashort ($\lesssim$ 50 fs, *c.f.* Sec. 4.2) THz pulses can be produced in the laser-plasma accelerator using only 2–3 TW laser power; such devices are commercially available (*e.g.*, Thales, Amplitude Technologies, etc.) and could provide an application-oriented table-top sized source of intrinsically synchronized high charge electron bunches, THz radiation and X-ray radiation (*c.f.* Chapter 5).

4.2 Temporal electron beam profile

Terahertz radiation produced by laser-plasma accelerators has received increasing attention as both a source and as a diagnostic of the performance of the accelerator. Because electron bunches produced by LPAs are very short ($\sim$ 10 fs), they can radiate coherently in the 0–4 THz frequency range when crossing a sharp dielectric boundary [77, 80]. The resultant THz pulses can have high electric fields, on the order of the megavolt per centimeter (MV/cm), and high energies, on the order of the microjoule (*c.f.* Sec. 4.1) in sub-picosecond pulse durations, making them attractive for both probing and pumping of samples. In addition, the intrinsic synchronization of these THz pulses with the laser system allows for multiple-pulse, multi-color experiments. Because the properties of the THz pulses are directly related to those of the electron bunches producing them, they are also well-suited for use as diagnostic to measure electron bunch parameters. In this thesis, several detection techniques were implemented and used to characterize the temporal, spectral and spatial profile of THz pulses emitted by electron bunches produced in a laser-plasma accelerator and infer the electron bunches' longitudinal length.

4.2.1 Basic description of transition radiation theory

The theory of transition radiation generated by relativistic electrons crossing a dielectric boundary such as a plasma-vacuum boundary has been extensively studied [112, 71, 77, 80, 81], as introduced in Sec. 1.4. Transition radiation is generated by electron beam induced polarization currents at the plasma-vacuum boundary when the plasma density drops below the critical density where $\omega_p = \omega$, see Appendix A, Eq. (A.55). The dielectric constant of the plasma satisfies $\epsilon \gg 1$ for the plasma densities used in the experiments, and the plasma can be modeled as a conductor for frequencies $\omega < \omega_p$. In addition, the transition from plasma to vacuum is approximated by a step function

conductor-vacuum provided the plasma density roll-off is shorter than the formation length (*c.f.* Sec. 1.4) [113, 80] given by:

$$L_f \approx \frac{\lambda_r}{1/\gamma^2 + \theta^2} \tag{4.1}$$

where λ_r is the radiation wavelength, θ is the observation angle with respect to the electron trajectory which is assumed to be normal to the plasma surface, and γ is the Lorentz factor associated with the electron crossing the boundary. For electron energies ranging from 1 to 100 MeV, an observation angle of 19 degrees and a radiation wavelength of 300 μm (1 THz), the formation length is of the order of $L_f \simeq 1.5$–3 mm and the plasma density roll-off is less than a millimeter, *c.f.* Sec. 3.1. The coherent differential radiated energy spectrum by solid angle Ω emitted by a bunch traveling normal to the plasma-vacuum boundary is given by [80, 81, 111]:

$$\frac{\partial^2 W}{\partial \omega_r \partial \Omega} = \frac{r_e m_e c}{\pi^2} N_b^2 \left| \int \mathcal{E}(\theta, u) D(\omega_r, \theta, u, \rho) F(\omega_r, \theta, u)\, g_{\parallel}(u) du \right|^2 \tag{4.2}$$

where $g_{\parallel}(u)$ is the normalized longitudinal energy distribution of the electron beam, $u = \gamma\beta$ is the electron momentum normalized to $m_e c$, ω_r is the radiation angular frequency and N_b is the number of electrons in the bunch. Functions $\mathcal{E}(\theta, u)$, $D(\omega_r, \theta, u, \rho)$ and $F(\omega_r, \theta, u)$ are defined below. It is assumed that the plasma-vacuum boundary can be approximated by a circular surface with radius $\rho \gg \sigma_\perp$ where $\sigma_\perp$ is the *rms* transverse size of the electron bunch. This condition is well satisfied given that typical plasma radii measured during the experiments, *c.f.* Sec. 3.1, are on the order of 200–400 μm and electron bunches have a transverse size on the order of a micron, *c.f.* Chapter 5.

The correction to the spectrum due to diffraction from the limited transverse extent

of the plasma is given by:

$$D = 1 - J_0(bu\sin\theta)\left[bK_1(b) + \frac{b^2}{2}K_0(b)\right] - \frac{b^2}{2}K_0(b)J_2(bu\sin\theta) \tag{4.3}$$

where the dimensionless impact parameter $b = k\rho/u$ is the ratio of the transverse size of the dielectric ρ to the transverse extent of the self-fields of the relativistic electrons ($\sim\ \gamma\lambda_r$). J_m and K_m are the m^{th} order regular and modified Bessel functions, respectively. For a large impact parameter, *i.e.*, $\rho \gg \gamma\lambda_r$, diffraction effects are negligible and $D \to 1$. For small impact parameters, *i.e.*, $\rho \lesssim \gamma\lambda_r/2\pi$, diffraction becomes a dominant effect and sets the low cutoff frequency of the spectrum. For electron parameters representative of gas jet experiments, such as a 20 MeV ($\gamma \sim 40$) electron beam and an average radiation of 1 THz ($\lambda_r \sim 300$ μm), the radiation emitted is diffraction limited since $\rho_{\text{diff.}} = \gamma\lambda_r/2\pi \sim 640$ μm.

The spatial form factor F, which describes the degree of coherence in the bunch, is the Fourier transform of the electron bunch spatial distribution. Assuming an uncorrelated spatial distribution the form factor can be written $F = F_\perp F_\parallel$ where $F_\perp$ is the form factor associated with the transverse profile of the bunch and $F_\parallel$ the form factor associated with the longitudinal profile. For a Gaussian spatial profiles, the form factor can be written:

$$F = \exp\left[-\frac{1}{2}\left(\frac{\omega\sigma_\parallel}{v}\right)^2 - \frac{1}{2}\left(\frac{\omega\sigma_\perp\sin\theta}{c}\right)^2\right] \tag{4.4}$$

$$\simeq \exp\left[-\frac{1}{2}\left(\frac{\omega\sigma_\parallel}{v}\right)^2\right] \tag{4.5}$$

where $\sigma_\parallel$ is the *rms* length of the electron bunch and provided that $\sigma_\perp\sin\theta \ll \sigma_\parallel$. The dependence of the form factor on the longitudinal bunch length $\sigma_\perp$ makes coherent transition radiation a tool to measure the electron bunch temporal profile. The form factor

shows that the emission becomes incoherent when the radiation wavelength exceeds the bunch length, $\lambda_r \gtrsim \sigma_\parallel$. As $\sigma_\parallel$ decreases, the high cutoff frequency of the spectrum increases. The spectral region of coherent radiation is then approximately defined by the longitudinal coherence (upper bound) and the diffraction effects (lower bound) [111]: $uc/\rho < \omega_r < c/\sigma_\parallel$, as illustrated in Fig. 4.4, which typically translates into a spectral range 0–4 THz.

Note that from Eq. (4.2), the differential energy radiated by a single electron ($N_b = 1$, $F = 1$) crossing a dielectric boundary with infinite transverse extent ($D = 1$) at normal incidence is retrieved [71, 73, 74]:

$$\frac{\partial^2 W_e}{\partial \omega_r \partial \Omega} = \frac{r_e m_e c}{\pi^2} \mathcal{E}(\theta, u)^2 = \frac{r_e m_e c}{\pi^2} \frac{u^2(1+u^2)\sin^2\theta}{(1+u^2\sin^2\theta)^2} \tag{4.6}$$

4.2.2 Characterization of downramp injected electrons

As discussed in Sec. 4.2.1, emission of coherent transition radiation at THz frequencies can be used to diagnose the electron bunch length. A first generation of measurements was performed to characterize the duration of low absolute-momentum-spread electron bunches produced in a plasma density gradient [2, 158].

An alternative injection method to the colliding pulse injection scheme discussed in Sec. 3.2 has been proposed [63, 159, 160] and demonstrated [2, 158] using a plasma density downramp. In a plasma density downramp, the plasma wavelength λ_p increases and the phase velocity of the plasma wave v_p decreases, *c.f.* Eq. (2.18), as the laser propagates through the plasma, thus reducing the trapping threshold by reducing the minimum electron energy necessary, *i.e.*, lowering the separatrix in phase-space (Eq. (A.79)). This trapping mechanism has been characterized by simulations [160, 65, 2] and the crucial parameter that determines the resulting electron beam quality is the rate of density decrease. An advantage of the downramp injection technique is that it requires only one

laser pulse and a thin gas jet, < 1 mm, providing good transmission of the laser mode through the plasma which allows coupling to a second low density acceleration module [161].

Experiments were performed on the 10 TW laser system. The 0.5 J, 47 fs FWHM laser pulse was focused to a 7.5 μm FWHM spot, providing a Rayleigh length $z_0 \simeq$ 220 μm, on the downstream edge of a slit gas jet oriented transversely to the laser propagation axis. The plasma, which was made of Hydrogen, had a near-Gaussian profile with a maximum density of $2.2 \pm 0.3 \times 10^{19}$ e^-/cm^3 and was 750 ± 100 μm FWHM wide. The short Rayleigh length compared to the downstream plasma density roll-off allowed selection of the rate of density decrease by scanning the slit jet longitudinal position relative to the laser focus. In these experiments, the magnetic spectrometer, used to characterize the electron bunch energy distribution, had a restricted acceptance. The magnetic spectrometer had a fixed 55 degree bending angle from the laser axis to its phosphor screen (Lanex, *c.f.* Sec. 3.2) and covered $\pm$14% about the central momentum determined by the magnet current with a resolution of $\pm$5% in momemtum. The electron bunch charge was determined by cross-correlating the intensity of the phosphor screen with the ICT signal. To circumvent the limited acceptance of the spectrometer, the presence of high energy electrons was monitored using γ-radiation detectors [36] measuring the bremsstrahlung radiation from the electron beam dump. Later experiments also verified the momentum distribution using an upgraded magnetic spectrometer which covered the full energy range.

Focusing the laser on the upstream edge of the gas jet, *i.e.*, on the up-ramp of the plasma, led to conventional self-trapping of plasma background electrons producing electron bunches with an exponential energy distribution extending to the tens of MeV, consistent with previous results [153]. The high charge, high energy bunches generated a peak in γ-radiation. As the focus of the laser was moved to the downstream edge

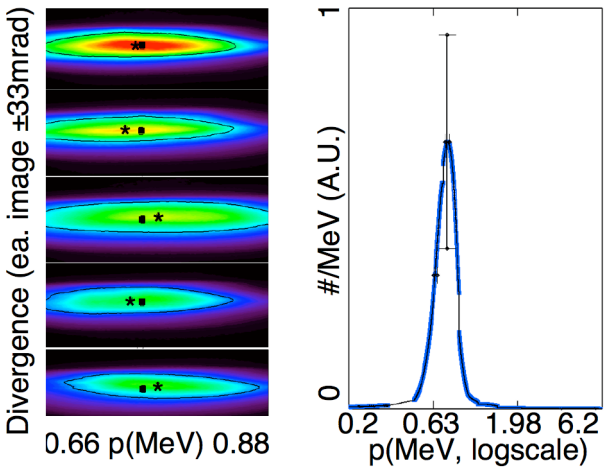

Figure 4.13: Energy distribution of electron bunches produced using plasma density downramp injection. The slit jet was 750 ± 100 μm FWHM long and the laser focus was located 300 μm downstream of the peak density. *(left)* Consecutive shots show the pointing and bunch stability by displaying the current ($*$) and average, over 45 shots, (.) centroids. *(right)* Average spectrum shows *rms* error bars for charge, mean energy and energy spread (FWHM). Figure from [2].

of the jet, *i.e.*, on the plasma downramp, the ICT signal increased by a few-% while the γ-radiation decreased, indicating the production of lower energy electron bunches. Different datasets on 3 different run days showed that this mode of operation was stable and repeatable over a week of operation. Over 78 shots of a dataset, electron bunches had a central momentum of 0.76 MeV/$c \pm 0.02$ MeV/c *rms* and a momentum spread of 0.17 MeV/c ($\sim 20\%$) $\pm$0.02 MeV/c *rms*. The electron bunch had a charge of 0.3–1 nC with a 40% *rms* stability. Pointing and divergence were observed in the out-of-plane direction and showed 20 mrad FWHM $\pm$1.8 mrad *rms* with a pointing stability of 1.5 *rms*, indicating a transverse bunch momentum of the order of 0.2 MeV/c. Particle-in-cell (PIC) simulations (VORPAL [44]) confirmed the production of MeV-class electron bunches with 10–20% level momentum spread for laser powers of 8–10 TW and plasmas with densities of $1.8\text{–}2.2 \times 10^{19}$ e^-/cm^3 and 0.5–1 mm FWHM widths [2, 158].

In addition to momentum spread measurements, the bunch duration of these stable

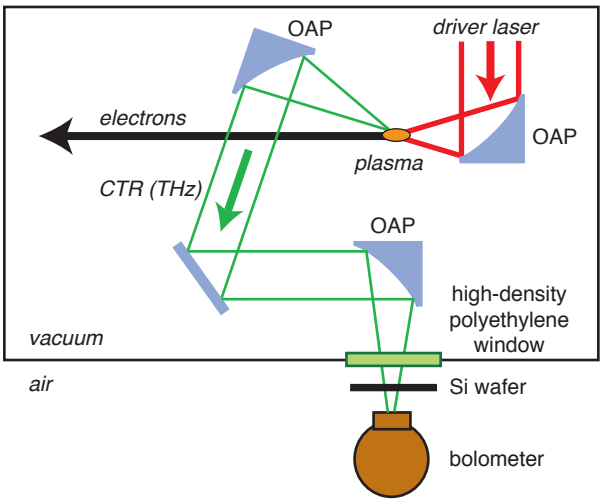

Figure 4.14: Setup for THz pulse energy generated by a downramp injected electron beams. A 6-inch effective focal length off-axis parabola (OAP) is used to collect part of the THz emission (CTR). A 7-inch OAP is used to focus it back into the bolometer aperture.

MeV-class electron beams were shown to be suitable for staging experiments by demonstrating that the bunch length is short enough to be post-accelerated in a second LPA. The bunch length τ_b was inferred from the THz emission at the plasma-vacuum interface. Since the amount of transition radiation produced by a 1 MeV beam is too small to be characterized by electro-optic techniques, which will be introduced in Secs. 4.2.3–4.2.4, a liquid-Helium-cooled Silicon composite bolometer [149, 141] with an acceptance of $f \simeq 0.3$–6 THz was used to measure the amount of THz energy emitted (Fig. 4.14). A bolometer is a sensitive energy detector ($< 10^{-14}$ J) made of a resistor connected to a heat sink. A constant current passes through the resistor creating a thermal equilibrium between the Ohmic heating and the energy dissipation in the heat sink. Thus, any radiation incident on the resistor will increase its temperature which will result in a change in resistance and voltage. The energy of the radiation collected is proportional to the induced voltage difference.

The THz emission was measured in four wavelength bands using two different filters to cut the spectrum: Teflon (1/4-inch thick) and Fluorogold (0.5 mm thick), with spec-

tral cutoffs at ~ 2 THz and ~ 1 THz, respectively. Assuming a Gaussian electron bunch profile, the bunch length was inferred by measuring the ratios of emission in each spectral band: $\tau_b \simeq 300^{+600}_{-200}$ fs using Teflon, and $\tau_b \simeq 210^{+120}_{-80}$ fs using Fluorogold. Note that Teflon has a less abrupt cutoff, reducing its precision. These lengths agree with bunch lengthening due to space charge in a plasma density downramp [65]. Simulations [162] indicate production of $\lesssim 10$ μm (30 fs) bunches inside the plasma and bunch lengthening in the plasma downramp up to ~ 50 μm (200 fs). Thus, injection into a second plasma channel could be achieved by using a sharp transition between the two stages.

In conclusion, experiments demonstrated control of the injection by lowering wake phase velocity and trapping threshold using negative plasma density gradients. Production of 0.76 ± 0.02 MeV/c bunches with 0.17 MeV/c longitudinal momentum spread and 0.02 MeV/c transverse momentum spread, was demonstrated. Coherent transition radiation measurements showed the bunch duration at the exit of the plasma was $\tau_b \sim 200 \pm 100$ fs, in agreement with simulations which indicate bunch durations inside the plasma of less than 30 fs. The combination of the high stability of these experiments and the high quality of the produced electron bunches shows the suitability of this technique as an LPA injector and could lead to $< 0.1\%$ energy spread GeV-class electron beams.

4.2.3 Electro-optic sampling of THz pulses

Because of its ability to resolve both spatial and temporal features with high resolution, optical probing is an important tool for the analysis of ultrafast phenomena. The simplest approach consists in probing at different delays the features to be observed with a short probe pulse. However, this scanning approach can be impractical for high shot-to-shot variation experiments or low repetition rates. In this thesis, we present both scanning and single-shot techniques to resolve the spatiotemporal content of the

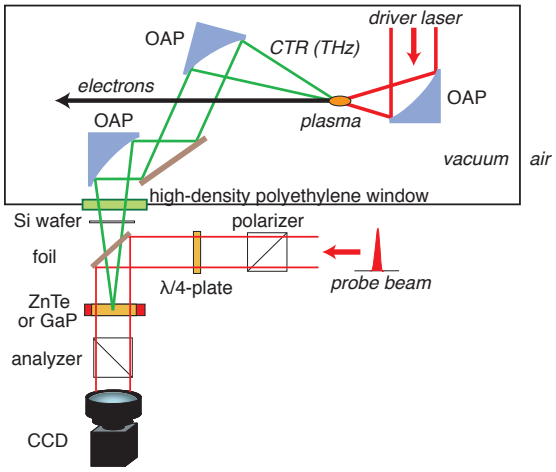

Figure 4.15: Setup for sign-resolved 2D-EO sampling. The THz pulse overlaps with a short circularly polarized probe pulse (couple polarizer – $\lambda/4$-plate) in a EO active crystal. The THz-induced birefringence causes a local polarization rotation which is converted to an amplitude modulation by a cross-polarized analyzer. The local amplitude modulation is measured as an intensity modulation by a CCD camera.

coherent transition radiation emitted by the relativistic electrons at the plasma-vacuum interface, *c.f.* Sec. 4.2.1. These techniques rely on a widely used measurement method for electron bunch durations and temporal structure, known as electro-optic (EO) sampling [163, 164, 165, 166, 167]. In this technique, the low frequency THz-electric field of the CTR induces a change of birefringence in an EO active crystal. A near-infrared (NIR) probe pulse, timed with the THz, is then used to probe the birefringence and measure the THz-field strength. The analysis of the measured THz waveforms are influenced by several effects [168, 145] such as the phase mismatch in the crystal between probe and THz pulses, the dispersion and absorption effects in the crystal, and limited time resolution due to the finite duration of the probe. However, these effects can be modeled since the crystals conventionally used for EO sampling (*e.g.*, ZnTe, GaP, GaAs) have well characterized dispersion functions in the THz domain [169, 170, 145].

The simplest EO experimental method employs a single linearly polarized probe pulse, shorter than the characteristic CTR pulse to be observed, which experiences a

polarization rotation as it propagates through the crystal. The polarization rotation is converted to an amplitude modulation by a polarizer, termed "analyzer", and the intensity variation is retrieved by scanning the delay between the probe and the THz pulse, using either a photodiode or CCD camera [70, 148, 171, 172]. When using a CCD camera, the technique is usually referred to as "2D-EO sampling" since it provides a two dimensional spatial slice of the THz pulse at a given time set by the probe delay. Two configurations of this technique have been implemented; in both configurations, the analyzer is set to minimize the probe transmission in the absence of THz, *i.e.*, the input polarizer which sets the polarization of the probe pulse and the analyzer are cross-polarized. The difference between the two configurations is in the probe pulse input polarization. In the "non sign-resolved" configuration, the probe is linearly polarized and in the absence of THz there is no signal on the CCD camera. In the "sign-resolved" configuration, the probe is circularly polarized by introducing a quarter-wave plate ($\lambda/4$-plate) between the polarizer and the analyzer (Fig. 4.15). While this configuration is not as sensitive as the previous one, it does resolve the sign of the THz electric field.

In the non sign-resolved configuration, the good extinction ratios of both the polarizer and the analyzer makes the technique very sensitive to low THz field strengths. The relative transmission of the probe intensity through the analyzer is given by [142]:

$$\frac{I_T}{I_0} = \sin^2 \frac{\Gamma_{\mathrm{THz}}}{2} \tag{4.7}$$

where $\Gamma_{\mathrm{THz}} = 2\pi L \Delta n/\lambda_0$ is the birefringent phase retardation with L the crystal thickness, $\lambda_0 = 800$ nm is the probe pulse wavelength and Δn is the difference in index of refraction between two principle axes of the index ellipse [173, 142, 29] which value depends on the geometrical configuration of the THz polarization with respect to the eigenvectors of the crystals. Here, a 200 μm thick Gallium Phosphide (GaP) crystal with a $\langle 110 \rangle$ cut was used and set so that its $\langle 001 \rangle$ axis was perpendicular to the THz

polarization to optimize the amount of polarization rotation of the short probe pulse ($\sim$ 50 fs). In this configuration, the phase retardation is given by:

$$\Gamma_{\mathrm{THz}} = 2\pi \frac{L}{\lambda_0} \eta^3 r_{41} E_{\mathrm{THz}} \tag{4.8}$$

where $\eta \simeq 3.57$ [174] is the index of refraction of GaP at the wavelength λ_0, $r_{41} \simeq 0.95 \times 10^{-12}$ [175, 29] is the second order nonlinear EO coefficient and E_{THz} is the THz electric field.

With an extinction ratio of the couple polarizer-analyzer of 10^{-3}–10^{-4}, which is limited by imperfections in both the polarizers and the EO crystal, the technique allowed the detection of THz fields as low as $\sim$ 3 kV/cm. The interpretation of the probe transmission becomes ambiguous for polarization rotations exceeding π, *c.f.* Eq. (4.7); in this experimental setup (200 μm GaP) the maximum theoretical THz electric field measurable was about $\pm$460 kV/cm.

While this configuration does not resolve the sign of the electric field, it provides a high sensitivity which in combination with the lack of sign-discernment makes it ideal for characterizing the distribution of energy in both space and time. A sequence of images, *i.e.*, spatial slices at different times, was acquired which was first summed to produce a time-integrated mode profile and then spatially integrated to produce a temporal profile. Both space and time profiles had near Gaussian distributions with full-width-at-half-maximum of 2.2 mm and 0.81 ps, respectively. The peak electric field was found to be of the order of 200 kV/cm and the total energy in the THz pulse was obtained by integrating both space and time: $\mathcal{E}_{\mathrm{THz}} \simeq 5.8$ μJ, in agreement with Golay cell measurements presented in Sec. 4.1 for similar laser-plasma parameters ($\sim$ 0.5 J, 45 fs driver laser pulse; $n_e \sim 4 \times 10^{19}$ e^-/cm^3 of Helium).

To analyze the structure of the THz electric field, the sign-resolved configuration of the 2D-EO sampling technique was also implemented [171, 172]. In this configuration,

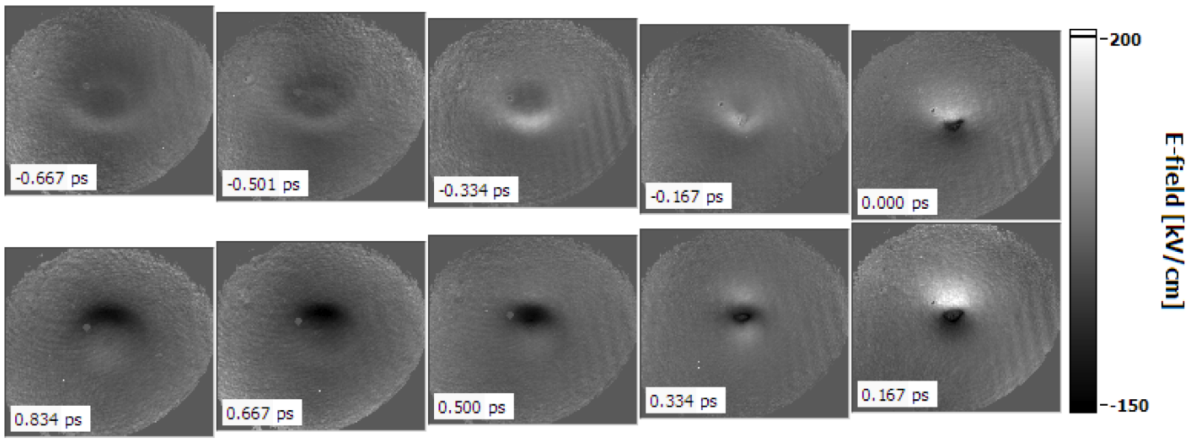

Figure 4.16: Evolution of the spatial profile of the THz electric field measured using sign-resolved 2D-EO sampling. The technique can resolve fine (< 0.1 μm) structures of the electric field. The "ring"-like structure of the THz indicate strong spatiotemporal coupling due to the single-cycle nature of the THz pulse.

the probe pulse has a circular polarization, providing a base level of polarization rotation so that in the crystal the THz-induced birefringence induces either an increase or a decrease in probe polarization, causing the transmission to vary with the sign of the THz electric field. The relative intensity transmission in this configuration is given by [142]:

$$\frac{I_T}{I_0} = \frac{1}{2}(1 - \cos\Gamma_{\mathrm{THz}}\cos^2 2\theta + \sin\Gamma_{\mathrm{THz}}\sin 2\theta) \tag{4.9}$$

where θ is the angle of the $\lambda/4$-plate relative to the $\langle 001\rangle$ axis of the crystal. For a linearly polarized probe beam $\theta = 0$ and we retrieve the result presented in Eq. (4.7). For a circularly polarized probe $\theta = \pi/4$ and Eq. (4.9) becomes:

$$\frac{I_T}{I_0} = \frac{1}{2}(1 + \sin\Gamma_{\mathrm{THz}}) \tag{4.10}$$

Because of the base level provided by the circular polarization of the probe pulse, this configuration had a reduced resolution compared to the non sign-resolved configuration with a minimum electric field detectable of $\sim$ 10–50 kV/cm. In addition, the maximum

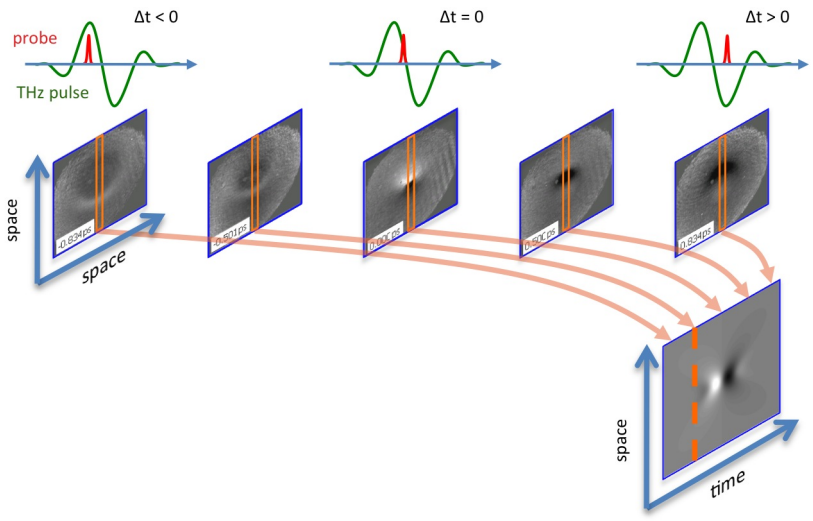

Figure 4.17: Principle of the spatiotemporal profile reconstruction. At each delay position of the probe pulse a vertical lineout is taken off the intensity map. By stacking the spatial lineouts, the spatiotemporal profile of the pulse is retrieved.

unambiguous electric field detectable is also lowered since the maximum transmission is reached for $\Gamma_{\mathrm{THz}} = \pi/2$. The theoretical maximum THz electric field detectable is calculated to be about ± 230 kV/cm; the observable maximum electric field is found to be ~ 350 kV/cm. The difference can be explained by uncertainties on the crystal thickness, the value of r_{41} and the index of refraction of the crystal; a 13% variation in index of refraction would be enough to explain the difference.

The timing scan performed in this configuration revealed additional details in the spatiotemporal structure of the THz pulse which could not be observed in non sign-resolved experiments. The spatial profiles presented a "ring"-like spatial structure as large as ~ 3 mm in diameter at delays of ± 1 ps, and as focused as ~ 0.3 mm in diameter with a negative electric field (Fig. 4.16). To reconstruct a spatiotemporal profile, a center vertical lineout was taken off each frame of the timing scan and combined with each other to form a space-time map (Fig. 4.17 and Fig. 4.18, *left*). The asymmetrical intensity in the ring structure corresponds to a curvature of the energy front of the THz

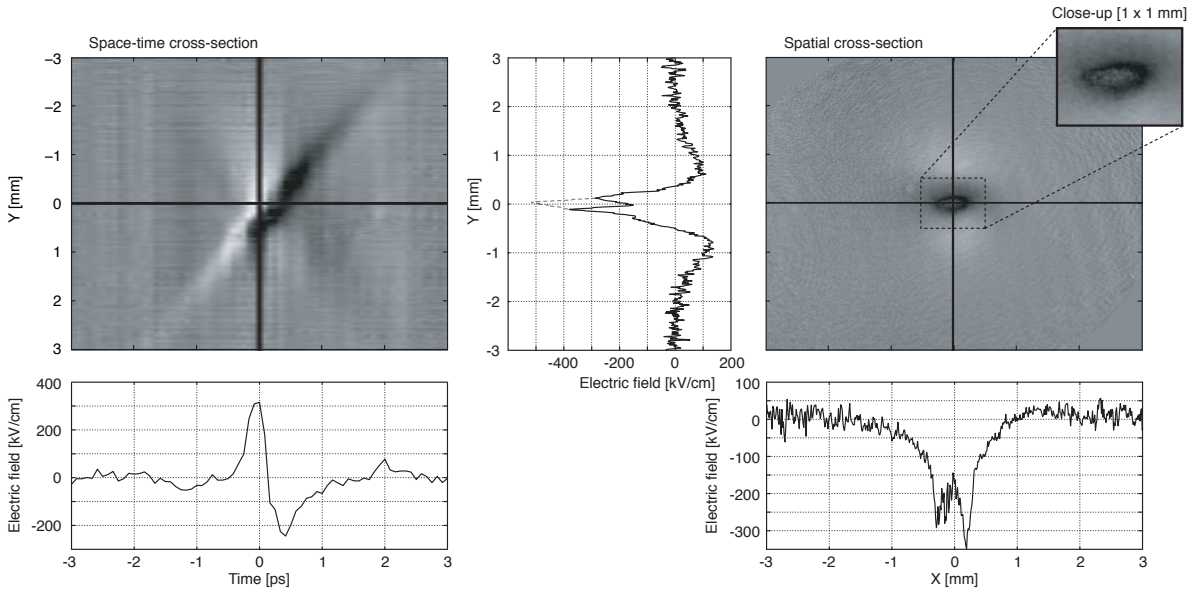

Figure 4.18: Sign-resolved 2D-EO sampling provides a spatiotemporal profile of the THz pulse *(left)*, confirming the single-cycle nature of CTR emitted from relativistic electrons crossing the plasma-vacuum boundary. At maximum polarization rotation, the spatial cross-section *(right)* shows the phase retardation exceeded $\pi/2$ and causes the derivative of the field to invert (close-up).

pulse which forms an "x"-shape with a slope of the order of $5 \times c$. This structure was also observed with single-shot spatiotemporal measurements which will be discussed in Sec. 4.2.4. A lineout at the center of the spatiotemporal map shows the near single-cycle profile of the THz pulse and provides a field strength of ~ 300 kV/cm and a pulse duration of ~ 0.4 ps. Figure 4.18 (*right*) shows the peak electric field of the THz could be even greater since it locally exceeded the field necessary for a full polarization rotation ($\Gamma_{\mathrm{THz}} \geq \pi/2$), causing the transmission to increase anomalously, as illustrated in the close-up. Accounting for this behavior, the corrected peak electric field is estimated to be ~ 0.5 MV/cm; a field strength suitable for pump-probe experiments.

4.2.4 Single-shot spatiotemporal measurements

The scanning EO technique discussed in the previous section can be successfully implemented for applications, such as the characterization of current dynamics in semi- and superconductors [176, 177, 178], because of the use of high repetition rate (kHz) laser systems and the stability of the material response function. However, the scanning nature of this technique makes it impractical for experiments with significant shot-to-shot fluctuations, including the temporal diagnostic of LPA-produced electron bunches, motivating the development of techniques capable of measuring the THz waveform in a single shot. Over the last decade, several single-shot techniques have been developed [179, 180, 181, 182, 183, 143, 4, 184, 3].

The first of these techniques, known as *spectral encoding* [179, 180, 181], is based on EO modulation of a chirped (wavelength is function of time) probe by the THz pulse. The birefringence is encoded as a spectral amplitude modulation that can be measured in an optical spectrometer. Although this technique has the advantages of being easy to set up and of being able to adjust the temporal window by varying the amount of chirp in the probe, it can suffer from distortions due to the amplitude modulation which affects the wavelength-to-time mapping [185, 186]. Another configuration, the *nonlinear cross-correlation geometry* [183, 143], addressed this issue but with a cumbersome setup involving two laser probe beams and the THz pulse, and two nonlinear processes (EO effect and frequency doubling in a BBO crystal). In addition, because this technique requires a high-intensity probe, the probe beam is typically focused onto the EO crystal which implies the risk of damaging it and limits the spatial information that can be retrieved. The electro-optic sampling measurements discussed in Sec. 4.2.3 revealed a complex spatiotemporal structure of the focused THz pulse. Therefore, to avoid the loss of critical information, it is important to resolve the spatial variations as well as the temporal waveform of the THz.

During this thesis, several scanning and single-shot techniques have been developed and implemented [4, 184, 172, 171, 3]. In this section, we present a technique called *temporal electric-field cross-correlation* (TEX), which overcomes the limitations discussed above. This technique allows measurement of THz waveforms with high temporal resolution while providing one-dimensional spatial information. TEX was successfully implemented to measure in a single-shot spatiotemporal profiles of intense THz pulses emitted from the LPA. The ability to retrieve the full electric field of an optical probe is not unique to TEX, but is shared by other techniques, such as frequency domain holography (FDH) [187, 188, 172] and single-shot super-continuum spectral interferometry (SSSI) [189]. The key advantage of TEX over FDH and SSSI is that recovery of the probe amplitude and phase does not require any reference data and is obtained from the TEX interferograms by a single fast Fourier transform (FFT) operation, making it significantly easier to use than the others. On the other hand, FDH and SSSI provide the pure electric-field retrieval of the probe without convolution.

TEX is based on the measurement of the linear cross-correlation of a long chirped pulse (probe) with a short reference pulse (reader) using spectral interferometry. The full electric-field information of the probe, convolved with that of the reader, is retrieved, allowing signals to be encoded onto either the phase or the amplitude of the probe, or both. This dual capability is not present in previous EO methods and makes TEX applicable to the measurement of a wide range of phenomena beyond EO sampling, *i.e.*, in principle, to any phase sensitive experiment. Because the detection is linear, TEX can be implemented with low-cost, non-amplified laser systems, and because it does not require focusing of the chirped probe, spatial information can be recorded and retrieved. The temporal detection window is easily tunable in the several picosecond range by adjusting the chirp of the probe pulse (within the spectral acceptance of the spectrometer), and the temporal resolution of the phase and amplitude retrieval is set

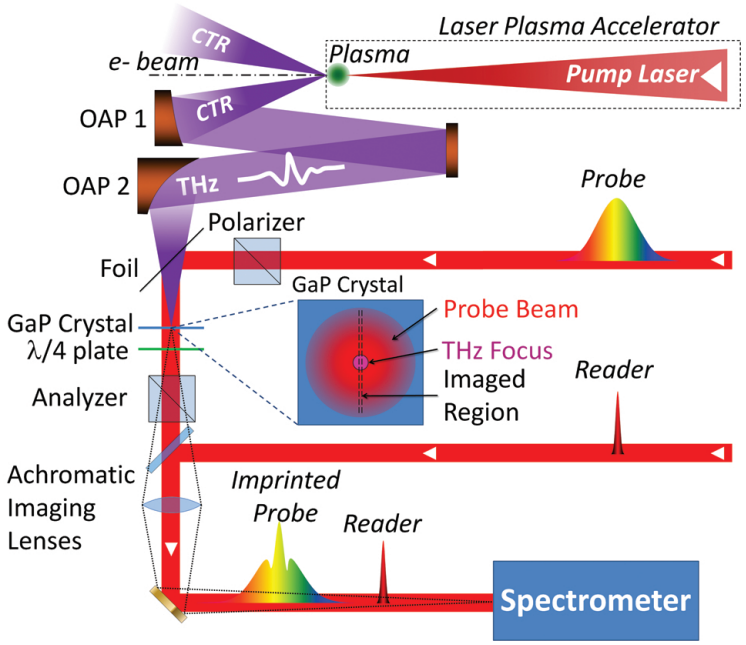

Figure 4.19: Schematic of the experimental setup for temporal electric-field cross-correlation (TEX) detection of intense ultrashort THz pulses emitted from an LPA. Figure from [3].

by the duration of the reader pulse, which is convolved with the signal.

The schematic of the TEX detection scheme implemented on an LPA-based THz source [77, 142] is shown in Fig. 4.19. Using ~ 0.4 J, 800 nm, 45 fs FWHM laser pulses focused into a 2.2 mm gas jet of Helium, electron bunches with large energy spreads (exponential-like distributions) and sub-picosecond bunch durations were produced, resulting in the generation of CTR in the range of 0–4 THz. A portion of the radially polarized cone of THz emission is asymmetrically sampled by collection with an OAP. The resulting collimated beam of THz is primarily linearly polarized, with a residual transversely polarized component analytically estimated to be at the 10% level [142]. The THz beam is then refocused with a second OAP onto a 200 μm thick GaP crystal with a $\langle 110 \rangle$ cut. An optical pulse split from the driver laser beam that generated the electrons is partially compressed, resulting in a temporally chirped pulse with a FWHM duration of 2 ps onto which phase and amplitude information of the THz pulse will be

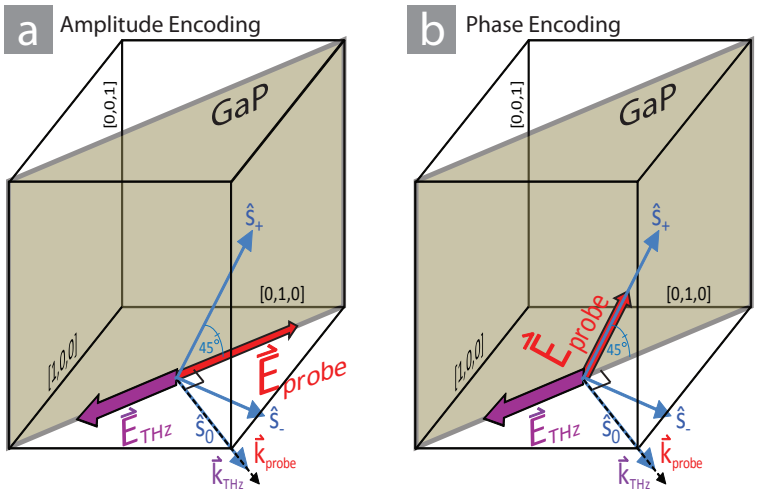

Figure 4.20: *(a)* Amplitude-encoding geometry. The probe polarization is aligned between the principal axes $(\hat{S}_+, \hat{S}_-)$ of the THz-induced birefringence, resulting in polarization rotation only. *(b)* Phase-encoding geometry. The probe polarization is parallel with one of the principal axes, resulting in phase shifting only. Figure from [3].

imprinted. A second fully compressed optical pulse (reader), measured to have a FWHM duration of 45 fs, is also split from the driver. Probe and the THz pulses overlap colinearly in the GaP crystal, resulting in the EO interaction. A polarizer and $\lambda/4$-plate are used to set the circular polarization of the probe, as in the sign-resolved 2D-EO sampling technique discussed in Sec. 4.2.3, allowing both positive and negative THz electric fields to be resolved. The analyzer is used to convert polarization rotations into amplitude modulations. The transmitted probe pulse is then combined colinearly with, but temporally offset from, the reader and is sent into a 0.27 m imaging spectrometer with a 14 bit, 1 megapixel cooled CCD detector, producing a spectral interferogram image, coined "TEXogram". A pair of achromatic lenses is used to image the interaction plane (GaP crytal) to the input plane of the spectrometer, where the spectrometer slit is used to select a spatial slice (a vertical slice of the THz focus here) of the probe.

The choice to encode the THz signal onto either the amplitude or the phase of the probe field is made by appropriately choosing the polarization state of the incident

probe (Fig. 4.20). If the polarization is aligned at 45° to the principal axes of the THz-induced index ellipse, the probe polarization will be rotated in proportion to the THz field strength [110], but the phase-shift contribution from each of the axes will cancel out, resulting in a pure amplitude modulation (Fig. 4.20a). However, if the probe polarization is aligned along one of the principal axes of the index ellipse, the probe will experience a temporally varying phase shift, but no polarization rotation, resulting in pure phase modulation (Fig. 4.20b). For other polarization states, the THz imprint is mixed between phase and amplitude with a strongly nonlinear dependence on the field strength, making waveform retrieval unreliable.

The recovery of THz waveform occurs in two distinct steps. The first step is the recovery, post-interaction, of the spatiotemporal electric field of the probe, which can be written $E_p(y,t) = \mathcal{E}(y,t)\exp\{i\Phi(y,t)\}$, where t is the time, y is the spatial coordinate, and $\mathcal{E}(y,t)$ and $\Phi(y,t)$ are the probe's temporal amplitude and phase, respectively. The second step is the determination of the THz waveform spatiotemporal profile, $E_{\mathrm{THz}}(y,t)$, from the THz-induced modulations of either the probe amplitude or the probe phase, depending on the encoding method.

In the first step, $E_p(y,t)$ is obtained from the TEXogram by applying a single one-dimensional FFT operation independently to each row of the spectral image. The TEXogram is described by:

$$\mathcal{S}_{\mathrm{TEX}}(y,\omega) = |E_p(y,\omega) + E_r(y,\omega)|^2 \tag{4.11}$$

$$= |E_p(y,\omega)|^2 + |E_r(y,\omega)|^2 + E_p(y,\omega)E_r^*(y,\omega) + E_p^*(y,\omega)E_r(y,\omega) \tag{4.12}$$

where ω is the optical angular frequency, the upper-script " * " denotes the complex conjugate and, $E_p(y,\omega)$ and $E_r(y,\omega)$ are respectively the electric fields of the probe and reader pulses in the frequency domain. The FFT results in a time-domain signal

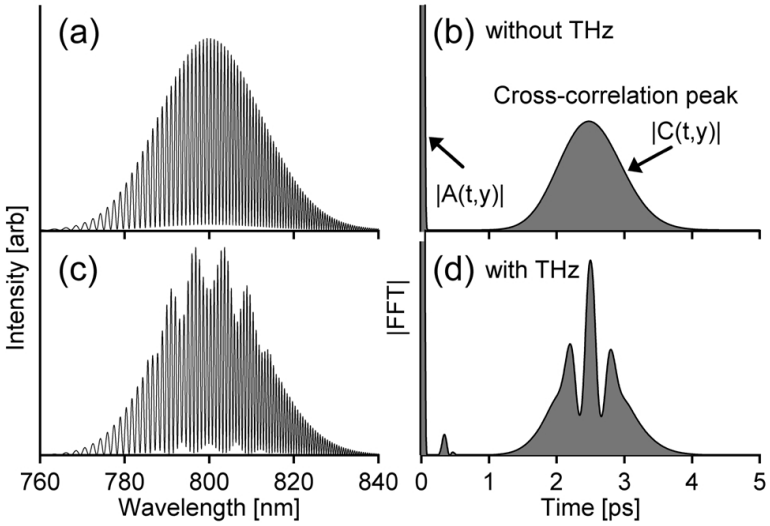

Figure 4.21: *(a)* Simulated TEX interferogram in the absence of THz showing interference in the spectrometer between co-propagating probe and reader pulses separated in time by 2.5 ps. *(b)* Modulus of the FFT of the interferogram in *(a)* showing a broad side peak at 2.5 ps, which represents the amplitude of the cross correlation between the probe and reader electric fields. *(c)* Simulated TEX interferogram with THz present. *(d)* Modulus of the complex FFT of the interferogram in *(c)*, showing a THz-induced modulation in the side peak amplitude. Figure from [3].

containing four components corresponding to the four terms in Eq. (4.12). The first two terms of $\mathcal{S}_{\mathrm{TEX}}$ produce overlapping peaks known as "coherence spikes" at $t = 0$, while the third and fourth terms, *i.e.*, the cross-terms, which are responsible for the fringes in the TEXogram, produce side peaks at $t = \pm\Delta t$, where Δt is the delay of the probe behind the reader (Fig. 4.21). The Fourier transform of the TEXogram spectrum can be written:

$$\mathcal{F}[\mathcal{S}_{\mathrm{TEX}}(y,\omega)](t) = A(y,t) + C(y,t) + C^*(y,-t) \tag{4.13}$$

where $A(y,t)$ is the FFT of the first two terms of $\mathcal{S}_{\mathrm{TEX}}$ and $C(y,t) = \mathcal{F}[E_p(y,\omega)E_r^*(y,\omega)](t)$ is the Fourier transform of the first cross term. Since the Fourier transform of a product

is equal to the convolution, noted $\otimes$, of the Fourier transforms, we have:

$$C(y,t) = \mathcal{F}[E_p(y,\omega)](t) \otimes \mathcal{F}[E_r(y,\omega)](t) \tag{4.14}$$

$$= \int_{-\infty}^{\infty} E_p(y,\tau) E_r^*(y,\tau - t)\, d\tau \tag{4.15}$$

For a reader with suitably short duration and negligible spectral phase, $E_r(y,t) \sim \delta(t)$, with $\delta(t)$ the Dirac delta function, and the side peak in the time-domain TEXogram approximates the chirped probe pulse in both amplitude and phase: $C(y,t) \approx E_p(y,t)$.

In the second step, the THz waveform is recovered by determining the modulation to either $\mathcal{E}(y,t)$ or $\Phi(y,t)$. In the amplitude-encoding method (Fig. 4.20a), the transmitted probe amplitude is given by:

$$\mathcal{E}_T^2(y,t) = (\mathcal{E}_0^2/2)\left[1 + \sin\left(\Gamma_{\mathrm{THz}}(y,t)\right)\right] \tag{4.16}$$

where $\Gamma_{\mathrm{THz}}(y,t) = (2\pi\eta^2 r_{41} L/\lambda_0) \times E_{\mathrm{THz}}(y,t) \equiv \alpha E_{\mathrm{THz}}(y,t)$ is the birefringent phase retardation introduced in Sec. 4.2.3 Eq. (4.8), with L the crystal thickness, λ_0 the reader wavelength, η the linear index of refraction of the crystal in the absence of THz, r_{41} is the second order nonlinear EO coefficient, and the subscripts "$_0$" and "$_T$" denote field quantities before and after the interaction, respectively. In the phase-encoding method, the transmitted phase is given by:

$$\Phi_T(y,t) = \Phi_0(y,t) \pm \Gamma_{\mathrm{THz}}(y,t)/2 \tag{4.17}$$

where the sign depends on the choice of principal axis of the index ellipse $(\hat{S}_+, \hat{S}_-)$, see Fig. 4.20. As $\mathcal{E}_0(y,t)$ and $\Phi_0(y,t)$ are not simultaneously acquired in the presented TEX configuration, a separate "null" shot in the absence of THz is required. The

reconstructed waveform is thus given by:

$$E_{\mathrm{THz}}(y,t) = (1/\alpha)\arcsin\left[\mathcal{E}_T^2(y,t)/\mathcal{E}_{\mathrm{null}}^2(y,t) - 1\right] \tag{4.18}$$

for the amplitude-encoding configuration, and:

$$E_{\mathrm{THz}}(y,t) = (2/\alpha)\left[\Phi_T(y,t) - \Phi_{\mathrm{null}}(y,t)\right] \tag{4.19}$$

for the phase-encoding configuration.

The temporal resolution of the THz waveform retrieval is determined by two independent factors: the duration of the reader pulse, which determines the temporal resolution of the probe electric-field recovery, and the thickness of the EO crystal, which determines the EO sampling phase-matching bandwidth [170, 145]. Calculations simulating the probe field retrieval process in both phase- and amplitude-encoding configurations for a 45 fs reader confirm accurate reconstruction of the encoded signal for frequencies beyond $\sim$ 8 THz , which is the resolution limit set by the 200 μm GaP crystal. The limitation to the temporal range of the detection is set by the bandwidth and spectral resolution of the imaging spectrometer, which must be capable of resolving the spectral fringes over the full bandwidth of the probe.

A sample THz spatiotemporal waveform image acquired using TEX in the amplitude-encoding configuration is shown in Fig. 4.22a. The measured waveform is nearly single cycle and displays sharp temporal features of the order of 100 fs, illustrating the need for high temporal resolution. As in 2D-EO sampling (Sec. 4.2.3, Fig. 4.18 *left*), the waveform exhibits strong spatiotemporal coupling, in the shape of an "x" which can be understood as a combination of the Gouy phase shift of a single-cycle pulse (temporal profile) and the wavelength-dependent waist of a broadband spectrum (transverse profile) [190, 191, 192]. Correlation between the spatiotemporal waveforms of the THz with the accelerator

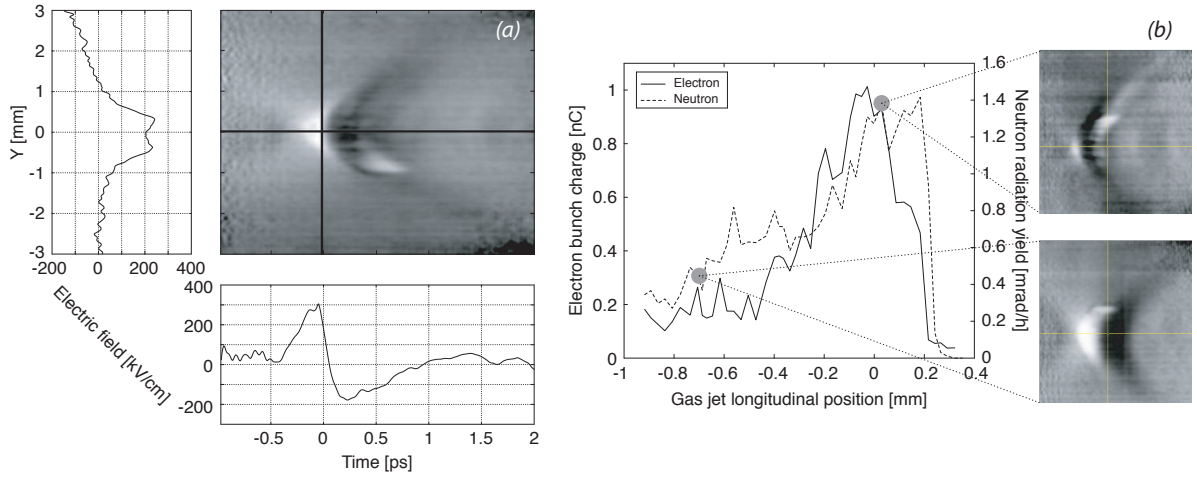

Figure 4.22: Space-time cross section obtained in a single-shot using the TEX detection scheme. *(a)* Both the complex spatiotemporal coupling and the near single-cycle shape of the waveform, previously observed using 2D-EO sampling (Fig. 4.18 *left*), are reproduced. *(b)* Spatiotemporal waveforms of the THz correlate with the accelerator performance. This is shown by scanning the longitudinal position of the gas jet relative to the vacuum focus of the diver laser ($p = 0$ mm). As higher charge (ICT charge signal, *solid line*) and higher energy (neutron yield, *dashed line*) electron bunches are being produced, the THz waveforms sharpens indicating presence of high frequencies, *i.e.*, compression of the bunch.

performance was verified by performing a scan of the longitudinal position of the gas jet relative to the driver laser focus (Fig. 4.22b). As the upstream edge of the jet approaches the laser focus, higher charge (ICT charge signal, *solid line*) and higher energy (neutron yield, *dashed line*) electron bunches are generated [153], and the THz waveforms display sharper features (high frequency content) indicating a compression of the bunch. Throughout the scan the extent of the THz bandwidths varied from 1 THz to 3–4 THz.

To diagnose the structure of the electron bunch, the spectrum of the THz waveform shown in Fig. 4.22a was calculated and compared with theory. The spatial and temporal features of the spectral image were modeled (Fig. 4.23) by using CTR emission theory [80] with the inclusion of collection and propagation effects [29]. To accurately model both the low- and high-frequency parts of the spectral image, two bunches of

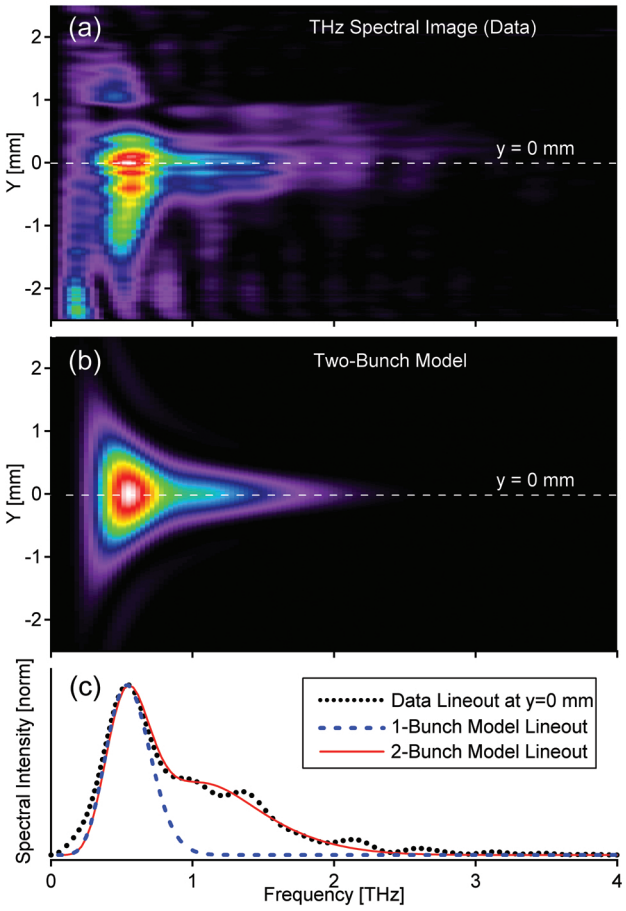

Figure 4.23: *(a)* Power spectrum of the THz waveform shown in Fig. 4.22a. *(b)* Spectral image calculated using a two-bunch model. *(c)* Central lineouts of spectral images corresponding to the data (*black dotted line*), a one-bunch model (*blue dashed line*), and a two-bunch model (*red solid line*). Comparison shows that a two-bunch model yields a significantly better fit than a one-bunch model. Figure from [3].

different duration and charge (90% of the charge in a 140 μm *rms* bunch and 10% in a 50 μm bunch) were required. Comparison of a one-bunch model (containing only the longer bunch) with the two-bunch model shows that the contribution to THz emission above ~0.75 THz comes entirely from the shorter bunch, despite its small relative charge (Fig. 4.23c). This high sensitivity to the presence of the shorter electron bunch is an important confirmation of the practicality of the THz-based diagnostic for characterizing LPAs, since the high-energy, low-charge electron bunch component of interest is often

accompanied by a lower energy component containing the bulk of the charge [153]. The electron energy spectrum, measured simultaneously, does, in fact, show a two-component distribution with a large thermal component and a smaller quasi-monoenergetic component. The importance of recovering the spatial variations in the THz waveform is illustrated by the strong spatial dependence of the spectrum of the focused THz pulse: the higher-frequency component from the short bunch is more localized to the axis. A spatially integrated technique would under-represent this component, thus diminishing sensitivity to the presence of the short bunch. In addition, because the transverse focal size of a given spectral component is strongly dependent on not only the wavelength but also the spectrally varying far-field intensity distribution, the nice correspondence between the data and model of the shape of the spectral image provides a confirmation of the THz emission patterns predicted by CTR theory.

In conclusion, a new single-shot technique (TEX) was demonstrated for measurement of ultrafast phenomena resulting in temporal phase or amplitude modulations. TEX provides high temporal resolution and one-dimensional imaging simultaneously for the first time in EO sampling, enabling analysis of spatiotemporal and spatiospectral coupling in THz waveforms. TEX is significantly easier to set up than previous high-resolution, single-shot EO techniques because it does not require the use of nonlinear processes other than the linear Pockels effect used for EOS. Because TEX is linear in the probe field strength, low-power, low-cost, unamplified laser systems may be used, making it highly accessible. In addition, its dual phase- and amplitude-encoding capability makes it applicable to a wide range of phenomena. The temporal resolution is set by the duration of the reader pulse, and can be made smaller than the intrinsic limitation set by phase matching in the EO sampling process. The single-shot temporal detection window is tunable in the range of several to tens of picoseconds and limited by the bandwidth and spectral resolution of the spectrometer. Numerical analysis confirms the capability

of TEX to reproduce THz waveforms in both temporal and spectral domains without significant distortion. Waveforms of THz pulses generated as CTR from an LPA were measured using the amplitude-encoding configuration and analyzed. The resultant THz spectral images were used to demonstrate the presence of heterogeneous electron-bunch structure from the LPA. The dependence of the THz spectrum on the electron-bunch duration makes it possible to detect the presence of short electron-bunch substructure with high sensitivity.

Chapter 5

Betatron X-ray Radiation

5.1 Introduction

In this Chapter, single-shot direct X-ray spectra from betatron motion of electrons produced by an LPA are presented [7], demonstrating the synchrotron nature of the radiation. Simultaneous single-shot measurements of the electron and X-ray distributions, in the low wiggler parameter limit, allowed sub-μm resolution of the beam size for both high- and low energy-spread electron beams. This provides a measure of the normalized transverse geometric emittance of 0.5 GeV-class LPA-produced electrons and allows inference of the accelerator wake electric-field. In addition, the betatron emission serves as a compact source of collimated keV X-rays [85, 193] which would otherwise require a multi-GeV accelerator using a conventional undulator with cm- or mm-scale periodicity. Measurements demonstrate the spectral form, brightness and scaling of the betatron X-ray radiation.

In previous experiments, Fresnel-edge diffraction of the betatron X-ray beams provided an upper bound measurement of few microns for the transverse size of the electron beam produced in the LPA [194, 193, 7]. The presence of the high intensity laser driver

limits magnification and hence resolution. Far-field spatial distribution measurements [86] and multi-shot diffractive spectral characterization of the betatron emission [87] showed that the electron bunch size was on the order of a micron. Approximate spectra have also been obtained using filter techniques assuming a synchrotron spectrum [114]. Pepper-pot measurements have been used to characterize low energy electron beams [195, 196, 197]. Simulations [101] and theory [12] indicate that beam source size may be of order 0.2 μm in experiments producing beams at 0.1 GeV [39, 40, 41]–1 GeV [10]. This indicates much lower emittance than has been measured, which would be important for FEL [127] and Compton γ-sources [198], and a step towards collider requirements [199].

In the next Section, laser-plasma acceleration theory [12] is used to provide a simple ballistic model relating electron beam transverse size to beam divergence, and a model [82] of the on-axis betatron X-ray radiation is described. Section 5.3 presents the two laser-plasma accelerators on which the experiments were performed. Section 5.4 discusses the validity and limitations of the single-shot high-resolution X-ray detection method, emphasizing its advantages over filter-based techniques. In Section 5.5, betatron radiation from broadband electron beams is analyzed. The synchrotron nature of the X-ray radiation is demonstrated. The betatron radiation model limitations in describing the betatron spectrum of broadband low-energy electron beams are discussed and numerical simulations are used to provide a good fit of the data. In Section 5.6, agreement between model and data is demonstrated for high energy ($\sim$ 0.5 GeV) quasi-monoenergetic electron beams. The electron beam size within the plasma is calculated using both a knife-edge technique [114] and single-shot measurements of the electron beam divergence. An estimate of the plasma wakefield amplitude is calculated. The accelerator is shown to provide a high flux 5 keV collimated X-ray source for potential industrial applications (*e.g.*, medical, military, commercial).

5.2 Theoretical framework

The laser pulse propagation in the plasma is affected by a variety of phenomena [12], including relativistic self-focusing, which occurs when the laser power exceeds the critical power $P \geq P_c[\mathrm{TW}] \simeq 17.4 \times 10^{-3} \lambda_p^2/\lambda^2$ where λ and λ_p are respectively the laser and plasma wavelengths. Experiments presented in this Chapter satisfied this condition ($P \sim$ 9–22 TW $> P_c \simeq$ 1–4 TW) and self-focusing was the dominant mechanism for optical guiding of the laser pulse, allowing the acceleration length to overcome the diffraction limit, *i.e.*, the Rayleigh length.

In the "bubble" regime [94, 200] (*c.f.* Sec. 2.3), accelerating electrons undergo betatron motion induced by the strong focusing fields of the ion bubble formed behind the driver laser pulse. As a result the electron beam size and divergence are related [82]. In the self-trapping regime, in which the present experiments operated, LPAs rely on the transverse wavebreaking effects [19] of highly nonlinear plasma waves [57] to inject electrons into the accelerating phase of the electron density wave, providing off-axis injection to initialize the betatron motion. The strong transverse focusing field associated with the ion channel, whose diameter is typically much greater than the bunch radius [89, 201], induces oscillations of the electron bunch at the betatron wavelength $\lambda_\beta = \lambda_p \sqrt{2\gamma} \propto \sqrt{\gamma/n_e}$, where n_e is the plasma density. The anticipated amplitude of the betatron orbits, which defines the transverse size of the electron beam, can be sub-μm [86] and knife-edge methods have not had enough resolution to provide a good measurement [114, 194] of such dimensions.

An estimate of the electron beam size can be provided by means of single-shot energy and divergence measurements of the electron beams via a simple ballistic model. The transverse oscillations of an electron inside a relativistic ion bubble can be described by

[94, 200] the following equations:

$$dx/ds = \beta_x \tag{5.1a}$$

$$d\beta_x/ds = -k_\beta^2 x \tag{5.1b}$$

where s is the moving coordinate, x is the transverse position, $\beta_x = v_x/c$, and $k_\beta = k_p/\sqrt{2\gamma}$, in the limit of small amplitude betatron orbit, is the betatron oscillation wavenumber and k_p the plasma wavenumber. Solving Eqs. (5.1) yields:

$$\langle x^2 \rangle = \langle x_0^2 \rangle/2 + \langle u_{x_0}^2 \rangle/2\gamma^2 k_\beta^2 \tag{5.2a}$$

$$\langle \theta^2 \rangle = k_\beta^2 \langle x_0^2 \rangle/2 + \langle u_{x_0}^2 \rangle/2\gamma^2 \tag{5.2b}$$

where $\langle\rangle$ denotes the arithmetic average, (x_0, u_{x_0}) are the initial transverse position and normalized momentum and $\langle \theta^2 \rangle \simeq \langle u_x \rangle/\gamma$ is the beam divergence variance. For a matched beam, $\langle x^2 \rangle = \langle x_0^2 \rangle$, it comes ($\sigma_x \equiv \langle x^2 \rangle^{1/2}$ and $\sigma_\theta \equiv \langle \theta^2 \rangle^{1/2}$):

$$\sigma_x = \frac{\lambda_p}{\pi}\sqrt{\frac{\gamma}{2}}\sigma_\theta \tag{5.3}$$

For electron beam parameters representative of the present experiments, such as a 20 MeV electron beam [153] with 20 mrad *rms* divergence produced in a plasma of 3×10^{19} e^-/cm^3, and a 400 MeV, 1 mrad *rms* divergence electron beam [10] produced in a plasma of 7×10^{18} e^-/cm^3, Eq. (5.3) yields respectively, an electron beam size inside the plasma of $\sigma_x \simeq 0.17$ μm and $\sigma_x \simeq 0.08$ μm, in reasonable agreement with particle-in-cell simulations described in [202]. From the electron bunch size, the normalized transverse geometric emittance is calculated as $\epsilon_x \approx \beta_z \gamma \sigma_x \sigma_\theta$. For the 20 MeV electron beam, the normalized emittance is $\epsilon_x \simeq 0.14$ mm.mrad, one order of magnitude lower than that reported in recent single-shot pepper-pot measurements of electron bunches produced

in an LPA [196]. For the 400 MeV electron beam, the normalized transverse geometric emittance is $\epsilon_x \simeq 0.06$ mm.mrad; such electron beams would be suitable for free-electron laser experiments [127]. Equation (5.3) breaks down if the electron beam adiabatically expands before reaching ballistic motion. Such expansion can occur at the downstream edge of the plasma [196] if the *bubble* regime applies, *i.e.*, the density downramp is much longer than λ_β and, the laser pulse energy is not depleted.

The width of the X-ray shadow of crossed thin wires, acting as knife edges, provides a measure of the bunch size [194, 193, 7]. Based on particle code simulations [202, 8] or theory [82], for typical experimental electron beam and plasma parameters the X-ray source distribution can be approximated by a Gaussian distribution ($1/\sqrt{2\pi\sigma^2} \cdot \exp\left[(r_0-\mu_0)^2/2\sigma^2\right]$), for which the shadow intensity profile, for a wire radius r_w and a magnification M, is described by:

$$I(r) = 1 + \frac{1}{2}\,\mathrm{erf}\left(\frac{r+(M-1)\mu_0 - Mr_w}{\sqrt{2}(M-1)\sigma}\right) - \frac{1}{2}\,\mathrm{erf}\left(\frac{r+(M-1)\mu_0 + Mr_w}{\sqrt{2}(M-1)\sigma}\right) \qquad (5.4)$$

where $\mathrm{erf}(x) = \frac{2}{\sqrt{\pi}}\int_0^x e^{-t^2}dt$ is the error function. A line-by-line and column-by-column fit of a high signal-to-noise image provides a measurement of the X-ray source size. Knife-edge methods have, however, had a limited resolution of few microns [114, 194].

A more detailed understanding of the bunch size is available by analyzing the X-ray betatron spectrum. A theoretical description of betatron X-ray radiation in plasma-focusing channels was developed for electrons with constant longitudinal momentum [82]. Electrons emit directional synchrotron radiation within a cone of angles [82, 86]:

$$\begin{cases} \theta_\parallel \simeq a_\beta/\gamma \text{ for } a_\beta \gg 1, \text{ and } \theta_\parallel \simeq 1/\gamma \text{ for } a_\beta \ll 1 \\ \\ \theta_\perp \simeq 1/\gamma \end{cases} \qquad (5.5)$$

where $\theta_\parallel$ is the emission angle in the plane of the electron orbit, $\theta_\perp$ is the emission angle

in the plane normal to the electron orbit, and

$$a_\beta = \gamma k_\beta r_\beta \simeq 1.33 \times 10^{-10} \sqrt{\gamma n_e [e^-/\mathrm{cm}^3]}\, r_\beta [\mu\mathrm{m}] \tag{5.6}$$

is the betatron or wiggler strength parameter, and r_β is the amplitude of the betatron orbit. In the undulator regime, $a_\beta \ll 1$, the betatron radiation of a single electron is emitted in a narrow photon-energy band. For larger betatron strength parameters, higher order harmonics are generated and in the wiggler regime, $a_\beta \gg 1$, an electron radiates a broadband continuum. In the present experiments, $a_\beta \simeq 1$ and each electron radiates a train of harmonics. At first order, the betatron strength parameter a_β can be considered constant since, in the wake of the laser pulse, the electron beam focuses on-axis (smaller betatron orbit amplitude r_β) as it accelerates (greater energy γ). In the limits $\gamma^2 \gg 1$, $\theta^2 \ll 1$ where θ is the observation angle from the ion channel axis $\boldsymbol{z}$, and $a_\beta^2/\gamma^2 \ll 1$, the on-axis photon spectrum of the radiation emitted by a single electron is given by [82]:

$$\frac{1}{\hbar\omega}\frac{\partial^2 I}{\partial \hbar\omega \partial\Omega} = \frac{4\alpha_f \gamma^2 N_\beta^2}{1 + a_\beta^2/2} \sum_{n=1}^{+\infty} \frac{R_n F_n}{\hbar\omega_n} \tag{5.7}$$

where $\partial^2 I/\partial\hbar\omega\partial\Omega$ is the energy radiated per frequency ω per solid angle Ω, n is the nth odd harmonic number, $\omega_n = nM_0 ck_\beta$ is the nth resonant frequency, $M_0 = 2\gamma^2/(1+a_\beta^2/2)$ is the relativistic Doppler upshift factor, $\alpha_f \simeq 1/137$ is the fine structure constant, $N_\beta = L/\lambda_\beta$ is the number of betatron periods that the electron undergoes, L is the propagation length, R_n is the nth resonance function and F_n is the nth harmonic amplitude function, respectively defined as:

$$R_n = \left\{ \frac{\sin[n\pi N_\beta(\omega/\omega_n - 1)]}{n\pi N_\beta(\omega/\omega_n - 1)} \right\}^2 \tag{5.8}$$

$$F_n = n\alpha_z [J_{(n-1)/2}(\alpha_z) - J_{(n+1)/2}(\alpha_z)]^2 \tag{5.9}$$

where J_m are Bessel functions of the first kind and

$$\alpha_z = \frac{\omega}{\omega_\beta}\frac{a_\beta^2}{8\gamma^2} \tag{5.10}$$

The energy spectrum per frequency interval per solid angle radiated by a single particle in Eq. (5.7) derives from an approximation of the integrated by parts general equation [203]:

$$\frac{\partial^2 I}{\partial\hbar\omega\partial\Omega} = \frac{\alpha_f}{4\pi^2}\left|\int_{-\infty}^{\infty}\frac{\boldsymbol{n}\times[(\boldsymbol{n}-\boldsymbol{\beta})\times\dot{\boldsymbol{\beta}}]}{(1-\boldsymbol{\beta}\cdot\boldsymbol{n})^2}e^{i\omega(t-\boldsymbol{n}\cdot\boldsymbol{r}(t)/c)}dt\right|^2 \tag{5.11a}$$

$$= \frac{\alpha_f\omega^2}{4\pi^2}\left|\int_{-T/2}^{T/2}\boldsymbol{n}\times(\boldsymbol{n}\times\boldsymbol{\beta})e^{i\omega(t-\boldsymbol{n}\cdot\boldsymbol{r}(t)/c)}dt\right|^2 \tag{5.11b}$$

where the acceleration is considered different from zero only for $-T/2 \leq t \leq T/2$, implying non-physical instantaneous suspending or setting in motion of the particle. For a given motion $\boldsymbol{r}(t)$, $\boldsymbol{\beta}(t) = \dot{\boldsymbol{r}}(t)/c$ and $\dot{\boldsymbol{\beta}}(t) = \ddot{\boldsymbol{r}}(t)/c$ can be calculated and the integral evaluated in the observation direction defined by the unit vector $\boldsymbol{n}$ ($\boldsymbol{n} = \boldsymbol{z}$ for $\theta = 0$), which is considered constant in time since the observation point is assumed to be far away from the region of space where the motion occurs. It can be shown [8] that, under this approximation, the energy spectrum calculated (Eq. (5.7)) does not converge to zero at high frequencies when $a_\beta \gg 1$ (high frequency generation) and $N_\beta \sim 1$. A parallel numerical code was developed [8] based on the work of Thomas *et al.* [202] which calculates the trajectories of a bunch of particles in a giving external electromagnetic field structure, a uniform ion channel here, and outputs the final radiation radiated in the far field. To provide convergence at high frequencies, the approximation was applied to Eq. (5.11a), before integration by parts, which introduced a correction term related

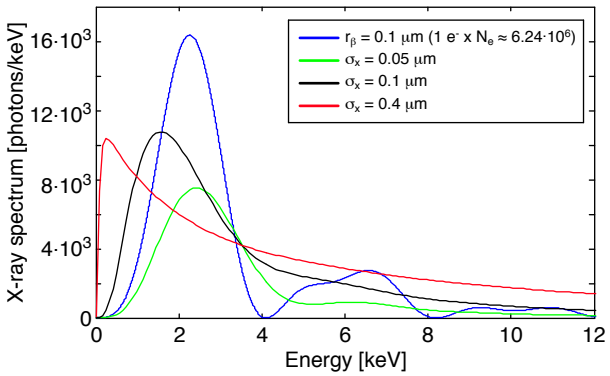

Figure 5.1: Examples of on-axis X-ray betatron spectra calculated using Eqs. (5.7–5.10) for a single electron orbiting at $r_\beta = 0.1$ μm (*blue*) and for Gaussian electron distributions centered on-axis with standard deviation radii of 0.05 μm (*green*), 0.1 μm (*black*) and 0.4 μm (*red*), for which $a_\beta \simeq 0.5$, 1 and 3.9 respectively. The spectra were calculated for a 1 pC, 400 MeV, 5% FWHM energy-spread electron bunch and a propagation length of 0.5 mm ($N_\beta \simeq 1$). The single electron spectrum is dominated by the 1st harmonic and the peak energy of the bunch-integrated spectra varies with the bunch *rms* radius σ_x.

to the trajectories end points:

$$\frac{\partial^2 I}{\partial\hbar\omega\partial\Omega} = \frac{\alpha_f}{4\pi^2}\left|\left[\frac{\boldsymbol{n}\times(\boldsymbol{n}\times\boldsymbol{\beta})}{1-\boldsymbol{\beta}\cdot\boldsymbol{n}}e^{i\omega(t-\boldsymbol{n}\cdot\boldsymbol{r}(t)/c)}\right]_{-T/2}^{T/2} - i\omega\int_{-T/2}^{T/2}\boldsymbol{n}\times(\boldsymbol{n}\times\boldsymbol{\beta})e^{i\omega(t-\boldsymbol{n}\cdot\boldsymbol{r}(t)/c)}dt\right|^2 \tag{5.12}$$

The theoretical on-axis spectrum of X-ray radiation emitted by a single electron with $E_z = 400$ MeV and $r_\beta = 0.1$ μm, for a propagation length in the plasma channel of 0.5 mm is shown in Fig. 5.1. For comparison with the spectra of electron bunches, the amplitude of the spectrum is multiplied by the number of electrons contained in 1 pC of charge, $N_e \simeq 6.24\times10^6$. Because the betatron strength parameter is low, $a_\beta \simeq 1$, the spectrum of X-ray radiation emitted by a single electron is composed of distinct peaks near the resonant frequencies ω_n [82]. For a given harmonic, the radiation spectrum is dominated by the resonant function R_n and the frequency width at the resonant frequency ω_n is given by $\Delta\omega_n \approx \omega_n/nN_\beta = M_0\omega_L \propto \gamma/n_e r_\beta^2$ with $\omega_L = 2\pi c/L$. In the low N_β limit, $N_\beta \simeq 1$ in this thesis, the harmonic peaks broaden and the summation over all harmonics results in a continuum spectrum. The peak energy of the distribution

is located near the energy of the first harmonic $\hbar\omega_1 = M_0\omega_\beta$. In Figure 5.1, the peak energy of the summation over all odd harmonics is $\hbar\omega_{\text{peak}} \simeq 2.27$ keV whereas the peak energy of the first harmonic is $\hbar\omega_1 \simeq 2.1$ keV ($< 10\%$ error) with a FWHM bandwidth of $\Delta\hbar\omega_1 \simeq 2$ keV.

In a bunch, the electrons radiate X-rays incoherently since the length on which the bunch has structure [70, 3] (~ 10 μm) is much greater than the characteristic emission wavelength ($\sim$ 0.6 nm). The integrated X-ray radiation spectrum is then obtained by summing individual electron contributions. Figure 5.1 shows three bunch-integrated spectra for 1 pC, 400 MeV with 5% full-width-at-half-maximum (FWHM) energy-spread distributions of electrons with $\sigma_x = 0.05$, 0.1, 0.4 μm *rms* radii. The dependence of the spectral peak energy on σ_x makes single-shot X-ray measurements a good diagnostic of the transverse size (< 1 μm resolution) and, in combination with electron beam divergence and energy measurements, the geometric emittance of the electron beam.

Because the betatron radiation length can be inferred by fitting the observed spectral amplitude to theory, betatron radiation also provides information on the length over which the electrons remain at high energy, and hence on the accelerating electric field. The length over which an electron initially at rest accelerates to a Lorentz factor γ depends on the electric field in the plasma: $L \simeq \sqrt{\gamma^2 - 1} m_e c^2 / eE_0$ with c the speed of light. For a plasma density of 7×10^{18} e^-/cm^3 and an electric field equal to the linear cold relativistic wavebreaking field [51], $E_0 = m_e c\omega_p / e$, with m_e and e the electron mass and charge, and ω_p the plasma angular frequency, the acceleration length to reach an electron energy $E_z = 400$ MeV is on the order of the focusing dephasing length $L \simeq L_\phi \simeq \lambda_p \gamma_p^2 / 2 \simeq 1.5$ mm, where $\gamma_p \sim \lambda_p / \lambda$ is the relativistic Lorentz factor associated with the phase velocity of the plasma wave. However, for laser pulse lengths on the order of the plasma wavelength, $L_{\text{laser}} \simeq 1\text{–}2 \times \lambda_p$, as in this thesis, the initial intensity profile may shorten and steepen as the plasma density wave feeds back on the laser pulse,

resulting in a highly nonlinear wakefield and electron self-injection. In the limit of the one-dimensional nonlinear cold relativistic wavebreaking electric field amplitude [50, 56] $E_{\mathrm{WB}} = \sqrt{2(\gamma_p - 1)}E_0 > E_0$, the acceleration length necessary to reach the same energy (400 MeV) would be limited to $L \simeq 0.29$ mm.

5.3 LPA setup and diagnostics

Experiments were conducted in the LOASIS facility at the Lawrence Berkeley National Laboratory, on two different laser-plasma accelerators. Both accelerators use a 800-nm laser pulse produced using a 10 Hz Ti:Al_2O_3 chirped-pulse amplification system. The X-ray betatron radiation emitted by the electrons inside the plasma was measured using a cooled back-illuminated charge coupled device (CCD) camera detailed in Sec. 5.4. Single-shot diagnostics were used to characterize the electron bunches generated, including a magnetic dipole spectrometer for the electron bunch energy distribution [68] which provided energy, charge and divergence measurements.

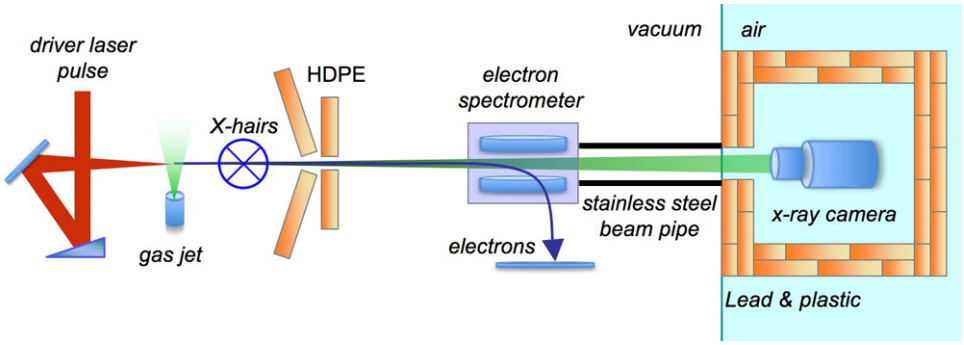

Figure 5.2: Schematic diagram of the gas jet laser-plasma accelerator. A 800-nm laser pulse was focused using a $f/4$ off-axis parabola into supersonic Hydrogen gas. The plasma density was scanned by varying the gas jet backing pressure (1–6 $\times$ 10^{19} e^-/cm^3). Thin crosshairs were placed 22 cm, and the X-ray camera CCD chip 220 cm, downstream of the plasma. X-ray background radiation was mitigated using high-density-polyethylene (HDPE) plates and Lead bricks. The line of sight was further restricted by a rectangular stainless steel pipe fitting to the CCD chip. The electron beam was analyzed using a broadband magnetic spectrometer ($\sim$ 10–100 MeV, $\pm$25 mrad).

In the first accelerator [40, 153], a 0.45 J, 45 fs FWHM, linearly polarized laser pulse was focused (7.2 μm FWHM intensity spot size) into Hydrogen gas from a 2.2 mm inner diameter supersonic nozzle (Fig. 5.2). This accelerator operated at a normalized vector potential $a_0 \simeq 1.9$ (Eq. 2.7), and plasma densities ranging from 1–6 $\times$ 10^{19} e^-/cm^3, for which the focusing dephasing length [12], L_ϕ (Eq. 2.32), varies from $\sim$ 60 to 900 μm. In these experiments, plasma density measurements were performed using a trans-

verse folded-wave interferometer [1]. Electron bunches produced typically had a two-component structure: a low energy exponential-like distribution containing most of the total charge ($\gtrsim$ 90%) and a high energy ($\simeq$ 40 MeV), low charge ($\lesssim$ 10% of total) quasi-monoenergetic distribution [153, 3].

The X-ray radiation was collected in the first accelerator with the camera placed 220 cm downstream from the exit of the plasma. In both accelerators camera placement was constrained by available space in the beamline. Shielding and apertures were used to ensure good control of bremsstrahlung background radiation, due to secondary collisions of low energy background electrons, and to collimate of the measured X-ray beam. The camera was coupled to the vacuum chamber with a single window made of 0.1 μm of Aluminum, 14 μm of polycarbonate, 18 μm of Kapton, and 25 μm of Beryllium, enhancing the acquired X-ray spectral range. Strong defocusing of the laser after interaction with the plasma, due to the small $f/\#$, meant that the crosshairs, made of gold plated tungsten (12.5 μm and 50 μm diameter), were protected from laser damage at their location, 22 cm downstream from the exit of the plasma, providing 10 times magnification imaging of the X-ray source.

The second accelerator [10] channeled a 1.3 J, 56 fs FWHM, linearly polarized laser pulse in a 3.3 cm long, 250 μm diameter, Hydrogen gas-filled capillary discharge waveguide (Fig. 5.3). This accelerator operated at a smaller input normalized vector potential, $a_0 \simeq 1$, and lower plasma densities, 0.4–1 $\times$ 10^{19} e^-/cm^3, for which the focusing dephasing length varies from $\sim$ 0.9 to 3.6 mm. The on-axis plasma density inside the capillary was calculated by substituting the capillary discharge current calibration provided by B. H. P. Broks *et al.* [204] and the perfect gas law (n_{H_2} [$\mathrm{H}_2/\mathrm{cm}^3$] $\simeq 3.29 \times 10^{16} \times P_i$ [Torr]), where P_i is the pressure inside the capillary, in the on-axis density calibration of Hydrogen-gas-filled capillary discharge waveguides provided by A. J. Gonsalves *et al.* [205]. Typical electron spectra had low divergence,

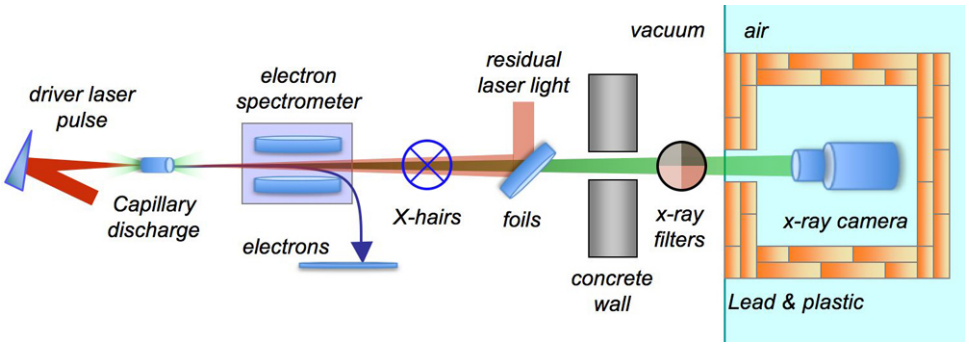

Figure 5.3: Schematic diagram of the capillary-guided laser-plasma accelerator. A 800-nm laser pulse was focused using a $f/25$ off-axis parabola into a Hydrogen gas-filled capillary discharge waveguide. The plasma density was scanned by varying the backing pressure (0.4–1×10^{19} e^-/cm^3). Thin crosshairs were placed 176 cm, and the X-ray camera CCD chip 473 cm, downstream of the plasma. Residual laser light after interaction with the plasma was filtered out using a succession of foils. X-ray background radiation was mitigated by the presence of a meter-thick concrete wall and the use of Lead bricks. A movable quadrant of filters was placed in front the X-ray camera window to test the validity of the measurements. The electron beam was analyzed using a broadband magnetic spectrometer ($\sim$ 10–975 MeV, $\pm$25 mrad).

$\lesssim$ 5 mrad FWHM, and quasi-monoenergetic charge distribution centered about 400–600 MeV with $\sim$ 10% FWHM energy-spread [206].

The X-ray radiation was collected in the second accelerator with the X-ray camera placed 4.7 m downstream from the exit of the plasma. The X-ray CCD camera was better shielded from background bremsstrahlung X-rays than in gas jet experiments. In addition to a lead brick castle around the camera and a greater distance to the source, a meter thick concrete wall with a one-foot diameter aperture separated the camera from the capillary (Fig. 5.3). In this setup, laser diffraction was weaker increasing damage risk. Because of this, the crosshairs (made of stainless steel wires of 680 μm diameter) was placed 1.7 m downstream from the exit of the plasma, providing $\simeq$ 2.7 times imaging magnification imaging of the X-ray source. An additional set of foils was used to dump the laser energy and avoid damaging the X-ray CCD camera. This set of foils had a thickness of 33.3 μm of Mylar (6.35 μm at 11°), 73.4 μm of polycarbonate (14 μm at 11°), and 19.2 μm of nitrocellulose (3 foils of 5 μm, 1 at 90°, 2 at 45°).

5.4 X-ray detector setup and analysis

A pixelated Silicon-based detector [207] was used to resolve the X-ray photons emitted by the LPA both spatially and spectrally. The CCD camera had a 1024×256 pixel chip, with 26 μm square pixels, a 40 μm depletion region of Silicon, a ~ 5 μm dead Si layer, and provided a broad detection range ($\gtrsim 4\%$ absorption for $\sim$ 1–20 keV). The CCD was calibrated for single pixel absorption spectroscopy, spectral yield was characterized versus occupancy and analysis thresholds, and the accuracy was validated using both synthetic data and experimental filter spectra.

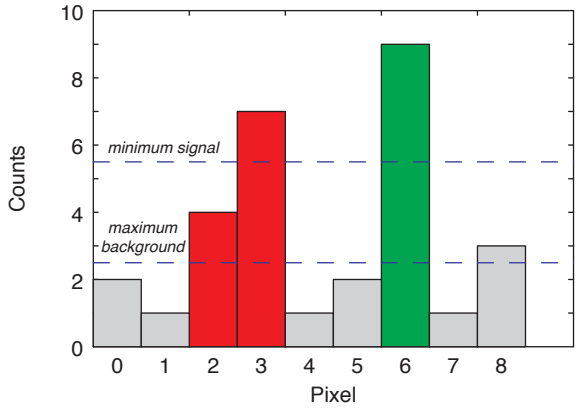

Figure 5.4: Principle of the single pixel absorption events (SPAE) detection method. *Gray* pixels in this one-dimensional detector have noise signal, *red* pixels could be due to either two single-photon events or to a shared current generated by a single photon, and hence are not being counted. The *green* pixel satisfies the SPAE conditions and is being counted.

Single-shot X-ray spectra were calculated by generating a histogram of the image acquired by the CCD camera after background subtraction. Only single pixel absorption events (SPAE) were considered. An SPAE is an isolated X-ray hit on the CCD, for which surrounding pixels level do not exceed the background level (Fig. 5.4). Thus, the number of counts in a pixel for an SPAE is directly proportional to the energy of the absorbed X-ray [208, 7]. An offline calibration using a ^{55}Fe radioactive source was performed and provided a conversion of 31.25 eV/count and a resolution of 0.25 keV FWHM [7]. The

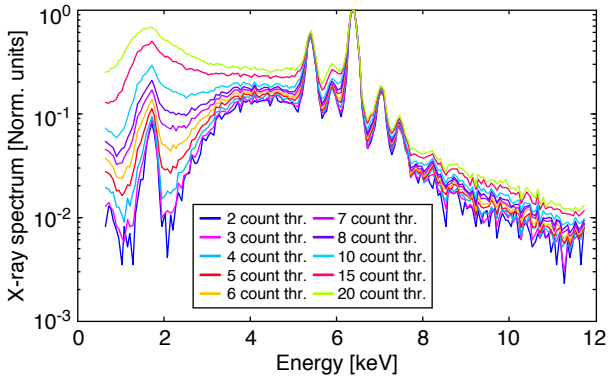

Figure 5.5: Example of single pixel absorption event (SPAE) spectrum measured for different background threshold levels: 2, 3, 4, 5, 6, 7, 8, 10, 15, 20 camera counts (from *bottom* to *top* curve). Each spectrum is an average over 200 shots collected during gas jet experiments. For thresholds below 4–5 counts, the spectral shape does not change, only the amplitude is affected and the spectrum correctly represents the betatron emission. At higher thresholds the spectra are distorted by contribution of split charge hits.

X-ray hits were binned in natural integer factors of camera units to respect the camera digitization and avoid interpolation. Because of the continuum nature of the betatron radiation (*c.f.* Sec. 5.2) the choice was made to present the X-ray spectra in photons per unit of energy [ph./keV] to have a constant energy bin size throughout the spectrum. To obtain the spectra in unit of photons per solid angle [sr] per 0.1% of bandwidth [ph./sr/0.1% BW], the spectra would be multiplied by 0.1% of the bins energy ($10^{-3}\hbar\omega$) and normalized by the solid angle subtended by the detector, which during gas jet and capillary experiments was, respectively, $\simeq 26 \times 10^{-6}$ sr and $\simeq 5.5 \times 10^{-6}$ sr, satisfying the small observation angle condition in Eq. (5.7).

The efficiency of the SPAE method depends on the flux of X-rays. If every pixel is illuminated (100% occupancy) there are no SPAE, hence no spectral information. The occupancy effect was characterized on the capillary-based accelerator by inserting a set of filters in front of the camera (Fig 5.7). The ratio SPAE number to total local charge was found to be 0.3% (31.9% occupancy), 0.89% (21.5% occupancy), 2.07% (14.3% occupancy), and 2.63% (10.9% occupancy) for respectively no filters, 10 μm Cu, 100 μm

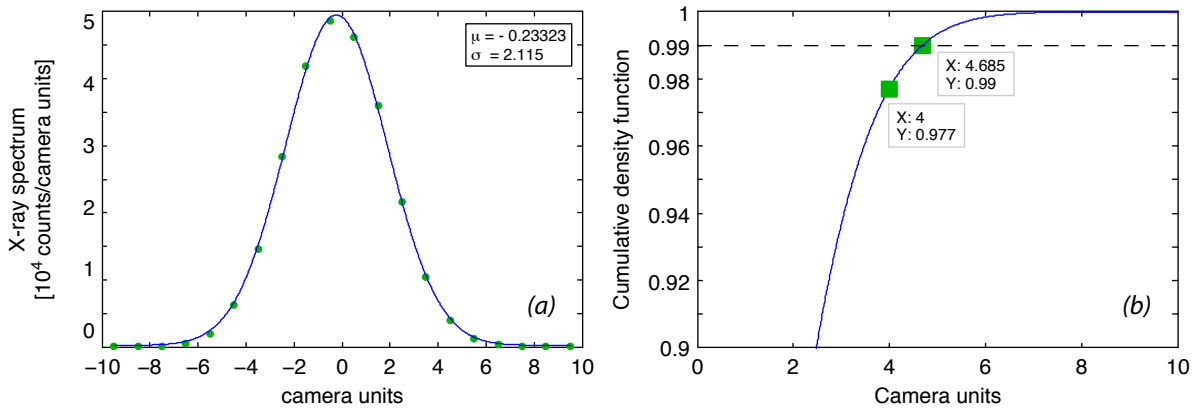

Figure 5.6: Noise characterization of the X-ray CCD camera using a background shot. *(a)* SPAE histogram and Gaussian fit. *(b)* Cumulative density function.

Al, and 10 μm Cu and 100 μm Al. To compensate for the occupancy effect, the SPAE spectra are normalized to the total charge collected within the spectral acceptance of the detection. For these measurements the accelerator was tuned to maximize the X-ray yield by increasing the bunch charge with the trade-off of lowering the electron bunch energy. The average electron beam distribution was centered around 250 MeV, had a $\simeq$ 20.7% energy-spread and $\simeq$ 11 pC of charge.

The choice of background threshold determines how discriminating the SPAE algorithm is and ultimately how accurately the measured spectrum represents the X-ray betatron emission. The higher the background threshold the more hits on the camera are being counted as SPAE. Eventually, split charge hits, which are clusters of two or more pixels charged by a single X-ray photon, are being counted as SPAE and included in the spectrum erroneously, distorting the spectrum (Fig. 5.5). Conversely, for small thresholds the probability of rejecting a valid SPAE increases and the spectrum has a poor signal-to-noise value. To select a value for the background threshold the histogram of a background shot (no driver laser) was analyzed (Fig. 5.6a). The cumulative density function of the measured noise distribution was calculated, providing the probability of a given threshold to be within the noise (Fig. 5.6b). For gas jet experiments, the back-

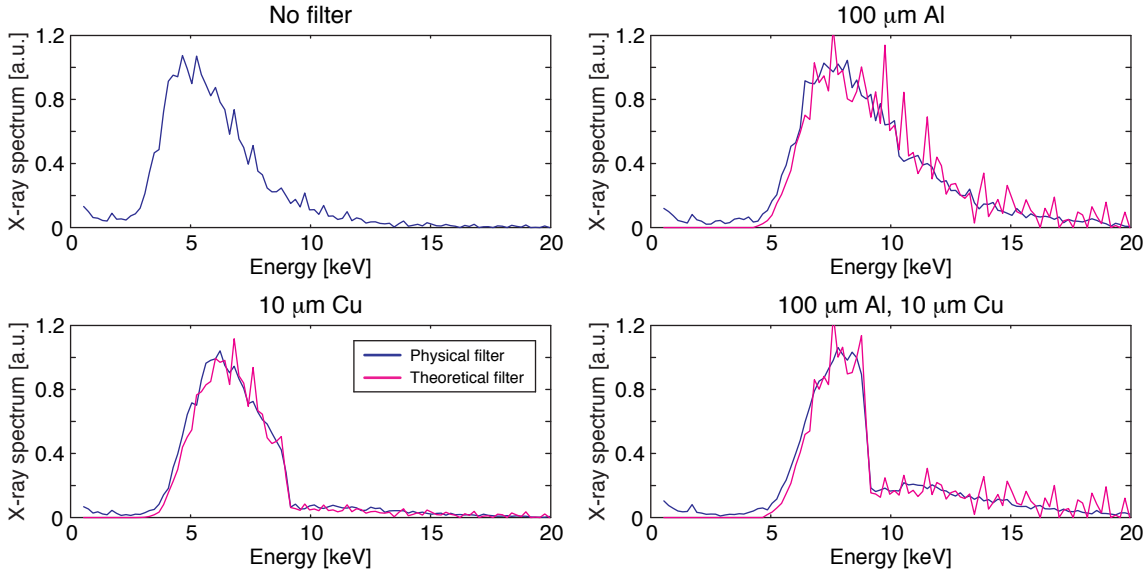

Figure 5.7: Average (111 shots) single pixel absorption event (SPAE) spectra of four regions of the CCD camera, in front of which different filters were placed (no filters, 10 μm Cu, 100 μm Al, and 10 μm Cu and 100 μm Al). Each spectrum matches with the convolution of the non-filtered spectrum with the transfer function of each filter convoluted with the detector response, indicating the SPAE method is robust throughout the detection range of the detector.

ground threshold was set at 4 camera counts for which the probability for a single pixel of being outside the noise was 97.7% (Fig. 5.6b). Hence, the probability of rejecting a valid single hit event due to noise was $(1 - 0.977^8) \times 100 \simeq 17\%$, since each pixel is surrounded by 8 pixels. On capillary experiments, the background threshold was set at 5 camera counts, for which the SPAE rejection probability was 12.2%. Figure 5.5 shows an example of gas jet experiments SPAE spectrum calculated for different background thresholds. Convergence is obtained for thresholds of 2–4; the choice of a threshold of 4 assured good statistics while minimizing spectral distortion due to un-accounted-for charge sharing.

A set of synthetic images generated with spectra, occupancy, and backgrounds representative of those in the experiments was analyzed to further evaluate SPAE accuracy. Double hit counts, which occur when two low-energy photons hitting a single pixel are counted as a high-energy SPAE, become significant for occupancies of 40% or above.

The experiments typically operated below 10% occupancy in which cases pile up was not significant and the spectra are accurate. Similarly, using simple estimates for charge splitting, convergence of the recovered spectrum to the correct (input) value was observed for background threshold values of 3–4 as chosen in the experiments.

The validity of the SPAE method over the energy detection range of the Silicon CCD camera was confirmed by placing in front of the camera a quadrant filter, described above, and comparing the SPAE spectra measured over the area of the CCD covered by each filter (Fig. 5.3). A transfer function was calculated for each filter by convolving the 0.25 keV FWHM Gaussian response of the detector with the filter photoabsorption cross sections, derived from semi-empirical atomic scattering factors, tabulated [209] by the Center for X-ray Optics (www.cxro.lbl.gov). The detector response smoothes the transfer functions at the sharp 8.98 keV absorption edge of Copper. The spectra measured for each of the three areas placed behind a filter match the spectrum resulting from the multiplication of the non-filtered spectrum by the respective transfer functions and an arbitrary normalization factor (Fig 5.7). Thus, the SPAE method provides a valid measure of the X-ray spectrum over the detection range of the detector and confirms the spectral continuity of the X-ray betatron radiation emitted by electrons accelerated in an LPA, allowing detailed fits to the theory of Sec. 5.2.

5.5 Broadband electron beam experiments

Gas jet experiments produced broadband exponential-like electron distributions with characteristic roll-off energy (*i.e.*, damping energy) on the order of 10–20 MeV. The high energy tail, $\gtrsim 10$ MeV, of these electron distributions typically had a few pC of charge. Figure 5.8a shows an example electron distribution where the charge (Q) distribution has a two-component structure with a high-charge ($\simeq 4.9$ pC) exponential-like distribution having a damping energy $E_d \simeq 15$ MeV ($\delta Q/\delta E_z \propto \exp(-E_z/E_d)$), and a low charge component of $\simeq 0.3$ pC, 45 MeV and 5% energy-spread. In addition to a broadband energy distribution, the typical angular charge distribution was also a complex function of the electron energy. Figure 5.8b shows an example of electron distribution where the angular divergence, θ_{div}, is an approximate exponential function of the electron energy, $\delta\theta_{\text{div}}/\delta E_z \propto \exp(-E_z/E_d)$, with $E_d \simeq 27$ mrad.

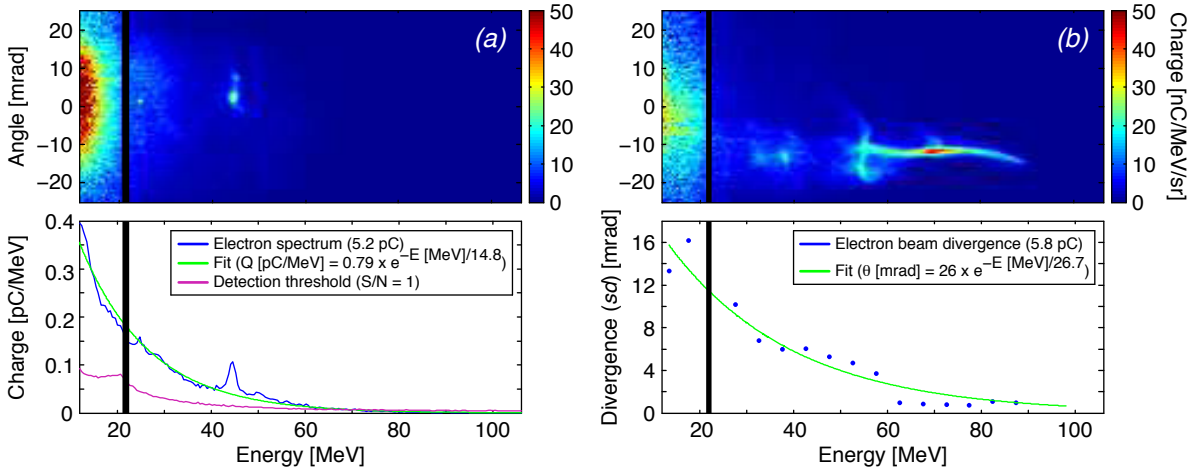

Figure 5.8: Examples of electron charge distributions produced during gas jet experiments. *(a)* Detail of an angle-integrated charge distribution with a two-component structure, a exponential-like and a quasi-monoenergetic distributions. *(b)* Detail of the energy-integrated divergence distribution.

The transverse size of the electron bunch was first evaluated using the penumbra technique (Eq. (5.4)). At a plasma density of 2.8×10^{19} e^-/cm^3, the average image of 200 X-ray shadowgrams yield a source size of less than 5 ± 2.5 μm *rms* which is on the

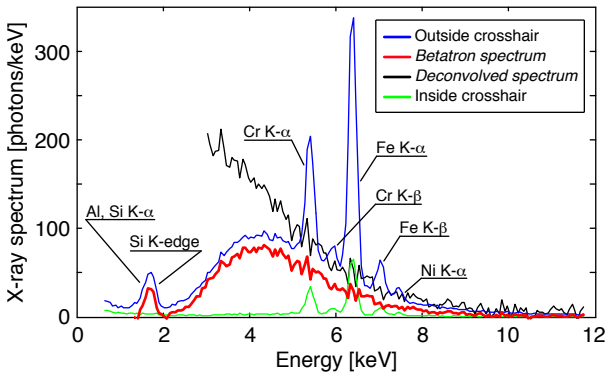

Figure 5.9: Average (200 shots) single pixel absorption event (SPAE) spectra measured inside and outside the shadow of crosshairs. Using the SPAE method, the fluorescence emitted by bremsstrahlung in stainless steel was resolved and subtracted from the signal to provide the betatron continuum. The X-ray spectrum at the source (*deconvolved spectrum*) was retrieved by dividing the betatron continuum by filters and camera transmissions.

order of the driver laser focal spot. Note that imaging of the crosshairs onto the CCD chip proves the X-rays originated from the plasma itself.

Single-shot and shot integrated X-ray betatron spectra were measured using the SPAE technique (*c.f.* Sec. 5.4). During gas jet experiments, for shielding the line of sight of the camera was restricted by a rectangular stainless steel pipe that fitted to the size of the CCD chip. The K-shell fluorescence lines from X-rays generated by collisions of low-energy (< 10 MeV), high-divergence (> 10 mrad) electrons with the stainless steel (Fe, Cr, Ni), as well as Al and Si K-shell fluorescence lines from the window and the CCD dead layer were observed (Fig. 5.9). Since the vacuum pipe was placed downstream from the crosshairs, this fluorescence formed a uniform background throughout the CCD chip. Although not desired for betatron measurements, these fluorescence lines provided an additional energy calibration and resolution measurement of the detector which agreed with the offline ^{55}Fe radioactive source calibration.

By measuring the X-ray spectrum inside and outside the crosshairs shadow, the X-ray betatron continuum was retrieved by subtracting the inner spectrum multiplied by a fitting parameter (which represents the fluorescence), from the outer spectrum (Fig. 5.9).

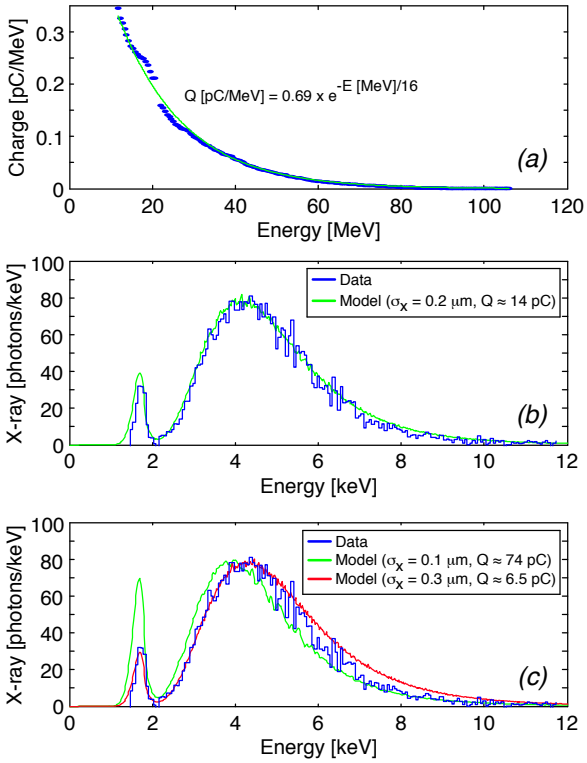

Figure 5.10: *(a)* Average (200 shots) electron bunch charge distribution produced during gas jet experiments. The distribution is fitted by an exponential-like distribution with a 16 MeV damping energy. *(b)* Average X-ray betatron spectrum measured at the CCD camera. The fit was obtained for an initial transverse Gaussian electron distribution of *rms* radius of 0.2 μm, the energy distribution of figure *(a)* and a total charge of 14 pC. *(c)* Confidence range of the fit of figure *(b)* obtained for initial transverse distributions of 0.1 and 0.3 μm *rms* radius, and respective total charge of 74 pC and 6.5 pC.

The spectrum of betatron X-rays incident on the camera was then retrieved by dividing the betatron continuum by the transmission functions of the vacuum window, the Silicon dead layer of the CCD, and the absorption of the depletion region of Silicon (Fig. 5.9). Without the high spectral resolution of these measurements, the fluorescence peaks would be smeared over the spectrum and counted as betatron radiation.

To model accurately the X-ray betatron radiation emitted by the complex electron energy distributions produced during gas jet experiments, and hence to provide a correct understanding of both electron dynamics and plasma wave structure, numerical integration [202, 8] of Eq. (5.12) over discretely sampled trajectories of electrons oscillating in

an ion channel was performed. The initial transverse electron distribution was assumed Gaussian, centered on-axis and was sampled over 262144 particles which produced good numerical convergence. The electron energy distribution was assumed to be exponential with a 16 MeV damping energy which well models the average experimental energy distribution (Fig. 5.10a) whose high-energy tail ($\geq$ 11.8 MeV) had $\simeq$ 5 pC of charge. The output spectrum was convolved with the vacuum window and camera transfer functions and the 0.25 keV FWHM Gaussian response of the detector.

Figure 5.10b shows the comparison between the betatron spectrum, obtained after fluorescence subtraction (as in Fig. 5.9), and the best fit calculated spectrum which was calculated for a 5 μm Si dead layer of the CCD camera and a *rms* radius of the bunch of 0.2 μm. The acceleration length was assumed to be the focusing dephasing length, $L \sim \lambda_p \gamma_p^2/2 \simeq 196$ μm ($n_e = 2.8 \times 10^{19}$ e^-/cm^3). The amplitude was matched by increasing the simulated bunch charge to $\simeq$ 14 pC. As the bunch accelerates, some of the electrons pass dephasing and lose energy before exiting the plasma [153]. Although these electrons do not exit the plasma at high energy, they contribute to the X-ray betatron radiation.

Several electron beam parameters were used to provide a confidence range for the transverse bunch size and an estimate of the beam emittance. While a simulated bunch radius of 0.1 μm (Fig. 5.10c) provided a good fit of the high energy tail of the X-ray betatron spectrum, it failed to represent the low energy part of the spectrum. On the other hand, a bunch radius of 0.3 μm provided a good fit of the low energy X-ray photon spectrum but overestimated the high energy tail (Fig. 5.10c). This gives a confidence range on the *rms* radius of the electron beam inside the plasma, $\sigma_x \simeq 0.2 \pm 0.1$ μm.

The divergence for a matched beam of the radius inferred from the betatron radiation (Eq. (5.3)) is $\sigma_\theta \lesssim 30$ mrad, about twice the measured divergence at the magnetic spectrometer, and the normalized transverse geometric emittance is inferred to be $\epsilon_x \simeq$

0.24 ± 0.12 mm.mrad for 20 MeV electrons. The discrepancy between the betatron fit radius of 0.2 μm and the ballistic radius of 0.13 μm calculated using Eq. (5.3) can be explained by the decrease of transverse momentum of the electron bunch as it crosses and adiabatically expands in the downstream edge of the plasma [196]. The plasma density downramp was measured [1] to be long compared to the betatron wavelength, $\sigma_w \simeq 150\ \mu\text{m} \sim 9\text{–}12\times\lambda_\beta$, where the ramp was modeled by an error function $n_e(z) = n_e(0)/2\times(1 - \text{erf}(z/\sqrt{2}\sigma_w))$. As the plasma density decreases, the plasma wavelength increases inducing a decrease in focusing strength of the plasma wakefield, an expansion of the beam and a decrease in angular spread. This effect is difficult to model quantitatively since at the downstream edge of the plasma the laser energy is partially depleted and the full "bubble" regime might not apply, in which case the electron trajectories would not be strongly affected by the plasma density roll-off.

Using the SPAE method, high spectral resolution of betatron radiation emitted from the oscillation of electrons accelerated in the wake of a laser-plasma accelerator was obtained. Measured amplitudes of the X-ray spectra were correlated with the electron bunch charge [7]. Direct X-ray spectra had enough counts to allow calculation of the X-ray cut-off frequency and verify, within the detection range of the CCD camera ($\sim$ 2–20 keV), the theoretical shape of betatron X-ray spectra that filter based techniques assume [210, 193]. X-ray measurements based on the relative absorption of different filters have a limited resolution (one energy bin per filter) and may occult important spectral features.

5.6 High-energy low-energy-spread electron beam experiments

Capillary experiments produced high energy (400–600 MeV), quasi-monoenergetic ($\Delta E <$ 20%) electron beams. Figure 5.11 shows an example of single-shot energy distribution close-up (the full range was about ±30 mrad, 5–975 MeV) and betatron spectrum of a 463 MeV ($\gamma = 907$), 6.6% FWHM energy-spread, electron beam with a 1.15 mrad *rms* divergence angle.

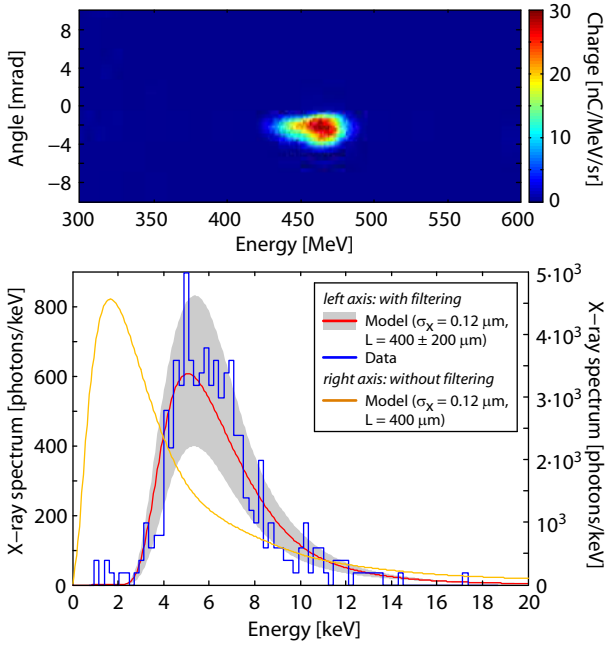

Figure 5.11: Example of simultaneous single-shot electron energy distribution and X-ray betatron spectrum. The electron beam is centered about 463 MeV, has 6.6% FWHM energy-spread and a 1.15 mrad *rms* divergence. The matched transverse size of the electron bunch, $\sigma_x \simeq 0.12$ μm, was calculated for a Gaussian distribution of electrons using Eq. (5.3). The theoretical X-ray spectrum was calculated using Eq. (5.7), summing over the first 101 odd harmonics to reach numerical convergence, and assuming a propagation length of 400 ± 200 μm. The X-ray spectrum at the source (*Data/Model without filters*) was retrieved by dividing the betatron spectrum by filters, foils and camera transmissions.

X-ray shadowgrams of the crosshairs were used to infer an upper bound measurement of the transverse size of the electron bunch. During capillary experiments, the source

size measurements were limited to the single-pixel resolution $\simeq 4$ μm, ~ 6 times smaller than the focal spot ($w_0 \simeq 23$ μm).

The transverse size of the beam was accurately resolved by fitting the spectrum of the X-ray emission. No fluorescence was observed in the X-ray spectra and the simple model of electrons propagating in a uniformly charged cylindrical ion channel [82] (Eq. (5.7)) provided a good fit of the data (Fig. 5.11). With a backing pressure of 250 Torr Hydrogen gas, the on-axis electron density was calculated (*c.f.* Sec. 5.3) to be $\simeq 4.7 \pm 2.3 \times 10^{18}$ e^-/cm^3 and, using Eq. (5.3), the standard deviation radius of the electron bunch inside the plasma was estimated at $\sigma_x \simeq 0.12 + 0.05 - 0.02$ μm, providing $a_\beta \simeq 1$. With a normalized transverse geometric emittance of $\epsilon_x \simeq 0.12$ mm.mrad, this 463 MeV electron beam is suitable for injection into a free-electron laser (FEL) [127] for radiation production.

Because the length of the plasma downramp, $\sigma_w \simeq 350$ μm, was only a few times longer than the betatron wavelength of these high energy electrons, $\sigma_w \simeq 3 \times \lambda_\beta$ at $\gamma = 907$, the adiabatic expansion of the beam at the downstream edge of the plasma was neglected. Simulations also show that the laser is strongly depleted and the electron bunch dephased at the end of the 3.3 cm channel, such that the electron beam is no longer executing strong betatron oscillations [102]. In addition, since no low energy electron tail was measured on the magnetic spectrometer, the total collected charge, $Q \simeq 0.4$ pC, was assumed to be the total amount of charge which contributed to the X-ray betatron emission.

The measured beam size is in close agreement with particle-in-cell simulations [42, 44], confirming that the transverse beam dynamics of LPAs is accurately understood. Simulations of laser and plasma parameters close to those of the experiment [102, 101] showed production of electron beams near 300 MeV with 5% FWHM energy spread, 2 fs FWHM and 1.3 mrad *rms* divergence, consistent with the experimental measurements

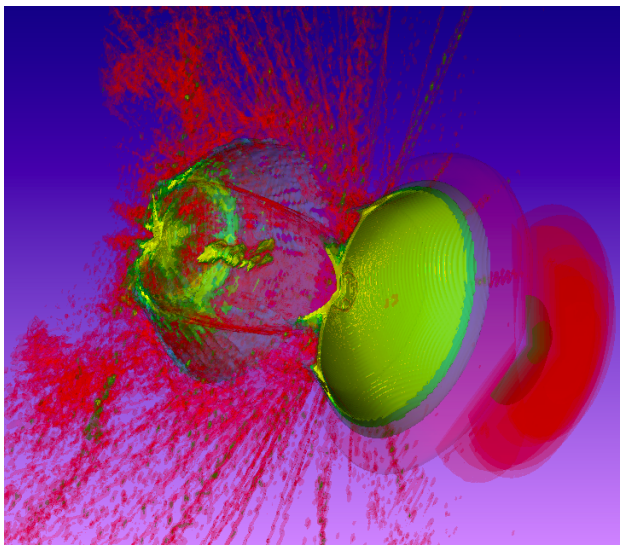

Figure 5.12: Three dimensional VORPAL particle-in-cell simulation of the laser-plasma accelerator. The picture represents in false colors the plasma density. For clarity, a section formed by the intersection of two planes at about 120 degrees from each other has been cut out. This simulation produced a 300 MeV, 5% FWHM energy spread, 2 fs FWHM long, 1.3 mrad *rms* electron beam.

above. The simulations observed a 0.1 μm *rms* transverse beam size, which had not previously been measurable experimentally due to resolution limitations. The present experiments confirm the predicted beam size and hence the presence of a low emittance beam. The simulated divergence in the plasma is similar to the experimental divergence, which is consistent with the ramp having a small effect on the beam divergence. In addition to the short ramp length, the simulations have shown that at the plasma channel exit the laser pulse is strongly depleted and the electron beam is dephased from the wake [102], which would further suppress the ramp effects [196]. Close agreement of both beam divergence and size indicates that the physical picture of particles trapping transversely in the wake observed in the simulations [211, 103, 101] is quantitatively correct. Comparison of 2D and 3D simulations showed that the wake structure differs significantly [102]: a higher density spike is produced at the back of the bubble in 3D because the plasma is converging in two transverse dimensions. This spike has an important role in injection, as particles on injection trajectories pass close to it and its field

repels them, resulting in lower transverse beam momentum in 3D than in 2D. It has been previously observed that 3D simulations better reproduce the experimental beam divergence [101] (Fig. 5.12). The present experiments demonstrate that the observed beam radius as well as divergence matches the 3D simulated result, indicating accurate understanding of the transverse injection dynamics of LPAs and the reduction of transverse momentum due to the spike at the back of the bubble, which are important physical processes governing beam quality.

The theoretical spectrum in Fig. 5.11 was matched to the experimental amplitude by varying the propagation length, using the ballistic radius $\sigma_x \simeq 0.12$ μm. Different radii were also tried providing an upper bound radius of $\sigma_x \sim 0.4$–0.5 μm. Using the ballistic radius, best fit was found for a propagation length $L = 400 \pm 200$ μm ($N_\beta \sim 1$) $< L_\phi \simeq 2.9 + 4.9 - 1.3$ mm, where L is the length over which the electrons radiated $\gtrsim 2$ keV betatron X-rays.

The X-ray betatron spectrum at the source was retrieved by dividing the collected X-ray spectrum by the transmission functions of the vacuum window, the laser energy dumping foils and the CCD, convoluted with the camera energy resolution (Fig. 5.11, *right scale*). The peak energy of the X-ray betatron spectrum is found to be $\hbar\omega_{\rm peak} \simeq 1.7$ keV. Assuming the emittance was conserved during the acceleration, the minimum energy of an electron with orbit amplitude $r_\beta \simeq 0.12$ μm, for which the individual spectral peak energy is greater or equal to the experimental value of $\hbar\omega_{\rm peak}$ can be computed using Equation (5.7): $\gamma^{min} \simeq 666$ or $E_z^{min} \simeq 340$ MeV. An estimate of the accelerating electric-field, *i.e.*, the plasma wakefield amplitude, is given by $E_{\rm WF} \simeq \Delta E_z/eL \simeq 3 \times 10^{11}$ [V/m] $\simeq 1.5 \times E_0$, in reasonable agreement with laser-plasma acceleration theory [12] and within 30% of the simulated field.

Linear scaling of the X-ray yield on-detector, for plasma densities ranging from 4 to 8×10^{18} e^-/cm^3, with the electron bunch charge was verified. The foils used to dump the

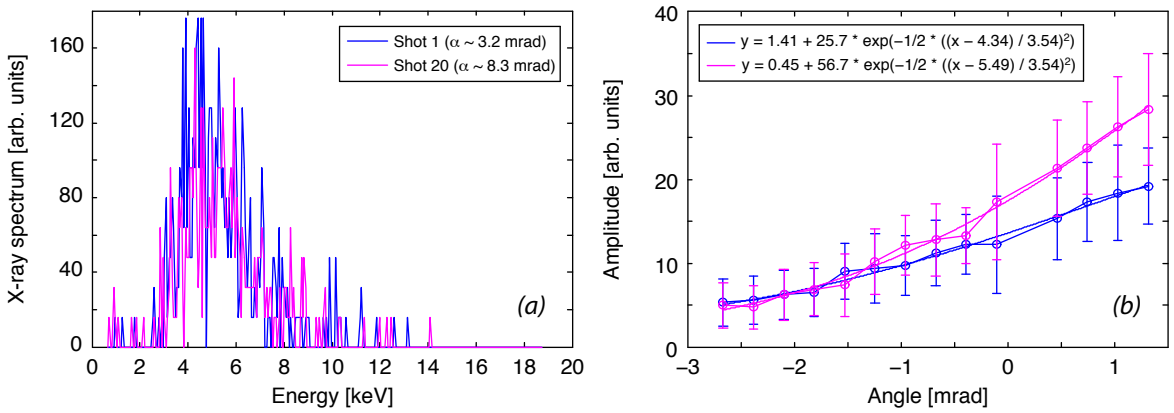

Figure 5.13: Observation of X-ray angular steering by scanning the transverse position of the capillary. *(a)* Single-shot X-ray betatron spectra emitted by two 350 MeV electron bunches produced for two transverse positions of the capillary. The centroid position of these bunches relative to the axis of the magnetic spectrometer were $\alpha \simeq 3.2$ mrad and $\alpha \simeq 8.3$ mrad. *(b)* Vertically integrated spatial distribution of the respective X-ray betatron emissions.

laser energy and protect the instruments acted as bandpass filters, limiting the sensibility of the spectrum to the experimental parameters. In addition, preliminary tests showed the possibility of angular steering of the X-ray beam by scanning the capillary transverse position, in the horizontal plane, to the laser focal position (Fig. 5.13). The intrinsic synchronization of this bright X-ray beam with the ultrashort ($\lesssim$ 50 fs) laser pulse makes it an interesting table-top source for pump/probe, diffraction experiments as well as medical, military, and commercial applications.

Assuming the X-ray pulse duration is on the same order than the electron bunch duration given by [83] $\tau \sim \lambda_p/4c \simeq 12.8$ fs, the peak spectral brightness in Fig. 5.11 was $B_{\rm max} \sim (10^{-3}/\tau\sigma_x^2) \times \partial^2 I_{\rm max}/\partial\hbar\omega\partial\Omega \simeq 3 \times 10^{22}$ ph./s/mm^2/mrad^2/0.1% BW, where $\Omega\,[\rm sr] \approx 10^{-6}\pi\theta^2\,[\rm mrad^2]$. The average X-ray yield over 158 shots was 14% lower than that of Fig. 5.11 and the accelerator had a $f \simeq 1$ Hz repetition rate; hence, the average brightness was $B_{\rm avg} \sim (10^{-3} f/\sigma_x^2)\times\partial^2 I_{\rm max}/\partial\hbar\omega\partial\Omega \simeq 3.3\times10^8$ ph./s/mm^2/mrad^2/0.1% BW.

The effective peak spectral brightness and average brightness available behind the foils were, respectively, $B_{\rm max}^{\rm eff.} \simeq 0.8 \times 10^{22}$ ph./s/mm^2/mrad^2/0.1% BW and $B_{\rm avg}^{\rm eff.} \simeq$

0.88×10^8 ph./s/mm^2/mrad^2/0.1% BW. While the effective brightness is still high, the X-ray peak energy is fixed ($\simeq$ 5 keV) and determined by the choice of foils and the X-ray yield is determined by the bunch charge, making this X-ray source tunable in peak energy, bandwidth, and amplitude.

The SPAE method allowed single-shot high resolution spectral analysis of X-ray spectra. Because of setup constraints the betatron radiation emitted during both gas jet and capillary experiments was strongly attenuated by filters, foils, and the camera vacuum window. Placing the camera in vacuum and an intelligent choice of filters to dump the laser energy should enhance the acquired X-ray spectral range. However, to measure such broader X-ray energy range, which can extend up to $\sim$ 100 keV [111, 193], using the SPAE method, would require the development of thicker pixelated detectors, possibly made of Silicon [212] or Cadmium Zinc Telluride (CZT) [213], sensitive to high energy X-rays.

5.7 Conclusion

Single-shot direct measurements of betatron radiation generated by gas jet and capillary-based laser-plasma accelerators was demonstrated using the single photon absorption event technique. The analysis method was shown to provide high resolution, reliable single-shot spectral information throughout the sensitivity range of the detector ($\sim$ 2–20 keV), a pixelated X-ray Silicon CCD camera. Both single-shot and shot integrated betatron spectra were presented and the theoretical continuum-like shape of these spectra, which filter based techniques assume, was observed.

The high spectral resolution allowed accurate retrieval of betatron continua produced by high charge ($>$ 1 pC), low energy ($<$ 100 MeV), high energy-spread electron beams by deconvolving a narrowband X-ray background from the raw spectra. An upper bound of the electron beam size, $\sigma_x < 5 \pm 2.5$ μm, was provided using X-ray shadowgrams. A parallel numerical code [8] was used to successfully fit the X-ray betatron spectra and provide a measurement of the size of the electron bunch inside the plasma wave, $\sigma_x \simeq 0.2 \pm 0.1$ μm. An explanation for the discrepancy of these spectral fits with the ballistic model developed in this thesis was provided [196]. For downstream plasma density ramp much greater than the betatron wavelength, $\sigma_w \gg \lambda_\beta$, and for an non-depleted laser pulse, an adiabatic expansion of the electron beam occurs as it exits the plasma, inducing a decrease in angular spread. The larger electron beam radius for lower energy electrons is also consistent with space charge affecting these lower energy beams [214] or un-matched propagation.

Simultaneous single-shot analysis of the electron and X-ray distributions of low charge ($<$ 1 pC), high energy ($\sim$ 0.5 GeV), low energy-spread ($<$ 10%) electron beams were presented. X-ray shadowgram analysis provided an upper bound for the transverse electron beam size of $\sigma_x < 4$ μm. In this case, the ballistic projected electron beam size, $\sigma_x \simeq 0.12$ μm, was shown to be accurate. The normalized transverse geometric emittance

was calculated to be $\epsilon_x \simeq 0.12$ mm.mrad, making these electron beams good candidates for FEL experiments [127]. In addition, an estimate of the plasma wakefield amplitude, $E_{\rm WF} \simeq 3 \times 10^{11}$ [V/m] $\simeq 1.5 \times E_0$, was calculated using single-shot measurement of the X-ray peak energy, $\hbar\omega_{\rm peak} \simeq 1.7$ keV.

The total X-ray yield was correlated with the electron bunch charge in both types of experiments. An average brightness of 3.3×10^8 ph./s/mm^2/mrad^2/0.1% BW was achieved with $\sim$ 0.5 GeV electron beams. A single-shot peak spectral brightness of 3×10^{22} ph./s/mm^2/mrad^2/0.1% BW was calculated. The capillary-based laser-plasma accelerator was shown to be a stable, tunable, source of collimated 5 keV X-ray photons at the detector with peak spectral brightness and average brightness suitable for X-ray experiments and commercial applications.

Chapter 6

Discussion and Conclusions

This thesis presented a suite of diagnostics , designed to handle the advantages and disadvantages inherent in laser-plasma accelerators compared to conventional RF accelerators. The diagnostics have been chosen because they provide non-destructive measurement of the key attributes of the accelerated electron bunches in a single-shot format. These diagnostics include the characterization of the electron bunch charge or the detection of γ-radiation due to bremsstrahlung from the deceleration of electrons in the target chamber using commercially available product such as an Integrated Charge Transformer (ICT) and a Health Physics Instruments (HPI) Model 6020 Geiger-Mueller (GM) γ-ray monitor (Fig. 6.1a). It includes also single-shot electron spectroscopy (Fig. 6.1b), high-sensitivity plasma density measurements (Fig. 6.1c), single-shot betatron X-ray spectroscopy (Fig. 6.1d), and single-shot spatiotemporal characterization of coherent transition radiation (CTR) (Fig. 6.1e).

To simplify plasma density measurements which provides key parameters of the accelerator such as the dephasing length and the pump depletion length, a wavefront sensor was used (Sec. 3.1). The ease of use is greatly improved since the design requires only one arm of a non-perturbative probe laser beam and the analysis is limited to an Abel

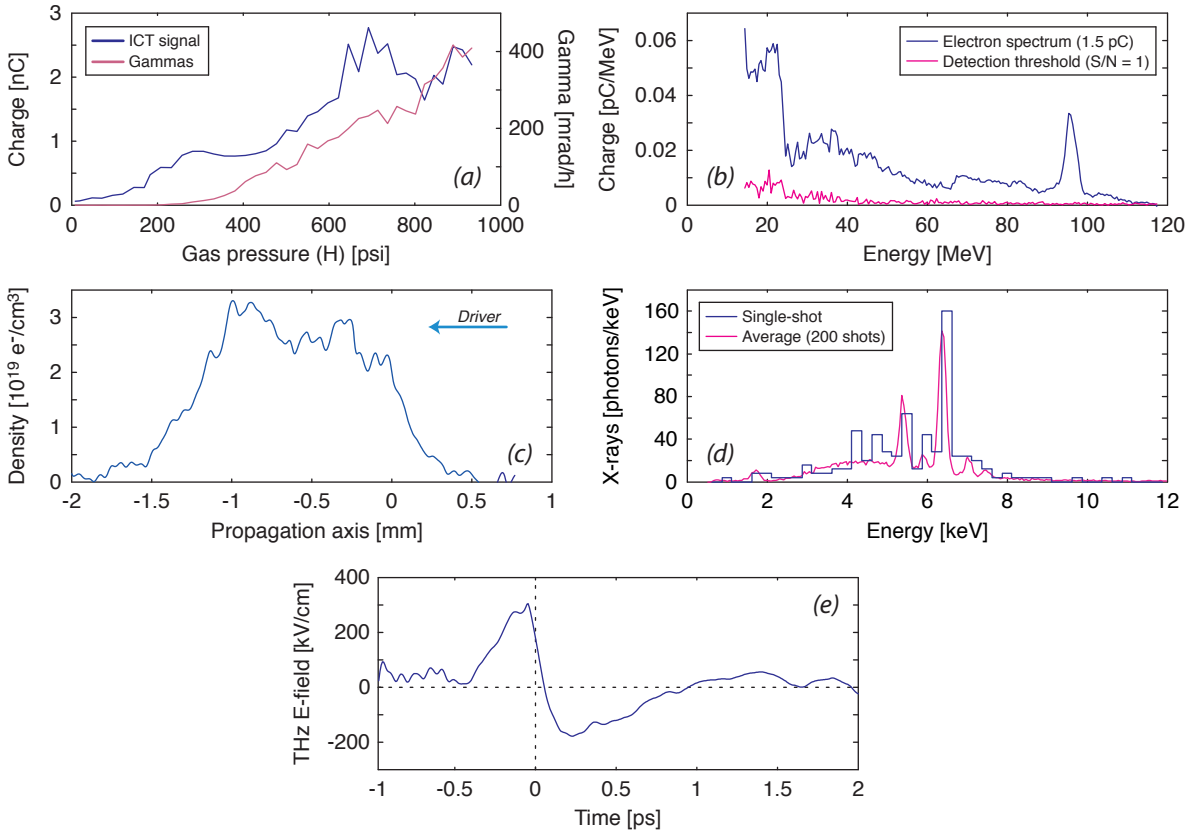

Figure 6.1: Simultaneous single-shot diagnostics available at the LOASIS. *(a)* Integrated Charge Transformer (ICT) measurements of the bunch charge and Geiger-Mueller (GM) γ-ray monitoring as a function of the backing pressure of the gas jet. *(b)* Broadband electron spectroscopy provides the energy distribution of the electron bunches. *(c)* Transverse interferometry provides the plasma density, *i.e.*, the plasma wavelength. *(d)* X-ray spectroscopy provides a measurement of the transverse size of the bunch and, in combination with electron spectroscopy, an estimate of the transverse emittance. *(e)* Characterization of the coherent transition radiation (CTR) provides a measurement of the bunch length.

inversion. The technique, which can be used for any phase sensitive measurement, was benchmarked with folded-wave interferometry-based measurements at different uniform plasma densities and for steep density gradients. It was shown the wavefront sensor-based technique provides about 8 times higher phase sensitivity than conventional interferometry. The characterization of the plasma density has been used in the experiments presented in this thesis as an optimization tool of the laser-plasma accelerator.

An important step toward the control of an accelerator is to provide a reliable, con-

trollable injection mechanism. Using an active beam pointing system of the laser, a stable colliding pulse optical injector was developed (Sec. 3.2). Experiments demonstrated repeatable operation over hours with $\sim$ 20% charge stability. It was shown that timing, density and collider intensity experimental scans are consistent with simulations. Because the low energy of the resulting electron bunches is attributed to the limited acceleration length, future experiments will include guiding of the driver using a third laser pulse to provide a plasma channel (Sec. 2.4). Simulations indicate that for a guided driver, the colliding pulse technique may produce ultrashort 200–400 MeV electron bunches of tens of pico-Coulombs of charge and narrow energy spread.

Analysis of the electron bunch temporal profiles is necessary in order to demonstrate the production of high-quality bunches and the applicability of the LPA as a future collider and for femtosecond pump-probe applications. In an LPA, the accelerated electrons emit coherent transition radiation (CTR) in the THz regime as they cross the plasma-vacuum boundary (dielectric discontinuity). Such high peak-power THz pulses, of the order of 100's of MV/cm, suitable for high-field pump-probe experiments, also provide a non-invasive bunch-length diagnostics.

In Sec. 4.1, the ability to generate THz pulses with more than 5 μJ of energy was demonstrated. A new design of the optical setup provided a good (near Gaussian) focus mode quality and the production of peak electric field of the order of 0.3 MV/cm. The pre-pulse dynamics of the driver laser was shown to significantly affect the performance of the LPA and the generation of THz radiation. The implementation of a pulse contrast enhancement technique, the crossed-polarized-wave filtering technique (XPW), showed a dramatic increase in the production of charge ($\sim$ 4 times), THz, γ-rays, and neutrons, but also a dramatic decrease in shot-to-shot variability, from a 100% level prior to XPW implementation to a 10% level after implementation.

In addition to providing an intense source of ultrashort THz pulses, CTR was used to

characterize the duration of the electron bunches produced in the LPA. Both scanning and single-shot techniques were used to provide a bunch-length measurements. A first series of temporal measurements was performed on low energy electron beams produced in a plasma downramp by measuring the amount of CTR energy emitted in four wavelength bands using two different filters to cut the spectrum (Sec. 4.2.2). The bunch duration at the end of the plasma downramp was calculated to be 200 ± 100 fs, in agreement with simulations, indicating the production inside the plasma of 30 fs long electron bunches, making plasma downramp injection a suitable LPA injector.

In Sec. 4.2.3, the spatiotemporal profile of the focused THz pulse was measured using two-dimensional electro-optic (EO) sampling. It was shown that the near single-cycle THz pulses experience strong spatiotemporal coupling which spatially distributes the spectral content of the pulses, indicating the necessity to measure the full spatiotemporal waveforms in order to provide an accurate bunch duration measurement. To this end, a new single-shot technique, temporal cross-electric field (TEX), which provides both high temporal resolution and one-dimensional imaging was demonstrated (Sec. 4.2.4). TEX is significantly easier to implement than previous high-resolution, single-shot EO techniques because it does not require the use of nonlinear processes other than the linear Pockels effect in the EO crystal. The spatiotemporal waveforms of THz pulses demonstrated the presence of a two-component structure with low-charge (10%), short (50 μm *rms*) bunch and a high-charge (90%), long (140 μm *rms*) bunch. The dependence of the THz spectrum on the electron-bunch duration makes it possible to detect the presence of short electron-bunch substructure with high sensitivity.

Single-shot X-ray spectroscopy measurements were reported of betatron radiation from both broadband sub-100 MeV and low-energy-spread 0.5 GeV electron beams produced by a laser-plasma accelerator. The measurements demonstrate the synchrotron nature (*i.e.*, continuum form) of the betatron emission from both gas-jet and capillary-

based laser-plasma accelerators. Measurement of single-shot spectra in the range 2–20 keV was enabled by using a detection array in the SPAE technique. Comparison of the measured spectra to analytical and numerical models of betatron radiation indicated the electron bunch radius inside the plasma to be $\sim$ 0.1–0.2 μm. In combination with divergence measurements, a normalized transverse emittance as low as 0.1 mm mrad was inferred for a 460 MeV, 2.8% *rms* energy-spread electron bunch. Reducing the beam emittance is necessary to enhance a variety of applications of relativistic electron beams, such as X-ray FELs and colliders for high energy physics. The data agree with simulated bunch size and divergence, consistent with the simulated physical picture of self-trapping and emittance.

In conclusion, new techniques have been successfully implemented: wavefront sensor-based plasma density measurements [1], several single-shot THz diagnostics (temporal cross-correlation, optical sideband, spectral encoding) [3, 184, 4], and single-shot x-ray spectroscopy [5, 6, 7]. These diagnostics have been used to characterize several operational mode of the LPA: channeled and unchanneled self-injection [148], colliding pulse injection [133] and downramp injection [2]. The electron bunches produced were shown to be suitable for a wide variety of applications that demand high-quality beams.

Time ran out and I did not have the chance to pursue further experiments. The development of permanent X-ray diagnostics on both gas jet and capillary setups would allow a more systematic correlation of the bunch size and wake structure with the accelerator performance. TEX offers a great ease of use and could provide a measure of fine structures in the electron bunch as a function of various parameters of the accelerator. In particular, it would be very profitable to observe the evolution of the bunch in colliding pulse experiments as the arrival time of the collider is scanned. Finally, additional simulations and engineering of the gas jet would provide an improved flatness of the density profiles currently available.

Further advances in the development of an LPA used as a collider and a reliable light source require improvements of the stabilization and efficiency of the acceleration. The enhancement of laser pulse contrast and the development of an active beam pointing system have shown dramatic increase of the accelerator performance both in electron bunch quality and shot-to-shot stability. Active laser mode control using a pair deformable mirror/wavefront sensor may provide additional control over the laser-plasma interaction and is being implemented at the LOASIS.

To compete with RF accelerators as colliders, LPAs have to demonstrate a systematic decoupling of the injection, the ability to accelerate both electrons and positrons, and the ability to stage its acceleration to produce high charge, high density, low emittance bunches with TeV-energies.

List of Publications

- *Ultra-low-emittance electron bunches from a laser-plasma accelerator measured using single-shot x-ray spectroscopy*,
  G. R. Plateau, C. G. R. Geddes, M. Chen, D. B. Thorn, S. Trotsenko, C. B. Schroeder, T. S. Kim, C. Benedetti, A. J. Gonsalves, K. Nakamura, N. H. Matlis, M. Battaglia, E. Esarey, T. Stoehlker and W. P. Leemans,
  Physical Review Letters, submitted (2011)

- *Wavefront-sensor-based electron density measurements for laser-plasma accelerators*,
  G. R. Plateau, N. H. Matlis, C. G. R. Geddes, A. J. Gonsalves, S. Shiraishi, C. Lin, R. A. van Mourik and W. P. Leemans,
  Review of Scientific Instruments, **81**(3), 033108 (2010)

- *Single-shot spatiotemporal measurements of ultrashort THz waveforms using temporal electric-field cross correlation*,
  N. H. Matlis, G. R. Plateau, J. van Tilborg and W. P. Leemans,
  Journal of the Optical Society of America B, **28**(1), 23 (2011)

- *Plasma-Density-Gradient Injection of Low Absolute-Momemtum-Spread Electron Bunches*,
  C. G. R. Geddes, K. Nakamura, G. R. Plateau, Cs. Tóth, E. Cormier-Michel, E. Esarey, C. B. Schroeder, J. R. Cary and W. P. Leemans,
  Physical Review Letters, **100**(21), 215004 (2008)

- *Single-shot measurement of the spectral envelope of broad-bandwidth terahertz pulses from femtosecond electron bunches*,
  J. van Tilborg, Cs. Tóth, N. H. Matlis, G. R. Plateau and W. P. Leemans,
  Optics Letters, **33**(11), 1186 (2008)

- *Spectroscopy of betatron radiation emitted from laser-produced wakefield accelerated electrons*,
  D. B. Thorn, C. G. R. Geddes, N. H. Matlis, G. R. Plateau, E. H. Esarey, M. Battaglia, C. B. Schroeder, S. Shiraishi, Th. Stohlker, C. Tóth and W. P. Leemans,
  Review of Scientific Instruments, **81**(10), 10E325 (2010)

- *Single-shot direct X-ray spectra of betatron emission from a laser-plasma accelerator*,
  G. R. Plateau, C. G. R. Geddes, D. B. Thorn, M. Chen, S. Trotsenko, T. S. Kim, C. B. Schroeder, C. Benedetti, A. J. Gonsalves, K. Nakamura, N. H. Matlis, J. van Tilborg, B. Shaw, D. E. Mittelberger, T. Sokollik, S. Shiraishi, C. Lin, C. Tóth, T. Stoehlker, M. Battaglia, E. Esarey and W. P. Leemans,
  Physics of Plasmas, in preparation (2011)

- *On the betatron radiation calculation of laser-plasma accelerators*,
  M. Chen, C. G. R. Geddes, G. R. Plateau, C. B. Schroeder, E. Esarey and W. P. Leemans,
  Physical Review Special Topics – Accelerators and Beams, in preparation (2011)

- *Colliding Laser Pulses for Laser-Plasma Accelerator Injection Control*,
  G. R. Plateau, C. G. R. Geddes, N. H. Matlis, E. Cormier-Michel, D. E. Mittelberger, K. Nakamura, C. B. Schroeder, E. Esarey and W. P. Leemans,
  AIP Conference Proceedings, AAC, **1299**(1), 180 (2010)

- *X-ray Emission from Electron Betatron Motion in a Laser-Plasma Accelerator*,
  G. R. Plateau, C. G. R. Geddes, D. B. Thorn, N. H. Matlis, D. E. Mittelberger, T. Stoehlker, M. Battaglia, T. S. Kim, K. Nakamura, E. Esarey and W. P. Leemans,
  AIP Conference Proceedings, AAC, **1299**(1), 139 (2010)

- *Optimization and single-shot characterization of ultrashort THz pulses from a laser plasma accelerator*,

G. R. Plateau, N. H. Matlis, J. van Tilborg, C. G. R. Geddes, C. Tóth, C. B. Schroeder and W. P. Leemans,
PAC Conference Proceedings, FR5RFP008 (2009)

- *Optimization of THz Radiation Generation from a Laser Wakefield Accelerator*,
  G. R. Plateau, N. H. Matlis, O. Albert, C. Tóth, C. G. R. Geddes, C. B. Schroeder, J. van Tilborg, E. Esarey and W. P. Leemans,
  AIP Conference Proceedings, AAC, **1086**(1), 107 (2009)

- *Experimental demonstration of ultrashort μJ-class pulses in the terahertz regime from a laser wakefield accelerator*,
  G. R. Plateau, N. H. Matlis, O. Albert, C. G. R. Geddes, J. van Tilborg, C. B. Schroeder, C. Tóth, E. Esarey and W. P. Leemans,
  EPAC Conference Proceedings, WEPP138 (2008)

- *Recent Progress at LBNL on Characterization of Laser Wakefield Accelerated Electron Bunches using Coherent Transition Radiation*,
  G. R. Plateau, J. van Tilborg, N. H. Matlis, C. Tóth, C. G. R. Geddes, C. B. Schroeder, E. Esarey and W. P. Leemans,
  PAC Conference Proceedings, THPMN114 (2007)

About the Author

Guillaume Robert Daniel Plateau was born in Le Blanc-Mesnil, France, on the 13th of August, 1980. He lived in Pierrefitte-sur-Seine en Seine-Saint-Denis up to 2001. He was accepted in Jules Ferry high-school, Paris, by choosing to learn Russian, English and ancient Greek, a combination only taught in Parisian high-schools (the beauty of the elitist and rigid French educational system). He received his "baccalauréat" (scientific major) in 1999. He attended the "classes préparatoires" at Jacques Decour high-school, Paris and was accepted in École Nationale Supérieure de Physique de Strasbourg (ENSPS) in 2002. In 2006, he obtained his engineering degree in Applied Physics from the ENSPS and his master's degree in "elementary particles and astroparticles" from the University of Strasbourg, Louis Pasteur I. During his years as a student, Guillaume participated in several student organizations and community programs: scientific journal of Jules Ferry high-school, administrative board of the ENSPS, teaching mathematics and physics to "difficult" pre-college students from Seine-Saint-Denis.

During his undergraduate studies, he participated in a two-month internship (summer 2003), developing a C++ routine modeling small (3–4) groups of galaxies, in the group of Dr. Victor Orlov at the University of Sciences in St-Petersburg, Russia; in a two-month internship (summer 2004), working on optimizing procedures and minimizing the staff exposure to ionizing radiation, in the group of Mme Lucile Bouton at the Société des Techniques en Milieu Ionisant (STMI), a branch of AREVA in Grenoble, France; and worked for a month (summer 2005), developing Matlab optimization routines, in the group of M. Guillaume Dutilleux at the Centre d'Études Techniques de l'Équipement (CETE) de l'Est in Strasbourg, France. In 2006, he participated in a 6-month internship in the group of Dr. Wim Leemans at the Lawrence Berkeley National Laboratory in Berkeley (LBNL), California, and started his Ph.D. in the LOASIS group in the fall of 2006. With Dr. Wim Leemans as local supervisor, Dr. François Amiranoff accepted to be his supervisor at the École Polytechnique in Palaiseau, France. In fall 2011, he will receive his Ph.D. degree in Physics.

Acknowledgments

More than five years just went by. During this Ph.D. I have met and connected with people I don't consider colleagues anymore but friends. I have experienced some of my most intense highs and lows, leaving me sometimes with bittersweet feelings. I found in California both professional and personal support, I have grown to become a researcher and a more balanced man. I feel very lucky and grateful for the chance I have had to work in a world-wide renown research laboratory, within one of the most personally satisfying regions. The Bay Area offers the social life of a large city while providing access to some of the most amazing landscapes on this planet: thousands of hikes through deserts, forests of giant sequoias and redwoods, the coast of the Pacific Ocean, and some of the most awe-inspiring mountains.

At the Lawrence Berkeley National Laboratory (LBNL), the good atmosphere of comradeship which prevails in the LOASIS group has always been my strongest motivating factor. And because a ship never steers itself, I want to express my deepest gratitude to Wim Leemans who gave me the opportunity and the support needed to accomplish this thesis. "People ask the difference between a leader and a boss. The leader leads, and the boss drives.", a quote from Theodore Roosevelt which summarizes what makes each one of us feel like a valued member of the LOASIS family. Thank you for your confidence in me and your guidance throughout my time in Berkeley. I want also to thank François Amiranoff at the Laboratoire pour l'Utilisation des Lasers Intenses (LULI) for being my advisor in France, for sharing his enthusiasm with me and for his indispensable support. I just wish we could have seen each other more often.

LOASIS is a wonderful eclectic group of people; whether permanent or sharing the ride for a while, every person I have worked with have been both hard working and altruistic. The work presented in this thesis is the fruit of teamwork. I want to thank the experimental team for their support, the uncountable number of hours and late night pizzas we shared together. Thank you Wim, Cameron, Nicholas, Csaba, Jeroen, Tony and Kei for your help throughout the years. Through my Ph.D. three members have

been particularly inspiring to me and I look at them as mentors: Jeroen van Tilborg who introduced me to the wonders of THz radiation, Nicholas Matlis with whom I shared philosophical, geo-political, religious, historical and sometimes physical conversations, Cameron Geddes who's experience and get-it-done approach helped me pass beyond my OCD. I want to express my gratitude to Eric, Carl, Min and Carlo for sharing their insight and knowledge of the theoretical concepts behind this thesis. During the course of my Ph.D., I have had the occasion to meet, work and enjoy the company of so many students, post-docs and guests, including Lin, Danny, Valentine, Satomi, Thomas S., Estelle, Reinier, Dmitriy, Bob, Pierre, Olivier, Kim, and Tanguy.

At LOASIS, experiments would not go forward without the excellent technical support provided by Don, Nathan, Zac, Ken, Mark, Greg, Joe and David. Thank you for all your hard and quality work, you are the backbone of the group. I want to thank Olivia, Martha and Tom for their administrative magic. If the LOASIS was a family, Olivia would be the Mom. Thank you Olivia for your help from setting up weekly meetings to organizing tea times and social events, or helping with my taxes. I hope you come to France one day so I can help you as much as you helped me these past few years.

I want to thank my friends who provided encouragement and personal support throughout my time in Berkeley. Without these people, I would have gone insane. I want to tell Aarash, Chouka, Christina, Alessandro, Bonnie, Aurélie, Poorav, and Felix, how much I appreciate having them in my life. I want to thank Peggy and George Farrell for providing housing for me, feeding me, hosting my wedding, and putting up with me taking over their dining room.

I want to thank my siblings, Ariane and Nicolas, for supporting me and not judging me for being abroad when my family needed me. I want to thank my Mom who always pushed me to move beyond my comfort zone and to look at the stars while keeping my feet on the ground. To you "mon p'tit dinosaure" I dedicate this work. I want to thank the LOASIS team and all my friends both in the U.S. and in France who supported me go through her death.

Finally, I want to thank a very special person. She made me jump out of a plane to get a hold of her, my wife, Samantha Russell-Plateau. Thank you for believing in me, you have been altogether best friend, shrink, coach, cook and spell/grammar checker. I can't wait to see what life has in store for us after this.

Bibliography

[1] G. R. Plateau, N. H. Matlis, C. G. R. Geddes, A. J. Gonsalves, S. Shiraishi, C. Lin, R. A. van Mourik, and W. P. Leemans, Review of Scientific Instruments **81**, 033108 (2010).

[2] C. G. R. Geddes, K. Nakamura, G. R. Plateau, C. Toth, E. Cormier-Michel, E. Esarey, C. B. Schroeder, J. R. Cary, and W. P. Leemans, Phys. Rev. Lett. **100**, 215004 (2008).

[3] N. H. Matlis, G. R. Plateau, J. van Tilborg, and W. P. Leemans, J. Opt. Soc. Am. B **28**, 23 (2011).

[4] J. van Tilborg, C. Tóth, N. H. Matlis, G. R. Plateau, and W. P. Leemans, Opt. Lett. **33**, 1186 (2008).

[5] G. R. Plateau, C. G. R. Geddes, M. Chen, D. B. Thorn, S. Trotsenko, C. B. Schroeder, T. S. Kim, C. Benedetti, A. J. Gonsalves, K. Nakamura, N. H. Matlis, M. Battaglia, E. Esarey, T. Stoehlker, and W. P. Leemans, Phys. Rev. Lett. (2011), Submitted.

[6] G. R. Plateau, C. G. R. Geddes, D. B. Thorn, M. Chen, S. Trotsenko, T. S. Kim, C. B. Schroeder, C. Benedetti, A. J. Gonsalves, K. Nakamura, N. H. Matlis, J. van Tilborg, B. Shaw, D. E. Mittelberger, T. Sokollik, S. Shiraishi, C. Lin, C. Tóth, T. Stoehlker, M. Battaglia, E. Esarey, and W. P. Leemans, Phys. of Plasmas (2011), In preparation.

[7] D. B. Thorn, C. G. R. Geddes, N. H. Matlis, G. R. Plateau, E. H. Esarey, M. Battaglia, C. B. Schroeder, S. Shiraishi, T. Stohlker, C. Toth, and W. P. Leemans, Review of Scientific Instruments **81**, 10E325 (2010).

[8] M. Chen, C. G. R. Geddes, G. R. Plateau, C. B. Schroeder, E. Esarey, and W. P. Leemans, Phys. Rev. ST Accel. Beams (2011), In preparation.

[9] T. Tajima and J. M. Dawson, Phys. Rev. Lett. **43**, 267 (1979).

[10] W. P. Leemans, B. Nagler, A. J. Gonsalves, Cs. Tóth, K. Nakamura, C. G. R. Geddes, E. Esarey, C. B. Schroeder, and S. M. Hooker, Nature Physics **2**, 696 (2006).

[11] E. Esarey, P. Sprangle, J. Krall, and A. Ting, IEEE Trans. Plasma Sci. **24**, 252 (1996).

[12] E. Esarey, C. B. Schroeder, and W. P. Leemans, Rev. Mod. Phys. **81**, 1229 (2009).

[13] A. Modena, Z. Najmudin, A. E. Dangor, C. E. Clayton, K. A. Marsh, C. Joshi, V. Malka, C. B. Darrow, C. Danson, D. Neely, and F. N. Walsh, Nature **377**, 606 (1995).

[14] K-C. Tzeng, W. B. Mori, and T. Katsouleas, Phys. Rev. Lett. **79**, 5258 (1997).

[15] D. Gordon, K.-C. Tzeng, C. E. Clayton, A. E. Dangor, V. Malka, K. A. Marsh, A. Modena, W. B. Mori, P. Muggli, Z. Najmudin, D. Neely, C. Danson, and C. Joshi, Phys. Rev. Lett. **80**, 2133 (1998).

[16] J. B. Rosenzweig, Phys. Rev. A **38**, 3634 (1988).

[17] F. Amiranoff, D. Bernard, B. Cros, F. Jacquet, G. Matthieussent, P. Miné, P. Mora, J. Morillo, F. Moulin, A. E. Specka, and C. Stenz, Phys. Rev. Lett. **74**, 5220 (1995).

[18] C. E. Clayton, K. A. Marsh, A. Dyson, M. Everett, A. Lal, W. P. Leemans, R. Williams, and C. Joshi, Phys. Rev. Lett. **70**, 37 (1993).

[19] S. V. Bulanov, F. Pegoraro, A. M. Pukhov, and A. S. Sakharov, Phys. Rev. Lett. **78**, 4205 (1997).

[20] D. Umstadter, J. K. Kim, and E. Dodd, Phys. Rev. Lett. **76**, 2073 (1996).

[21] E. Esarey, R. F. Hubbard, W. P. Leemans, A. Ting, and P. Sprangle, Phys. Rev. Lett. **79**, 2682 (1997).

[22] J. Faure, C. Rechatin, A. Norlin, A. Lifschitz, Y. Glinec, and V. Malka, Nature **444**, 737 (2006).

[23] T. Katsouleas and J. M. Dawson, Phys. Rev. Lett. **51**, 392 (1983).

[24] C. Joshi, W. B. Mori, T. Katsouleas, J. M. Dawson, J. M. Kindel, and D. W. Forslund, Nature **311**, 525 (1984).

[25] E. Brookner, Scientific American **252**, 94 (1985).

[26] D. Strickland and G. Mourou, Opt. Commun. **56**, 219 (1985).

[27] G. Mourou and D. Umstadter, Phys. Fluids B **4**, 2315 (1992).

[28] M. D. Perry and G. Mourou, Science **264**, 917 (1994).

[29] B. E. A. Saleh and M. C. Teich, *Fundamentals of Photonics*, Wiley Series in Pure and Applied Optics, Wiley-Interscience, Hoboken, New Jersey, second edition, 2007.

[30] C. E. Clayton, C. Joshi, C. Darrow, and D. Umstadter, Phys. Rev. Lett. **54**, 2343 (1985).

[31] H. Hamster, A. Sullivan, S. Gordon, W. White, and R. W. Falcone, Phys. Rev. Lett. **71**, 2725 (1993).

[32] K. Nakajima, D. Fisher, T. Kawakubo, H. Nakanishi, A. Ogata, Y. Kato, Y. Kitagawa, R. Kodama, K. Mima, H. Shiraga, K. Suzuki, K. Yamakawa, T. Zhang, Y. Sakawa, T. Shoji, Y. Nishida, N. Yugami, M. Downer, and T. Tajima, Phys. Rev. Lett. **74**, 4428 (1995).

[33] D. Umstadter, S.-Y. Chen, A. Maksimchuk, G. Mourou, and R. Wagner, Science **273**, 472 (1996).

[34] A. Ting, C. I. Moore, K. Krushelnick, C. Manka, E. Esarey, P. Sprangle, R. Hubbard, H. R. Burris, R. Fischer, and M. Baine, Phys. Plasmas **4**, 1889 (1997).

[35] C. Gahn, G. D. Tsakiris, A. Pukhov, J. Meyer-ter-Vehn, G. Pretzler, P. Thirolf, D. Habs, and K. J. Witte, Phys. Rev. Lett. **83**, 4772 (1999).

[36] W. P. Leemans, D. Rodgers, P. E. Catravas, C. G. R. Geddes, G. Fubiani, E. Esarey, B. A. Shadwick, R. Donahue, and A. Smith, Phys. Plasmas **8**, 2510 (2001).

[37] W. P. Leemans, P. Catravas, E. Esarey, C. G. R. Geddes, C. Toth, R. Trines, C. B. Schroeder, B. A. Shadwick, J. van Tilborg, and J. Faure, Phys. Rev. Lett. **89**, 174802 (2002).

[38] V. Malka, S. Fritzler, E. Lefebvre, M.-M. Aleonard, F. Burgy, J.-P. Chambaret, J.-F. Chemin, K. Krushelnick, G. Malka, S. P. D. Mangles, Z. Najmudin, M. Pittman, J.-P. Rousseau, J.-N. Scheurer, B. Walton, and A. E. Dangor, Science **298**, 1596 (2002).

[39] S. P. D. Mangles, C. D. Murphy, Z. Najmudin, A. G. R. Thomas, J. L. Collier, A. E. Dangor, E. J. Divall, P. S. Foster, J. G. Gallacher, C. J. Hooker, D. A. Jaroszynski, A. J. Langley, W. B. Mori, P. A. Norreys, F. S. Tsung, R. Viskup, B. R. Walton, and K. Krushelnick, Nature **431**, 535 (2004).

[40] C. G. R. Geddes, Cs. Toth, J. van Tilborg, E. Esarey, C. B. Schroeder, D. Bruhwiler, C. Nieter, J. Cary, and W. P. Leemans, Nature **431**, 538 (2004).

[41] J. Faure, Y. Glinec, A. Pukhov, S. Kiselev, S. Gordienko, E. Lefebvre, J.-P. Rousseau, F. Burgy, and V. Malka, Nature **431**, 541 (2004).

[42] J. M. Dawson, Rev. Mod. Phys, **55**, 403 (1983).

[43] R. Fonseca, L. Silva, F. Tsung, V. Decyk, W. Lu, C. Ren, W. Mori, S. Deng, S. Lee, T. Katsouleas, and J. Adam, in *Computational Science — ICCS 2002*, edited by P. Sloot, A. Hoekstra, C. Tan, and J. Dongarra, Springer Berlin / Heidelberg, 2002, volume 2331 of *Lecture Notes in Computer Science*, pp. 342–351.

[44] C. Nieter and J. R. Cary, Journal of Computational Physics **196**, 448 (2004).

[45] A. Pukhov, J. of Plasma Phys. **61**, 425 (1999).

[46] P. Sprangle, E. Esarey, and A. Ting, Phys. Rev. Lett. **64**, 2011 (1990).

[47] P. Sprangle, E. Esarey, and A. Ting, Phys. Rev. A **41**, 4463 (1990).

[48] L. M. Gorbunov and V. I. Kirsanov, Sov. Phys. JETP **66**, 290 (1987).

[49] S. V. Bulanov, V. I. Kirsanov, and A. S. Sakharov, JETP Lett. **50**, 198 (1989).

[50] A. I. Akhiezer and R. V. Polovin, Zh. Eksp. Teor. Fiz. **30**, 915 (1956).

[51] J. M. Dawson, Phys. Rev. **113**, 383 (1959).

[52] T. P. Coffey, Phys. Fluids **14**, 1402 (1971).

[53] T. Katsouleas and W. B. Mori, Phys. Rev. Lett. **61**, 90 (1988).

[54] P. Sprangle, E. Esarey, J. Krall, and G. Joyce, Phys. Rev. Lett. **69**, 2200 (1992).

[55] C. Max, J. Arons, and A. B. Langdon, Phys. Rev. Lett. **33**, 209 (1974).

[56] E. Esarey and M. Pilloff, Phys. Plasmas **2**, 1432 (1995).

[57] C. B. Schroeder, E. Esarey, and B. A. Shadwick, Phys. Rev. E **72**, 055401 (2005).

[58] C. B. Schroeder, E. Esarey, B. A. Shadwick, and W. P. Leemans, Phys. Plasmas **13**, 033103 (2006).

[59] E. Esarey, P. Sprangle, J. Krall, and A. Ting, IEEE J. Quantum Electron. **33**, 1879 (1997).

[60] P. Volfbeyn, E. Esarey, and W. P. Leemans, Phys. Plasmas **6**, 2269 (1999).

[61] D. J. Spence and S. M. Hooker, Phys. Rev. E **63**, 015401 (2000).

[62] A. Butler, D. J. Spence, and S. M. Hooker, Phys. Rev. Lett. **89**, 185003 (2002).

[63] S. Bulanov, N. Naumova, F. Pegoraro, and J. Sakai, Phys. Rev. E **58**, R5257 (1998).

[64] P. Tomassini, M. Galimberti, A. Giulietti, D. Giulietti, L. A. Gizzi, L. Labate, and F. Pegoraro, Phys. Rev. ST Accel. Beams **6**, 121301 (2003).

[65] G. Fubiani, E. Esarey, C. B. Schroeder, and W. P. Leemans, Phys. Rev. E **73**, 26402 (2006).

[66] G. Fubiani, E. Esarey, C. B. Schroeder, and W. P. Leemans, Phys. Rev. E **70**, 016402 (2004).

[67] J. Faure, C. Rechatin, A. Lifschitz, X. Davoine, E. Lefebvre, and V. Malka, IEEE Transactions on Plasma Science **36**, 1751 (2008).

[68] K. Nakamura, W. Wan, N. Ybarrolaza, D. Syversrud, J. Wallig, and W. P. Leemans, Review of Scientific Instruments **79**, 053301 (2008).

[69] J. van Tilborg, C. B. Schroeder, C. V. Filip, C. Tóth, C. G. R. Geddes, G. Fubiani, E. Esarey, and W. P. Leemans, Phys. Plasmas **13**, in press (2006).

[70] J. van Tilborg, C. B. Schroeder, C. V. Filip, Cs. Tóth, C. G. R. Geddes, G. Fubiani, R. Huber, R. A. Kaindl, E. Esarey, and W. P. Leemans, Phys. Rev. Lett. **96**, 014801 (2006).

[71] M. L. Ter-Mikaelian, *High-energy electromagnetic processes in condensed media*, Wiley, New York, 1972.

[72] D. J. Griffiths, *Introduction to Electrodynamics*, Prentice-Hall, third edition, 1999.

[73] U. Happek, A. J. Sievers, and E. B. Blum, Phys. Rev. Lett. **67**, 2962 (1991).

[74] Y. Shibata, T. Takahashi, T. Kanai, K. Ishi, M. Ikezawa, J. Ohkuma, S. Okuda, and T. Okada, Phys. Rev. E **50**, 1479 (1994).

[75] D. Mihalcea, C. L. Bohn, U. Happek, and P. Piot, Phys. Rev. ST Accel. Beams **9**, 082801 (2006).

[76] G. Fubiani, G. Dugan, W. Leemans, E. Esarey, and J. L. Bobin, AIP Conference Proceedings **647**, 203 (2002).

[77] W. P. Leemans, C. G. R. Geddes, J. Faure, Cs. Tóth, J. van Tilborg, C. B. Schroeder, E. Esarey, G. Fubiani, D. Auerbach, B. Marcelis, M. A. Carnahan, R. A. Kaindl, J. Byrd, and M. C. Martin, Phys. Rev. Lett. **91**, 074802 (2003).

[78] I. H. Hutchinson, *Principles of Plasma Diagnostics*, Cambridge University Press, 2nd edition, 2002.

[79] F. F. Chen, *Introduction to Plasma Physics and Controlled Fusion*, volume 1: Plasma Physics, Springer, second edition, 2006.

[80] C. B. Schroeder, E. Esarey, J. van Tilborg, and W. P. Leemans, Phys. Rev. E **69**, 016501 (2004).

[81] J. van Tilborg, C. B. Schroeder, E. Esarey, and W. P. Leemans, Laser Part. Beams **22**, 415 (2004).

[82] E. Esarey, B. A. Shadwick, P. Catravas, and W. P. Leemans, Phys. Rev. E **65**, 056505 (2002).

[83] K. T. Phuoc, R. Fitour, A. Tafzi, T. Garl, N. Artemiev, R. Shah, F. Albert, D. Boschetto, A. Rousse, D.-E. Kim, A. Pukhov, V. Seredov, and I. Kostyukov, Physics of Plasmas **14**, 080701 (2007).

[84] P. Catravas, E. Esarey, and W. P. Leemans, Meas. Sci. Tech. **12**, 1828 (2001).

[85] A. Rousse, K. T. Phuoc, R. Shah, A. Pukhov, E. Lefebvre, V. Malka, S. Kiselev, F. Burgy, J.-P. Rousseau, D. Umstadter, and D. Hulin, Phys. Rev. Lett. **93**, 135005 (2004).

[86] K. T. Phuoc, S. Corde, R. Shah, F. Albert, R. Fitour, J.-P. Rousseau, F. Burgy, B. Mercier, and A. Rousse, Phys. Rev. Lett. **97**, 225002 (2006).

[87] F. Albert, R. Shah, K. T. Phuoc, R. Fitour, F. Burgy, J.-P. Rousseau, A. Tafzi, D. Douillet, T. Lefrou, and A. Rousse, Phys. Rev. E **77**, 056402 (2008).

[88] P. Mora and T. M. Antonsen, Jr., Phys. Rev E **53**, R2068 (1996).

[89] A. Pukhov and J. Meyer-ter-Vehn, Appl. Phys. B **74**, 355 (2002).

[90] W. Lu, C. Huang, M. Zhou, W. B. Mori, and T. Katsouleas, Phys. Rev. Lett. **96**, 165002 (2006).

[91] W. Lu, C. Huang, M. Zhou, M. Tzoufras, F. S. Tsung, W. B. Mori, and T. Katsouleas, Physics of Plasmas **13**, 056709 (2006).

[92] W. Lu, M. Tzoufras, C. Joshi, F. S. Tsung, W. B. Mori, J. Vieira, R. A. Fonseca, and L. O. Silva, Phys. Rev. ST Accel. Beams **10**, 061301 (2007).

[93] B. Shadwick, G. Tarkenton, E. Esarey, and W. Leemans, Plasma Science, IEEE Transactions on **30**, 38 (2002).

[94] I. Kostyukov, A. Pukhov, and S. Kiselev, Physics of Plasmas **11**, 5256 (2004).

[95] C. G. Durfee III, J. Lynch, and H. M. Milchberg, Phys. Rev. E **51**, 2368 (1995).

[96] V. I. Berezhiani and I. G. Murusidze, Physica Scripta **45**, 87 (1992).

[97] E. Esarey, A. Ting, P. Sprangle, D. Umstadter, and X. Liu, IEEE Trans. Plasma Sci. **21**, 95 (1993).

[98] V. I. Berezhiani and I. G. Murusidze, Phys. Lett. A **148**, 338 (1990).

[99] F. V. Hartemann, D. J. Gibson, W. J. Brown, A. Rousse, K. T. Phuoc, V. Mallka, J. Faure, and A. Pukhov, Phys. Rev. ST Accel. Beams **10**, 011301 (2007).

[100] M. Fuchs, R. Weingartner, A. Popp, Z. Major, S. Becker, J. Osterhoff, I. Cortrie, B. Zeitler, R. Horlein, G. D. Tsakiris, U. Schramm, T. P. Rowlands-Rees, S. M. Hooker, D. Habs, F. Krausz, S. Karsch, and F. Gruner, Nat Phys **5**, 826 (2009).

[101] C. G. R. Geddes, E. Cormier-Michel, E. Esarey, C. B. Schroeder, J. Vay, W. P. Leemans, D. L. Bruhwiler, J. R. Cary, B. Cowan, M. Durant, P. Hamill, P. Messmer, P. Mullowney, C. Nieter, K. Paul, S. Shasharina, S. Veitzer, G. Weber, O. Rubel, D. Ushizima, Prabhat, W. Bethel, and J. Wu, SciDAC Review **13** (2009).

[102] C. G. R. Geddes, D. Bruhwiler, J. R. Cary, E. Cormier-Michel, E. Esarey, C. B. Schroeder, W. A. Isaacs, N. Stinus, P. Messmer, A. Hakim, K. Nakamura, A. J. Gonsalves, D. Panasenko, G. R. Plateau, C. Tóth, B. Nagler, J. van Tilborg, T. Cowan, S. M. Hooker, and W. P. Leemans, Journal of Physics: Conference Series **78**, 012021 (2007).

[103] F. S. Tsung, R. Narang, W. B. Mori, C. Joshi, R. A. Fonseca, and L. O. Silva, Phys. Rev. Lett. **93**, 185002 (2004).

[104] G. Z. Sun, E. Ott, Y. C. Lee, and P. Guzdar, Phys. Fluids **30**, 526 (1987).

[105] P. Sprangle, C. M. Tang, and E. Esarey, IEEE Trans. Plasma Sci. **PS-15**, 145 (1987).

[106] I. Blumenfeld, C. E. Clayton, F.-J. Decker, M. J. Hogan, C. Huang, R. Ischebeck, R. Iverson, C. Joshi, T. Katsouleas, N. Kirby, W. Lu, K. A. Marsh, W. B. Mori, P. Muggli, E. Oz, R. H. Siemann, D. Walz, and M. Zhou, Nature **445**, 741 (2007).

[107] T. Katsouleas, S. Wilks, P. Chen, J. M. Dawson, and J. J. Su, Part. Accel. **22**, 81 (1987).

[108] W. Lu, C. Huang, M. M. Zhou, W. B. Mori, and T. Katsouleas, Physics of Plasmas **12**, 063101 (2005).

[109] S. V. Bulanov, I. N. Inovenkov, V. I. Kirsanov, N. M. Naumova, and A. S. Sakharov, Phys. Fluids B **4**, 1935 (1992).

[110] R. W. Boyd, *Nonlinear Optics*, Academic Press, second edition, 2003.

[111] W. P. Leemans, E. Esarey, J. van Tilborg, P. A. Michel, C. B. Schroeder, C. Tóth, C. G. R. Geddes, and B. A. Shadwick, IEEE Trans. Plasma Sci. **33**, 8 (2005).

[112] V. L. Ginzburg and I. M. Frank, Zh. Eksp. Teor. Fiz. **16**, 15 (1946).

[113] J. V. Lepore and R. J. Riddell, Jr., Phys. Rev. D **13**, 2300 (1976).

[114] K. T. Phuoc, F. Burgy, J.-P. Rousseau, V. Malka, A. Rousse, R. Shah, D. Umstadter, A. Pukhov, and S. Kiselev, Physics of Plasmas **12**, 023101 (2005).

[115] B. M. Welsh, B. L. Ellerbroek, M. C. Roggemann, and T. L. Pennington, Appl. Opt. **34**, 4186 (1995).

[116] K. L. Baker, J. Brase, M. Kartz, S. S. Olivier, B. Sawvel, and J. Tucker, Review of Scientific Instruments **73**, 3784 (2002).

[117] T. Fukuchi, Y. Yamaguchi, T. Nayuki, K. Nemoto, and K. Uchino, Electrical Engineering in Japan **146**, 10 (2004).

[118] N. Qi, R. R. Prasad, K. Campbell, P. Coleman, M. Krishnan, B. V. Weber, S. J. Stephanakis, and D. Mosher, Review of Scientific Instruments **75**, 3442 (2004).

[119] N. E. Andreev, L. M. Gorbunov, V. I. Kirsanov, A. A. Pogosova, and R. R. Ramazashvili, Pis'ma Zh. Eksp. Teor. Fiz. **55**, 551 (1992).

[120] E. Esarey, J. Krall, and P. Sprangle, Phys. Rev. Lett. **72**, 2887 (1994).

[121] F. Martin, Appl. Opt. **19**, 4230 (1980).

[122] J. Primot and N. Guérineau, Appl. Opt. **39**, 5715 (2000).

[123] M. Takeda, H. Ina, and S. Kobayashi, J. Opt. Soc. Am. **72**, 156 (1982).

[124] W. W. Macy, Appl. Opt. **22**, 3898 (1983).

[125] P. Gao, B. Yao, J. Han, L. Chen, Y. Wang, and M. Lei, Appl. Opt. **47**, 2760 (2008).

[126] M. Kalal and K. A. Nugent, Appl. Opt. **27**, 1956 (1988).

[127] C. B. Schroeder, W. M. Fawley, F. Gruner, M. Bakeman, K. Nakamura, K. E. Robinson, C. Toth, E. Esarey, and W. P. Leemans, AIP Conference Proceedings **1086**, 637 (2009).

[128] R. W. Schoenlein, W. P. Leemans, A. H. Chin, P. Volfbeyn, T. E. Glover, P. Balling, M. Zolotorev, K. J. Kim, S. Chattopadhyay, and C. V. Shank, Science **274**, 236 (1996).

[129] K. Nakamura, G. Fubiani, C. G. R. Geddes, P. Michel, J. van Tilborg, C. Toth, E. Esarey, C. B. Schroeder, and W. P. Leemans, AIP Conference Proceedings **737**, 901 (2004).

[130] E. Cormier-Michel, V. H. Ranjbar, D. L. Bruhwiler, M. Chen, C. G. R. Geddes, E. Esarey, C. B. Schroeder, and W. P. Leemans, AIP Conference Proceedings **1299**, 215 (2010).

[131] C. B. Schroeder, P. B. Lee, J. S. Wurtele, E. Esarey, and W. P. Leemans, Phys. Rev. E **59**, 6037 (1999).

[132] E. Esarey, C. B. Schroeder, W. P. Leemans, and B. Hafizi, Phys. Plasmas **6**, 2262 (1999).

[133] G. R. Plateau, C. G. R. Geddes, N. H. Matlis, E. Cormier-Michel, D. E. Mittelberger, K. Nakamura, C. B. Schroeder, E. Esarey, and W. P. Leemans, AIP Conference Proceedings **1299**, 180 (2010).

[134] C. Rechatin, J. Faure, A. Ben-Ismail, J. Lim, R. Fitour, A. Specka, H. Videau, A. Tafzi, F. Burgy, and V. Malka, Phys. Rev. Lett. **102**, 164801 (2009).

[135] H. Kotaki, I. Daito, M. Kando, Y. Hayashi, K. Kawase, T. Kameshima, Y. Fukuda, T. Homma, J. Ma, L.-M. Chen, T. Z. Esirkepov, A. S. Pirozhkov, J. K. Koga, A. Faenov, T. Pikuz, H. Kiriyama, H. Okada, T. Shimomura, Y. Nakai, M. Tanoue, H. Sasao, D. Wakai, H. Matsuura, S. Kondo, S. Kanazawa, A. Sagiyama, H. Daidoa, and S. V. Bulanov, Phys. Rev. Lett. **103**, 194803 (2009).

[136] K. B. Unser, PAC Conference Proceedings **1**, 71 (1989).

[137] K. Nakamura, A. J. Gonsalves, C. Lin, A. Smith, D. Rodgers, R. Donahue, W. Byrne, and W. P. Leemans, Phys. Rev. ST Accel. Beams (2011), Submitted.

[138] Y. Glinec, J. Faure, A. Guemnie-Tafo, V. Malka, H. Monard, J. P. Larbre, V. D. Waele, J. L. Marignier, and M. Mostafavi, Review of Scientific Instruments **77**, 103301 (2006).

[139] S. Masuda, E. Miura, K. Koyama, and S. Kato, Review of Scientific Instruments **79**, 083301 (2008).

[140] A. Jullien, O. Albert, F. Burgy, J.-P. Rousseau, J.-P. Chambaret, F. Augé-Rochereau, G. Chériaux, J. Etchepare, N. Minkovski, and S. M. Saltiel, Opt. Lett. **30**, 920 (2005).

[141] W. P. Leemans, J. van Tilborg, J. Faure, C. G. R. Geddes, Cs. Tóth, C. B. Schroeder, E. Esarey, G. Fubiani, and G. Dugan, Phys. Plasmas **11**, 2899 (2004).

[142] J. van Tilborg, *Coherent terahertz radiation from laser-wakefield-accelerated electrons beams*, PhD thesis, Technische Universiteit Eindhoven, 2006.

[143] J. van Tilborg, C. B. Schroeder, Cs. Tóth, C. G. R. Geddes, E. Esarey, and W. P. Leemans, Opt. Lett. **32**, 313 (2007).

[144] J. A. Fülöp, L. Pálfalvi, G. Almási, and J. Hebling, Opt. Express **18**, 12311 (2010).

[145] J. Faure, J. van Tilborg, R. A. Kaindl, and W. P. Leemans, Opt. Quantum Electron. **36**, 681 (2004).

[146] G. R. Plateau, J. van Tilborg, N. H. Matlis, C. Tóth, C. G. R. Geddes, C. B. Schroeder, E. Esarey, and W. P. Leemans, PAC Conference Proceedings (2007).

[147] G. R. Plateau, N. H. Matlis, O. Albert, C. G. R. Geddes, J. van Tilborg, C. B. Schroeder, C. Tóth, E. Esarey, and W. P. Leemans, EPAC Conference Proceedings (2008).

[148] G. R. Plateau, N. H. Matlis, O. Albert, C. Toth, C. G. R. Geddes, C. B. Schroeder, J. van Tilborg, E. Esarey, and W. P. Leemans, AIP Conference Proceedings **1086**, 707 (2009).

[149] P. L. Richards, J. Appl. Phys. **76**, 1 (1994).

[150] E. Chiadroni, H. Delsim-Hashemi, L. Fröhlich, and O. Grimm, Report on the visit at FELIX, Technical report, FOM Rijnhuizen, 2005.

[151] C. G. Durfee III and H. M. Milchberg, Phys. Rev. Lett. **71**, 2409 (1993).

[152] P. Volfbeyn, P. B. Lee, J. Wurtele, W. P. Leemans, and G. Shvets, Phys. Plasmas **4**, 3403 (1997).

[153] C. G. R. Geddes, Cs. Tóth, J. van Tilborg, E. Esarey, C. B. Schroeder, D. Bruhwiler, C. Nieter, J. Cary, and W. P. Leemans, Phys. Plasmas **12**, 056709 (2005).

[154] C. G. R. Geddes, Cs. Tóth, J. van Tilborg, E. Esarey, C. B. Schroeder, J. Cary, and W. P. Leemans, Phys. Rev. Lett. **95**, 145002 (2005).

[155] W. P. Leemans, C. E. Clayton, W. B. Mori, K. A. Marsh, A. Dyson, and C. Joshi, Phys. Rev. Lett. **68**, 321 (1992).

[156] V. Chvykov, P. Rousseau, S. Reed, G. Kalinchenko, and V. Yanovsky, Opt. Lett. **31**, 1456 (2006).

[157] Cs. Tóth, J. Faure, J. van Tilborg, C. G. R. Geddes, C. B. Schroeder, E. Esarey, and W. P. Leemans, Opt. Lett. **28**, 1823 (2003).

[158] C. G. R. Geddes, E. Cormier-Michel, E. Esarey, K. Nakamura, G. R. Plateau, C. B. Schroeder, C. Toth, D. L. Bruhwiler, J. R. Cary, and W. P. Leemans, AIP Conference Proceedings **1086**, 12 (2009).

[159] H. Suk, N. Barov, J. B. Rosenzweig, and E. Esarey, Phys. Rev. Lett. **86**, 1011 (2001).

[160] R. G. Hemker, N. M. Hafz, and M. Uesaka, Phys. Rev. ST Accel. Beams **5**, 041301 (2002).

[161] A. J. Gonsalves, E. Esarey, C. G. R. Geddes, W. P. Leemans, C. Lin, K. Nakamura, D. Panasenko, C. B. Schroeder, and C. Tóth, PAC Conference Proceedings **TH4GBC03** (2009).

[162] C. G. R. Geddes, K. Nakamura, G. R. Plateau, C. Tóth, D. Panasenko, E. Michel, E. Esarey, C. B. Schroeder, W. P. Leemans, D. Bruhwiler, and J. Cary, PAC Conference Proceedings **WEOBK101** (2007).

[163] J. A. Valdmanis, G. Mourou, and C. W. Gabel, Appl. Phys. Lett. **41**, 211 (1982).

[164] G. Gallot and D. Grischkowsky, J. Opt. Soc. Am. B **16**, 1204 (1999).

[165] S. P. Jamison, A. M. MacLeod, G. Berden, D. A. Jaroszynski, and W. A. Gillespie, Opt. Lett. **31**, 1753 (2006).

[166] B. Yellampalle, K.-Y. Kim, J. H. Glownia, and A. J. Taylor, Opt. Lett. **32**, 1341 (2007).

[167] S. P. Jamison, A. M. MacLeod, G. Berden, D. A. Jaroszynski, and W. A. Gillespie, Opt. Lett. **32**, 1343 (2007).

[168] D. Côté, J. E. Sipe, and H. M. van Driel, J. Opt. Soc. Am. B **20**, 1374 (2003).

[169] D. T. F. Marple, Journal of Applied Physics **35**, 539 (1964).

[170] G. Gallot, Jiangquan Zhang, R. W. McGowan, T.-I. Jeon, and D. Grischkowsky, Appl. Phys. Lett. **74**, 3450 (1999).

[171] G. R. Plateau, N. H. Matlis, J. van Tilborg, C. G. R. Geddes, C. Tóth, C. B. Schroeder, and W. P. Leemans, PAC Conference Proceedings (2009).

[172] N. H. Matlis, G. R. Plateau, J. van Tilborg, C. G. R. Geddes, C. Toth, C. B. Schroeder, E. Esarey, and W. P. Leemans, AIP Conference Proceedings **1086**, 713 (2009).

[173] J. F. Nye, *Physical properties of crystals and their representation by tensors*, Oxford University Press, 1957.

[174] A. S. Barker, Jr., Phys. Rev. **165**, 917 (1968).

[175] A. Yariv, *Quantum Electronics*, Wiley, New York, 1988.

[176] R. A. Kaindl, R. Huber, B. A. Schmid, M. A. Carnahan, D. Hägele, and D. S. Chemla, physica status solidi (b) **243**, 2414 (2006).

[177] M. C. Beard, G. M. Turner, and C. A. Schmuttenmaer, Phys. Rev. B **62**, 15764 (2000).

[178] M. C. Hoffmann, J. Hebling, H. Y. Hwang, K.-L. Yeh, and K. A. Nelson, J. Opt. Soc. Am. B **26**, A29 (2009).

[179] Zhiping Jiang and X.-C. Zhang, Appl. Phys. Lett. **72**, 1945 (1998).

[180] F. G. Sun, Zhiping Jiang, and X.-C. Zhang, Appl. Phys. Lett. **73**, 2233 (1998).

[181] B. Yellampalle, K. Y. Kim, G. Rodriguez, J. H. Glownia, and A. J. Taylor, Appl. Phys. Lett. **87**, 211109 (2005).

[182] K. Y. Kim, B. Yellampalle, A. J. Taylor, G. Rodriguez, and J. H. Glownia, Opt. Lett. **32**, 1968 (2007).

[183] S. P. Jamison, Jingling Shen, A. M. MacLeod, W. A. Gillespie, and D. A. Jaroszynski, Opt. Lett. **28**, 1710 (2003).

[184] J. van Tilborg, N. H. Matlis, G. R. Plateau, and W. P. Leemans, AIP Conference Proceedings **1299**, 565 (2010).

[185] J. Fletcher, Opt. Express **10**, 1425 (2002).

[186] X.-Y. Peng, O. Willi, M. Chen, and A. Pukhov, Opt. Express **16**, 12342 (2008).

[187] S. P. L. Blanc, E. W. Gaul, N. H. Matlis, A. Rundquist, and M. C. Downer, Opt. Lett. **25**, 764 (2000).

[188] N. H. Matlis, S. Reed, S. S. Bulanov, V. Chvykov, G. Kalintchenko, T. Matsuoka, P. Rousseau, V. Yanovsky, A. Maksimchuk, S. Kalmykov, G. Shvets, and M. C. Downer, Nat Phys **2**, 749 (2006).

[189] K. Y. Kim, I. Alexeev, and H. M. Milchberg, Applied Physics Letters **81**, 4124 (2002).

[190] D. You and P. H. Bucksbaum, J. Opt. Soc. Am. B **14**, 1651 (1997).

[191] S. Feng, H. G. Winful, and R. W. Hellwarth, Opt. Lett. **23**, 385 (1998).

[192] Zhiping Jiang and X.-C. Zhang, Opt. Express **5**, 243 (1999).

[193] S. Kneip, C. McGuffey, J. L. Martins, S. F. Martins, C. Bellei, V. Chvykov, F. Dollar, R. Fonseca, C. Huntington, G. Kalintchenko, A. Maksimchuk, S. P. D. Mangles, T. Matsuoka, S. R. Nagel, C. A. J. Palmer, J. Schreiber, K. T. Phuoc, A. G. R. Thomas, V. Yanovsky, L. O. Silva, K. Krushelnick, and Z. Najmudin, Nat Phys **6**, 980 (2010).

[194] R. C. Shah, F. Albert, K. Ta Phuoc, O. Shevchenko, D. Boschetto, A. Pukhov, S. Kiselev, F. Burgy, J.-P. Rousseau, and A. Rousse, Phys. Rev. E **74**, 045401 (2006).

[195] S. Fritzler, E. Lefebvre, V. Malka, F. Burgy, A. E. Dangor, K. Krushelnick, S. P. D. Mangles, Z. Najmudin, J.-P. Rousseau, and B. Walton, Phys. Rev. Lett. **92**, 165006 (2004).

[196] C. M. S. Sears, A. Buck, K. Schmid, J. Mikhailova, F. Krausz, and L. Veisz, Phys. Rev. ST Accel. Beams **13**, 092803 (2010).

[197] E. Brunetti, R. P. Shanks, G. G. Manahan, M. R. Islam, B. Ersfeld, M. P. Anania, S. Cipiccia, R. C. Issac, G. Raj, G. Vieux, G. H. Welsh, S. M. Wiggins, and D. A. Jaroszynski, Phys. Rev. Lett. **105**, 215007 (2010).

[198] C. G. R. Geddes, D. L. Bruhwiler, J. R. Cary, E. H. Esarey, A. J. Gonsalves, C. Lin, E. Cormier-Michel, N. H. Matlis, K. Nakamura, M. Bakeman, D. Panasenko, G. R. Plateau, C. B. Schroeder, C. Toth, and W. P. Leemans, AIP Conference Proceedings **1099**, 666 (2009).

[199] W. Leemans and E. Esarey, Physics Today **62**, 44 (2009).

[200] A. G. R. Thomas, Physics of Plasmas **17**, 056708 (2010).

[201] C. G. R. Geddes, D. L. Bruhwiler, J. R. Cary, W. B. Mori, J. Vay, S. F. Martins, T. Katsouleas, E. Cormier-Michel, W. M. Fawley, C. Huang, X. Wang, B. Cowan, V. K. Decyk, E. Esarey, R. A. Fonseca, W. Lu, P. Messmer, P. Mullowney, K. Nakamura, K. Paul, G. R. Plateau, C. B. Schroeder, L. O. Silva, C. Toth, F. S. Tsung, M. Tzoufras, T. Antonsen, J. Vieira, and W. P. Leemans, Journal of Physics: Conference Series **125**, 012002 (2008).

[202] A. G. R. Thomas, Phys. Rev. ST Accel. Beams **13**, 020702 (2010).

[203] J. D. Jackson, *Classical Electrodynamics*, John Wiley & Sons, Inc., 605 Third Avenue, New-York, third edition, 1998.

[204] B. H. P. Broks, K. Garloff, and J. J. A. M. van der Mullen, Phys. Rev. E **71**, 016401 (2005).

[205] A. J. Gonsalves, T. P. Rowlands-Rees, B. H. P. Broks, J. J. A. M. van der Mullen, and S. M. Hooker, Phys. Rev. Lett. **98**, 025002 (2007).

[206] K. Nakamura, B. Nagler, C. Toth, C. G. R. Geddes, C. B. Schroeder, E. Esarey, W. P. Leemans, A. J. Gonsalves, and S. M. Hooker, Physics of Plasmas **14**, 056708 (2007).

[207] W. Fullagar, J. Uhlig, M. Walczak, S. Canton, and V. Sundstrom, Review of Scientific Instruments **79**, 103302 (2008).

[208] C. Fourment, N. Arazam, C. Bonte, T. Caillaud, D. Descamps, F. Dorchies, M. Harmand, S. Hulin, S. Petit, and J. J. Santos, Review of Scientific Instruments **80**, 083505 (2009).

[209] B. L. Henke, E. M. Gullikson, and J. C. Davis, Atomic Data and Nuclear Data Tables **54**, 181 (1993).

[210] S. Kneip, S. R. Nagel, C. Bellei, N. Bourgeois, A. E. Dangor, A. Gopal, R. Heathcote, S. P. D. Mangles, J. R. Marquès, A. Maksimchuk, P. M. Nilson, K. T. Phuoc, S. Reed, M. Tzoufras, F. S. Tsung, L. Willingale, W. B. Mori, A. Rousse, K. Krushelnick, and Z. Najmudin, Phys. Rev. Lett. **100**, 105006 (2008).

[211] C. G. R. Geddes, *Plasma Channel Guided Laser Wakefield Accelerator*, PhD thesis, University of California, Berkeley, 2005.

[212] S. Holland, D. Groom, N. Palaio, R. Stover, and M. Wei, Electron Devices, IEEE Transactions on **50**, 225 (2003).

[213] I. Jung, A. G. III, H. Krawczynski, A. Burger, M. Groza, J. Matteson, and R. T. Skelton, Test of thick pixelated orbotech detectors with and without steering grids, in *Hard X-Ray and Gamma-Ray Detector Physics and Penetrating Radiation Systems VIII*, edited by L. A. Franks, A. Burger, R. B. James, H. B. Barber, F. P. Doty, and H. Roehrig, volume 6319, p. 631910, SPIE, 2006.

[214] G. Fubiani, J. Qiang, E. Esarey, W. P. Leemans, and G. Dugan, Phys. Rev. ST Accel. Beams **9**, 064402 (2006).

[215] E. Esarey, P. Sprangle, J. Krall, A. Ting, and G. Joyce, Phys. Fluids B **5**, 2690 (1993).

[216] J. Krall, A. Ting, E. Esarey, and P. Sprangle, Phys. Rev. E **48**, 2157 (1993).

[217] J. Krall, E. Esarey, P. Sprangle, and G. Joyce, Phys. Plasmas **1**, 1738 (1994).

[218] R. Cubalchini, J. Opt. Soc. Am. **69**, 972 (1979).

[219] J. Y. Wang and D. E. Silva, Appl. Opt. **19**, 1510 (1980).

[220] D. L. Fried, J. Opt. Soc. Am. **67**, 370 (1977).

[221] L. Zhu, P.-C. Sun, D.-U. Bartsch, W. R. Freeman, and Y. Fainman, Appl. Opt. **38**, 6019 (1999).

Appendix A

LPA theory

In this Appendix, we present the calculation details of the cold fluid theory of the laser-plasma accelerator presented in Chapter 2. We first present a brief calculation of the minimum intensities necessary to fully ionize both Hydrogen and Helium gases. Using a Lagrangian description of a plasma wave, the cold non-relativistic wavebreaking electric field is calculated. The general equations of the Eulerian fluid model of the laser-plasma interaction [12] are derived and solutions in one dimension and under the quasi-static approximation (QSA) are presented. Laser propagation and plasma equations are then rewritten to include the transverse dimension of the laser pulse.

Ionization: Assuming the electric field of the laser is strong enough to fully ionize the plasma, the ionization threshold of a gas can be calculated by expressing the electric potential of a bounded electron:

$$V(r) = \underbrace{-\frac{Ze^2}{4\pi\epsilon_0|r|}}_{\text{atom}} - \underbrace{eEr}_{\text{laser}} \tag{A.1}$$

which is maximum for $dV(r)/dr = 0$, *i.e.*, $r_{\max} = \sqrt{Ze/4\pi\epsilon_0 E}$, where e is the charge of the electron, ϵ_0 is the permittivity of vacuum and Z is the atomic number. The laser electric field E diminishes the electric potential barrier that confines the electron. When the potential is dropped below the ionization energy of the electron, *i.e.*, $V(r_{\max}) < -E_i$, the bond is broken and the electron is free. Thus, the minimum laser field to ionize the

atom is given by:

$$V(r_{\max}) = -\frac{Ze^2}{4\pi\epsilon_0}\sqrt{\frac{Ze}{4\pi\epsilon_0 E}} - eE\sqrt{\frac{Ze}{4\pi\epsilon_0 E}} < -E_i \tag{A.2}$$

$$\Leftrightarrow E > \pi\epsilon_0 \frac{E_i^2}{Ze^3} \tag{A.3}$$

The average power per unit area carried by an electromagnetic wave is given by [72] $I = c\epsilon_0 E^2/2$. Hence, the laser intensity necessary to fully ionize a gas is given by:

$$I_{\min} = \frac{\pi^2 c\epsilon_0^3}{2e^6}\frac{E_i^4}{Z^2} \tag{A.4}$$

$$I_{\min}\,[\mathrm{W/cm^2}] \simeq 4\times 10^9 \frac{E_i^4\,[\mathrm{eV}]}{Z^2} \tag{A.5}$$

Table A.1 gives the ionization levels for Hydrogen (H^+) and Helium (He^{2+}):

	1+	2+
H	1.4×10^{14}	–
He	1.4×10^{15}	8.8×10^{15}

Table A.1: Ionization thresholds ([W/cm^2]) for Hydrogen and Helium based on Eq. (A.5).

Non-relativistic cold wavebreaking field: Using a one-dimensional Lagrangian description of the fluid, *i.e.*, following a particle, the non-relativistic cold wavebreaking electric field can be found [51]. At a given time the position of two sample particles is given by:

$$\begin{cases} z_1(t) = z_{0,1} + Z_1(z_{0,1}, t) \\ z_2(t) = z_{0,2} + Z_2(z_{0,2}, t) \end{cases} \tag{A.6}$$

where $z_{0,i}$ is the initial longitudinal position and Z_i is the separation. Wavebreaking occurs when the ordering of the particles is changed [51], which means that if at $t = 0, z_{0,1} < z_{0,2}, \exists t, z_1(t) < z_2(t)$. The non-wavebreaking condition is then given by $\forall t, z_2(t) - z_1(t) > 0 \Leftrightarrow Z_2 - Z_1 > -(z_{0,2} - z_{0,1}) \Leftrightarrow \partial Z/\partial z_0 > -1$.

The equation of motion provides a solution for $Z_i(z_{0,i}, t)$. The electric field is given by

solving the Gauss-Maxwell equation (ρ is the charge density and n the electron density):

$$\nabla \cdot \boldsymbol{E} = \rho/\epsilon_0 \tag{A.7}$$

$$\partial E/\partial z_i = \partial E/\partial Z_i = en/\epsilon_0 \tag{A.8}$$

$$E = \frac{en}{\epsilon_0} Z_i \tag{A.9}$$

and for an electron Newton's equation is given by:

$$m\frac{d^2 Z_i}{dt^2} = -eE \tag{A.10}$$

where m is the mass of the electron. Substituting Eq. (A.9) and Eq. (2.1) into Eq. (A.10) provides the following ODE:

$$\frac{d^2 Z_i}{dt^2} + \omega_p^2 Z_i = 0 \tag{A.11}$$

which solutions can be written $Z_i(z_{0,i}, t) = (A/k_p)\sin(k_p z_{0,i} - \omega_p t)$. The non-wavebreaking condition implies $|A| < 1$. Finally, the electric field is given by substituting this expression of $Z_i(z_{0,i}, t)$ into Eq. (A.9): $E(z_{0,i}, t) = A(en/\epsilon_0 k_p)\sin(k_p z_{0,i} - \omega_p t)$. At wavebreaking, $A = 1$ and:

$$E_{\max} \equiv E_0 = \frac{en}{\epsilon_0 k_p} = \frac{mc}{e}\omega_p = c\sqrt{\frac{mn}{\epsilon_0}} \tag{A.12}$$

Note that at a given time, t, the wave can be described by the following parametric equation (the subscript i is dropped):

$$\begin{cases} z(z_0, t) = z_0 + (A/k_p)\sin(k_p z_0 - \omega_p t) \\ E(z_0, t)) = AE_0 \sin(k_p z_0 - \omega_p t) \end{cases} \tag{A.13}$$

Cold fluid plasma equations: Maxwell's equations [72] are given by:

$$\nabla \cdot \mathbf{E} = q/\epsilon_0 \tag{A.14a}$$

$$\nabla \cdot \mathbf{B} = 0 \tag{A.14b}$$

$$\nabla \times \mathbf{E} = -\partial \mathbf{B}/\partial t \tag{A.14c}$$

$$\nabla \times \mathbf{B} = \mu_0 \mathbf{j} + \mu_0 \epsilon_0 \, \partial \mathbf{E}/\partial t \tag{A.14d}$$

where μ_0 is the permeability of vacuum ($\mu_o \epsilon_0 c^2 = 1$), $q = -e(n - n_0)$ is the volume charge density, with n_0 the initial electron density, and $\mathbf{j} = -en\mathbf{v}$ is the volume current

density. To simplify the problem we introduce the potentials $\mathbf{A}$ and V:

$$\begin{cases} \mathbf{B} = \nabla \times \mathbf{A} \\ \mathbf{E} = -\nabla V - \partial \mathbf{A}/\partial t \end{cases} \tag{A.15}$$

and we consider the Coulomb gauge ($\nabla \cdot \mathbf{A} = 0$) as to simplify the calculation of the scalar potential V which represents the low frequency ($\omega_p \ll \omega$) plasma density perturbation. In the Coulomb gauge, substituting Eq. (A.15) into Eq. (A.14a) yields Poisson's equation (potential equation):

$$\nabla^2 V = \frac{e}{\epsilon_0}(n - n_0) \tag{A.16}$$

Using the definition of the current crossing a surface $\mathcal{S}$ with normal vector $\mathbf{a}$ [72], $I = \int_{\mathcal{S}} \mathbf{j} \cdot d\mathbf{a}$, the total charge leaving a volume per unit of time is found to be $\oint_{\mathcal{S}} \mathbf{j} \cdot d\mathbf{a} = \int_{\mathcal{V}} (\nabla \cdot \mathbf{j}) d\tau = -d/dt \int_{\mathcal{V}} -end\tau = e \int_{\mathcal{V}} \partial n/\partial t d\tau$ which, since it is true $\forall\, \mathcal{V}$, yields $\nabla \cdot \mathbf{j} = e\partial n/\partial t$. Thus, the continuity equation (conservation of charge) is given by:

$$\nabla \cdot n\mathbf{v} = -\partial n/\partial t \tag{A.17}$$

The wave equation is obtained by substituting Eq. (A.15) into Eq. (A.14d):

$$\left(\nabla^2 - \frac{1}{c^2}\frac{\partial^2}{\partial t^2}\right)\mathbf{A} = \frac{en}{\epsilon_0 c^2}\mathbf{v} + \frac{1}{c^2}\frac{\partial}{\partial t}\nabla V \tag{A.18}$$

Starting from the Eulerian fluid equation [79] given by:

$$\left(\frac{\partial}{\partial t} + \mathbf{v} \cdot \nabla\right)\mathbf{p} = -e(\mathbf{E} + \mathbf{v} \times \mathbf{B}) \tag{A.19}$$

the momentum equation is obtained, after some algebra, by substituting Eq. (A.15) into Eq. (A.19). The product rule $\nabla(\mathbf{A}\cdot\mathbf{B}) = \mathbf{A}\times(\nabla\times\mathbf{B}) + \mathbf{B}\times(\nabla\times\mathbf{A}) + (\mathbf{A}\cdot\nabla)\mathbf{B} + (\mathbf{B}\cdot\nabla)\mathbf{A}$ yields $\nabla p^2 = 2[\mathbf{p}\times(\nabla\times\mathbf{p}) + (\mathbf{p}\cdot\nabla)\mathbf{p}] = 2\gamma m[\mathbf{v}\times(\nabla\times\mathbf{p}) + (\mathbf{v}\cdot\nabla)\mathbf{p}]$ where γ is the electron Lorentz factor. Also, $\mathbf{p} = \gamma m\mathbf{v}$ implies $\gamma = \sqrt{1 + p^2/m^2c^2}$ which provides the equation: $\nabla\gamma = (1/2\gamma m^2 c^2)\nabla p^2$. Thus, $(\mathbf{v}\cdot\nabla)\mathbf{p} = (1/2\gamma m)\nabla p^2 - \mathbf{v}\times(\nabla\times\mathbf{p}) = mc^2\nabla\gamma - \mathbf{v}\times(\nabla\times\mathbf{p})$

and:

$$(\partial/\partial t + \mathbf{v}\cdot\nabla)\mathbf{p} = e\left[\nabla V + \partial\mathbf{A}/\partial t - \mathbf{v}\times(\nabla\times\mathbf{A})\right] \tag{A.20}$$

$$\frac{\partial}{\partial t}(\mathbf{p} - e\mathbf{A}) + mc^2\nabla\gamma - \mathbf{v}\times(\nabla\times\mathbf{p}) = e\nabla V - \mathbf{v}\times(\nabla\times\mathbf{A}) \tag{A.21}$$

$$\frac{\partial}{\partial t}(\mathbf{p} - e\mathbf{A}) + \nabla(\gamma mc^2 - eV) = \mathbf{v}\times[\nabla\times(\mathbf{p} - e\mathbf{A})] \tag{A.22}$$

Calculating the curl of Eq. (A.22):

$$\frac{\partial}{\partial t}\nabla\times(\mathbf{p} - e\mathbf{A}) = \nabla\times\mathbf{v}\times[\nabla\times(\mathbf{p} - e\mathbf{A})] \tag{A.23}$$

shows that $\nabla\times(\mathbf{p} - e\mathbf{A})$ is stationary so that $\nabla\times(\mathbf{p} - e\mathbf{A}) = \nabla\times(\mathbf{p} - e\mathbf{A})|_{t=0} = 0$ since at $t = 0$ the laser is absent and there is no perturbation. Therefore, Eq. (A.22) can be written as follows:

$$\frac{\partial\mathbf{p}}{\partial t} = \nabla(eV - \gamma mc^2) + e\frac{\partial\mathbf{A}}{\partial t} \tag{A.24}$$

where $\mathbf{F}_p = -mc^2\nabla\gamma$ is the laser ponderomotive force.

Finally, introducing $u = \gamma\beta$, $k_p = \omega_p/c$, the normalized vector potential $\mathbf{a} = e\mathbf{A}/mc$, and the normalized scalar potential $\phi = eV/mc^2$, the general set of equations describing the laser-plasma interaction for a cold fluid plasma is found to be:

$$\nabla^2\phi = k_p^2\,(n/n_0 - 1) \tag{A.25a}$$

$$\nabla\cdot(n\mathbf{u}/\gamma) = -\partial n/\partial t \tag{A.25b}$$

$$\left(\nabla^2 - \frac{1}{c^2}\frac{\partial^2}{\partial t^2}\right)\mathbf{a} = k_p^2\frac{n\mathbf{u}}{\gamma n_0} + \frac{1}{c}\frac{\partial}{\partial t}\nabla\phi \tag{A.25c}$$

$$\partial\mathbf{u}/\partial t = c\nabla(\phi - \gamma) + \partial\mathbf{a}/\partial t \tag{A.25d}$$

One-dimensional plasma wake: Considering $\mathbf{z}$ the normalized vector of the propagation axis, $\nabla = \partial/\partial z\,\mathbf{z}$ and the Coulomb gauge can be written $\nabla\cdot\mathbf{a} = \partial a_z/\partial z = 0$, so that $a_z = a_z|_{t=0} = 0$ and $\mathbf{a} = \mathbf{a}_\perp$. Projecting the general momentum equation Eq. (A.25d) onto the transverse direction, it is shown that the transverse motion of the electron is due purely to the laser ($\mathbf{u}_\perp = \mathbf{a}_\perp = \mathbf{a}$).

It is convenient to introduce an algebraic transformation from the laboratory frame to the laser pulse frame $(z,t) \mapsto (\xi,\tau)$, with $\xi = z - ct$ and $\tau = t$. Here, the phase velocity of the plasma wave, *i.e.*, the group velocity of the laser, is considered equal to

the speed of light ($v_p \simeq v_g^L = c(1-\omega_p^2/\omega^2)^{1/2} \simeq c$ for $\omega_p \lll \omega$). As discussed in Sec. 2.6, the group velocity is responsible for one of the limitations to laser-plasma acceleration: the dephasing between the accelerated particles and the laser pulse.

In the moving frame (ξ, τ) and in the QSA, the continuity equation Eq. (A.25b) becomes $\partial\left[n(1-\beta_z)\right]/\partial\xi = 0$, so that $n(1-\beta_z) = n|_{t=0}(1-\beta_z|_{t=0}) = n_0$:

$$n/n_0 = (1-\beta_z)^{-1} \tag{A.26}$$

In the same manner, the longitudinal projection of the momentum equation Eq. (A.25d):

$$c\,\partial(\phi-\gamma)/\partial z = \partial u_z/\partial t \tag{A.27}$$

becomes $\partial\left[\phi-\gamma(1-\beta_z)\right]/\partial\xi = \partial u_z/\partial\tau = 0$, which provides the relation:

$$\gamma(1-\beta_z) = 1+\phi \tag{A.28}$$

Writing $\gamma = \sqrt{1+u_\perp^2+u_z^2} = \sqrt{1+a^2+\gamma^2\beta_z^2}$, the Lorentz factor associated with the electron is given by $\gamma = \sqrt{(1+a^2)/(1-\beta_z^2)}$. Substituting this expression of γ into Eq. (A.28) and noting $\gamma_\perp^2 = 1+a^2$, yields:

$$\beta_z = \frac{\gamma_\perp^2-(1+\phi)^2}{\gamma_\perp^2+(1+\phi)^2} \tag{A.29}$$

Hence,

$$\gamma = \frac{\gamma_\perp^2+(1+\phi)^2}{2(1+\phi)} \tag{A.30}$$

$$u_z = \frac{\gamma_\perp^2-(1+\phi)^2}{2(1+\phi)} \tag{A.31}$$

and Eq. (A.26) becomes:

$$\frac{n}{n_0} = \frac{\gamma_\perp^2+(1+\phi)^2}{2(1+\phi)^2} \tag{A.32}$$

where the potential ϕ of the plasma wave is solution of Poisson's equation, obtained by writing Eq. (A.25a) in the moving frame and substituting Eq. (A.32) into it:

$$\frac{\partial^2\phi}{\partial\xi^2} = \frac{k_p^2}{2}\left[\frac{\gamma_\perp^2}{(1+\phi)^2}-1\right] \tag{A.33}$$

Laser propagation: As discussed in Sec. 2.4, for an under-dense plasma ($\omega_p \ll \omega$), laser and plasma variables can be separated in high and low frequency components so we can write $\mathbf{a} \sim \mathbf{a}_f$, $\mathbf{u} = \mathbf{u}_f + \mathbf{u}_s$, $\phi \sim \phi_s$ and $n \sim n_s$ where the subscripts "$_f$" and "$_s$" denote the fast and slow response of each variable, respectively. In the quasi-static approximation (QSA), the second term on the right-hand side of Eq. (A.25c), $\partial\nabla\phi/\partial ct$, can be neglected and the wave equation in the frame of the laser pulse ($(z,t) \mapsto (\xi,\tau)$) is given by [215, 216]:

$$\left(\nabla_\perp^2 + \frac{2}{c}\frac{\partial^2}{\partial\xi\partial\tau} - \frac{1}{c^2}\frac{\partial^2}{\partial\tau^2}\right)\mathbf{a} = k_p^2\rho\,\mathbf{u} \tag{A.34}$$

where $\rho = n/\gamma n_0$. In the 1D case and in the Coulomb gauge ($\mathbf{a} = \mathbf{a}_\perp$) the projection of the momentum equation, Eq. (A.25d), onto the transverse dimension, $\partial\mathbf{u}_\perp/\partial t = c\nabla_\perp(\phi-\gamma)+\partial\mathbf{a}_\perp/\partial t$, provides the relation $\mathbf{u}_\perp = \mathbf{a}_\perp$. For a linearly polarized laser pulse with electric field of the form $\mathbf{a}_f = \mathbf{a}_s(r,\xi,\tau)e^{ik\xi}$, the term $\partial^2/\partial\tau^2$ in Eq. (A.34) can be neglected assuming the envelope $\mathbf{a}_s(r,\xi,\tau)$ evolves slowly:

$$\left(\nabla_\perp^2 + \frac{2}{c}\frac{\partial^2}{\partial\xi\partial\tau} + \frac{2ik}{c}\frac{\partial}{\partial\tau}\right)\mathbf{a}_s = k_p^2\rho\,\mathbf{a}_s \tag{A.35}$$

Finally, in the paraxial approximation where the pulse follows the main axis of propagation, spatial variations are slow and the term $\partial^2/\partial\xi\partial\tau$ is dropped, providing the paraxial wave equation:

$$\left(\nabla_\perp^2 + \frac{2ik}{c}\frac{\partial}{\partial\tau}\right)\mathbf{a}_s = k_p^2\rho\,\mathbf{a}_s \tag{A.36}$$

In the limit $v_p = c$ and in the QSA, it was shown, Eqs. (A.30, A.32), that $\rho = 1/(1+\phi)$ where ϕ is solution of Eq. (A.33), $\partial^2\phi/\partial\xi^2 = (k_p^2/2)[\gamma_\perp^2/(1+\phi)^2 - 1]$. Hence, the laser-plasma interaction can be calculated in 1D in an iterative fashion by solving Eq. (A.33) and update the laser pulse profile by solving Eq. (A.36).

Using Eq. (A.36) the usual propagation properties of Gaussian modes in vacuum can be retrieved. Gaussian modes are of interest because in the experiments the laser pulse transverse profiles are close to Gaussian distributions. In vacuum, $\rho = n/\gamma n_0 = 0$ and for $c\tau \equiv ct = z$, Eq. (A.36) becomes $(\nabla_\perp^2 + 2ik\partial/\partial z)\mathbf{a}_s = 0$. This equation is known as the Helmholtz paraxial equation [29]. A particular set of solutions to the Helmholtz paraxial equation are paraboloidal waves of the form $a_s(r) \equiv a_s = (A/z)\exp(-ikr^2/2z)$ which are the paraxial approximation of the spherical waves $(A/r)\exp(-ikr)$ for $r^2 \approx x^2 + y^2$ and $(x,y) \ll z$. A more general solution is given by replacing z by $q(z) = z - iz_0$ in

the Helmholtz paraxial equation, where z_0 is called the Rayleigh range and z_0/c is the characteristic laser evolution time. The function $1/q(z)$ can be separated into real and imaginary parts: $1/q(z) = 1/R(z) - i\lambda/\pi w(z)^2$ where $R(z) = z[1 + (z_0/z)^2]$ is the radius of curvature of the wavefront and $w(z) = w_0\sqrt{1 + (z/z_0)^2}$ is the waist of the beam and $w_0 = \sqrt{\lambda z_0/\pi}$ is the beam waist at focus. The paraboloidal wave equation then yields the solution:

$$a_s = A_0 \frac{w_0}{w(z)} e^{-r^2/w(z)^2} e^{-ikr^2/2R(z)+i\zeta(z)} \tag{A.37}$$

where $A_0 = A/iz_0$ is a constant and $\zeta(z) = \arctan(z/z_0)$ is the Gouy phase shift, *i.e.*, the phase difference between a Gaussian and a plane wave traveling along **z**.

Two-dimensional model: Plasma equations can be rewritten to include the transverse dimension of a laser pulse solution of the paraxial wave equation, assuming cylindrical symmetry [54, 215, 216, 217]. Poisson's equation, Eq. (A.25a), is given by $\nabla^2\phi = k_p^2(n - n_i)/n_0$ where $n_0 = n_i(r = 0)$ and can be written in the laser frame as follows:

$$\left(\nabla_\perp^2 + \frac{\partial^2}{\partial\xi^2}\right)\phi = k_p^2(\gamma\rho - \rho_0) \tag{A.38}$$

where $\rho_0 = \rho(t = 0) = n_i/\gamma_0 n_0$ with $\gamma_0 = 1$ for a cold plasma. The momentum equation, Eq. (A.25d), yields $\partial(\mathbf{u}-\mathbf{a})/\partial\tau - c\partial(\mathbf{u}-\mathbf{a})/\partial\xi = c\nabla(\phi-\gamma)$ where the term $\partial(\mathbf{u}-\mathbf{a})/\partial\tau$ can be neglected in the slow varying envelope approximation (SVEA):

$$\frac{\partial}{\partial\xi}(\mathbf{u}_s - \mathbf{a}_s) = \nabla(\gamma_s - \phi_s) \tag{A.39}$$

The wave equation on **a**, Eq. (A.34), can be written in the slowly varying envelope and paraxial approximations as:

$$\nabla_\perp^2 \mathbf{a}_s = k_p^2 \rho \mathbf{u}_s - \frac{\partial}{\partial\xi}\nabla\phi_s \tag{A.40}$$

In the laser frame $\overline{\boldsymbol{R}}$ the Hamiltonian of the 2D system is written (*c.f.* Sec. 2.5, Eq. (A.74)): $H_\mathrm{T} = m_e c^2[\overline{\gamma} - (\overline{\phi} - \overline{a})]$. Also, Eqs. (A.15) yield $\overline{\mathbf{E}} = -(E_0/k_p)(\nabla_\perp\overline{\phi} + \nabla_z\overline{\phi} + (1/c)\partial\overline{\mathbf{a}}/\partial\tau - \partial\overline{\mathbf{a}}/\partial z)$. Thus, in the SVEA the longitudinal component of the electric field becomes $E_z = \overline{E_z} = -(E_0/k_p)\partial(\overline{\phi} - \overline{a_z})/\partial z$ and $\overline{\phi} - \overline{a_z} = -(k_p\gamma_p/E_0)\int E_z(k_p u)du$ $= \gamma_p(\phi - a_z)$ (*c.f.* Sec. 2.5, Eqs. (A.71–A.73)). Finally, in the case of a cold plasma

$H_0 = H_\mathrm{T}/\gamma_p m_e c^2 = 1 = \gamma_s - \beta_p u_{z,s} - (\phi_s - a_{z,s})$ which yields the equation of energy:

$$\gamma_s - u_{z,s} = 1 + \phi_s - a_{z,s} \tag{A.41}$$

In the SVEA, the continuity equation, Eq. (A.25b), provides the relation $\partial(n_s/n_0)/\partial\xi = \partial(\rho_s\gamma_s)/\partial\xi = \nabla\cdot(\rho_s\mathbf{u}_s) = \nabla_\perp\cdot(\rho_s\mathbf{u}_{\perp,s}) + \partial(\rho_s u_{z,s})/\partial\xi$. Thus, $\partial[\rho_s(\gamma_s - u_{z,s})]/\partial\xi = \nabla_\perp\cdot(\rho_s\mathbf{u}_{\perp,s})$. Substituting Eq. (A.41) into this relation provides the following continuity equation:

$$\frac{\partial}{\partial\xi}\left[\rho_s(1+\Psi_s)\right] = \nabla_\perp\cdot(\rho\mathbf{u}_{\perp,s}) \tag{A.42}$$

where $\Psi_s = \phi_s - a_{z,s}$. Finally, Eqs. (A.38–A.42) can be combined, after some algebra, to provide the wake equation [54, 215, 216, 217]:

$$\frac{\partial^2\Psi_s}{\partial\xi^2} = (k_p^2\rho_s - \nabla_\perp^2)u_{z,s} + \frac{\partial}{\partial\xi}(\nabla_\perp\cdot\mathbf{u}_{\perp,s}) \tag{A.43}$$

where,

$$\rho_s = \frac{\rho_0 + (1/k_p^2)\nabla_\perp^2\Psi_s}{1+\Psi_s} \tag{A.44}$$

$$u_{z,s} = \frac{u_{\perp,s}^2 + a_s^2 - \Psi_s(2+\Psi_s)}{2(1+\Psi_s)} \tag{A.45}$$

$$\mathbf{u}_{\perp,s} = \frac{1}{k_p^2\rho_s}\frac{\partial}{\partial\xi}(\nabla_\perp\Psi_s) \tag{A.46}$$

and,

$$\gamma = \frac{1 + u_{\perp,s}^2 + a_s^2 + (1+\Psi_s)^2}{2(1+\Psi_s)} \tag{A.47}$$

Substituting Eq. (A.44) into the paraxial wave equation, Eq. (A.36), yields:

$$\left(\nabla_\perp^2 + \frac{2}{c}\frac{\partial^2}{\partial\xi\partial\tau} + \frac{2ik}{c}\frac{\partial}{\partial\tau}\right)\mathbf{a}_s = k_p^2\frac{\rho_0 + (1/k_p^2)\nabla_\perp^2\Psi_s}{1+\Psi_s}\mathbf{a}_s \tag{A.48}$$

Equations (A.43) and (A.48) describe the 2D cold axisymmetric, quasi-static laser-plasma interaction.

Refractive guiding: The index of refraction for a plane wave traveling in a plasma can be obtained by expressing the dispersion relation for that wave. Taking the curl of the Faraday equation (Eq. (A.14c)), substituting Ampère's law (Eq. (A.14d)) into it and using the vectorial identity $\nabla\times\nabla\times\mathbf{A} = \nabla(\nabla\cdot\mathbf{A}) - \nabla^2\mathbf{A}$ yields the wave equation:

$\nabla^2\mathbf{E} - \nabla(\nabla\cdot\mathbf{E}) - \mu_0\epsilon_0\partial^2\mathbf{E}/\partial\mathbf{t}^2 = \mu_0\partial\mathbf{j}/\partial t$. For monochromatic plane wave solutions of the form $\mathbf{E}(\mathbf{r},t) = \mathbf{E}_0\exp[i(\mathbf{k}\cdot\mathbf{r}) - \omega t]$, we have:

$$-k^2\mathbf{E} + \mathbf{k}(\mathbf{k}\cdot\mathbf{E}) + \frac{\omega^2}{c^2}\mathbf{E} = -i\omega\mu_0\mathbf{j} \tag{A.49}$$

Since electromagnetic waves are transverse waves $\mathbf{k}\cdot\mathbf{E} = 0$ and:

$$(\omega^2 - k^2c^2)\mathbf{E} = -i(\omega/\epsilon_0)\mathbf{j} \tag{A.50}$$

where $\mathbf{j} = -n_0e\mathbf{v}$ for an under-dense ($\omega_p \ll \omega$) plasma of uniform density n_0. In the linear theory and for a non-magnetic plasma Eq. (A.19) provides $m_e\partial\mathbf{v}/\partial t = -e\mathbf{E}$ which yields $\mathbf{v} = e\mathbf{E}/im_e\omega$. Substituting this expression and Eq. (2.1) into Eq. (A.50) yields the dispersion relation for the linear regime [79]:

$$\omega^2 = k^2c^2 + \omega_p^2 \tag{A.51}$$

The phase velocity of the laser is then given by ($k = \omega/v_p$):

$$v_p = c\,(1 - \omega_p^2/\omega^2)^{-1/2} \tag{A.52}$$

and the group velocity by ($v_g = \partial\omega/\partial k$):

$$v_g = c\,(1 - \omega_p^2/\omega^2)^{1/2} \tag{A.53}$$

Hence, in the linear regime the index of refraction of the plasma is given by ($\eta = c/v_p$):

$$\eta = \sqrt{1 - \omega_p^2/\omega^2} \tag{A.54}$$

Note that in Eq. (A.51), $k \in \mathbb{R}$ if $\omega^2 > \omega_p^2$, *i.e.*, $n_e < n_c$ (Eq. (2.1)), where n_c is the critical density above which the wave will not propagate through the plasma:

$$n_c = m_e\epsilon_0\omega^2/e^2 \tag{A.55}$$

$$= 4\pi^2 m_e/\mu_0\lambda^2e^2 \tag{A.56}$$

$$n_c\,[10^{19}\ \mathrm{cm}^{-3}] \simeq 111.5 \times \lambda^{-2}\,[\mu\mathrm{m}] \tag{A.57}$$

In the nonlinear regime, a corrective factor is applied to ω_p. Looking at the right-hand side of Eq. (A.36), the effective wavenumber is defined as $k_{p,\mathrm{eff.}}^2 = k_p^2\rho$ with $\rho = n/n_0\gamma$

and provides the relation $\omega_{p,\text{eff.}}^2 \equiv \omega_p^2 = \omega_{p,0}^2 \rho(r)$ where $\omega_{p,0} = \omega_p(n = n_0)$. Thus, the nonlinear index of refraction is given by:

$$\eta(r) = \sqrt{1 - \frac{n(r)\omega_{p,0}^2}{n_0 \gamma(r)\omega^2}} \tag{A.58}$$

where $n(r)$ and $\gamma(r)$ are respectively given by Eq. (A.44) and Eq. (A.47). Since the quiver motion is the main component of the electron's motion, γ can be written $\gamma \approx \gamma_\perp = \sqrt{1 + a_f^2}$.

As stated in Sec. 2.4, for a maximum on-axis, the radial dependency of the index of refraction can be used to provide refractive guiding of the laser pulse beyond the diffraction limited acceleration length, which is typically of the order of the Rayleigh length. In the presence of a preformed plasma channel of radius r_0, modeled by a quadratic function centered on-axis, and a laser-induced plasma density perturbation $\delta n(r)$, the density profile is given by $n = n_0 + [n(r_0) - n_0]r^2/r_0^2 + \delta n(r) \equiv n_0 + \Delta n(r) + \delta n(r)$. Hence, the index of refraction can be written:

$$\eta(r)^2 \approx 1 - \frac{\omega_{p,0}^2}{\gamma_\perp(r)\omega^2}\left[1 + \frac{\Delta n(r)}{n_0} + \frac{\delta n(r)}{n_0}\right] \tag{A.59}$$

From Eq. (A.59), it appears the phase velocity ($v_p = c/\eta$) increases as a function of the radial distance r for $\partial n/\partial r > 0$ or $\partial a_f/\partial r < 0$. A preformed plasma density channel with a minimum on-axis (channel guiding) or a laser pulse peaked on-axis (self-guiding) can lead to a propagation length inside the plasma of several Rayleigh lengths, a greater acceleration length and consequently higher electron energies [12].

For a preformed plasma channel of the form $\Delta n(r) = [n(r_0) - n_0]r^2/r_0^2$ and for a Gaussian laser pulse, it is possible to calculate the change of density required to guide the pulse through it. A generalized form of Eq. (A.37) is given by:

$$a_s = A_0 \frac{w_0}{r_g} \exp\left[i\zeta - (1 + i\alpha)\frac{r^2}{r_g^2}\right] \tag{A.60}$$

where $r_g \equiv w(z)$ is the guided spot size, $\alpha(z)$ and $\zeta(z)$ are respectively the wavefront curvature and phase shift. Substituting Eq. (A.60) into the paraxial wave equation,

$(\nabla_\perp^2 + 2ik\partial/\partial z)\mathbf{a}_s = k_{p,\text{eff.}}^2 \mathbf{a}_s$, leads to (identifying real and imaginary parts):

$$\left(\frac{2\alpha}{r_g^2} + k^2\frac{r_g'}{r_g}\right)\left(2\frac{r^2}{r_g^2} - 1\right) = 0 \tag{A.61a}$$

$$\left(-\frac{4}{r_g^2} - 2k\zeta'\right) + \frac{r^2}{r_g^2}\left[\frac{4}{r_g^2}(1-\alpha^2) + 2k\alpha' - 4k\alpha\frac{r_g'}{r_g}\right] = k_p^2 + \frac{r^2}{r_g^2}\frac{\Delta n(r)k_p^2 r_g^2}{n_0 r_0^2} \tag{A.61b}$$

where the right-hand side term of Eq. (A.61b) was given by $k_{p,\text{eff.}}^2 = k_p^2(1 + \Delta r^2/n_0 r_0^2)$ since prior arrival of the laser pulse $\delta n = 0$ and $\gamma_\perp = 1$. Since these equations are true $\forall\, r$, we have:

$$\begin{cases} \alpha = -k r_g r_g'/2 \\ (4/r_g^2)(1-\alpha^2) + 2k\alpha' - 4k\alpha r_g'/r_g = \Delta n(r) k_p^2 r_g^2/n_0 r_0^2 \end{cases} \tag{A.62}$$

Substituting the expression of α into the second equation of Eq. (A.62) and defining the normalized waist $R_g = r_g/r_0$ yields [120]:

$$\frac{d^2 R_g}{dz^2} = \frac{1}{Z_0^2 R_g^3}\left(1 - \frac{\Delta n}{\Delta n_c} R_g^4\right) \tag{A.63}$$

where $Z_0 = k r_0^2/2$ and [54],

$$\Delta n_c = 4n_0/k_p^2 r_0^2 \tag{A.64}$$

$$= 1/\pi r_e r_0^2 \tag{A.65}$$

$$\Delta n_c\,[10^{18}\ \text{cm}^{-3}] \simeq 113 \times r_0^{-2}\,[\mu\text{m}] \tag{A.66}$$

is the critical channel depth necessary to guide a spot of size $r_g = r_0$. Note that for a matched beam spot size $w_0 = r_0$, $Z_0 = z_0$, *i.e.*, the Rayleigh length of the Gaussian beam. Thus, for parameters close to the capillary experiments performed at the LOASIS such as an initial plasma density $n_0 = 3 \times 10^{18}\ e^-/\text{cm}^3$ and a matched beam spot size $w_0 = r_0 = 20\ \mu$m, $\Delta n_c \simeq 0.3 \times 10^{18}\ e^-/\text{cm}^3$, *i.e.*, 10% of n_0.

Trapping and acceleration: To describe the injection and acceleration of electrons in a plasma wave, it is possible to analyze the motion of a test electron in a 1D plasma wave using Hamiltonian dynamics [56], *i.e.*, calculating the energy of that particle. In this model, the frame of the laser, moving at the phase velocity v_p in the laboratory frame, is called $\overline{\boldsymbol{R}}$. The laboratory frame in which the test electron has the velocity v_z

is called $\boldsymbol{R}$. In the moving frame, the Hamiltonian (*i.e.*, total energy) of the electron is given by:

$$\mathcal{E}_{\text{tot}} = H_{\text{T}} = \mathcal{E}_{\text{kinetic}} + \mathcal{E}_{\text{potential}} + \mathcal{E}_{\text{mass}} = (\overline{\gamma} - 1)m_e c^2 - \overline{V}e + m_e c^2 \tag{A.67}$$

which can be written using the normalized scalar potential $\overline{\phi} = e\overline{V}/m_e c^2$ as:

$$H_{\text{T}} = m_e c^2(\overline{\gamma} - \overline{\phi}) \tag{A.68}$$

To express $\overline{\gamma}$ and $\overline{\phi}$ in the laboratory frame, let's consider the Lorentz transformation:

$$\boldsymbol{T_L} : (\boldsymbol{R} \to \overline{\boldsymbol{R}}) = \begin{cases} \overline{z} = \gamma_p(z - v_p t) = \gamma_p \xi \\ \overline{t} = \gamma_p(t - \beta_p z/c) \end{cases} \tag{A.69}$$

which yields $\overline{v_z} = d\overline{z}/d\overline{t} = (v_z - v_p)/(1 - \beta_p\beta_z)$ and ($\gamma \equiv \gamma_z$):

$$\overline{\gamma} = \gamma\gamma_p(1 - \beta_p\beta_z) \tag{A.70}$$

In addition, the longitudinal electric field is unchanged by the Lorentz transformation: $\overline{\mathbf{E}_\parallel} = \mathbf{E}_\parallel$ and, in the Coulomb gauge ($\mathbf{A} = \mathbf{A}_\perp \Rightarrow A_z = 0$): $E_z = \overline{E_z} = -\partial\overline{\Phi}/\partial\overline{z} - \partial\overline{A_z}/\partial\overline{t} = -\partial\overline{\Phi}/\partial\overline{z} = -(m_e c^2/e)\partial\overline{\phi}/\partial\overline{z}$. Using Eq. (2.1) and Eq. (2.8) we have $m_e c^2/e = E_0/k_p$. The transformed wavenumber is found using Eqs. (A.69): $k_p\xi = (k_p/\gamma_p)\overline{z} \equiv \overline{k_p}\overline{z}$ and the longitudinal electric field can be expressed as:

$$E_z(k_p\xi) = E_z(\overline{k_p}\overline{z}) = -\frac{E_0}{k_p}\frac{\partial\overline{\phi}}{\partial\overline{z}} \tag{A.71}$$

Hence,

$$\overline{\phi} = -\frac{k_p}{E_0}\int E_z(\overline{k_p}\overline{z})d\overline{z} \tag{A.72}$$

Using the change of variable $\overline{z} \mapsto \gamma_p u$, for which $\overline{k_p}\overline{z} = \overline{k_p}\gamma_p u = k_p u$ and $d\overline{z} = \gamma_p du$, Eq. (A.72) becomes:

$$\overline{\phi} = -\frac{k_p\gamma_p}{E_0}\int E_z(k_p u)du = \gamma_p\phi \tag{A.73}$$

Finally, the normalized Hamiltonian ($H = H_\mathrm{T}/(\gamma_p m_e c^2)$) [56] of the test electron is obtained by substituting Eqs. (A.70, A.73) into Eq. (A.68):

$$H = \gamma(1 - \beta_p\beta_z) - \phi \tag{A.74}$$

Note that this equation could be found directly from the momentum equation, Eq. (A.25d). Applying $(z,t) \mapsto (\xi,\tau)$ to its projection onto $\mathbf{z}$ (Eq. (A.27)) yields [47]:

$$\frac{\partial}{\partial\xi}\left[\gamma(1 - \beta_p\beta_z) - \phi\right] = -\frac{1}{c}\frac{\partial u_z}{\tau} \tag{A.75}$$

In the QSA, Eq. (A.75) writes $\gamma(1 - \beta_p\beta_z) - \phi = [\gamma(1 - \beta_p\beta_z) - \phi]_{t=0} = H_0$.

A general solution of Eq. (A.74) can be found in terms of γ for an electron with initial position ξ_0, initial potential ϕ_0 and initial energy γ_0 by solving $H = H_0 = \gamma - \beta_p u_z - \phi = \gamma - \beta_p\sqrt{\gamma^2 - 1} - \phi$:

$$\gamma = \gamma_p^2(H_0 + \phi) \pm \beta_p\gamma_p\sqrt{\gamma_p^2(H_0 + \phi)^2 - 1} \tag{A.76}$$

For an electron initially at rest, $H_0 = 1$ since $\phi_0 = 0$ and $\gamma_0 = 1$, the momentum equation becomes:

$$\gamma = \gamma_p^2(1 + \phi) \pm \beta_p\gamma_p\sqrt{\gamma_p^2(1 + \phi)^2 - 1} \tag{A.77}$$

and describes an open orbit in phase-space or "fluid" orbit.

The Hamiltonian map (*e.g.*, Fig. 2.4a) shows local minima (stable points) and maxima (unstable points) where the potential ϕ is respectively maximum and minimum. At the limit between closed and open orbits, $\gamma = \gamma_p$ and the Hamiltonian values corresponding to the local extrema are given by ($u_z|_{t=0} = u_p = \gamma_p\beta_p$):

$$\begin{cases} H_\mathrm{min} = 1/\gamma_p - \phi_\mathrm{max} \\ H_\mathrm{max} = 1/\gamma_p - \phi_\mathrm{min} \end{cases} \tag{A.78}$$

The two trajectories for which $H = H_\mathrm{max}$ form the separatrix, a boundary in phase-space separating the fluid orbits from the trapped ones (Fig. 2.4b, *black dashed curves*). The maximum energy gain occurs when an electron is trapped on the closed orbit just inside the *lower* separatrix and exit the plasma after reaching the maximum of the *upper* separatrix (ideal case). Defining $\Delta\phi = \phi - \phi_\mathrm{min}$ and substituting the expression of H_max

in Eq. (A.76) yields [56]:

$$\gamma(\phi) = \gamma_p(1 + \gamma_p\Delta\phi) \pm \beta_p\gamma_p\sqrt{(1 + \gamma_p\Delta\phi)^2 - 1} \tag{A.79}$$

Hence, $\gamma_{\text{min, max}} = \gamma(\phi_{\text{max}})^{\mp}$ and the maximum gain $\Delta\gamma = \gamma_{\text{max}} - \gamma_{\text{min}}$ can be written:

$$\Delta\gamma = 2\beta_p\gamma_p\sqrt{(1 + \gamma_p\Delta\phi)^2 - 1} \tag{A.80}$$

which, in the limit $\gamma_p\Delta\phi \gg 1$ simplifies as:

$$\Delta\gamma \approx 2\beta_p\gamma_p^2\Delta\phi \tag{A.81}$$

Note that from Eq. (A.79) we have $\gamma_{\text{min}} = \gamma_p$ for $\phi = \phi_{\text{min}}$ corresponding to the local maxima in Fig. 2.4 (unstable points). In the example of Fig. 2.4, $\phi_{\text{min, max}}$ are found by solving Eq. (A.33) to be $\phi_{\text{min}} \simeq -0.147$ and $\phi_{\text{max}} \simeq 0.331$. Since it is a mildly nonlinear case ($a_0 = 1$), the phase velocity is calculated using the linear formula: $v_p = c(1 - \omega_p^2/\omega^2)^{1/2}$; and we get $\beta_p \simeq 1 - 1.15 \times 10^{-3}$ and $\gamma_p \simeq 20.9$. Thus, the maximum energy gain is calculated to be $\Delta\gamma \simeq 456$, for which the maximum electron energy at the exit of the plasma is $\mathcal{E}_{\text{max}} = (\gamma_{\text{max}} - 1)m_ec^2 \simeq 230$ MeV.

For a "square"-like laser pulse, it is possible to calculate $\Delta\phi$ analytically as a function of the maximum normalized electric field generated by the plasma density wave, $\tilde{E}_{\text{max}} = E_{\text{max}}/E_0$ [56]. For a square pulse, $a(\psi) \equiv a(k_p\xi)$ is a piecewise constant function. Thus, $\gamma_\perp^2 = 1 + u_\perp^2 = 1 + a^2$ can be treated as a constant in Eq. (2.5) and the first integral calculated. Noting $x(\psi) = 1 + \phi(\psi)$ and $x' = dx/d\psi$, we have $d^2\phi/d\psi^2 = x'dx'/dx$ and:

$$\int_0^{x'} \tau' d\tau' = \int_{x_0}^{x} \gamma_p^2 \left[\frac{\beta_p}{\sqrt{1 - \gamma_\perp^2/\gamma_p^2\tau^2}} - 1\right] d\tau \tag{A.82}$$

where $x(\psi) = x_0$ when $x'(\psi) = 0$. Since ϕ can be positive, we have $\gamma_p x \geq 0$ and:

$$x'^2 = 2\gamma_p^2\left[x_0 - x + \beta_p\left(\sqrt{x^2 - \gamma_\perp^2/\gamma_p^2} - \sqrt{x_0^2 - \gamma_\perp^2/\gamma_p^2}\right)\right] \tag{A.83}$$

Note that since $E_z = -E_0 d\phi/d\psi$ (Eq. (A.73)), $x'^2 = \tilde{E}^2$. The electric field can then be written:

$$\tilde{E}(x) = \sqrt{2}\gamma_p\left(-x + \beta_p\sqrt{x^2 - \gamma_\perp^2/\gamma_p^2} + \alpha\right) \tag{A.84}$$

where $\alpha = x_0 - (x_0^2 - \gamma_\perp^2/\gamma_p^2)^{1/2}$. Solving $d\tilde{E}/dx = 0$ yields the extremum $x = 1$ ($\phi = 0$). Finally, the minimum and maximum normalized electric fields are obtained for $\gamma_\perp = 1$, $x_0 = x_{\min} = 1 + \phi_{\min}$ and $x_0 = x_{\max} = 1 + \phi_{\max}$ (subscript "$_{\rm m}$" denotes both extrema):

$$\tilde{E}_{\rm m}^2/2 = \gamma_p^2 x_{\rm m} - 1 - \beta_p \gamma_p^2 \sqrt{x_{\rm m}^2 - 1/\gamma_p^2} \tag{A.85}$$

which yields [56]:

$$\phi_{\rm m} = \tilde{E}_{\rm m}^2/2 \pm \beta_p \sqrt{(1 + \tilde{E}_{\rm m}^2/2)^2 - 1} \tag{A.86}$$

and,

$$\Delta\phi = 2\beta_p \sqrt{(1 + \tilde{E}_{\rm m}^2/2)^2 - 1} \tag{A.87}$$

which can be substituted into Eq. (A.80) to calculate the maximum energy gain of a trapped electron.

In the cold fluid relativistic model, wavebreaking occurs as a limitation of the model; Eq. (2.5) presents a singularity for $\phi \to -1 + \gamma_\perp/\gamma_p$ ($x_{\rm m} \to 1/\gamma_p \in [0, 1]$). The physical solution is found for $x_{\min} \to 1/\gamma_p$ which yields, *c.f.* Eq. (A.85), $\tilde{E}_{\rm m}^2 = 2(\gamma_p - 1)$. Using Eq. (A.87), it comes $x_{\max} = x_{\min} + \Delta x = x_{\min} + \Delta\phi \to (2\gamma_p^2 - 1)/\gamma_p$, which yields a potential difference at wavebreaking of $\Delta\phi_{\rm WB} = 2(\gamma_p^2 - 1)/\gamma_p = 2\beta_p^2\gamma_p$. The cold fluid relativistic wavebreaking electric field [50, 56] is then found by solving Eq. (A.87):

$$E_{\rm WB} = \sqrt{2(\gamma_p - 1)} E_0 \tag{A.88}$$

For a plasma density of 4×10^{18} e^-/cm^3 (Fig. 2.4), $E_0 \simeq 1.9$ GV/cm and $E_{\rm WB} \simeq 6.3 \times E_0 \simeq 12$ GV/cm. Substituting $\Delta\phi_{\rm WB}$ into Eq. (A.79), the maximum electron energy at the exit of the plasma is calculated to be $\mathcal{E}_{\max} \simeq 18.5$ GeV.

Appendix B

THz Wavefront Characterization

In this Appendix, we present a simple ray model of the THz transport line. The THz pulse is emitted at the downstream surface of the plasma. A 3-inch diameter parabola with 6-inch effective focal length collects part of the radiation and collimates it. The wavefront of the THz beam is described in terms of Zernike polynomials. These polynomials have several interesting properties like being a complete set of polynomials in two real variables, ρ and θ that are orthogonal in a continuous fashion over a unit circle. They have simple rotational properties that lead to a polynomial product which has the form of $Z = R(\rho) \cdot G(\theta)$ where $G(\theta)$ is a continuous periodic function (T = 2 π) and satisfies a rotational independence: $G(\theta + \alpha) = G(\theta)G(\alpha)$. The set of trigonometric functions $G(\theta) = e^{\pm im\theta}$ where m is any positive integer or zero, meets these requirements.
Other properties of Zernike polynomials are that the radial function must be a polynomial in ρ of degree n such as $m \leqslant n$ and that $R(\rho)$ must be even if m is even and odd if m is so. Radial polynomials can be derived as a special case of Jacobi polynomials and tabulated as $R_n^m(\rho)$. Their orthogonality and normalization properties are given by:

$$\int_0^1 R_n^m(\rho) \cdot R_{n'}^m(\rho) \cdot \rho \, d\rho = \frac{1}{2(n+1)} \, \delta_{nn'} \tag{B.1}$$

and $R_n^m(1) = 1$. Finally, first order Zernike polynomials are listed in Tab. B.1 and commented by what aberration they correspond to.

The model we propose is based on ray optics assuming in first order that the transition radiation is composed of a narrow bandwidth. The calculation of the wavefront is done in a cartesian frame. We first made calculations in case of a perfect alignment of the

n	m	Name	Polynomial	Aberration
0	0	0	1	Piston
1	1	1	$\rho\cos\theta$	Tilt X
		2	$\rho\sin\theta$	Tilt Y
	0	3	$2\rho^2-1$	Defocus
2	2	4	$\rho^2\cos 2\theta$	0° Astigmatism
		5	$\rho^2\sin 2\theta$	45° Astigmatism
	1	6	$(3\rho^2-2)\cdot\rho\cos\theta$	Coma X
		7	$(3\rho^2-2)\cdot\rho\sin\theta$	Coma Y
	0	8	$6\rho^4-6\rho^2+1$	Spherical

Table B.1: First order Zernike polynomials and aberrations. Note that the classification we present is not universal, other classifications may be used.

parabola in order to check if we retrieved a flat and circular wavefront as the theory predicts. The frame in which we defined the problem was the parabola's frame, $\mathcal{R}_{OAP}$ (see Fig. B.1).

In this way the origin is the focus (plasma) and the middle of the OAP stands at the coordinates $(0\,;0\,;6)$ since parabola's effective focal length is 6 inches. From this, one can deduce the surface equation (paraboloid) of the OAP, Eq. (B.2).

$$y=\frac{1}{12}\left(x^2+z^2\right)-3 \tag{B.2}$$

However, the OAP is only a part of the surface that Eq. (B.2) describes. A parametric description of the contour of our OAP was used since the contour can be calculated as the intersection between a 3 inch diameter cylinder and the paraboloid surface. The base (circle) of the cylinder is given by:

$$\begin{cases} x(t')=-\frac{3}{2}\sin t' \\ z(t')=\frac{3}{2}\cos t'+6 \end{cases} \tag{B.3}$$

where $t'\in[0\,;2\pi]$ is a parameter. Combining Eq. (B.2) and Eq. (B.3) one finds for the

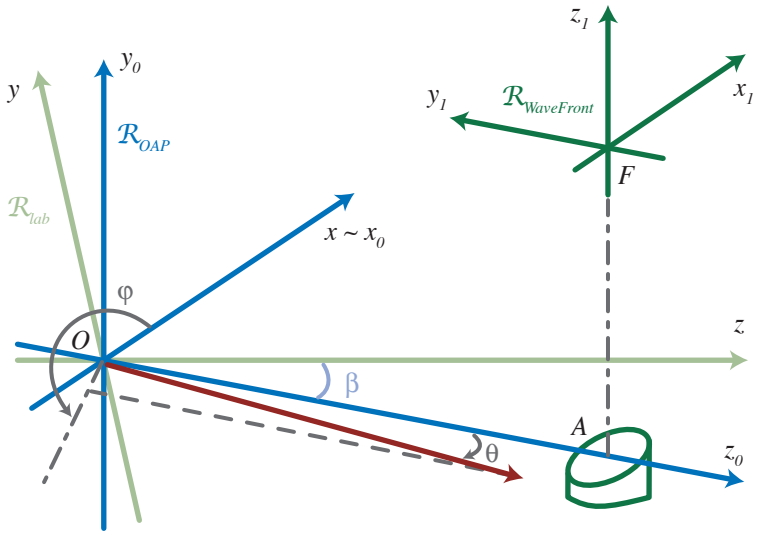

Figure B.1: Frames used to describe the wavefront of a misaligned off-axis parabola. $\mathcal{R}_{OAP}$ is the so called parabola's frame β-rotated from $\mathcal{R}_{lab}$, the laboratory's frame. In order to describe the optical system as a centered one we consider the frame $\mathcal{R}_{WaveFront}$ ($\mathcal{R}_{WF}$) in which the origin is on the reflected path of the photon, $(\theta\,;\varphi) = (0\,;0)$, which hurt the parabola in its center.

contour's equation ($t' \in [0\,;2\pi]$):

$$\begin{cases} x(t') = -\frac{3}{2}\sin t' \\ y(t') = \frac{3}{2}\cos t' + \frac{3}{16} \\ z(t') = \frac{3}{2}\cos t' + 6 \end{cases} \tag{B.4}$$

Now that we defined our parabolic mirror in space we can imagine a photon coming from the origin and being reflected by the mirror. Considering a bunch of them, all defined by emission angles $(\theta\,;\varphi)$ as illustrated in Fig. B.1, we can find their position along the time in our cartesian frame. The angle θ is the one between the beam traced by the photon we consider and z_o-axis such as $\theta \in [0\,;\pi]$.

Since we study aberrations introduced by a misalignment due to translations in space we will consider that photons are not emitted from the origin of $\mathcal{R}_o$ but from a source point shifted by a vector $(\delta_x\,;\delta_y\,;\delta_z)$ such as the evolution in time t of its position $\overrightarrow{OM}$

after virtual emission can be expressed (c is the speed of light):

$$\overrightarrow{OM} = \begin{cases} x(t) = ct\sin\theta\cos\varphi + \delta_x \\ y(t) = ct\sin\theta\sin\varphi + \delta_y \\ z(t) = ct\cos\theta + \delta_z \end{cases} \tag{B.5}$$

Equations (B.2) and (B.5) yield the time after which the photon hits the parabola and thus on which point of the parabola:

$$t_1 = 6\,\frac{\alpha - \tau + \mu}{\lambda \cdot c} \tag{B.6}$$

with,

$$\alpha = \sqrt{1 + \tau(\tau - 2\mu) - \frac{\gamma}{3}\lambda} \tag{B.7}$$

$$\lambda = \sin^2\theta\cos^2\varphi + \cos^2\theta \tag{B.8}$$

$$\mu = \sin\theta\sin\varphi \tag{B.9}$$

$$\tau = \frac{\delta_x}{6}\sin\theta\cos\varphi + \frac{\delta_z}{6}\cos\theta \tag{B.10}$$

$$\gamma = \frac{\delta_x^2}{12} + \frac{\delta_z^2}{12} - \delta_y \tag{B.11}$$

Consider A the point on the parabola hurt by the considered beam $(\theta\,;\varphi)$, see Eq. (B.12). Since we know the surface equation, Eq. (B.2), of the OAP one can calculate the normal vector $\overrightarrow{n}$ to this surface at a given point, Eq. (B.13).

$$\overrightarrow{OA} = \begin{cases} 6\,\frac{\alpha-\tau+\mu}{\lambda}\cdot\sin\theta\cos\varphi + \delta_x \\ 6\,\frac{\alpha-\tau+\mu}{\lambda}\cdot\sin\theta\sin\varphi + \delta_y \\ 6\,\frac{\alpha-\tau+\mu}{\lambda}\cdot\cos\theta + \delta_z \end{cases} \tag{B.12}$$

$$\overrightarrow{n} = \begin{cases} \frac{1+\mu}{\lambda}\cdot\sin\theta\cos\varphi \\ -1 \\ \frac{1+\mu}{\lambda}\cdot\cos\theta \end{cases} \tag{B.13}$$

To define the reflected beam we need to choose a point either in time or in space where the measure of the wavefront takes place. Let us consider t_f the time after a photon's

emission we measure its position (P). The reflected beam's norm is then $AP = c(t_f - t_1)$ and using Snell–Descartes laws:

$$\overrightarrow{AP} = \alpha_1 \cdot \overrightarrow{OA} + \alpha_2 \cdot \overrightarrow{n} \tag{B.14}$$

Note that the base $(\overrightarrow{OA}, \overrightarrow{n})$ is not orthogonal which means that we need to project, Eq. (B.14), in this base and to solve the obtained system of equations. Solutions are given by:

$$\alpha_1 = -AP \cdot \frac{2\cos i}{n} \tag{B.15}$$

$$\alpha_2 = \frac{AP}{OA} \tag{B.16}$$

where i is the oriented angle $(\overrightarrow{OA}, \overrightarrow{n})$, n and OA are norms of the respective vectors. OA can be easily calculated from Eq. (B.12) and thus yields n and i:

$$\cos i = \frac{\overrightarrow{OA} \cdot \overrightarrow{n}}{OA \times n} \tag{B.17}$$

$$n = \sqrt{\frac{2}{1-\mu}} \tag{B.18}$$

where:

$$\overrightarrow{OA} \cdot \overrightarrow{n} = 6\,\frac{\alpha - \tau + \mu}{\lambda} + \frac{\delta x}{1-\mu} \cdot \sin\theta\cos\varphi - \delta y + \frac{\delta z}{1-\mu} \cdot \cos\theta \tag{B.19}$$

Now in order to express the wavefront in the frame $\mathcal{R}_{WF}$ (Fig. B.1) one can write $\overrightarrow{FP} = \overrightarrow{OP} - \overrightarrow{OF}$ in the frame $\mathcal{R}_{OAP}$. In this expression, $\overrightarrow{OP} = \overrightarrow{OA} + \overrightarrow{AP} = (\alpha_1 + 1) \cdot \overrightarrow{OA} + \alpha_2 \cdot \overrightarrow{n}$ and $\overrightarrow{OF} = \overrightarrow{OA_F} + \overrightarrow{A_F F}$. To simplify notations we write $\overrightarrow{OA} = (x_A\,;y_A\,;z_A)$ and $\overrightarrow{n} = (n_x\,;n_y\,;n_z)$. The optical system we are dealing with is not a centered optical system but it might be possible to treat it as a centered one by the following transformation (Fig. B.1):

$$\begin{cases} x_1 \equiv x_0 \\ y_1 \equiv -z_0 \\ z_1 \equiv y_0 \end{cases} \tag{B.20}$$

Since $\overrightarrow{OA_F} = (0\,;0\,;6)$ and $\overrightarrow{A_F F} = \alpha_1^F \cdot \overrightarrow{OA} + \alpha_2^F \cdot \overrightarrow{n}$, see Eq. (B.14), we finally have the expression of $\overrightarrow{FP}$ which defines in the cartesian frame $\mathcal{R}_{WF}$ the beam's wavefront:

$$\overrightarrow{FP} = \begin{cases} (1+\alpha_1-\alpha_1^F)\cdot x_A + (\alpha_2-\alpha_2^F)\cdot n_x \\ 6 - (1+\alpha_1-\alpha_1^F)\cdot z_A - (\alpha_2-\alpha_2^F)\cdot n_z \\ (1+\alpha_1-\alpha_1^F)\cdot y_A + (\alpha_2-\alpha_2^F)\cdot n_y \end{cases} \tag{B.21}$$

Moreover calculations have been implemented in a Matlab's file where any user can define a shift for the parabola (misalignment) in the laboratory's frame (Fig. B.1) through variables $(\Delta x\,;\Delta y\,;\Delta z)$ related to $(\delta x\,;\delta y\,;\delta z)$ via (Fig. B.1):

$$\begin{cases} \delta x = -\Delta x \\ \delta y = -\cos\beta\,\Delta y - \sin\beta\,\Delta z \\ \delta z = \sin\beta\,\Delta y - \cos\beta\,\Delta z \end{cases} \tag{B.22}$$

To characterize the calculated wavefront we need to proceed to a projection of its surface onto the Zernike polynomials base that we introduced. Since many publications [218, 219, 220, 221] treat this problem we will just summarize basics of calculations we used in our Matlab program. One may express the measured quantity φ_i (phase in units of length or time) in terms of Zernike polynomials as:

$$\varphi_i(\mathbf{r}_i) = \sum_{j=1}^{N} a_j Z_j(\mathbf{r}_i) + \delta\phi(\mathbf{r}_i) \quad \text{for } i = 1, 2, \cdots, M \tag{B.23}$$

where N is the total number of Zernike polynomials used, $Z_j(\mathbf{r}_i)$ is (see Tab. B.1) the j^{th} Zernike polynomial's value at the position $\mathbf{r}_i$, a_j is its coefficient, and $\delta\phi(\mathbf{r}_i)$ is the error due to the truncation of using only N Zernike polynomials. In our program we used the first 37 Zernike polynomials which is enough for the required. M is the number of measurements. Furthermore, Eq. (B.23) can be written in a matrix form:

$$\underbrace{\begin{pmatrix} Z_1(\mathbf{r}_1) & \cdots & Z_N(\mathbf{r}_1) \\ \vdots & \ddots & \vdots \\ Z_1(\mathbf{r}_M) & \cdots & Z_N(\mathbf{r}_M) \end{pmatrix}\begin{pmatrix} a_1 \\ \vdots \\ a_N \end{pmatrix}}_{\mathbf{Z\,a}} = \underbrace{\begin{pmatrix} \varphi_1 \\ \vdots \\ \varphi_M \end{pmatrix}}_{\mathbf{\Phi}} \tag{B.24}$$

Note that we need to consider a number M of measurements such as $M \geqslant N$ to make the system of equations determined. The Matlab routine gets a well overdetermined system since we choose usually $M = 1000$ whereas $N = 37$. To find a good fit one can minimize a least-square within a normalized beam aperture in order to keep Zernike polynomials orthogonal, *i.e.*,

$$\Delta = \sum_{i=1}^{M} \left(a_j Z_j(\mathbf{r}_i) - \varphi_i(\mathbf{r}_i)\right)^2 \tag{B.25}$$

which can be written in the matrix form:

$$\mathbf{Z}^{\mathrm{T}}\,\mathbf{Z}\,\mathbf{a} = \mathbf{Z}^{\mathrm{T}}\,\mathbf{\Phi} \tag{B.26}$$

and yields the coefficients through a direct inversion of the matrix (37×37):

$$\mathbf{a} = (\mathbf{Z}^{\mathrm{T}}\,\mathbf{Z})^{-1}\,\mathbf{Z}^{\mathrm{T}}\,\mathbf{\Phi} \tag{B.27}$$

Finally, two wavefront examples are shown in Fig. B.2 to illustrate calculations previously discussed. To compare the wavefront to what it should be in case of a perfect alignment, we plot for each both the misaligned wavefront and the one that we would get for $(\Delta x\,;\Delta y\,;\Delta z) = (0\,;0\,;0)$. We also present partially their Zernike coefficients. We give polynomial coefficients a_1 to a_8 corresponding to polynomials Z_1 to Z_8 (see Tab. B.1) which are mainly the ones we are interested in. These coefficients are normalized in order to reveal the relative importance of these coefficients. The next step is to evaluate the coefficients' evolution when we change $(\delta x\,;\delta y\,;\delta z)$ in order to be able to anticipate during experiments what translation we should apply to the OAP-down. In Fig. B.2 one may interpret coefficients such as for the left plot tilt X and defocus effects are equivalent whereas the tilt Y is dominating, and for the right plot a domination of the tilt X effect but with a strong defocusing. Actually we can correlate this meant with figures since on the left we see strong gradient along the Y-axis and on the right a strong one along the X-axis.

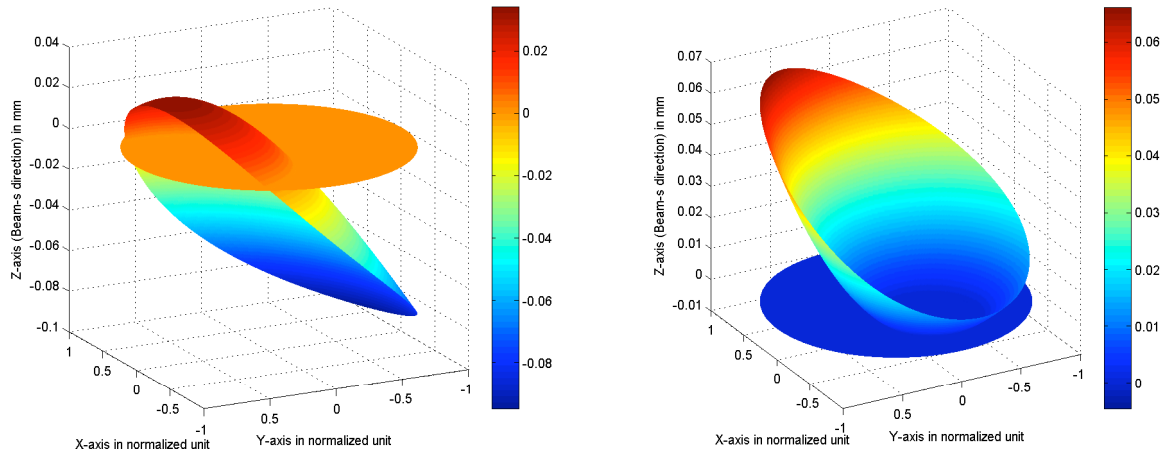

Plot	Tilt X	Tilt Y	Defoc.	0° Ast.	45° Ast.	Coma X	Coma Y	Spher.
Left	-0.2817	1	-0.3166	-0.1392	-0.0406	0.0014	-0.0651	-0.0012
Right	1	0.4799	0.7324	-0.0515	0.1094	-0.0055	0.1038	-0.0017

Figure B.2: Theoretical wavefronts of collimated beams collected by a misaligned off-axis parabola. Flat discs on both figures are flat wavefront one tries to get with a perfect alignment. On the left, we have in millimeters $(\Delta x\,;\Delta y\,;\Delta z) = (0.07\,;0.67\,;-1.08)$ and on the right $(\Delta x\,;\Delta y\,;\Delta z) = (-0.1\,;-0.35\,;1.1)$. Moreover, normalized coefficients of the Zernike polynomials decomposition are given for these plots in the table below curves.